ALMA MATER STUDIORUM – UNIVERSITA’ DI BOLOGNA

FACOLTA’ DI INGEGNERIA
Corso di Laurea Specialistica in Ingegneria Civile

D.I.C.A.M.
Dipartimento di Ingegneria Civile, Ambientale e dei Materiali

Tesi di Laurea in
Progetti di Strutture

SHAKE-TABLE TEST ON A FULL-SCALE BRIDGE REINFORCED CONCRETE COLUMN

Tesi di Laurea di:	Relatore:
CARREA FRANCESCO	Chiar.mo Prof. Ing. MARCO SAVOIA

Correlatori:
Chiar.mo Prof. Ing. CLAUDIO MAZZOTTI
Chiar.mo Prof. Ing. JOSE’ RESTREPO
Dott. Ing. MATTHEW SCHOETTLER
Dott. Ing. GABRIELE GUERRINI

Sessione III
Anno Accademico 2009/2010

Acknowledgments

First, I would like to thank Professor José I. Restrepo, my supervisor at the University of California - San Diego, for having conveyed to me his passion and motivation for research. I admire his special humanity with which he gave me precious teachings that turned out to be real life advices.

I would like to thank Matthew J. Schoettler, the post-doctoral investigator of the project, for having always found the time to explain everything to me and answer my many questions, even if under pressure. I admire his helpfulness, understanding and right amount of joy in work which made easier also the hardest job.

I would also like to thank Gabriele Guerrini, the PHD student involved in the project, for his assistance in the whole process of my thesis and enormous patience for reviewing my drafts. I admire his simplicity, honesty, availability through which he clarified all my doubts and gave me precious advice to overcome problems.

It was a pleasure to work with all the staff of the Englekirk Structural Engineering Center, at the University of California - San Diego, and everyone who worked at the project. The success of the experimental test is also due to them.

I acknowledge the University of Bologna, with special thanks to Prof. Marco Savoia, and the University of California - San Diego, for providing me with such a great opportunity for a new research experience.

I would like to thank my parents, who economically supported my experience at UCSD and helped me overcome difficult moments. Their generous love and understanding was very important for me to successfully finish my studies in Bologna.

Finally, I would like to remember my grandfather Giovanni, who is watching me from up there, whom I owe the discipline to work and my passion for this major.

Contents

1. Introduction

A full-scale, circular reinforced concrete bridge column, designed in accordance with the California Department of Transportation's (Caltrans) *Seismic Design Criteria* [Caltrans, 2006-a] and *Bridge Design Specifications* [Caltrans, 2004] guidelines, has been tested under seismic excitation. The experiment was conducted on the University of California – San Diego (UCSD) and Network for Earthquake Engineering Simulation (NEES) Large High Performance Outdoor Shake Table (LHPOST).

Under the auspices of the Pacific Earthquake Engineering Research Center (PEER), the Federal Highway Administration (FHWA), Caltrans, NEES, and industry sponsorships from Skanska and the Concrete and Reinforcing Steel Institute (CRSI), this research project tested a 1.22-m (4-ft) diameter cantilever column spanning 7.31 m (24 ft) above the footing. The inertia forces were generated by a massive 2322.3 kN (521.9 kips) reinforced concrete block supported on top of the column. A global view of the test specimen mounted on the shake table is given in Figure 1.1. This picture, taken the day before testing, shows also the restraint devices and the instrumentation installed on the specimen.

The column was tested under ten ground motions, starting with low-intensity jolts and bringing the column progressively to near-collapse conditions. The loading protocol included

Figure 1.1: Test specimen: reinforced concrete bridge column

records from historical earthquakes as well as white-noise excitation and ambient vibration tests. The latter allowed quantification of change in the system dynamic properties. The design earthquake for bridge columns according to Caltrans *Seismic Design Criteria* [Caltrans, 2006-a] has a 5% probability of exceedance in 50 years. For such earthquake cantilever columns are expected to sustain a displacement ductility demand of 4.0 and fully maintain their vertical load carrying capacity.

The objective of testing was to induce nonlinear deformation demands on the column and monitor the evolution of the dynamic response to increase the confidence in the current analysis methods and validate, or improve, the current design practice. Comparison with reduced-scale shake table tests, conducted at the University of California – Berkeley, provided also an assessment of the adequacy of reduce-scale models.

2. Test description

The experimental program consisted of a unidirectional shake-table test. It was conducted on a single specimen intended to represent a full-scale reinforced concrete bridge column.

2.1 Test setup

The test setup included, in addition to the test specimen, a restraint device to provide protection to site personnel and equipment, and about 270 sensors to monitor the dynamic response of the structure.

2.1.1 Test specimen

The specimen consisted of the reinforced concrete column, its footing, and a supported mass, as shown in Figure 2.1. The test specimen represents a fictitious bridge column designed to current Caltrans design guidelines. The footing provided to fix the specimen to the shake table through a post-tensioning system. The supported mass generated the inertial forces in order to mobilize the column capacity.

Figure 2.1: Test specimen: footing, column, superstructure

2.1.1.1 Footing

Normal weight concrete was used to cast the footing. The specified concrete compressive cylinder strength was 27.6 MPa (4.0 ksi), the ones measured at 28 and 45 days (first day of testing) were 38.8 MPa (5.6 ksi) and 42.0 MPa (6.1 ksi) respectively; the latter two values were obtained as the average from tests on three and six standard cylinders.

The measured concrete unit weight was 23.47 kN/m^3 (149.4 pcf); this value was obtained by averaging the unit weights of nine standard concrete cylinders. The cylinder weights are presented in Table A.1 of Appendix A.

An accurate evaluation of the footing weight, accounting for through holes and reinforcing steel, provided a total estimate of 298.1 kN (67.0 kips).

The footing was designed in accordance to Caltrans *Seismic Design Criteria* [Caltrans, 2006-a] and *Bridge Design Specifications* [Caltrans, 2004] guidelines. It consisted of a 5.49-m (18-ft) long, 1.83-m (6-ft) wide, 1.22-m (4-ft) deep reinforced concrete beam. Twenty-four #11 (36-mm diameter) bent bars provided longitudinal reinforcement, while two #4 (13-mm diameter) vertical "U" stirrups, spaced at 152 mm (6 in.) on-center constituted the transverse reinforcement. The moment resisting connection between the footing and the column was designed as to a superstructure "T" joint in accordance to Paragraph 7.4.4 of [Caltrans, 2006 a]. According to these provisions, six sets of three #4 (13-mm diameter) horizontal ties, longitudinally spaced at 457 mm (18 in.) on-center, were added in the joint zone. To satisfy the longitudinal face reinforcement requirement three #4 (13-mm diameter) bars were placed along the north and south sides. All the reinforcing steel in the footing consisted of Grade 60 bars conforming to the ASTM Designation A615. Footing details are shown in Figures 2.2 to 2.4.

The footing was post-tensioned to the shake table through twelve 44-mm (1.75-in.) diameter high strength bars, with a post-tensioned force of 979 kN (220 kips) each. The purpose of the post-tensioning system was to provide:

1. Normal contact force at the shake table-footing interface to prevent decompression under the maximum expected overturning moment;
2. Interface shear force transfer between the shake table and the footing without sliding;
3. Composite action among footing and platen, to better resist flexural shear.

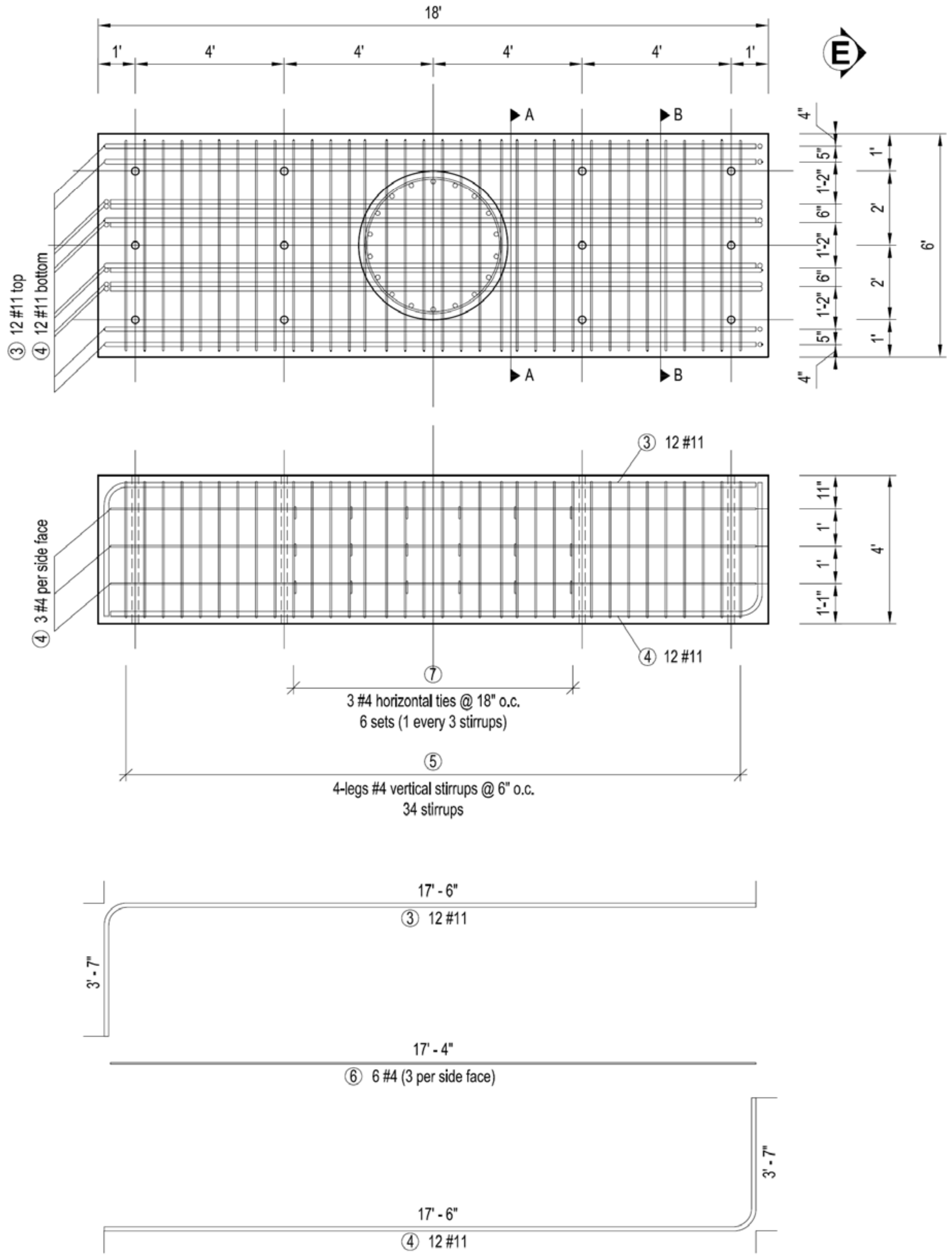

Figure 2.2: Footing details (scale 1:50)

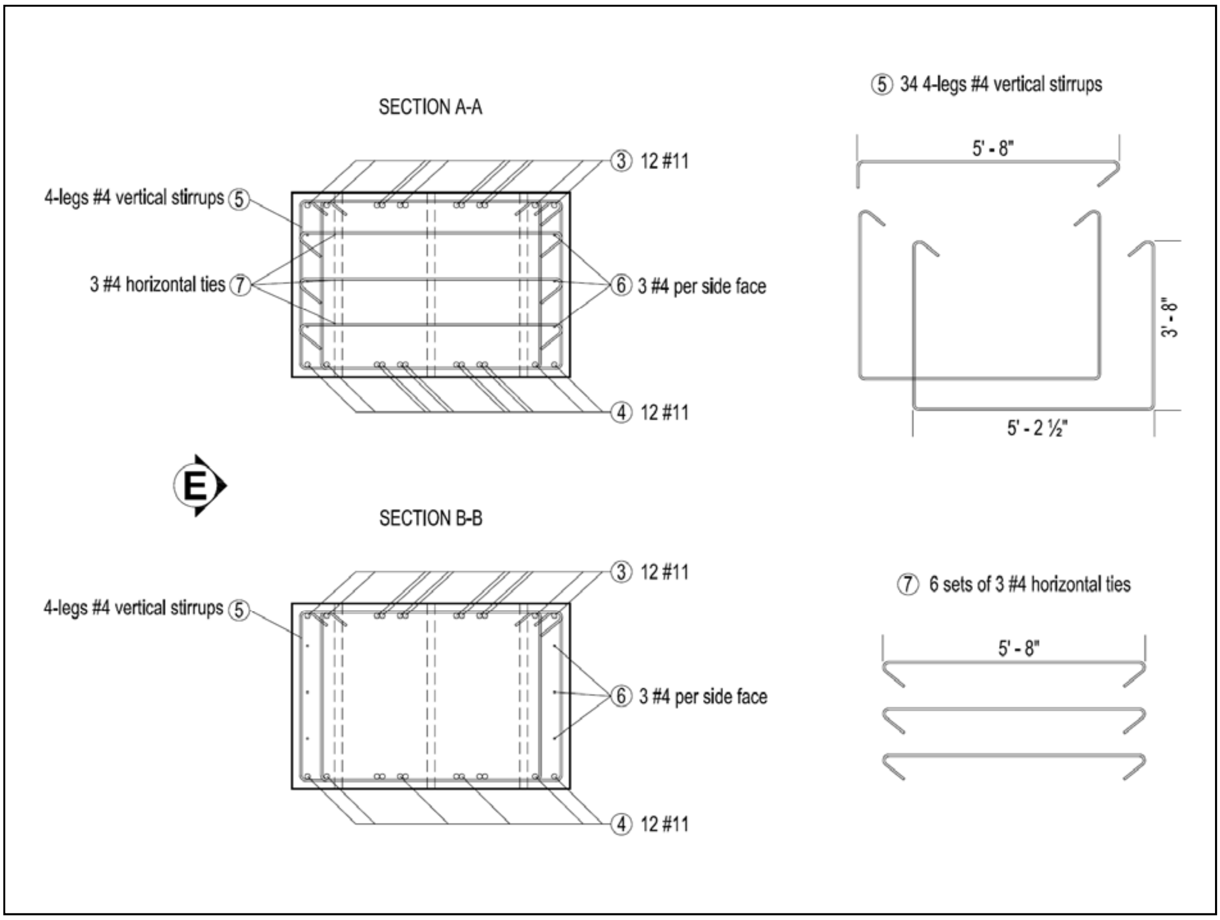

Figure 2.3: Footing details: cross sections (scale 1:50)

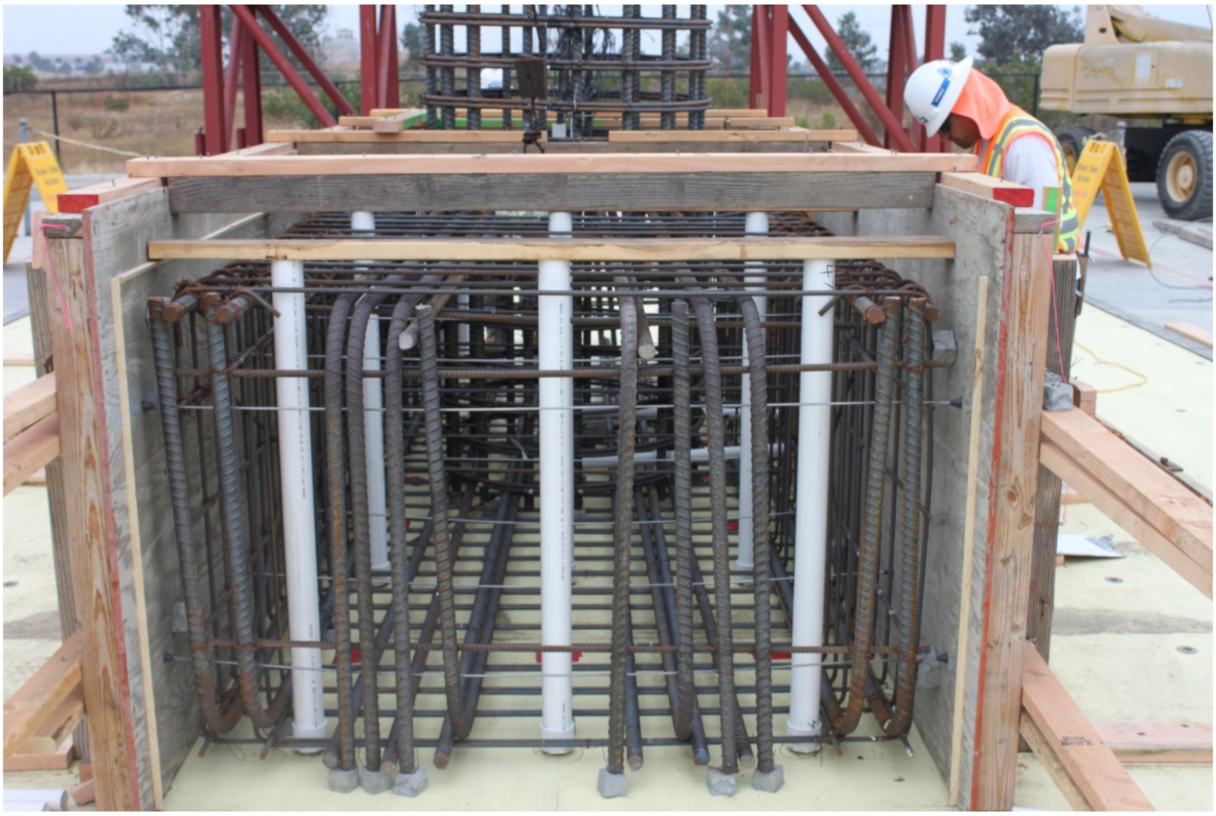

Figure 2.4: Footing during construction

2.1.1.2 Column

The column was designed in accordance to Caltrans *Seismic Design Criteria* [Caltrans, 2006-a] and *Bridge Design Specifications* [Caltrans, 2004] guidelines. The 1.22-m (4-ft) diameter cantilever column spanned 7.31 m (24 ft) above the footing. The longitudinal reinforcement consisted of eighteen #11 (36-mm diameter) straight bars evenly spaced around the column perimeter. Butt-welded, double #5 (16-mm diameter) hoops, spaced at 152 mm (6 in.) on-center were used as transverse reinforcement. The term “double” refers to fact that two hoops were bundled together at each 152 mm (6 in.) spacing. Clear cover to the hoops was 51 mm (2 in.). Column details are shown in Figures 2.5 and 2.6.

A longitudinal reinforcement ratio ρ_l of 1.55%, typical of current practice, was chosen for the column, with ρ_l defined as:

$$\rho_l = \frac{n_{bl} \cdot A_{bl}}{A_g}$$

where n_{bl} is the number of longitudinal bars, A_{bl} is the bar area, and A_g is the gross area of the concrete cross-section.

Normal weight concrete was used to cast the column. The specified compressive cylinders strengths f'_c was 27.6 MPa (4 ksi) and the expected one according to the producer f'_{ce} was 33.9 MPa (4.9 ksi). The compressive cylinder strengths obtained from material tests are summarized in Table 2.1, where $f'_{c,29}$, $f'_{c,42}$, $f'_{c,43}$ are the measured strengths at 29 days, 42 days (first day of testing), and 43 days (second day of testing) respectively. A measured concrete unit weight of 23.58 kN/m^3 (150.1 pcf) was obtained by averaging the unit weights of eighteen standard concrete cylinders. The cylinder weights are presented in Table A.2 of Appendix A.

Both longitudinal and transverse reinforcement were made of Grade 60 steel conforming to the ASTM Designation A706. Their measured yield strength f_y and ultimate strength f_u are shown in Table 2.2.

	(MPa)	**(ksi)**
$\boldsymbol{f'_{c,29}}$	40.3	5.8
$\boldsymbol{f'_{c,42}}$	40.9	5.9
$\boldsymbol{f'_{c,43}}$	42.0	6.1

Table 2.1: Compressive cylinder strengths of the column concrete

	Longitudinal reinforcement		Transverse reinforcement	
	(MPa)	**(ksi)**	**(MPa)**	**(ksi)**
f_y	518.5	75.2	375.1	54.4
f_u	706.7	102.4	592.2	85.9

Table 2.2: Measured yield and ultimate strengths of the column reinforcing steel

An accurate evaluation of the column weight, accounting for the rebars, provided a total value of 212.6 kN (47.8 kips).

Transverse reinforcement provided a volumetric confining ratio ρ_s equal to 0.953%, with ρ_s defined as:

$$\rho_s = \frac{4 \cdot A_{sh}}{D' \cdot s}$$

where A_{sh} is the area of the hoop cross-section (2 #5 in this case), D' is the diameter of the confined core (measured between the hoop centerlines), and s is the hoop spacing.

Both longitudinal and transverse reinforcement complied with the minimum and maximum requirements of [Caltrans, 2004] and [Caltrans, 2006-a] provisions.

A 2224.1 kN (500 kips) seismic weight was initially intended to be supported by the column, leading to a design axial-load ratio of 0.075 defined as:

$$\frac{P}{f'_c \cdot A_g}$$

where P is the design axial load which was equal to 2419.8 kN (544 kips) and f'_c is the specified concrete strength.

The estimated mass based on measured material weights applied a vertical force P_a of 2534.9 kN (569.7 kips). The latter provided the axial-load ratios at 19 days, 42 days, and 43 days respectively, defined as:

$$\frac{P_a}{f'_{c,29} \cdot A_g} = 0.054$$

$$\frac{P_a}{f'_{c,42} \cdot A_g} = 0.053$$

$$\frac{P_a}{f'_{c,43} \cdot A_g} = 0.052$$

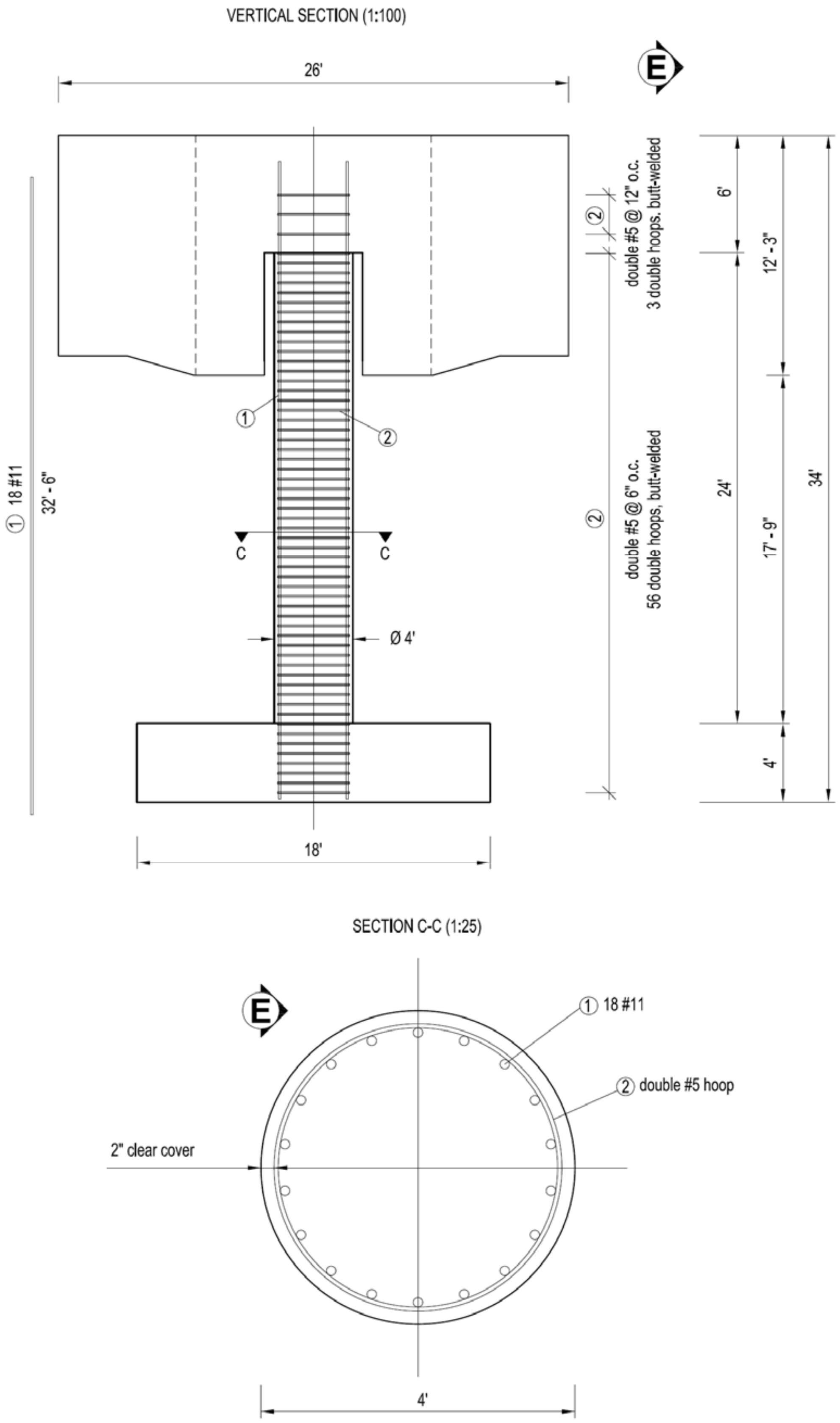

Figure 2.5: Column details (Scale varies)

Figure 2.6: Column during construction

2.1.1.3 Superstructure

High-early strength concrete was used to cast the superstructure. The specified concrete compressive cylinder strength was 35.0 MPa (5.1 ksi) and the expected one, according to the producer, was 52.4 MPa (7.5 ksi). The measured concrete unit weight was 23.68 kN/m^3 (150.7 pcf). This value was obtained by averaging the unit weights of twenty-eight standard concrete cylinders. The cylinder weights are presented in Table A.3 of Appendix A.

An accurate evaluation of the superstructure weight, accounting for through holes, reinforcing steel, and post-tensioning bars provided a total estimation of 2322.3 kN (521.9 kips).

The superstructure consisted of five reinforced concrete blocks: a central block cast on top of the column, and four blocks post-tensioned to it. The size of the blocks was based on the capacity of the crane used to disassemble the unit, to allow an off-table demolition. The weights of the superstructure blocks are presented in Table A.4 of Appendix A.

The column longitudinal reinforcement was anchored into the central block to obtain a moment resisting connection. The column extended within this block for 1.88 m (6.25 ft) so that the center of mass of the superstructure was located approximately on top of the column, as shown in Figure 2.7c-d. A 152-mm (6-in.) gap was left between the block and the column in this region, see Figure 2.7, to allow bending of the column.

Two blocks were attached to the East and West faces of the central block, held in place by six 44-mm (1.75-in.) diameter post-tensioning bars running within 76-mm (3-in.) diameter PVC pipes; these are referred to as “end blocks”. Two other blocks were connected to the North and South faces of the central block with eleven 44-mm (1.75-in.) diameter post-tensioning bars running within 76-mm (3-in.) diameter PVC pipes; these are referred to as “side blocks”. The layout of the post-tensioning system is provided in Figures 2.7 to 2.9.

Each post-tensioning bar was prestressed to 50% of its capacity, corresponding to 890 kN (200 kips) in order to prevent decompression and sliding between the blocks under gravity and lateral forces.

Skin reinforcement, consisted of Grade 60 steel bars conforming to the ASTM Designation A615, was also provided in the superstructure blocks according to minimum requirements.

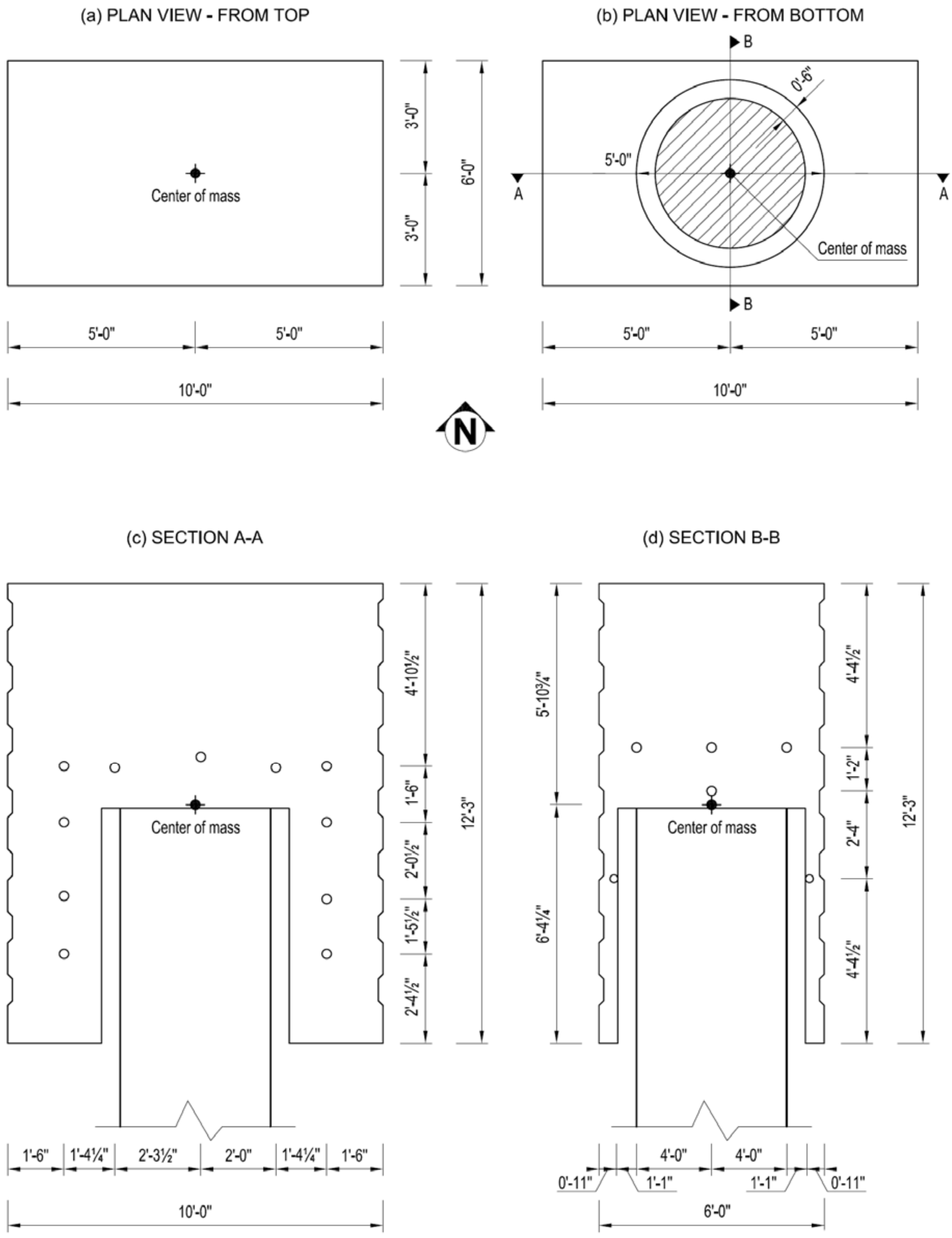

Figure 2.7: Superstructure details: central block (scale 1:50)

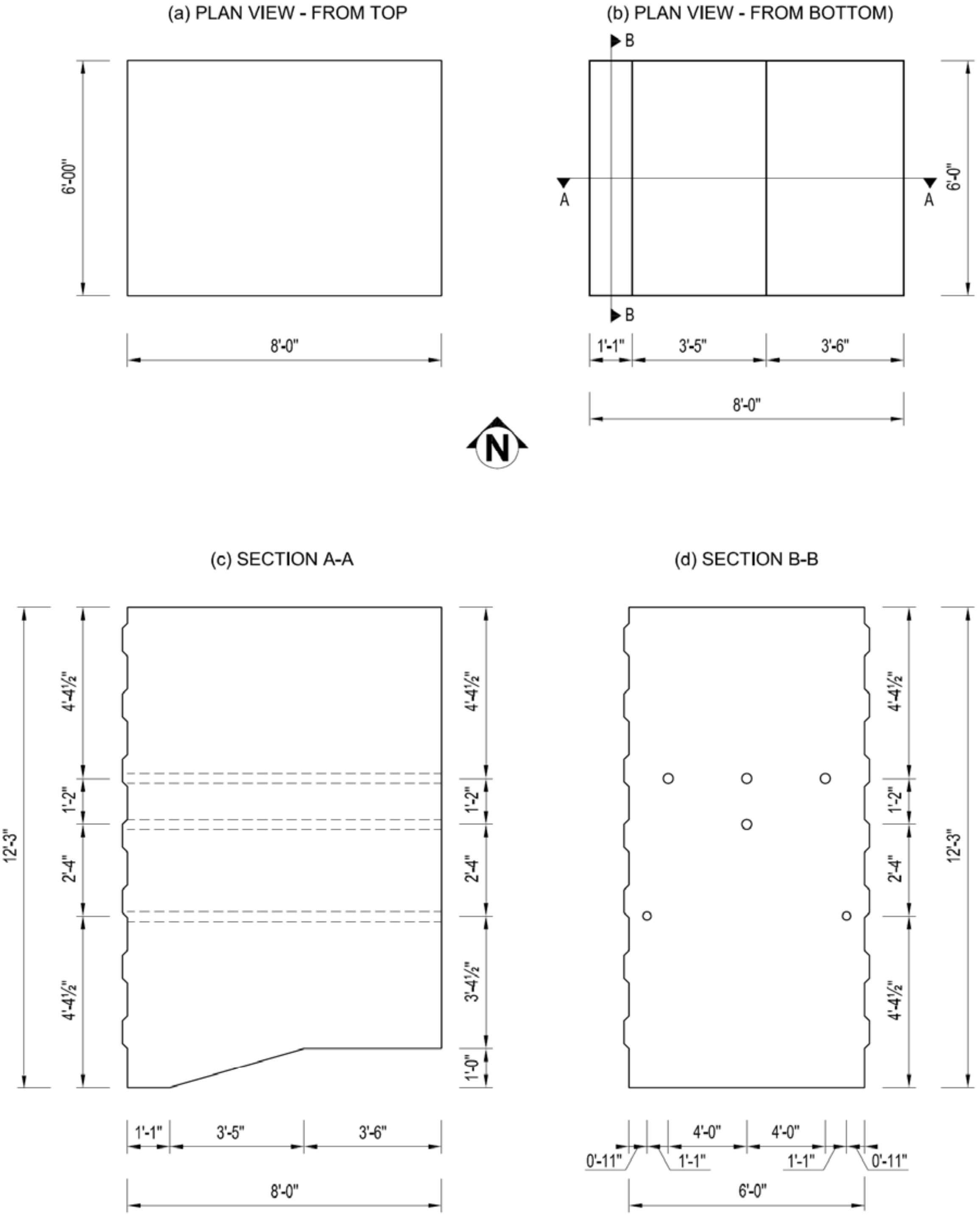

Figure 2.8: Superstructure details: end block (scale 1:50)

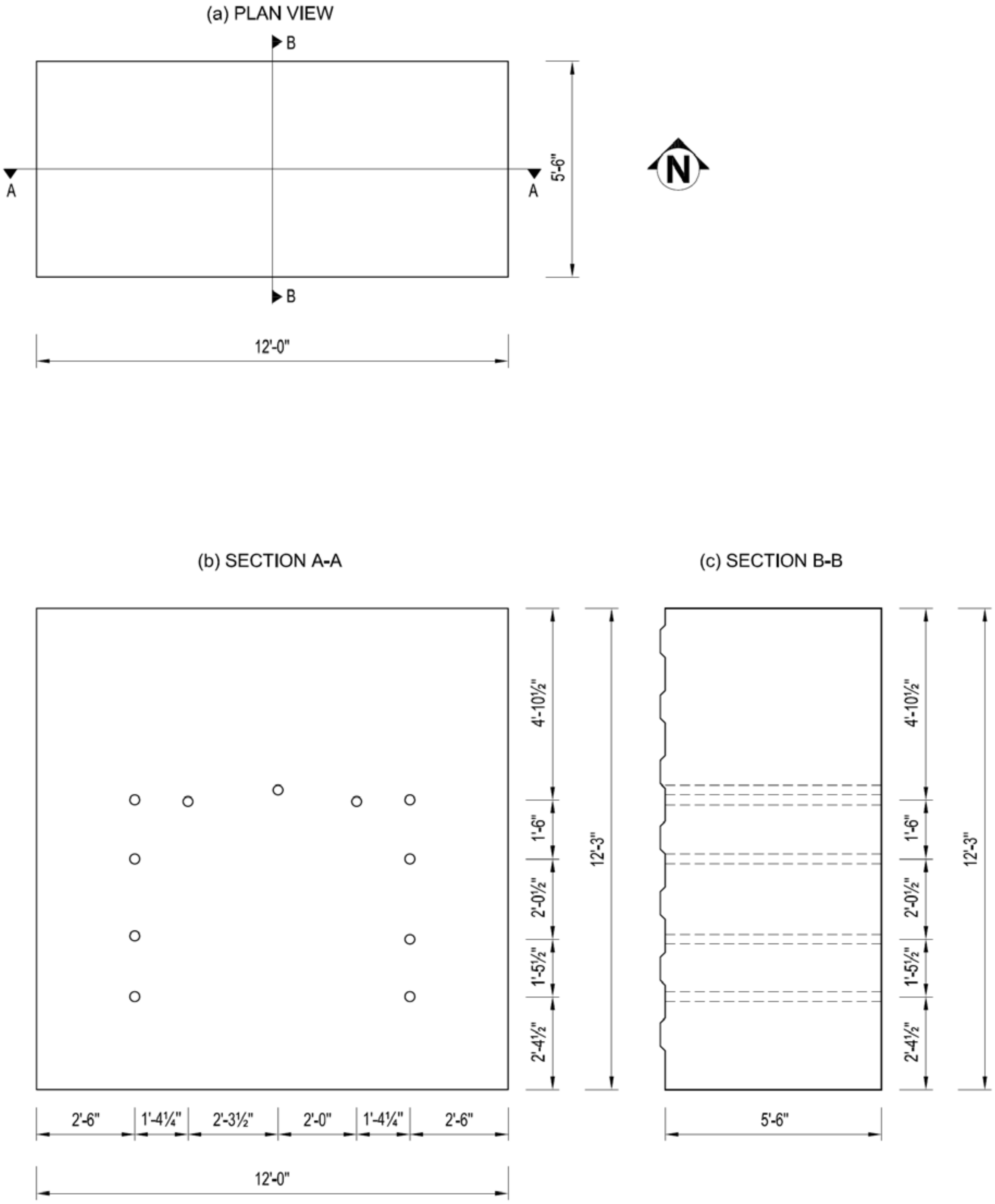

Figure 2.9: Superstructure details: side block (scale 1:50)

2.1.2 Restraint devices

2.1.2.1 Safety columns

The primary purpose of the safety columns is to limit lateral deflection to a drift ratio of 10% and support the superstructure in case of column collapse. For these reasons, two inclined column were provided in the East and West side of the specimen, as shown in Figure 2.10.

Each column was made of two W36×302 steel beams, inclined 78.4° on the horizontal and interconnected by 305 × 152 × 6.3 mm (12 × 6 × 0.25 in.) steel plates. Each beam was anchored to a reinforced concrete footing by ten #8 headed reinforcing bars running parallel with and welded to its flanges. While these bars allowed bending moment transfer between the beams and the footing, shear transfer was obtained by embedding the steel members in the concrete for 38 mm (1.5 in.). A debonded length equal to ten bar diameters was provided on each anchoring bar to allow strain penetration. Wood blocks, confined and held in place by threaded rods and steel angles, allowed energy dissipation upon impact of the mass on the inclined column (Figure 2.11). Each column footing was post-tensioned to the shake table through five 44-mm (1.75-in.) diameter bars. Each bar was post-tensioned to 890 kN (200 kips).

Figure 2.10: Safety columns

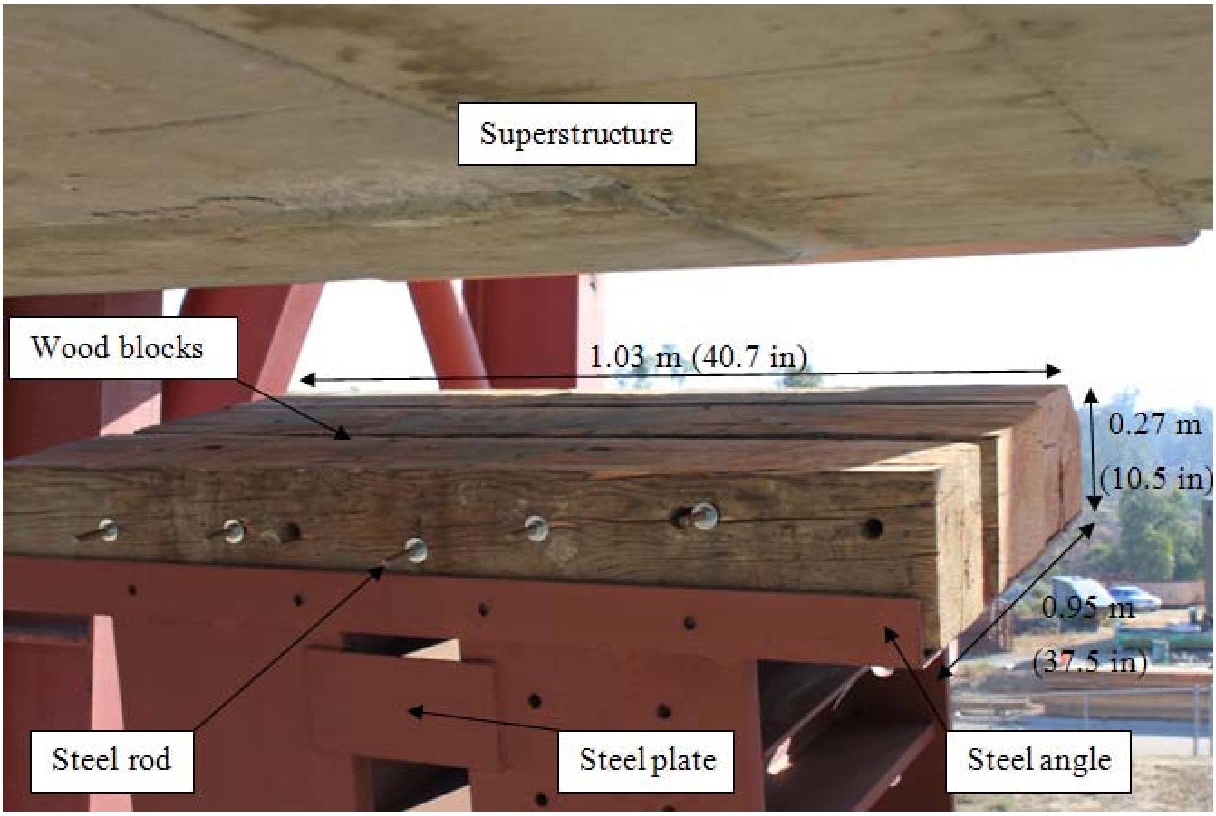

Figure 2.11: Wood blocks atop of the safety columns

2.1.2.1 Restraint towers

Four steel-truss towers (Figure 2.12) were used to limit transverse and torsional displacements of the specimen, which may be caused by tolerances in column verticality, alignment between the top block and the shaking direction, and distribution of the superstructure mass.

The towers were able to resist a 222.4-kN (50-kips) point load anywhere on the column flanges or a combination of point loads totaling 222.4 kN (50 kips) over the entire frame. The load should have been delivered directly to the column flanges [NEES].

Two 2.44-m (8-ft) long horizontal HSS×6×4×¼ steel tubes were welded to the straight columns of each tower, at 7.72 m (25.3 ft) and 8.94 m (29.3 ft) above the ground, to guide the superstructure (Figure 2.13). A 6-mm (0.25-in.) gap was left between the tubes and the North and South faces of the end blocks to allow sliding of the superstructure along the shaking direction; This interface was greased in order to reduce friction between concrete and steel.

Each tower was secured to the shake table through six 44-mm (1.75-in.) diameter post-tensioning bars, which were each post-tensioned to 890 kN (200 kips).

Additional information about the towers can be obtained from NEES at UCSD web site [NEES].

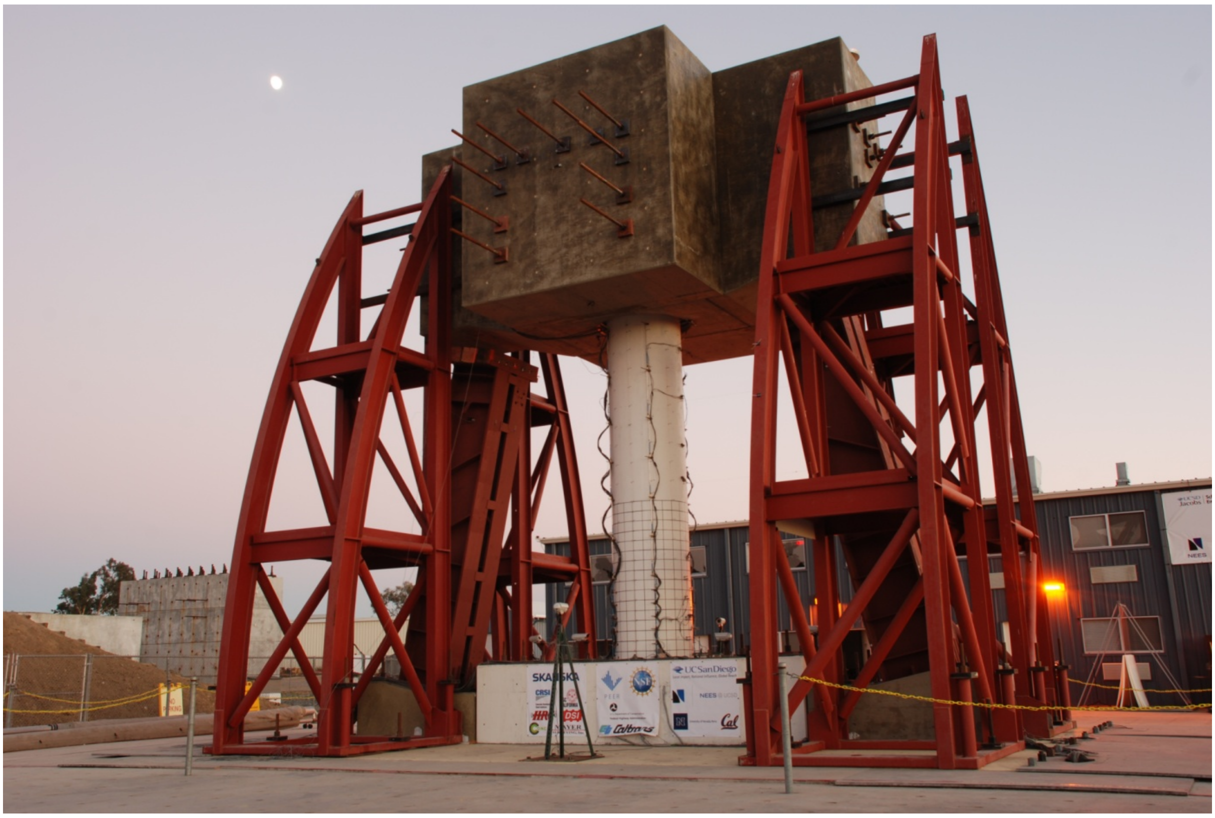

Figure 2.12: Restraint towers

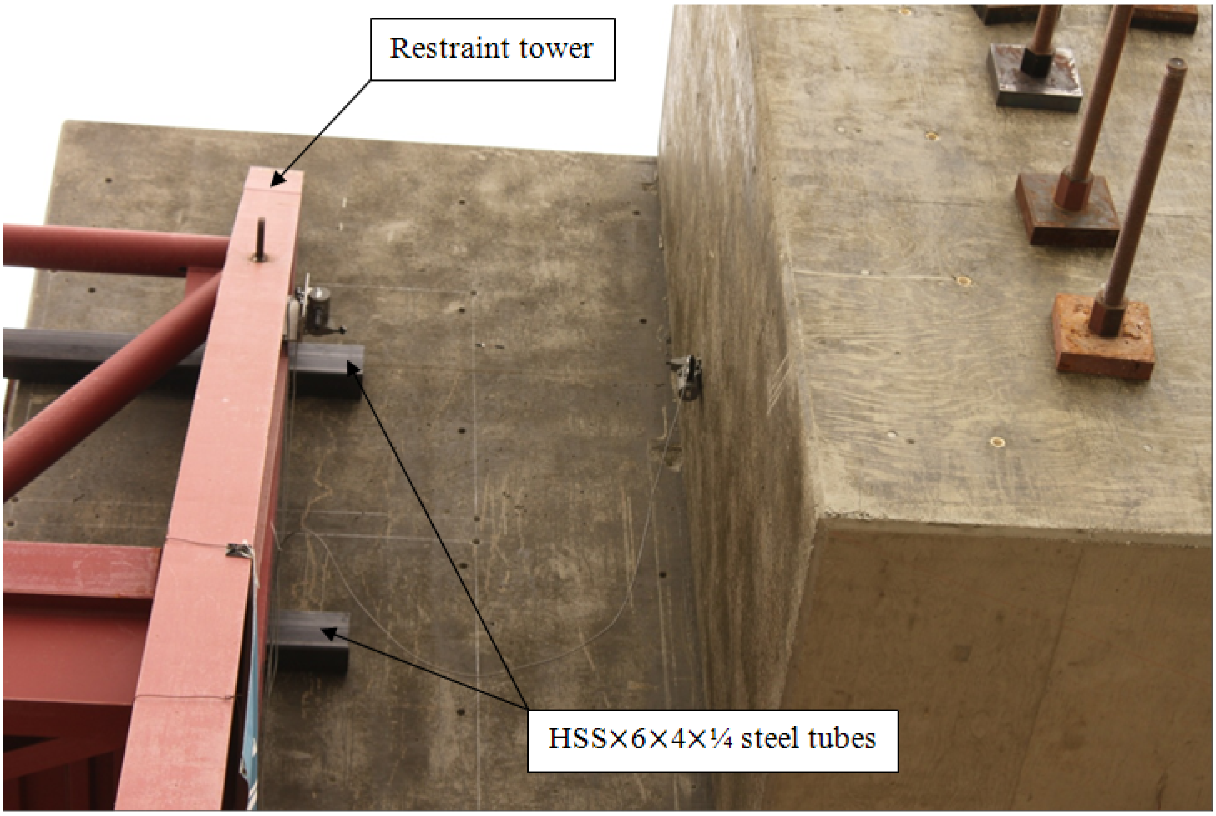

Figure 2.13: Steel tubes welded to the towers

2.1.3 Instrumentation

The test specimen was monitored with strain gauges, linear and string potentiometers, accelerometers, and GPS antennae to measure internal, local, and global deformations during testing.

Internally, electrical resistance strain gauges were symmetrically installed on two longitudinal reinforcing bars at both East and West faces of the column to monitor axial strains. These gauges were placed in pairs on both sides of each bar in the direction of shaking to monitor any bending in the bar. The predicted position of each longitudinal strain gauge is shown in Figure 2.14.

Strain gauges were also installed on the exterior face of the hoops at the East and West sides of the column. The purpose of these gauges was to monitor the hoops' axial dilation caused by radial dilation of the concrete core and longitudinal bars buckling. The predicted position of each transverse strain gauge is shown in Figure 2.14.

Prior to installation of the gauges, the steel reinforcement was filed by hand to expose a smooth surface, free of mill scale, scratches, protrusions and other imperfections. All gauges on the longitudinal bars were installed prior to the fabrication of the cage while the gauges on the hoops were installed on the fabricated column cage.

Externally, linear displacement sensors with either a 50-mm (2-in.) or 100-mm (4-in.) stroke were installed to monitor column deformations; they are referred to as curvature Linear Variable Differential Transformers (LVDTs) or shear deformation LVDTs. These potentiometers were mounted on steel rods cast horizontally in the column in the north-south direction. The rods were placed parallel and as close as possible to the expected neutral axis position to prevent their detachment due to concrete spalling. They were encased in plastic hose to debond them from the concrete core. To reduce rod vibrations where needed, approximately 5-mm (2-in.) long segments at the ends of rods were epoxied to the concrete. A 203-mm (8-in.) vertical spacing of the rods was used starting 50.8 mm (2 in.) above the column base and extending one column diameter, whereas 610-mm (24-in.) and 787-mm (31-in.) spacings were used outside of that area. Both curvature and shear LVDTs were installed on the South face of the column, whereas only curvature LVDTs were mounted on the North face. Figures 2.15 and 2.16 shows the specified layout of curvature and shear LVDTs.

Four vertical spring LVDTs were installed to determine the fix-end rotation of the column. They were mounted on the four curvature rods located 51mm (2 in.) above the column-footing interface and they targeted the top of the footing as shown in Figures 2.15 and 2.16.

(a) LONGITUDINAL STRAIN GAUGES

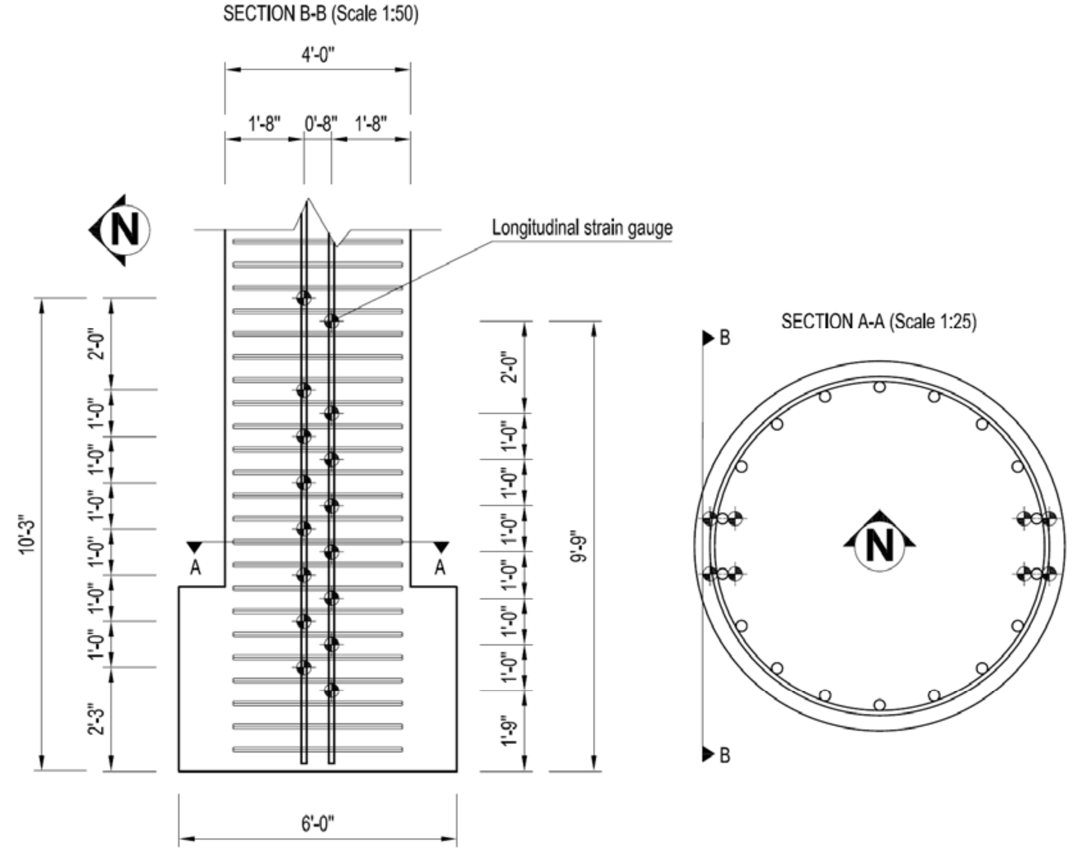

(b) TRANSVERSE STRAIN GAUGES

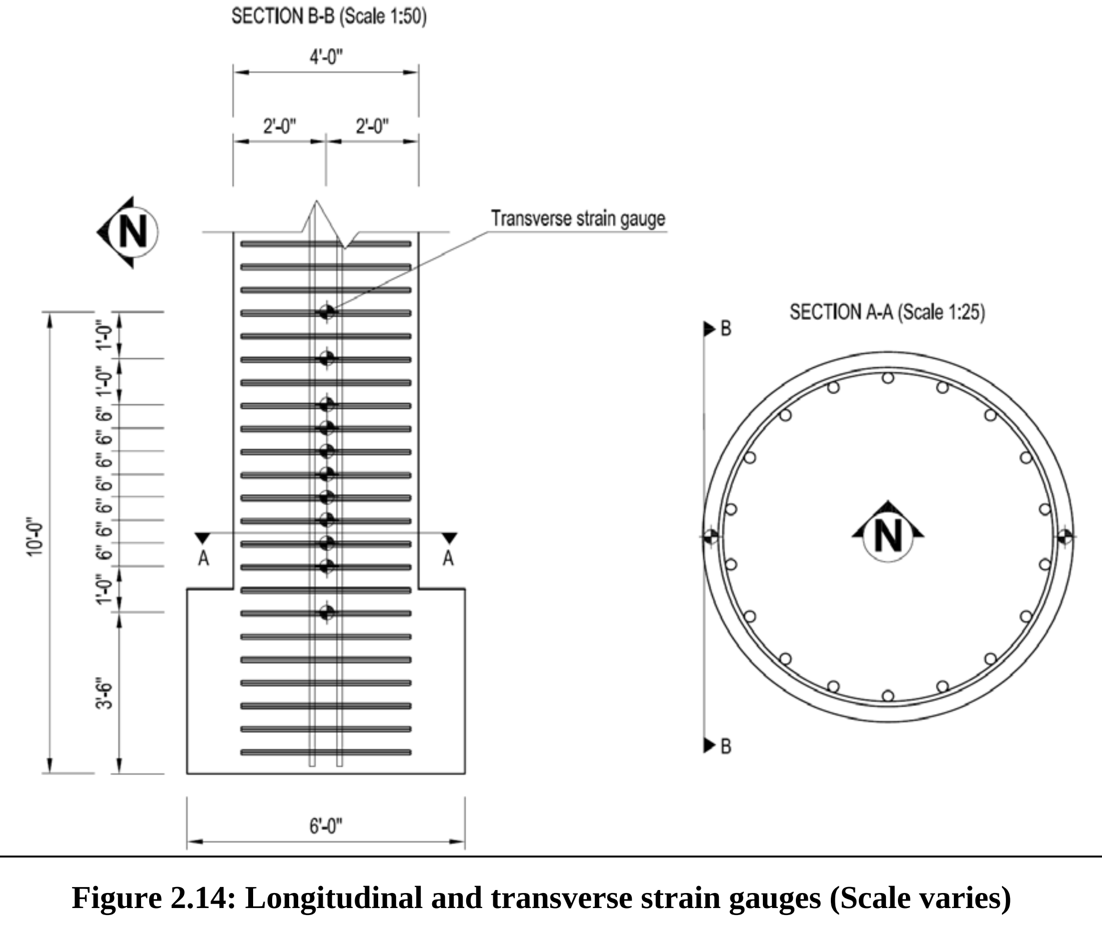

Figure 2.14: Longitudinal and transverse strain gauges (Scale varies)

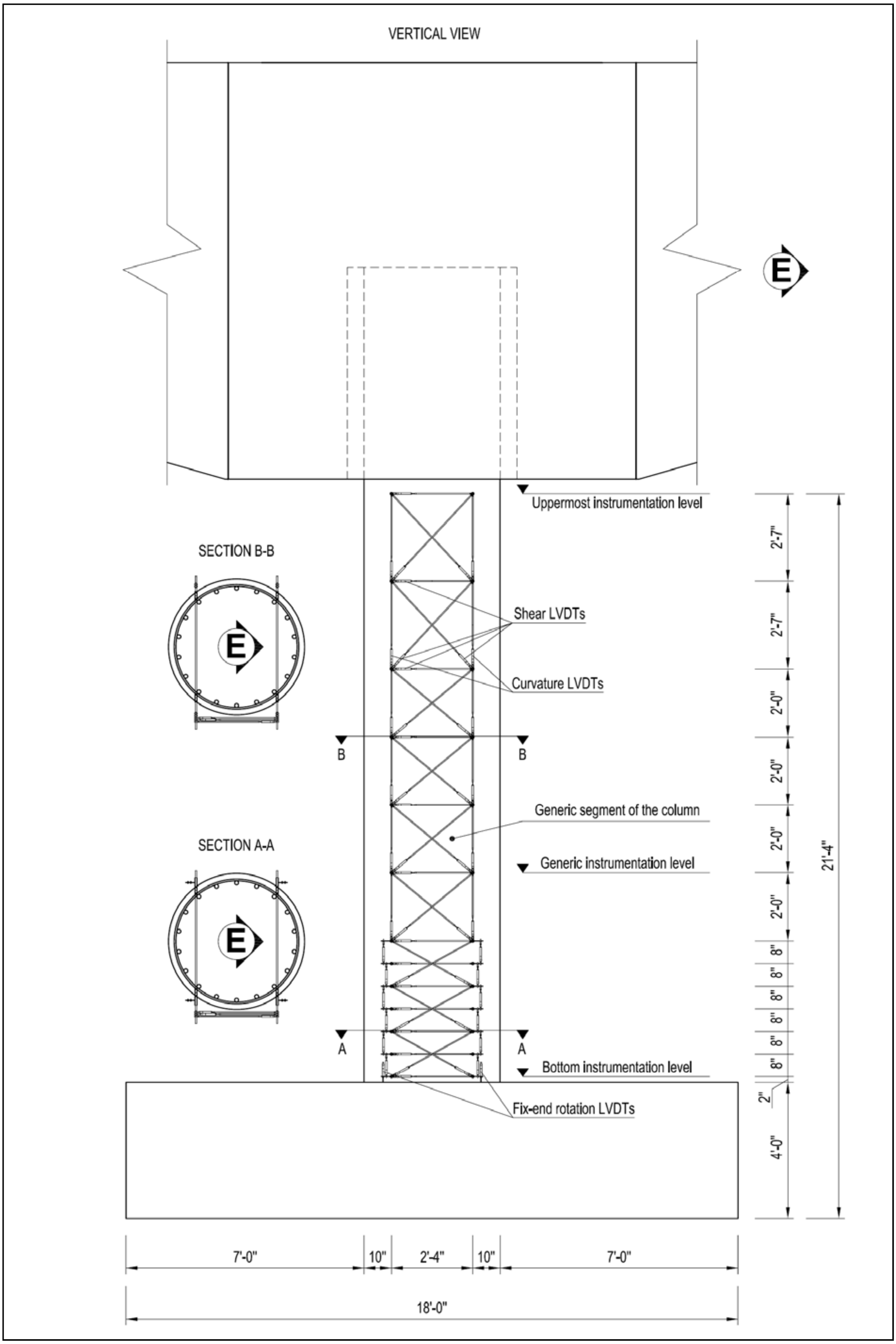

Figure 2.15: Curvature and shear LVDTs on the South side of the column (Scale 1:50)

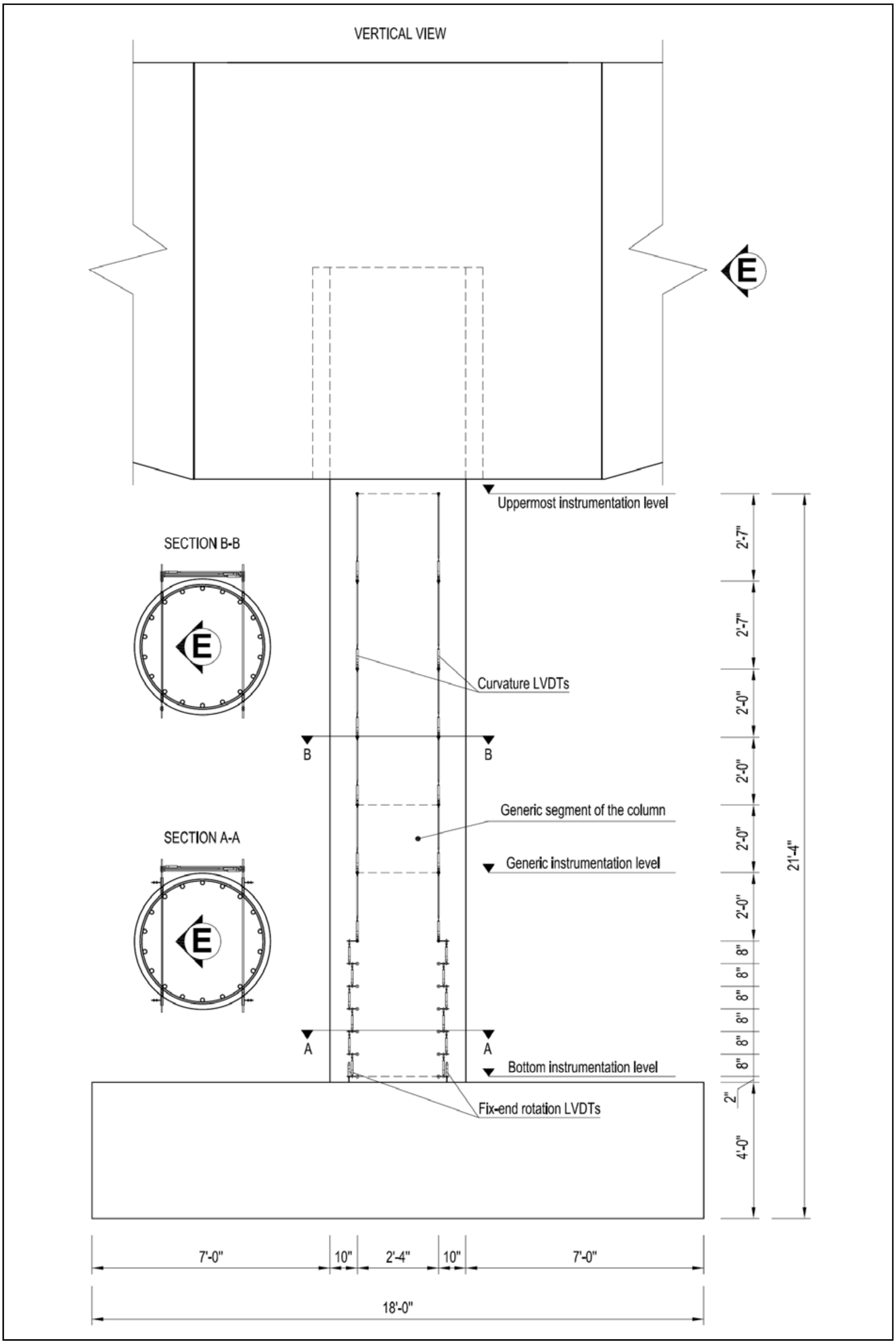

Figure 2.16: Curvature and shear LVDTs on the North side of the column (Scale 1:50)

Two horizontal spring loaded LVDTs were installed to monitor the relative rotation between the column and the superstructure mass. These sensors were mounted on the lower face of the central block and they targeted the East and West faces of the column, as shown in Figure 2.17.

LVDTs were installed to measure the bond slip between the longitudinal bars and the concrete of the footing. In particular, one bar at the East and one bar at the West face of the column were monitored. Steel brackets were clamped on these bars using three sharpen screws and they were placed just below the column-footing interface. Two steel targets were welded to each brace to prevent slip of the spring LVDTs. The distances from the center of the bar to the center of each target were 119 mm (4.7 in.) and 208 mm (8.2 in.). The sensors were placed on a rigid support bolted to the footing at sufficient distance from the column, as shown in Figure 2.18.

Spring loaded linear displacement sensors with a 25.4 mm (1-in.) stroke were installed to measure the radial dilation of the concrete core in the plastic hinge region; they are referred to as transverse hoop LVDTs. These potentiometers were mounted on steel rods which were cast into the column. The rods passed horizontally through the column along the diameter of its cross section. They were encased in steel pipes to inhibit bond with the surrounding concrete. However, a 127-mm (5-in.) long segment at the rod’s center remained exposed to fix the rods in a stable area of the column cross section. These sensors were aligned to concave steel targets which were welded to the exterior face of the hoops. The predicted positions of hoop LVDTs are shown in Figure 2.19.

A 25.4 mm (1 in.) stroke LVDT was installed to monitor shear slip between the base of the column and the footing along their interface. This potentiometer was placed on the column-footing interface at the South side, as shown in Figure 2.20.

The relative horizontal displacement between the shake table and the column was measured at different heights using five cable-extension position transducers; they are referred to as horizontal string potentiometer. These instruments were mounted to the stiff steel plates of the West safety column. Because of the column tip was embedded in the superstructure, four string potentiometers were installed between the restraining towers and the sides blocks to measure the relative horizontal displacement of the column top. The horizontal string potentiometer layout is shown in Figure 2.21.

Three analog sensors were installed to monitor the relative displacement of the column at 5.41 m (17.75-ft) above the top of the footing. They were placed on the North side of the column: one of them was vertically installed, whereas the others two were obliquely mounted as shown in Figure 2.18. This configuration allows the computation of the column elongation.

Accelerometers were installed to monitor the dynamic response of the specimen. These sensors were used to measure vertical and horizontal accelerations. They were installed on the East and West faces of the column in different locations along its height. Because of the column tip was embedded in the superstructure, two vertical and two horizontal accelerometers were placed on the North and South faces of the superstructure to measure the center of mass acceleration. The horizontal acceleration at the base of the column was measured using two accelerometers placed on the footing at North and South sides. The data of these sensors allowed the computation of the inertia forces generated on the specimen from the base excitation.

Vertical accelerometers were installed on the platen and on the footing to monitor the possible rotation of the shake table and column foundation in the shaking direction. Vertical and horizontal accelerometers were mounted on the superstructure mass to monitor its longitudinal, transverse and rotational response. Figures 2.22 and 2.23 show the specified layout of accelerometers.

The possible impact between the superstructure and the wood blocks located atop of the safety columns was measured by four accelerometers and four strain gauges installed on each column.

Eight other accelerometers were installed on the restraining towers to measure their response and correct the column's top displacement measurements which included the tower's response.

A data acquisition system, operating at 240 Hz, was used to interpret the signals provided by each instrumentation channel and to convert them into a digital information. It consisted of eight PXI chasses, each chassis loaded with an embedded controller based on Windows XP running the Lab View applications, and eight SCXI-1520 signal conditioning modules. With this configuration, each chassis had a total of sixty-four channels, resulting in the availability of fifty-hundred-twelve total channels. The system is synchronized with the PC based video recording system. These information has been obtained from NEES at UCSD web site [NEES].

A network of three NAVCOM ANT-2004T antennae provided global displacement monitoring in three coordinates of the specimen. Two GPS antennae were mounted on top of the superstructure mass and one was used as a reference on the ground. The GPS acquisition system is separate from the table's data acquisition system and it used RTD-NET software by Geodetics. The dedicated standalone computer allowed continuous monitoring via three NAVCOM NTC-2030M receivers operating at 50 Hz. Additional information about the GPS system can be obtained from NEES at UCSD web site [NEES].

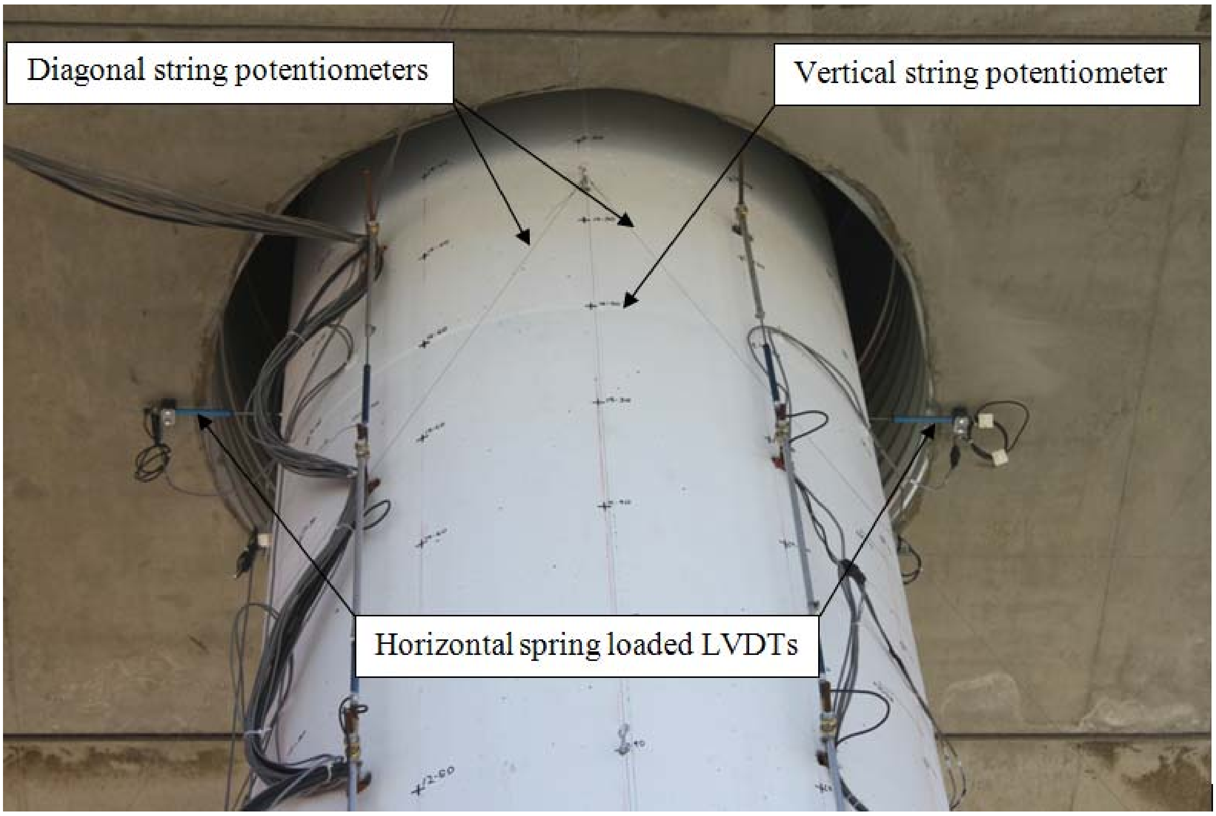

Figure 2.17: Superstructure relative rotation LVDTs, and vertical and diagonal string potentiometers

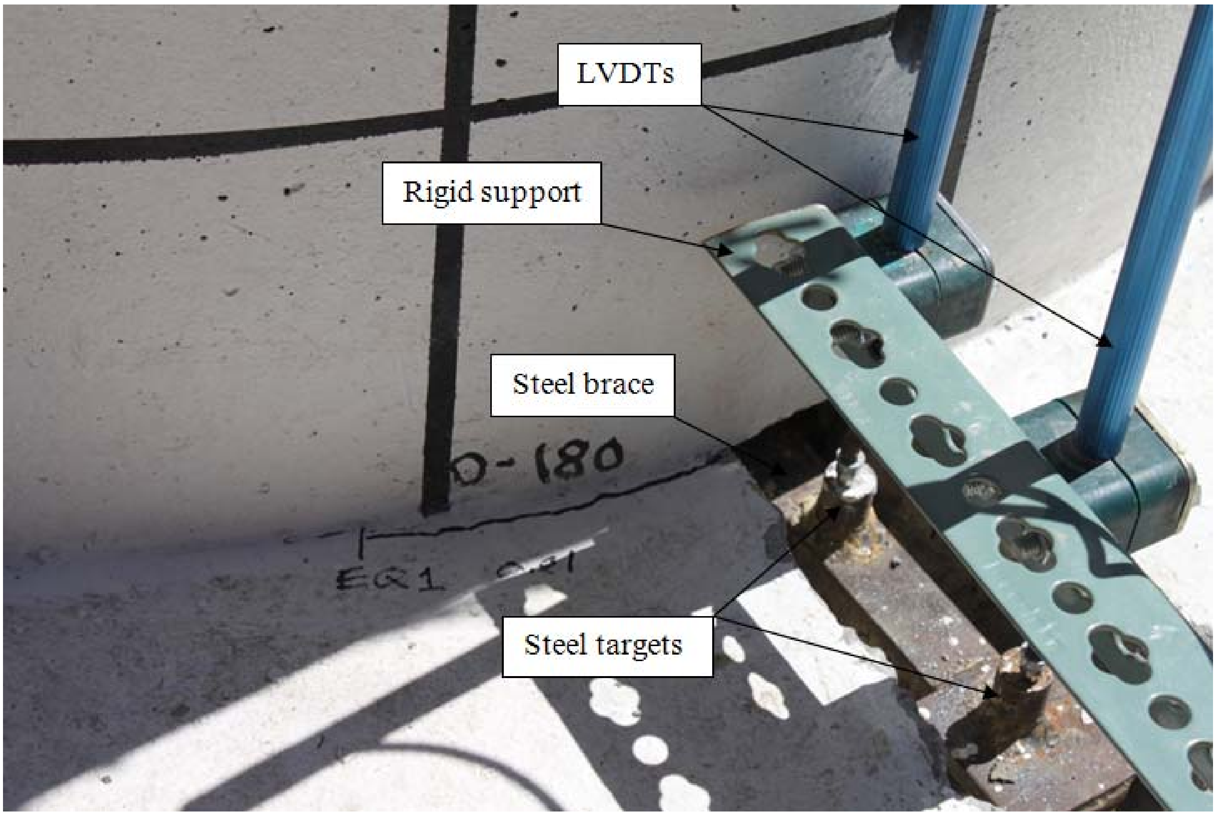

Figure 2.18: Bond slip LVDTs

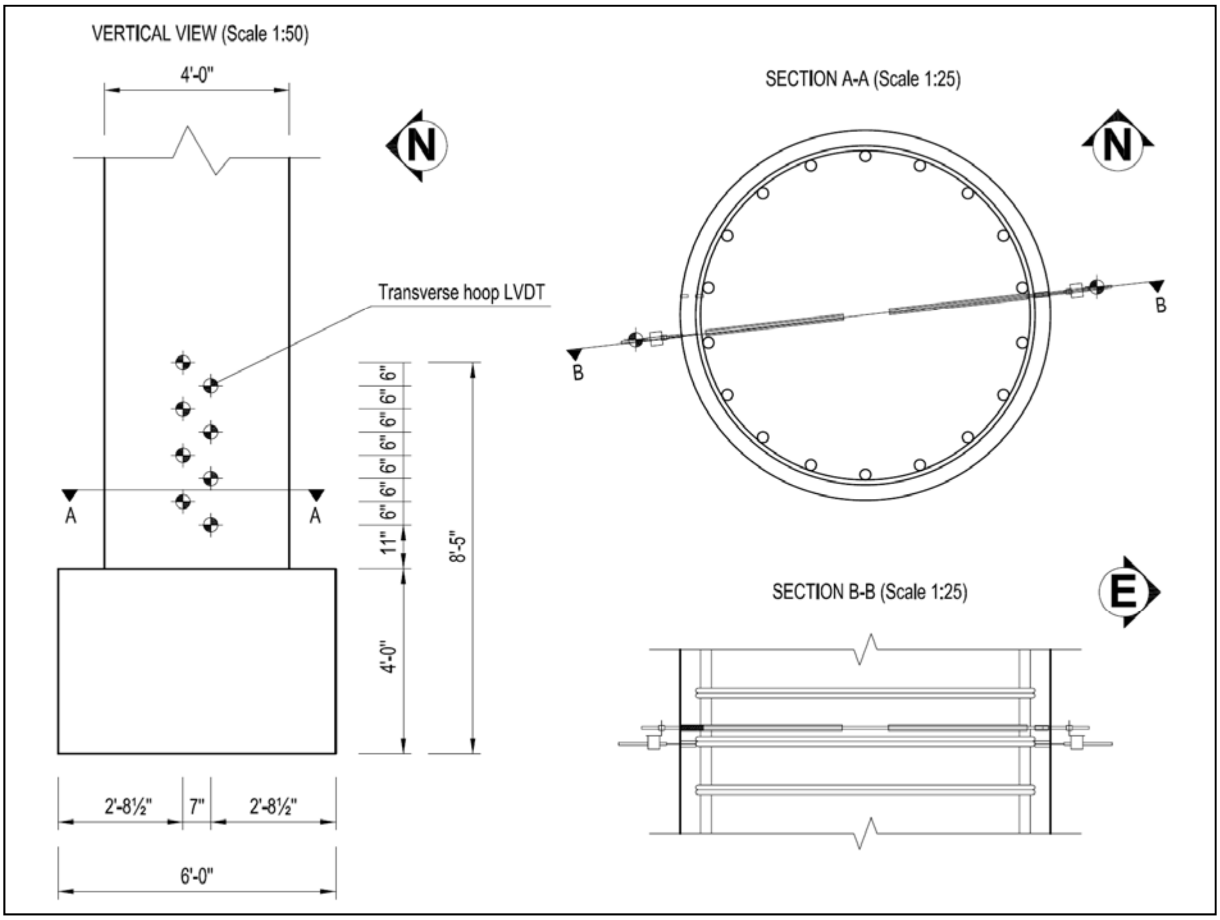

Figure 2.19: Transverse hoop LVDTs (Scale varies)

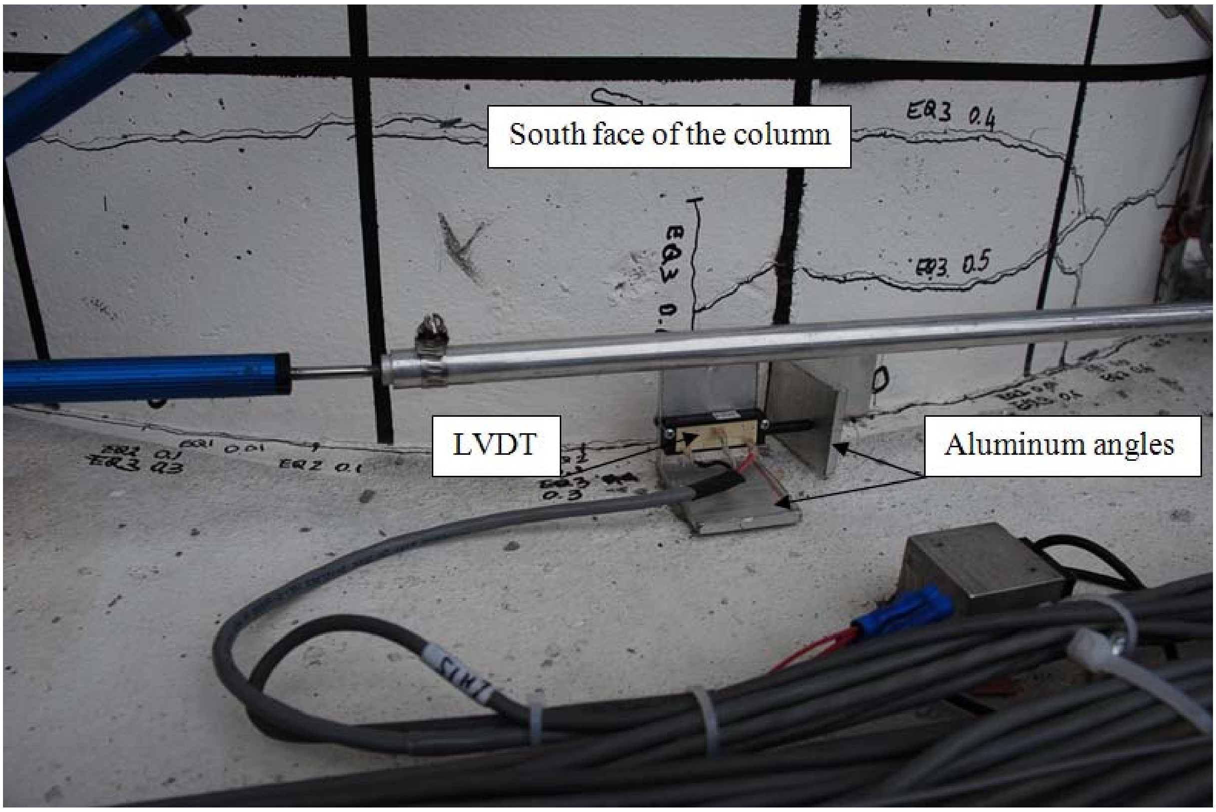

Figure 2.20: Shear slip potentiometer

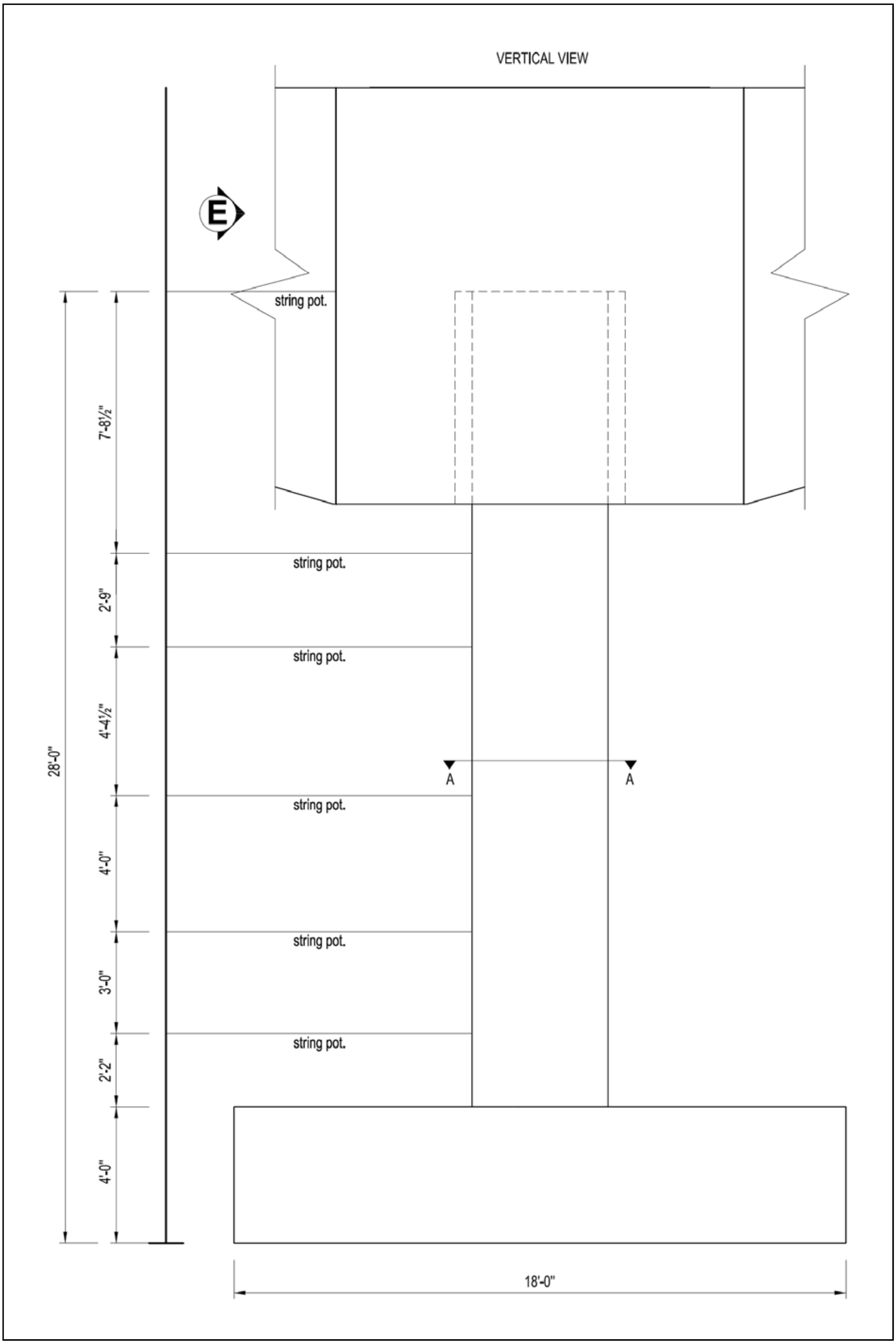

Figure 2.21: Horizontal string potentiometers (Scale 1:50)

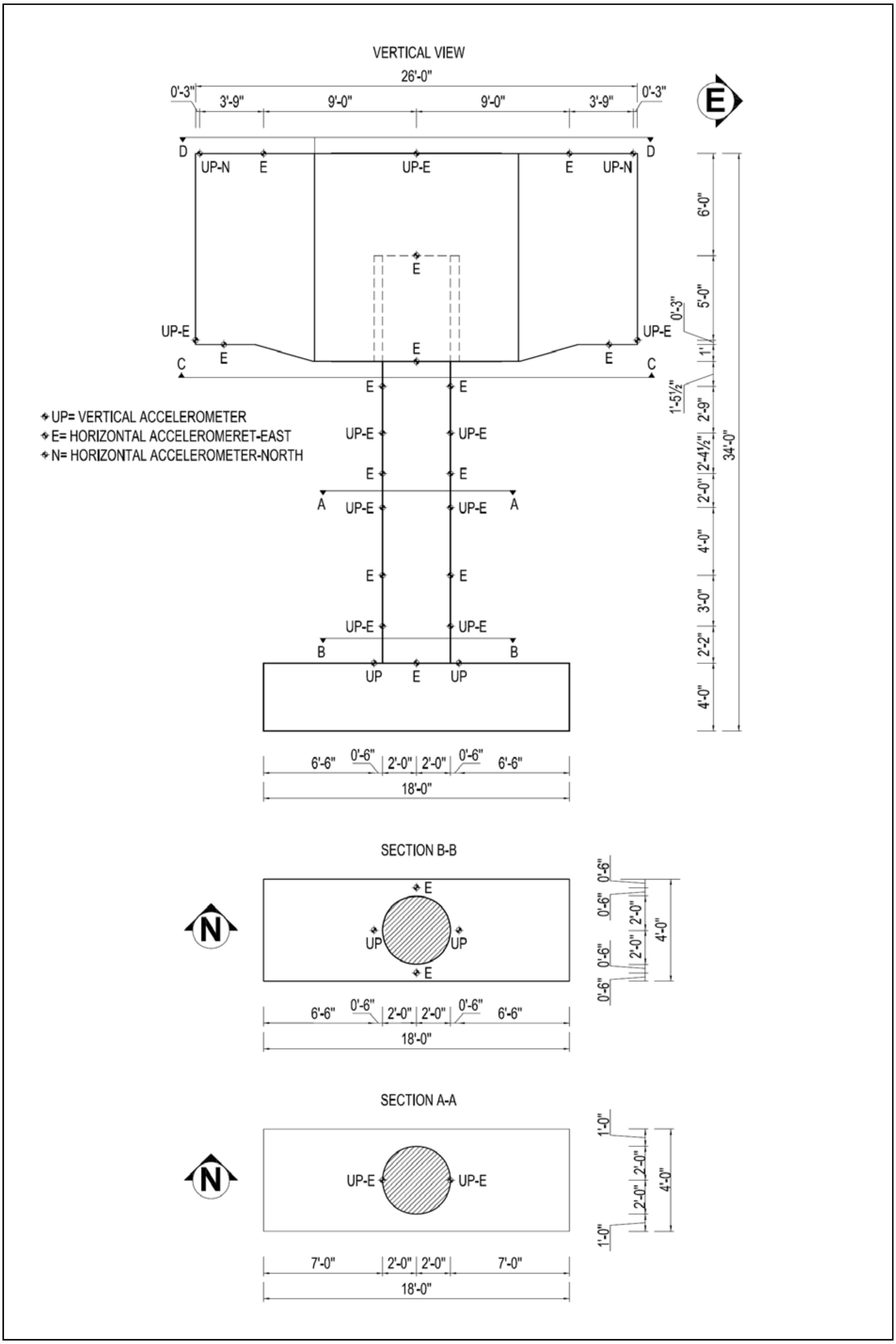

Figure 2.22: Accelerometers layout - 1 (Scale 1:100)

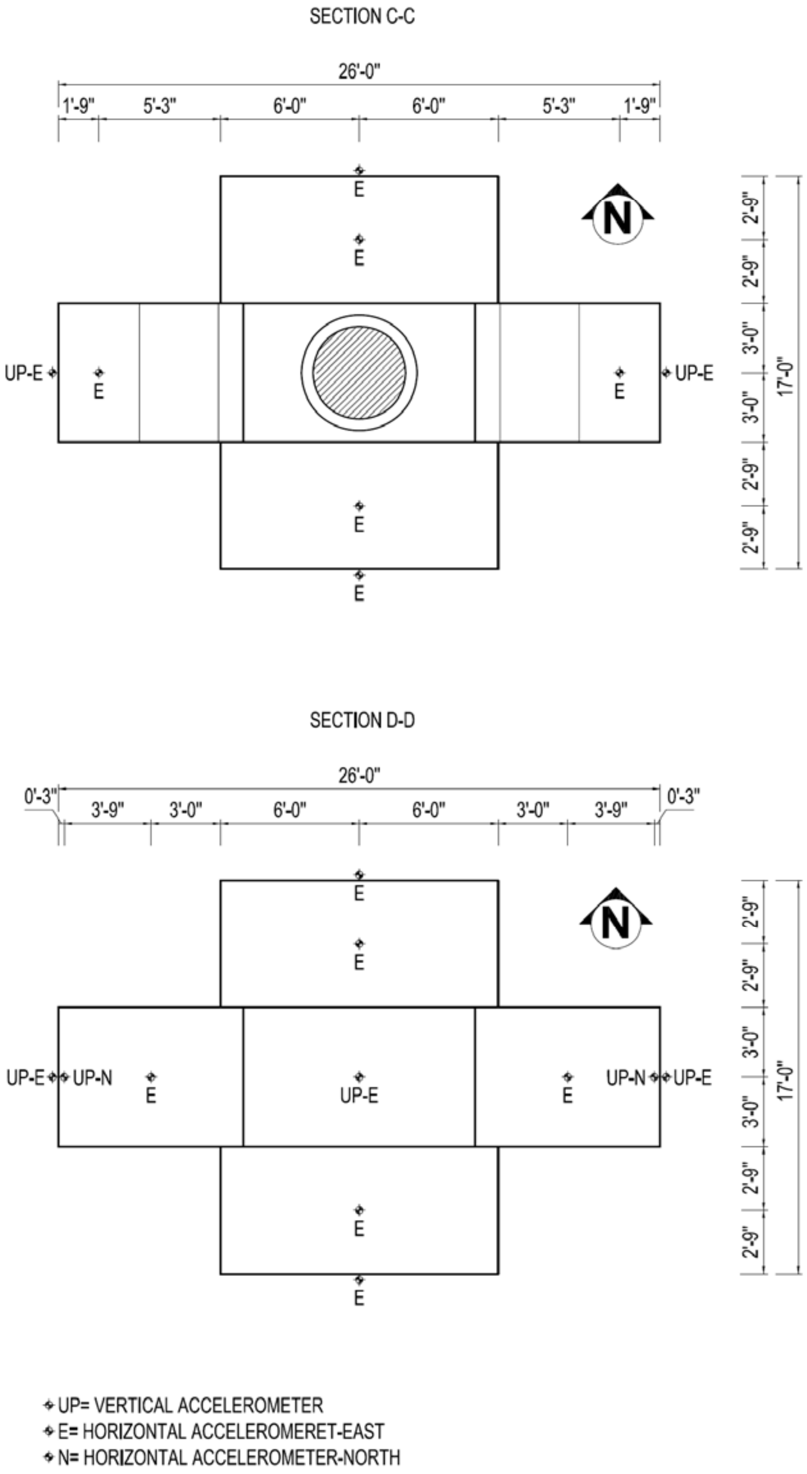

Figure 2.23: Accelerometers layout - 2 (Scale 1:100)

Six video cameras were mounted on the shake table zooming on the plastic hinge region: four of them were placed on the footing pointing to the East and West sides of the column and two were installed on rigid supports bolted to the platen pointing to the North and South faces of the column. Several video cameras were installed outside the shake table to record the tests form different angles.

The base excitation was applied to the specimen using the NEES Large High Performance Outdoor Shake Table (LHPOST) at UCSD’s Englekirk Structure Engineering Center. The 7.6 × 12.2 m (25 × 40 ft) shake table allowed testing of the column under a wide range of ground motions, starting with low-intensity shaking and bringing the column progressively towards near-collapse conditions. Its performance parameters such as peak velocity and acceleration, stroke and force capacity of actuators, maximum gravity payload and overturning moment, and frequency bandwidth, available from NEES at UCSD web site [NEES], are summarized in Table 2.3.

Parameters		**SI Units**	**US Units**
Size		7.60×12.20 m	25×40 ft
Peak acceleration	Bare table	4.2 g	
	400 ton payload	1.2 g	
Peak velocity		1.8 m/s	71 in/sec
Stroke		±0.75 m	29 in
Maximum gravity payload		20 MN	4496 kips
Force capacity of actuator		6.8 MN	1529 kips
Maximum overturning moment	Bare table	35 MNm	25824 kip-ft
	400 ton specimen	50 MNm	36878 kip-ft
Frequency bandwidth		0-33 Hz	

Table 2.3: Shake table parameters

2.2 Material properties

Material tests were carried out in order to measure the mechanical properties of the materials used to construct the specimen. In particular, only the material properties of the column are presented in this chapter.

2.2.1 Concrete

Normal weight concrete was used to cast the column. A unit weight of 23.58 kN/m^3 (150.1 pcf) was obtained by averaging the unit weights of eighteen concrete standard cylinders.

The specified compressive cylinder strength, f'_c, was 27.6 MPa (4 ksi) and the expected one according to the producer, f'_{ce}, was 33.9 MPa (4.9 ksi). The experimental concrete compressive cylinders strengths are summarized in Table 2.1 (as already shown in Paragraph 2.1.1.2), where $f'_{c,29}$, $f'_{c,42}$, $f'_{c,43}$ are the measured strengths at 29 days, 42 days (first day of testing), 43 days (second day of testing) respectively.

Standard compressive tests of fourteen 152-mm (6-in.) diameter by 305-mm (12-in.) high cylinders provided the data for the latter three values; the first one was obtained by averaging the strengths of a single set of three cylinders, whereas the last two were mean values of five (one set of two cylinder and one set of three cylinders) and six cylinders (two sets of three cylinders) respectively.

The stress-strain relationship, as shown in Figure 2.24, was available only for one cylinder of each set of three cylinders. For each set, two cylinders were made from the first batch of concrete delivered and one cylinder was made from the second batch of concrete. Defects in one cylinder resulted in five cylinders tested at 42 days rather than six.

The concrete modulus of elasticity E_c, defined as the slope of the secant line at 45% of the compressive cylinder strength, and the strain at peak stress ε_{c0} have been obtained from these curves and are summarized in Table 2.4. The values at 43 days were obtained by averaging the two available curves.

	(MPa)	**(ksi)**
$\boldsymbol{f'_{c,29}}$	40.3	5.8
$\boldsymbol{f'_{c,42}}$	40.9	5.9
$\boldsymbol{f'_{c,43}}$	42.0	6.1

Table 2.1: Compressive cylinder strengths of the column concrete

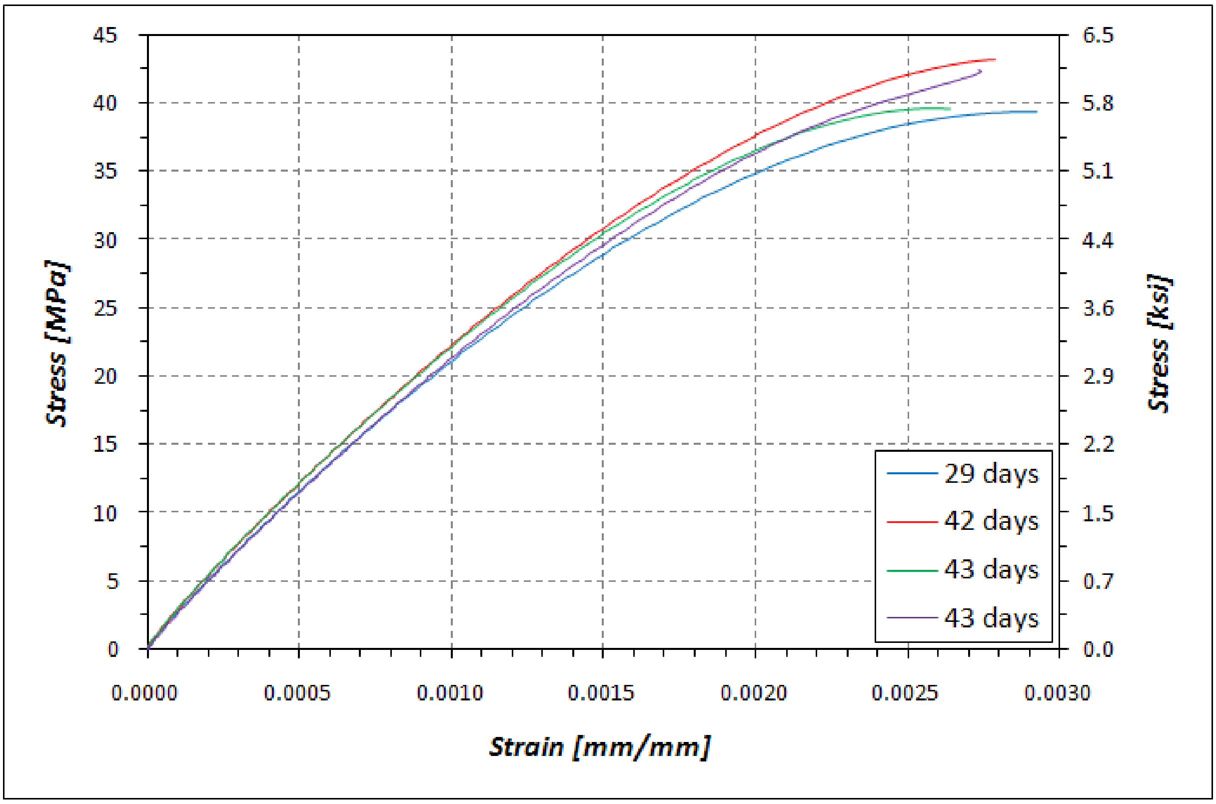

Figure 2.24: Experimental concrete stress-strain relationships at 29, 42, 43 days

Days	E_c		ε_{c0}
	(MPa)	(ksi)	(%)
29	21798.1	3161.5	0.288
42	22801.0	3307.0	0.279
43	22324.5	3237.9	0.266

Table 2.4: Concrete properties obtained from stress-strain curves

2.2.2 Reinforcing steel

Both longitudinal and transverse reinforcement were made of Grade 60 steel conforming to the ASTM Designation A706. Three samples of the #11 (36-mm diameter) column longitudinal bars were tested in monotonic tension. The mean yield strength f_y and ultimate strength f_u of the longitudinal reinforcing steel are shown in Table 2.5.

A detailed stress-strain curve was obtained using a pair of strain gauges (Figure 2.25). The yield strength was identified as the average of two samples which had been instrumented with strain gauges. The ultimate strength was identified as the average of three samples.

	(MPa)	(ksi)
f_y	518.5	75.2
f_u	706.7	102.4

Table 2.5: Measured yield and ultimate strengths of the longitudinal reinforcement

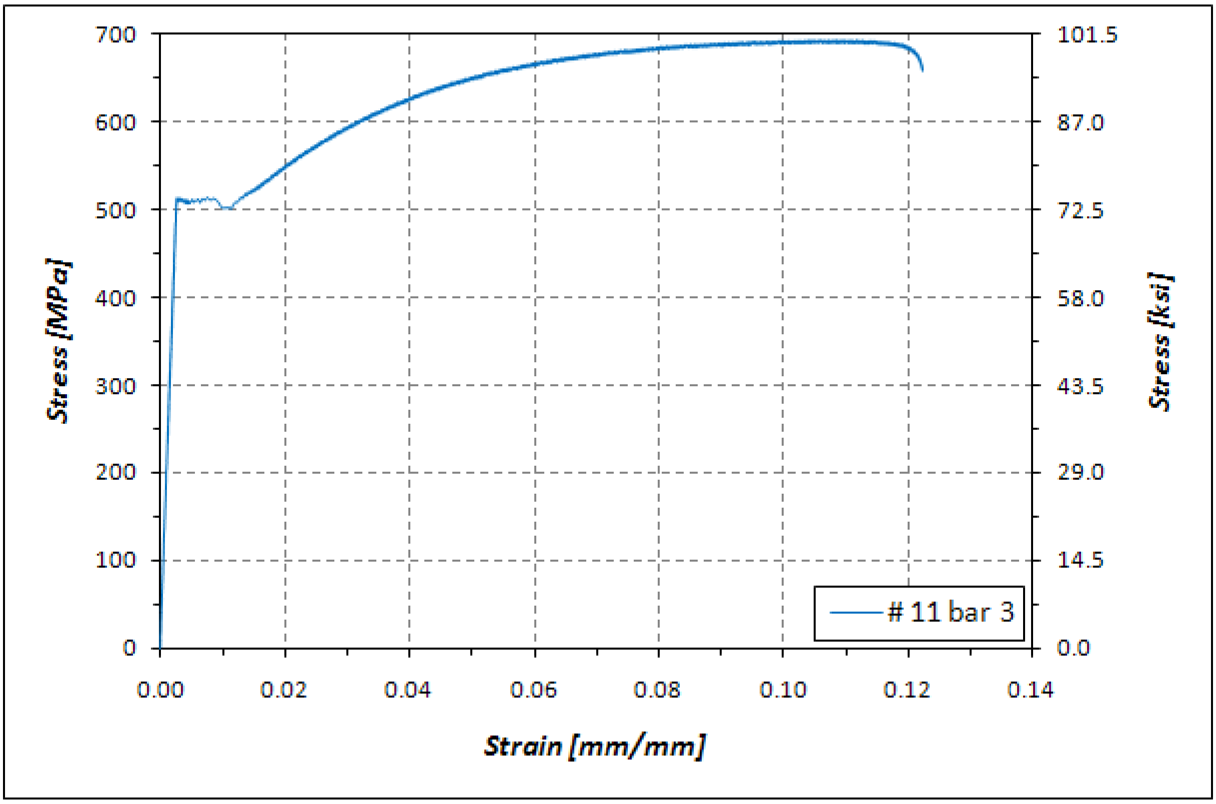

Figure 2.25: Experimental stress-strain relationship of the longitudinal steel

The steel modulus of elasticity E_s, initial hardening modulus E_{sh}, yield strain ε_y, strain at peak stress ε_u, and strain at the beginning of hardening ε_{sh} obtained from this curve are summarized in Table 2.6.

Five samples of the #5 column hoops were tested in monotonic tension. The samples were taken from three hoops ordered for material testing. Portions of each of these hoops

E_s		E_{sh}		ε_y	ε_u	ε_{sh}
(MPa)	(ksi)	(MPa)	(ksi)	(%)	(%)	(%)
196057.2	28435.7	5515.8	800.0	0.26	12.21	1.11

Table 2.6: Longitudinal steel properties obtained from stress-strain curve

containing the butt weld were tested according to Caltrans *Standard Specification* [Caltrans, 2006-b] and each sample passed. The stress-strain curves obtained from the tension tests, conducted on the bent bars, did not show a yield plateau. For this reason the yield strength f_{yh}, presented in Table 2.7, was obtained from the intersection of the experimental curve and a line with slope equal to E_s^*, cutting the offset along the strain axis by 0.002. The elastic modulus E_s^* was defined as the slope of the secant line at 300.0 MPa (40.5 ksi).

Strain gauges of the first three specimens saturated prematurely, so only two full stress-strain relationship were obtained as shown in Figure 2.26. However, the ultimate stress was obtained as the average of the five samples tested.

	(MPa)	(ksi)
f_{yh}	377.9	54.8
f_{uh}	592.2	85.9

Table 2.7: Measured yield and ultimate strength of the transverse reinforcement

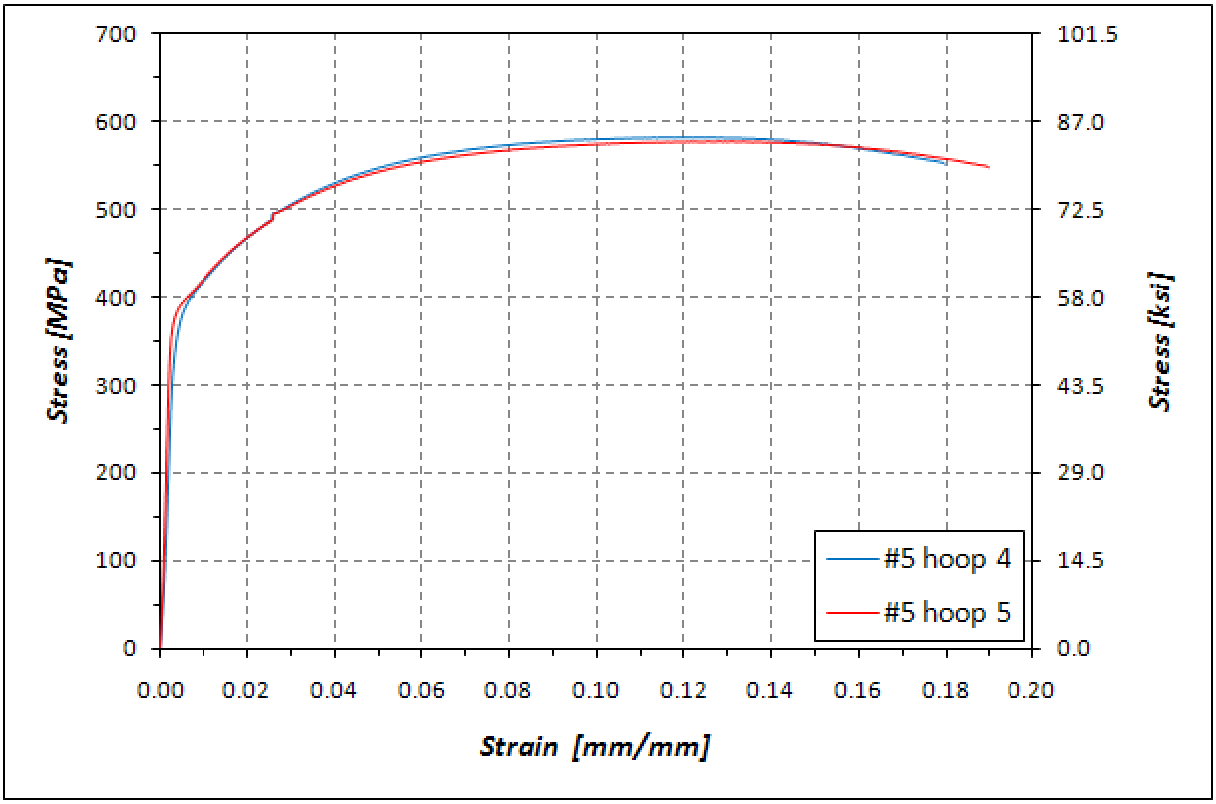

Figure 2.26: Experimental stress-strain relationship of the transverse steel

2.3 Test protocol

The specimen was tested under a range of ground motions, starting with low-intensity shaking and bringing the column progressively towards collapse. The test protocol included historical ground motions with white-noise excitation between them. The latter allowed for quantification of change in the system dynamic properties. Ambient vibration recordings were also taken for this purpose at intervals corresponding with changes in the damage state.

Four historical records (Table 2.8) were selected for this experiment, to meet the following requirements:

1. source representative of the San Francisco Bay Area seismicity (strike-slip faulting);
2. sensitivity to damping in the predicted first-mode period range of the structure (0.72 sec undamaged, 1.07 sec fully cracked);
3. target displacement ductility demand as shown in Table 2.9;
4. unscaled ground motions to achieve the desired displacement demands.

The selection of the ground motions was based on their elastic displacement response spectra assuming equal elastic and inelastic displacement demands, and on the results of a nonlinear dynamic time history analysis. Based on the results these analyses, the Takatori record was scaled down as shown in Table 2.9.

The input ground motion EQ1 was intended to represent a low-intensity earthquake with high probability of occurrence. Under this excitation, the column was expected to reach nominal capacity or an idealized yield displacement demand of 88 mm (3.47 in.), which was obtained from a displacement-driven pushover analysis using *Ruaumoko* [Carr, 2008]. The elastic displacement and pseudo-acceleration response spectra of the Agnew State Hospital ground motion are presented in Figures 2.27 and 2.28, for a damping ratio of 1%. The spectra of this ground motion are compared with the one reproduced by the table during testing.

Test	Earthquake	Date	Moment magnitude	Station	Component
EQ1	Loma Prieta	10/18/1989	6.9	Agnew State Hospital	090
EQ2	Loma Prieta	10/18/1989	6.9	Corralitos	090
EQ3	Loma Prieta	10/18/1989	6.9	LGPC	000
EQ4	Loma Prieta	10/18/1989	6.9	Corralitos	090
EQ5	Kobe	01/16/1995	6.9	Takatori	000
EQ6	Loma Prieta	10/18/1989	6.9	LGPC	000

Table 2.8: Ground motions: general information

Test	Target displacement ductility	Scale factor
EQ1	μ_Δ=1.0	1.0
EQ2	μ_Δ=2.0	1.0
EQ3	μ_Δ=4.0	1.0
EQ4	μ_Δ=2.0	1.0
EQ5	μ_Δ=8.0	-0.8
EQ6	μ_Δ=4.0	1.0

Table 2.9: Ground motions: target displacement ductility and scale factor

Corralitos record was chosen as EQ2 to simulate a medium-intensity excitation, inducing a displacement ductility demand of 2.0. Its response spectra are presented in Figures 2.29 and 2.30.

The ground motion selected to represent the design event was the Los Gatos Presentation Center record from 1989 Loma Prieta event (EQ3). According to Caltrans *Seismic Design Criteria* [Caltrans, 2006-a] the design event has a 5% probability of exceedance in 50 years. For such earthquake columns are expected to undergo a displacement ductility demand of 4.0 and fully maintain their load carrying capacity. The response spectra for EQ3 and the design spectra are shown in Figures 2.31 and 2.32. The design acceleration response spectrum for a damping ratio of 5% was obtained from Caltrans ARS online [Caltrans] for a latitude of 37.77019055, a longitude of -122.41790771 and a shear wave velocity V_{s30} of 350 m/s (1148 ft/s). The spectral accelerations corresponding to periods larger than 1 sec were increased by 20% and the ones within 0.5 sec and 1 sec were determined by linear interpolation to account the near fault effects [Caltrans, 2006 a]. The design spectra for a damping ratio of 1% was obtained by dividing the spectral acceleration at 5% damping by 0.8, according to *NEHRP Guidelines for the Seismic Rehabilitation of Building* [FEMA-273, 1997].

The Corralitos record was repeated as EQ4 to reproduce the effects of a medium-intensity aftershock. The new response spectra are shown in Figures 2.29 and 2.30, together with those obtained from EQ2. The table-structure interaction is observed in these figures as damage-induced changes of the specimen’s dynamic properties influences the base excitation reproduced by the table.

An earthquake with very large nonlinear demands was chosen for EQ5. The Takatori record of 1995 Kobe earthquake scaled at 80% was used for an expected displacement ductility demand equal to 8.0. Its response spectra are presented in Figures 2.33 and 2.34.

Los Gatos record (EQ6) was repeated as an aftershock of EQ5. Its response spectra are shown in Figures 2.31 and 2.32, where again the effect of table-specimen interaction can be observed.

To bring the specimen to near-collapse conditions, the column was subjected to the additional ground motions presented in Tables 2.10 and 2.11. Their response spectra can be found in Figures 2.35 to 2.38.

White-noise excitations with root-mean-square acceleration equal to 3% of gravity were run between the historical records in order to assess the dynamic properties of the system before and after each test. Ambient vibration tests were also performed before testing, after EQ3, after EQ5, and after EQ6.

The response spectra of the original ground motions were obtained after filtering historical records found in PEER's Ground Motion Database [PEER]. The records were band pass filtered using and FIR filter of order 5000 with a cutoff frequencies of 0.25 and 25-Hz.

Test	**Earthquake**	**Date**	**Moment magnitude**	**Station**	**Component**
EQ7	Kobe	01/16/1995	6.9	Takatori	000
EQ8	Kobe	01/16/1995	6.9	Takatori	000
EQ9	Kobe	01/16/1995	6.9	Takatori	000
EQ10	Kobe	01/16/1995	6.9	Takatori	000

Table 2.10: Added ground motions: general information

Test	**Target displacement ductility**	**Scale factor**
EQ7	Not applicable	1.0
EQ8	Not applicable	-1.2
EQ9	Not applicable	1.2
EQ10	Not applicable	1.2

Table 2.11: Added ground motions: target displacement ductility and scale factor

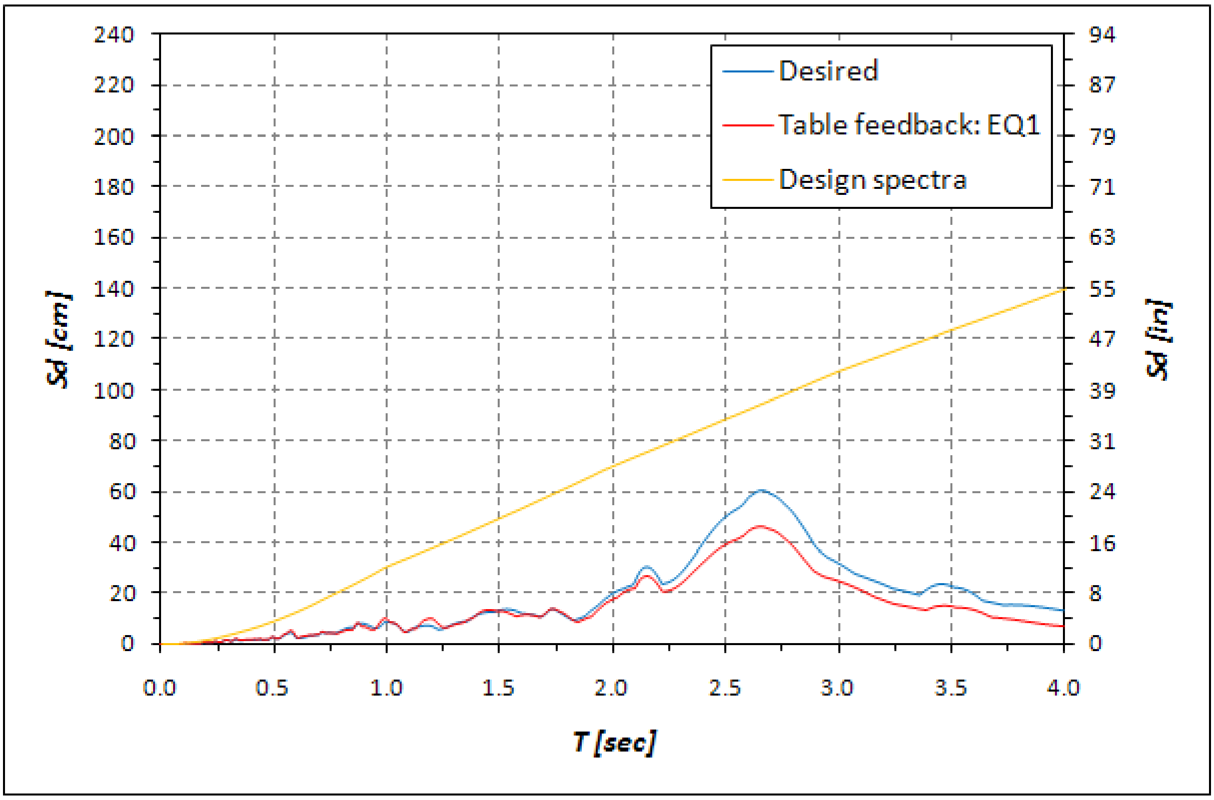

Figure 2.27: Elastic displacement response spectra of Agnew State Hospital - damping ratio of 1% and design spectra - damping ratio of 1%

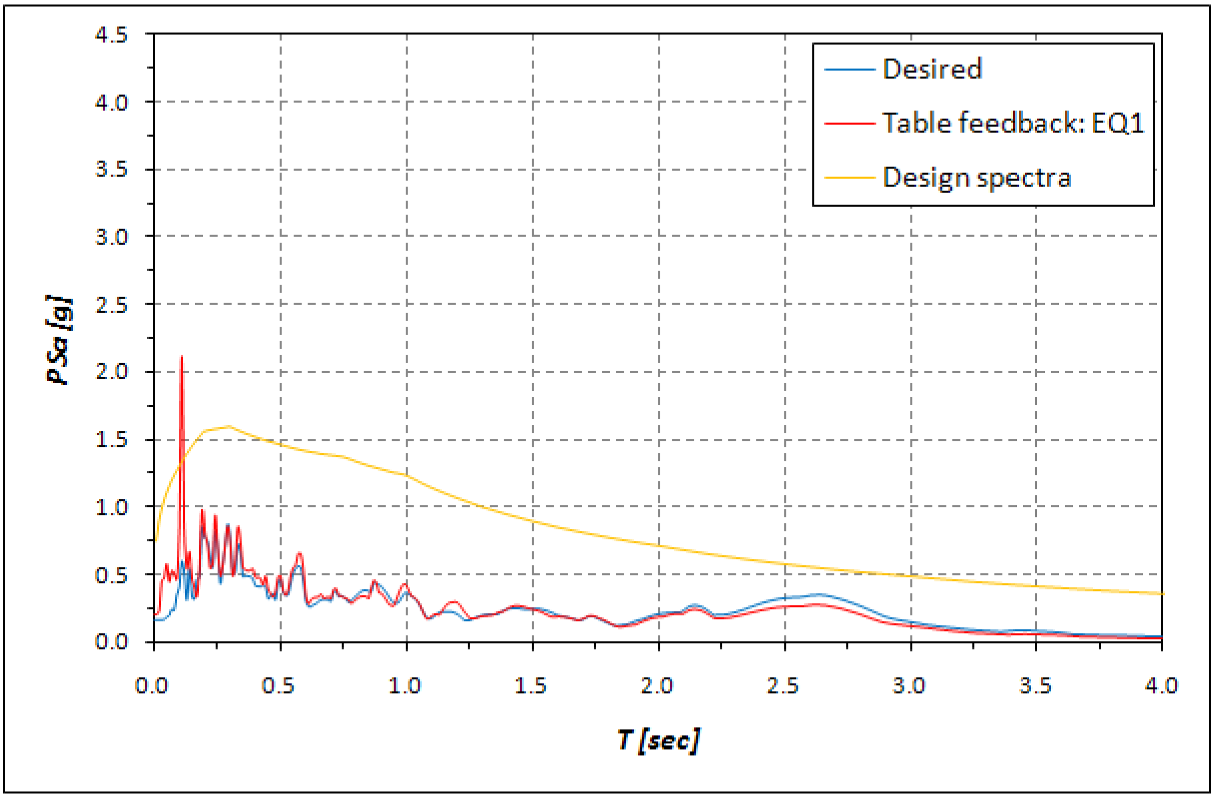

Figure 2.28: Elastic pseudo-acceleration response spectra of Agnew State Hospital - damping ratio of 1% and design spectra - damping ratio of 1%

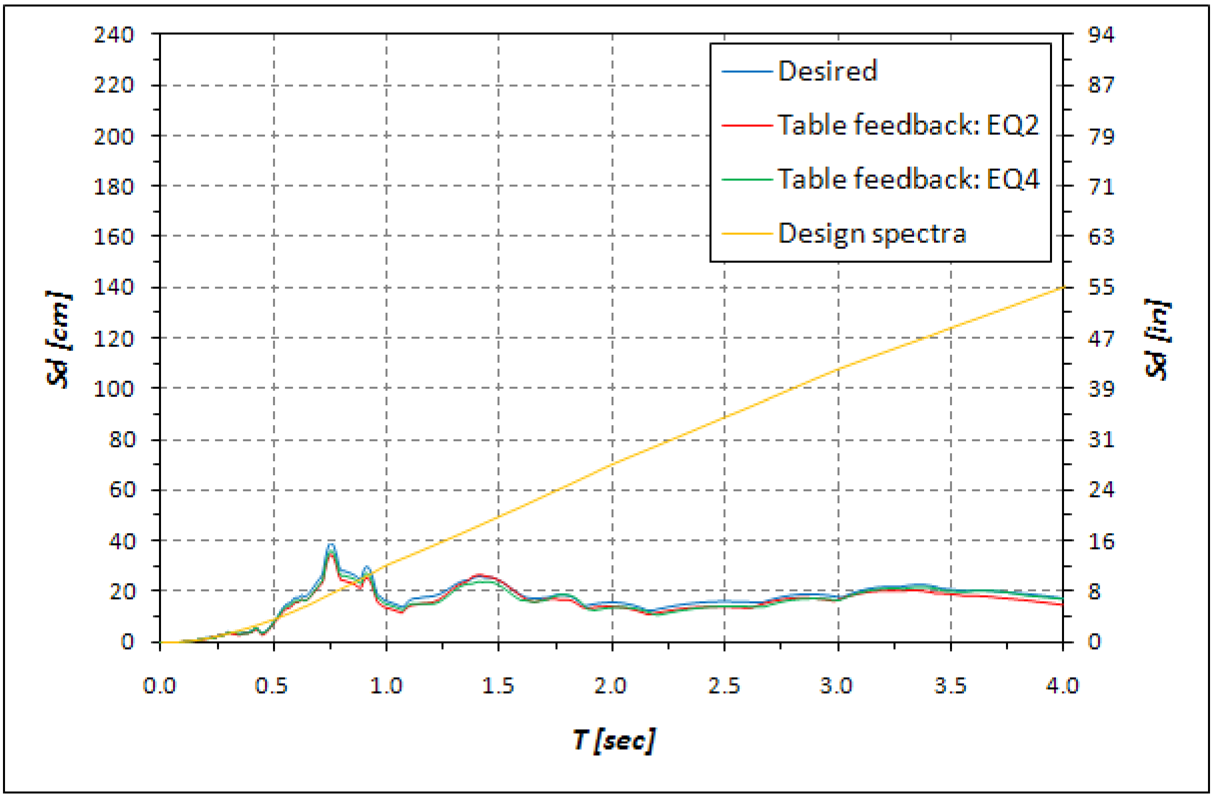

Figure 2.29: Elastic displacement response spectra of Corralitos - damping ratio of 1% and design spectra - damping ratio of 1%

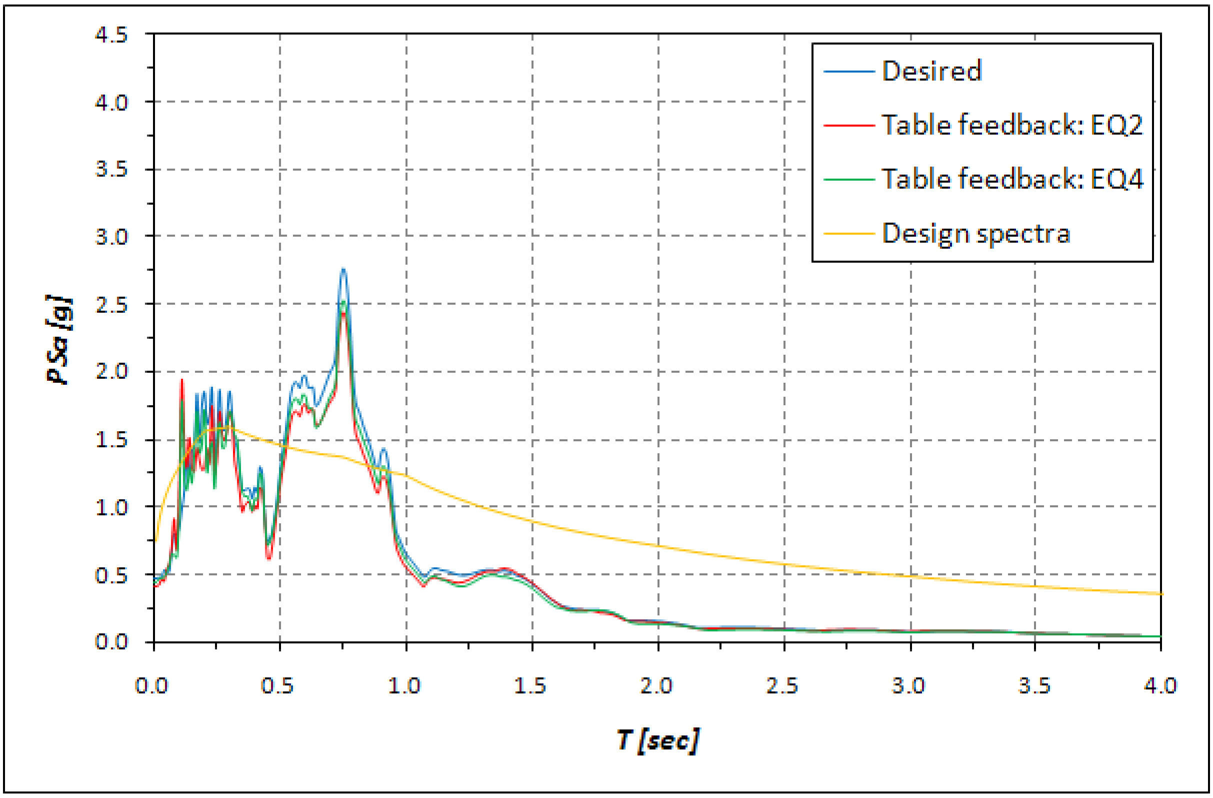

Figure 2.30: Elastic pseudo-acceleration response spectra of Corralitos - damping ratio of 1% and design spectra - damping ratio of 1%

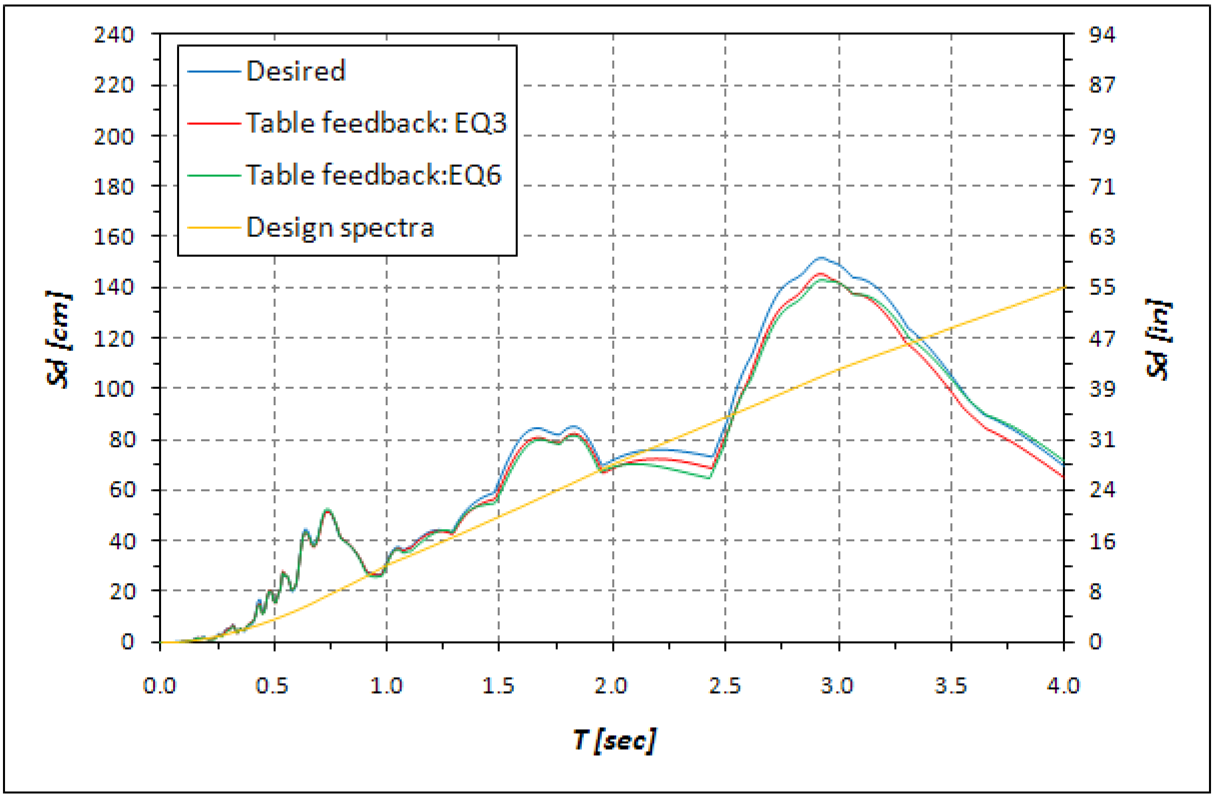

Figure 2.31: Elastic displacement response spectra of Los Gatos - damping ratio of 1% and design spectra - damping ratio of 1%

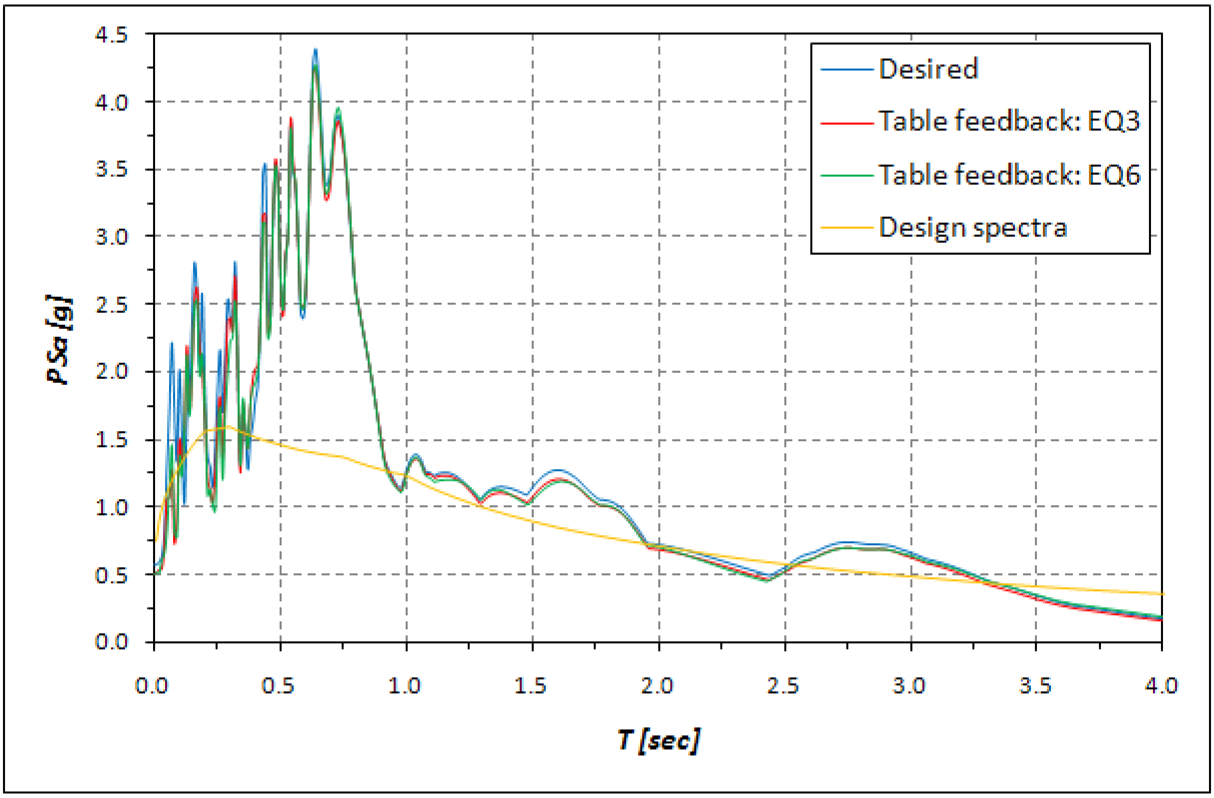

Figure 2.32: Elastic pseudo-acceleration response spectra of Los Gatos - damping ratio of 1% and design spectra - damping ratio of 1%

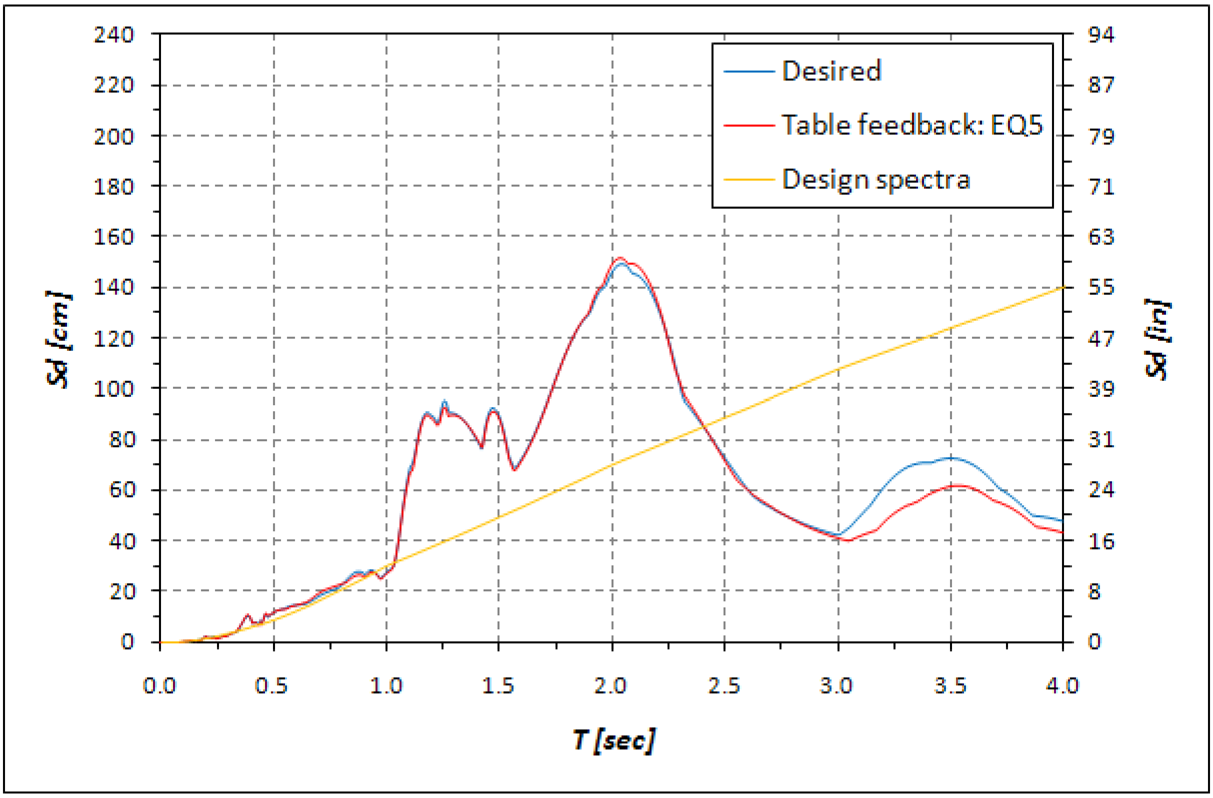

Figure 2.33: Elastic displacement response spectra of Takatori 80% scaled - damping ratio of 1% and design spectra - damping ratio of 1%

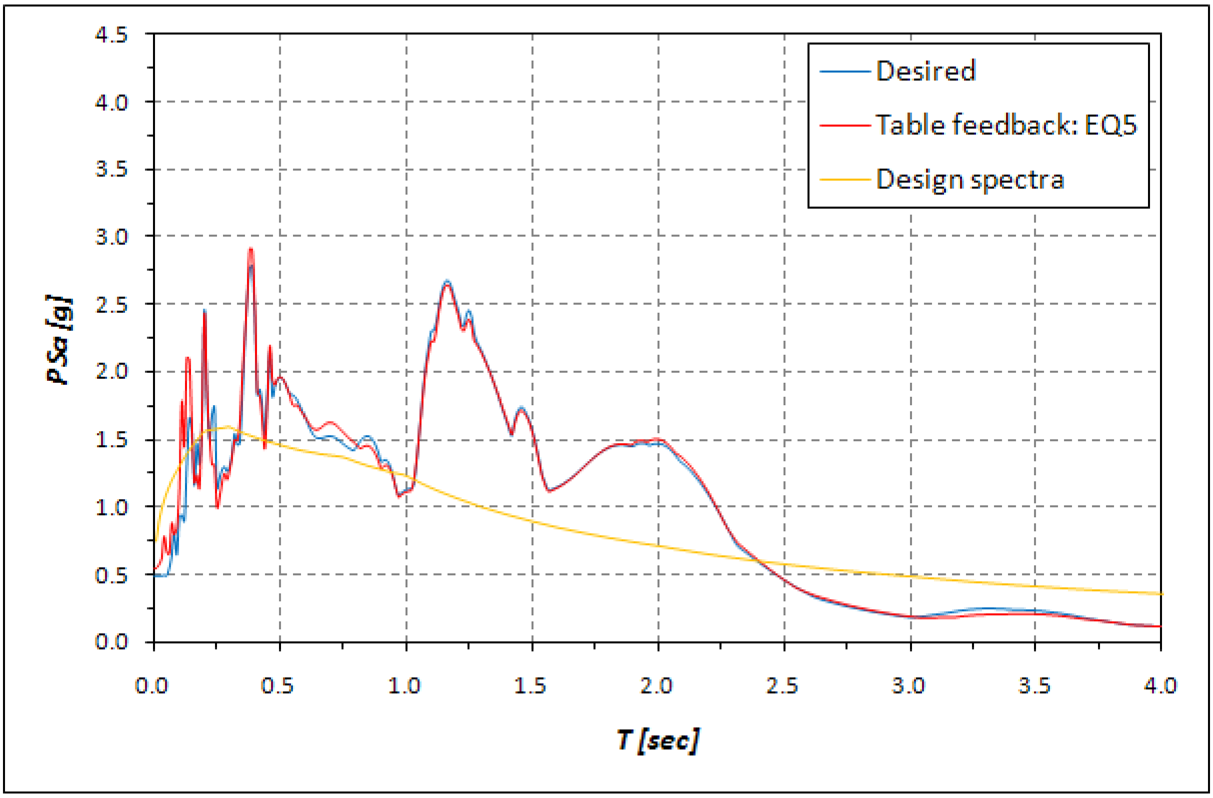

Figure 2.34: Elastic pseudo-acceleration response spectra of Takatori 80% scaled - damping ratio of 1% and design spectra - damping ratio of 1%

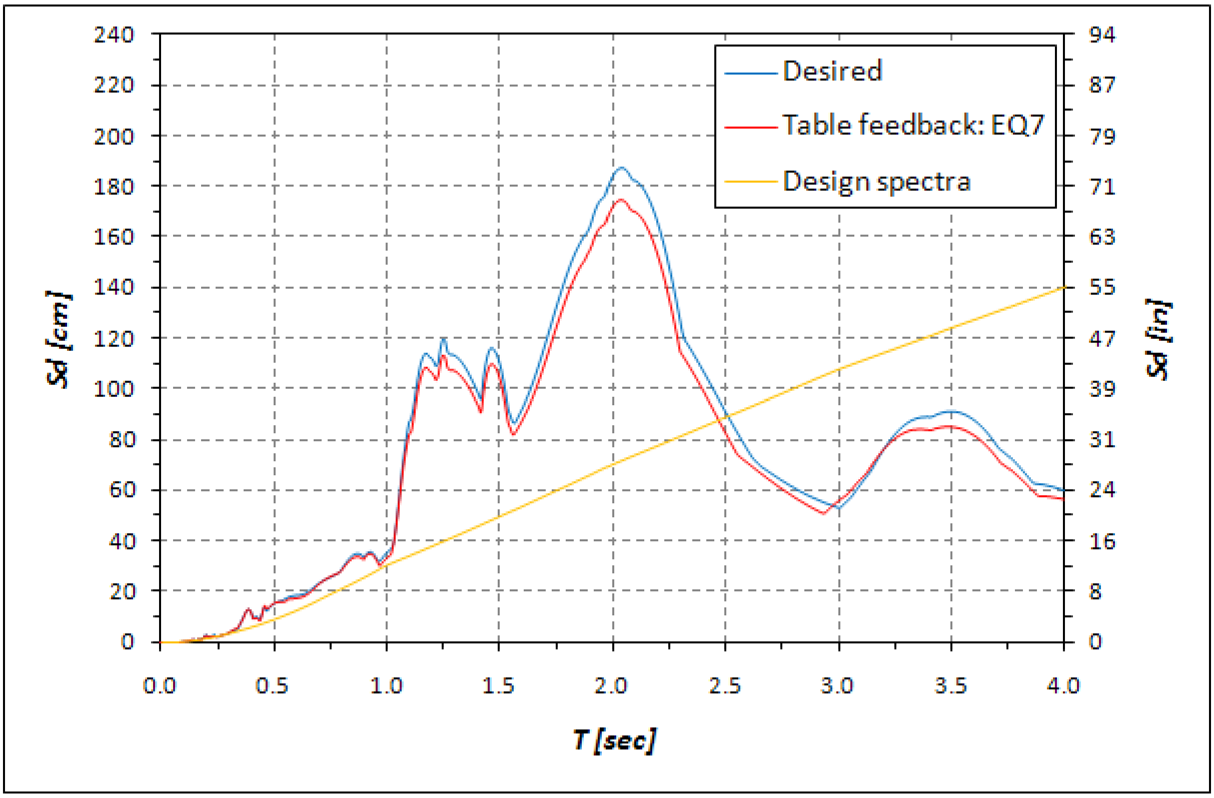

Figure 2.35: Elastic displacement response spectra of Takatori - damping ratio of 1% and design spectra - damping ratio of 1%

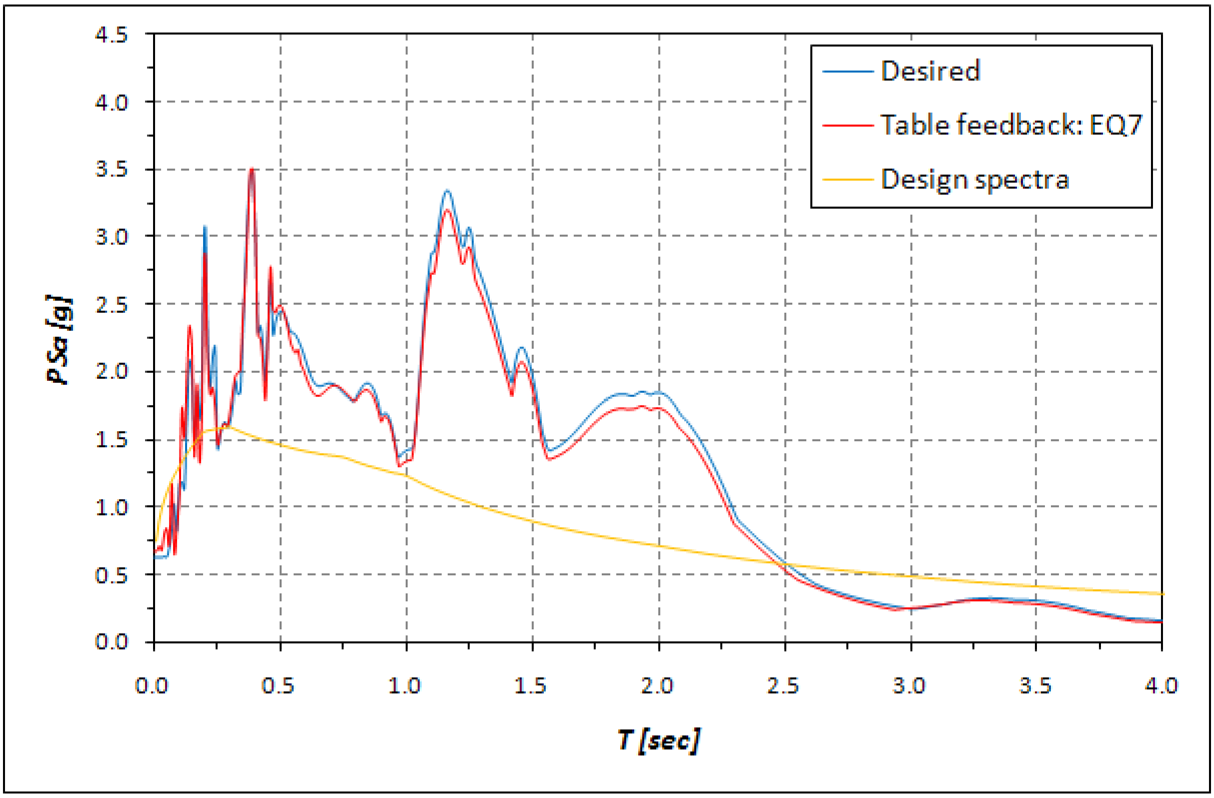

Figure 2.36: Elastic pseudo-acceleration response spectra of Takatori - damping ratio of 1% and design spectra - damping ratio of 1%

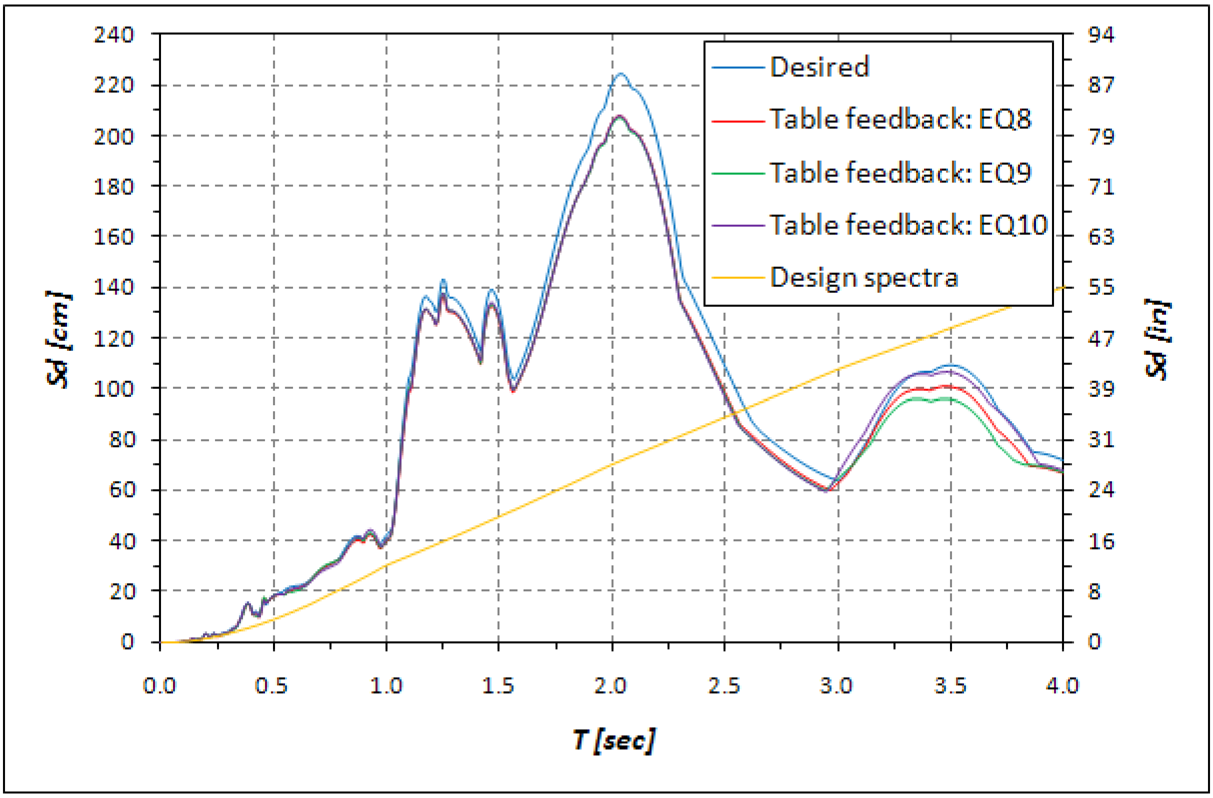

Figure 2.37: Elastic displacement response spectra of Takatori 120% scaled - damping ratio of 1% and design spectra - damping ratio of 1%

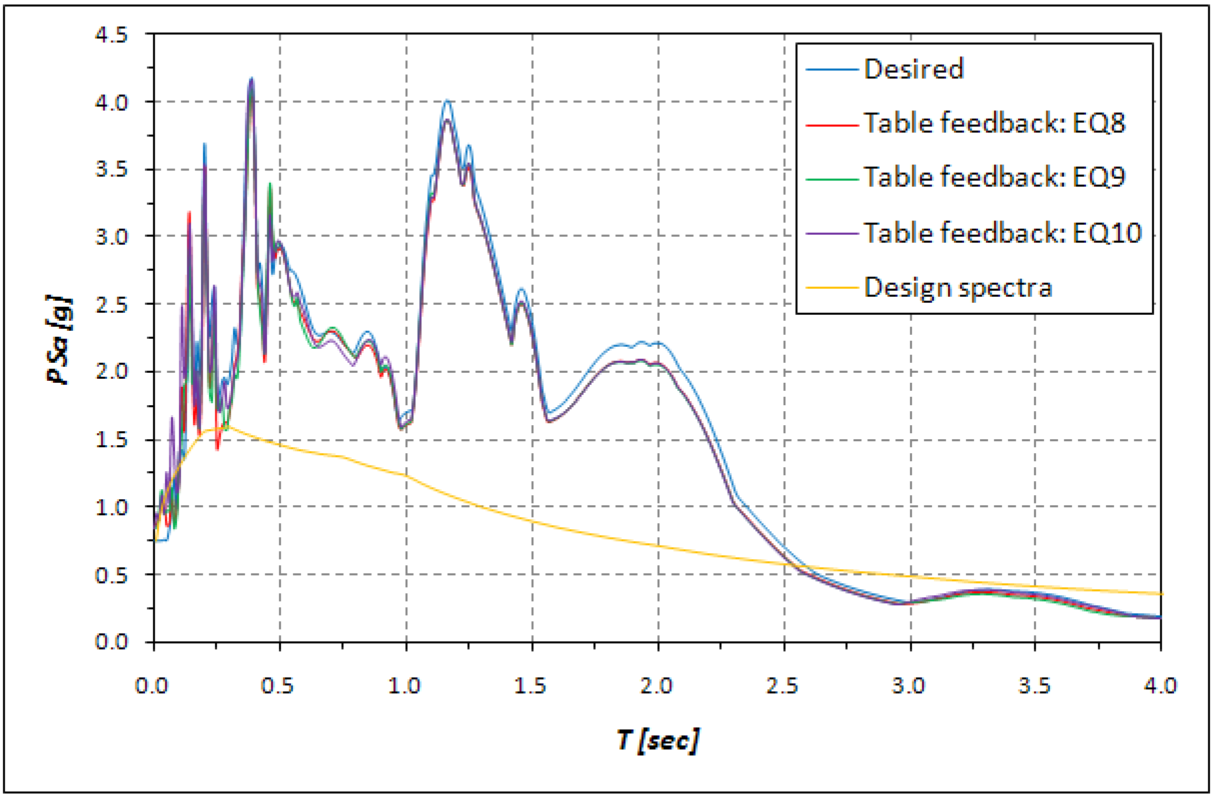

Figure 2.38: Elastic pseudo-acceleration response spectra of Takatori 120% scaled - damping ratio of 1% and design spectra - damping ratio of 1%

3. Analytical modeling

This chapter describes the analytical model developed to simulate the column dynamic response. First, a moment-curvature analysis was performed using the program *Columna* [Kuebitz, 2002] to identify the column cross-section behavior. Than a static pushover analysis and a time-history analyses were carried out using the program *Ruaumoko* [Carr, 2008].

3.1 Moment-curvature analysis

An incremental analysis was performed to obtain the moment-curvature relationship of the column cross section under a constant applied axial load [Kuebitz, 2002]. This analysis is accomplished by discretizing the cross section into fibers of area A_j. Material properties are assigned to each fiber, depending on its position within the cross-section; unconfined concrete in the cover, confined concrete in the core, steel at longitudinal reinforcement locations. Assuming plane sections remain plane, under any curvature increment the strain distribution on the section remains linear with the curvature as the slope. Therefore, at any curvature step φ_i, a trial strain profile is assumed with slope φ_i. The stress on each fiber σ_{ij} is computed from the corresponding strain ε_{ij} and the constitutive material model; consequently the fiber force is determined as $A_j \cdot \sigma_{ij}$. If the sum of all the fiber forces is not equal to the applied axial load P, the strain profile is iteratively shifted, keeping the slope constant, until the desired axial resultant is obtained. Finally, the moments of the fiber forces, with respect to the section centroid, are summed to find the current moment M_i. This process is repeated until the ultimate strain of the steel or confined concrete is reached on any fiber. A flowchart of the moment-curvature analysis steps is presented in Figure 3.1.

3.1.1 Input properties

3.1.1.1 General input parameters and section geometry

An actual applied axial load P_a of 2534.9 kN (569.7 kips), corresponding to the measured weight of column and superstructure, and a volumetric confining ratio ρ_s of 0.953% were assigned. The cross-section perimeter was approximated by a 32-point polygonal line. The confined region was assigned as the area enclosed within hoop, and longitudinal reinforcing bars were introduced at their locations. The resulting cross section was discretized by a 100×100 mesh, see Figure 3.2.

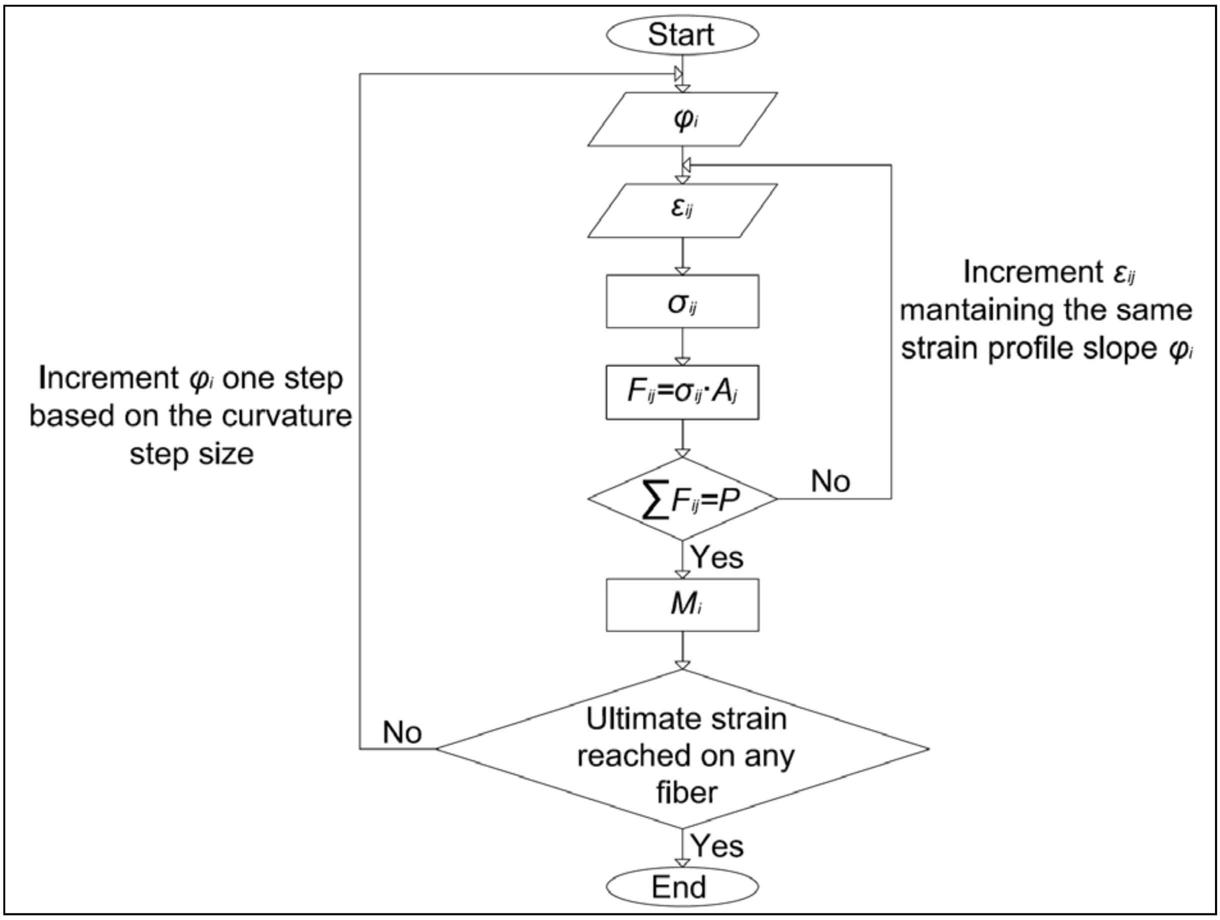

Figure 3.1: Flowchart of moment-curvature analysis

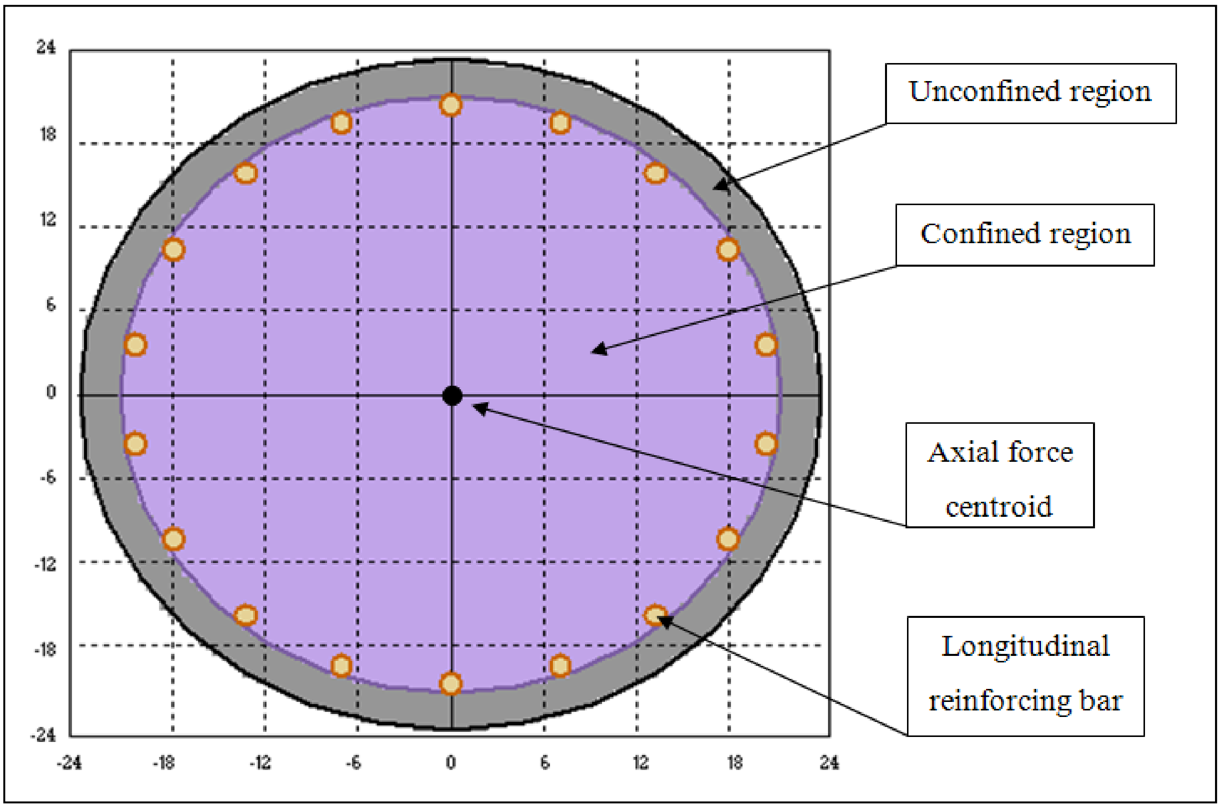

Figure 3.2: Column cross-section in *Columna*

3.1.1.2 Longitudinal reinforcing steel

The assigned longitudinal reinforcing steel mechanical properties are presented in Table 3.1. The initial hardening modulus E_{sh}, the ultimate strain ε_u, and the strain at the beginning of hardening ε_{sh} were obtained from the single experimental stress-strain curve fully available (Figure 2.25). The yield strength $f_{y,adj}$ and the ultimate one $f_{u,adj}$ were adjusted to account for strain-rate effects on the reinforcing steel cyclic behavior [Restrepo-Posada, 1994].

Stresses were amplified by 5% along the initial elastic portion; 5% of the measured yield strength was added to the rest of the curve. A steel modulus of elasticity of 200000 MPa (29000 ksi) was used in the analysis. The experimental stress-strain curve, the one adjusted for strain-rate effects, and the one implemented in *Columna* [Kuebitz, 2002] are shown in Figure 3.3. The steel analytical constitutive model of the steel accurately approximates the adjusted experimental stress-strain relationship.

$f_{y,adj}$		$f_{u,adj}$		E_{sh}		ε_u	ε_{sh}
(MPa)	**(ksi)**	**(MPa)**	**(ksi)**	**(MPa)**	**(ksi)**	**(%)**	**(%)**
535.0	77.6	719.1	104.3	5515.8	800.0	12.21	1.11

Table 3.1: Longitudinal reinforcing steel properties

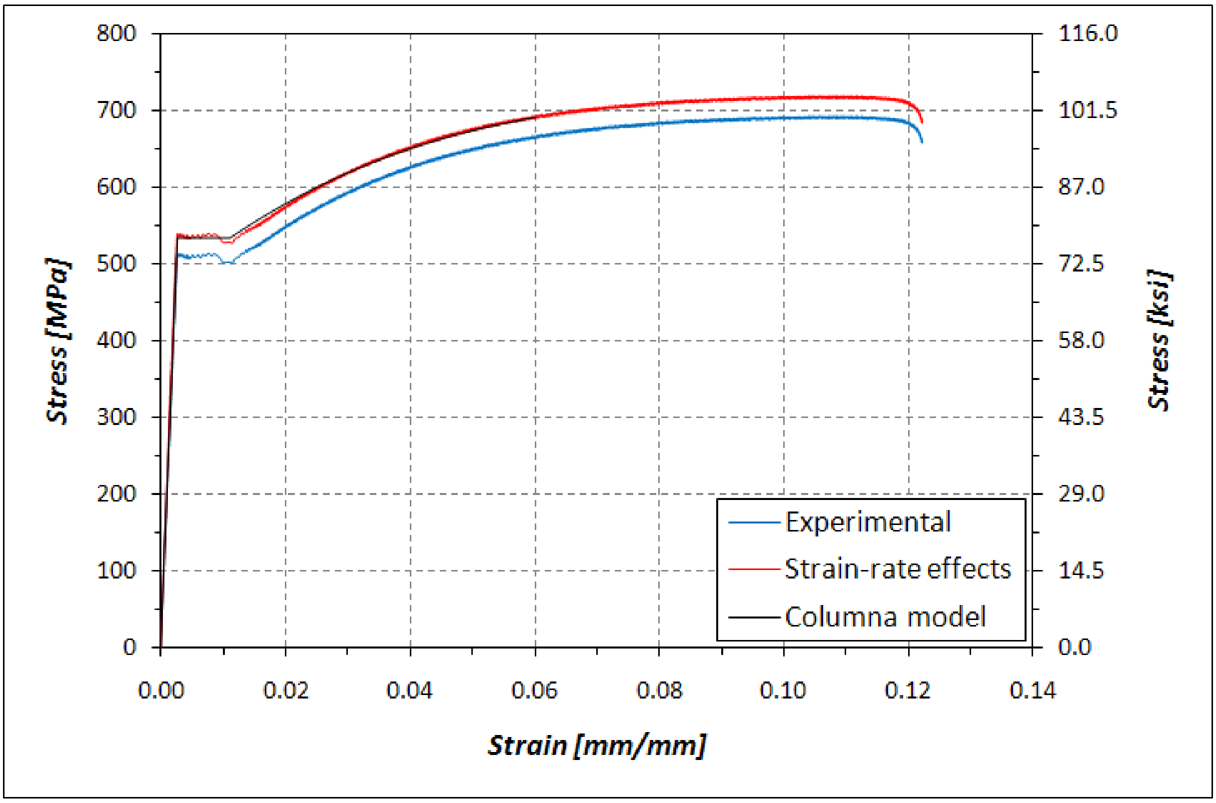

Figure 3.3: Stress-strain relationships of the longitudinal reinforcing steel

3.1.1.3 Concrete

Mander 1984 Model [Mander, 1988] is used by *Columna* [Kuebitz, 2002] to define the compressive stress-strain relationship of both confined and unconfined concrete. The unconfined compressive cylinder strength of the concrete $f'_{c,avg}$, the modulus of elasticity $E_{c,avg}$ and the peak strain $\varepsilon_{c0,avg}$ were assigned as the average of the values at 42 days and 43 days, see Tables 2.1 and 2.5. These values, as well the full-spalling strain ε_{sp} of the unconfined concrete, are given in Table 3.2.

Figure 3.4 shows that the experimental stress-strain curves at 42 days and 43 days were not accurately reproduced by analytical model. In particular, the analytical constitutive relationship resulted to be stiffer than the experimental ones. The concrete modulus of elasticity obtained from Mander's stress-strain relationship was about 25% larger than the average experimental value. This incongruence was corrected reducing the initial slope of the idealized trilinear moment-curvature relationship used in Ruaumoko [Carr, 2008] as explained in Paragraph 3.2.2.

Collins and Mitchell 1987 Model [Collins and Mitchell, 1991] was adopted by *Columna* to define the concrete tensile behavior. Tension stiffening was accounted for both confine and unconfined concrete.

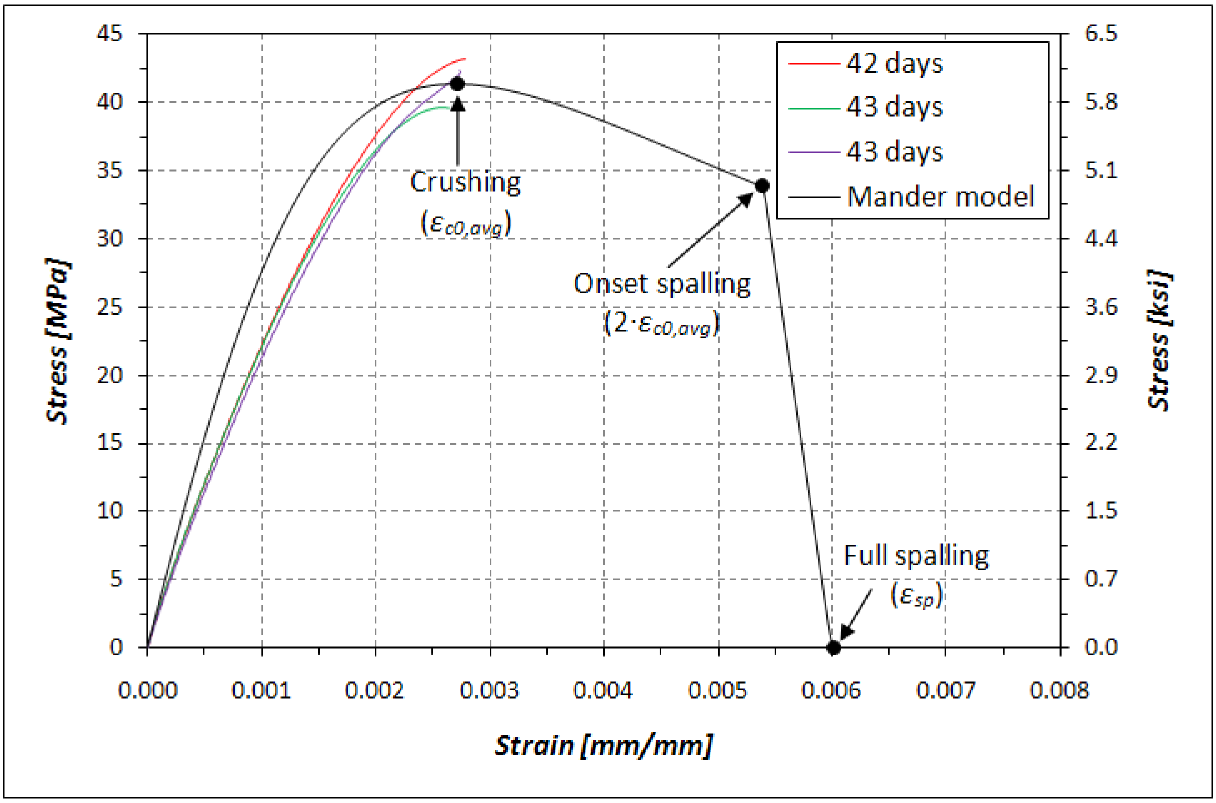

Figure 3.4: Stress-strain relationship of the unconfined concrete

$f'_{c,avg}$		$E_{c,avg}$		$\varepsilon_{c0,avg}$	ε_{sp}
(MPa)	**(ksi)**	**(MPa)**	**(ksi)**	**(%)**	**(%)**
41.4	6.0	22483.1	3260.9	0.27	0.60

Table 3.2: Concrete properties

3.1.2 Results

Figure 3.5 shows the moment-curvature relationship of the column cross-section obtained from *Columna* [Kuebitz, 2002]. The moment M was normalized by the product $W \cdot H$, where W is the total weight of column and superstructure, and H is the column height. The curvature φ was normalized by the ratio ε_y/D, where D is the diameter of the cross-section and ε_y is the yield strain of the longitudinal reinforcement obtained from the experimental stress-strain relationship, see Figure 2.25. Table 3.3 summarized the quantities used for normalization. In Figure 3.5, material strain limit states are also indicated on the moment-curvature relationship.

Concrete limit state Ci is reached first. It corresponds to first cracking and occurs when the tensile strain on the extreme unconfined concrete fiber ε_{ct} reaches a concrete cracking strain ε_{cr} given by:

$$\varepsilon_{cr} = \frac{f_{cr}}{E_{c,avg}} = 9.5 \cdot 10^{-5}$$

where f_{cr} is the concrete tensile strength equal to:

$$f_{cr} = 4 \cdot \sqrt{f'_{c,avg}[ksi]} = 0.3\ ksi\ (2.1\ MPa)$$

The corresponding first-cracking moment M_{cr} and curvature φ'_{cr}, are equal to 838.7 kNm (618.6 kip-ft) and $2.19 \cdot 10^{-4}$ rad/m ($5.57 \cdot 10^{-6}$ rad/in), respectively.

Steel limit-state Si, corresponding to first yield of the most tensile longitudinal bar, is subsequently attained. It occurs when the tensile strain on the extreme steel fiber ε_s reaches the yield strain ε_y shown in Table 3.3. The first-yield moment M'_y and curvature φ'_y, are equal to 4569.9 kNm (3370.6 kip-ft) and $3.73 \cdot 10^{-3}$ rad/m ($9.48 \cdot 10^{-5}$ rad/in), respectively.

The strain limits Sii and Cii are closely located on the moment-curvature relationship. Sii is achieved when 1% strain is reached on the extreme steel fiber in tension, whereas Cii is achieved when -0.4% strain is attained on the extreme unconfined concrete fiber in compression. The first occurring among Sii and Cii gives the expected moment of the cross section. It is identified with the moment M_e and the curvature φ_e, equal to 5793.1 kN-m (4272.7 kips-ft) and $1.24 \cdot 10^{-2}$ rad/m ($3.15 \cdot 10^{-4}$ rad/in), respectively.

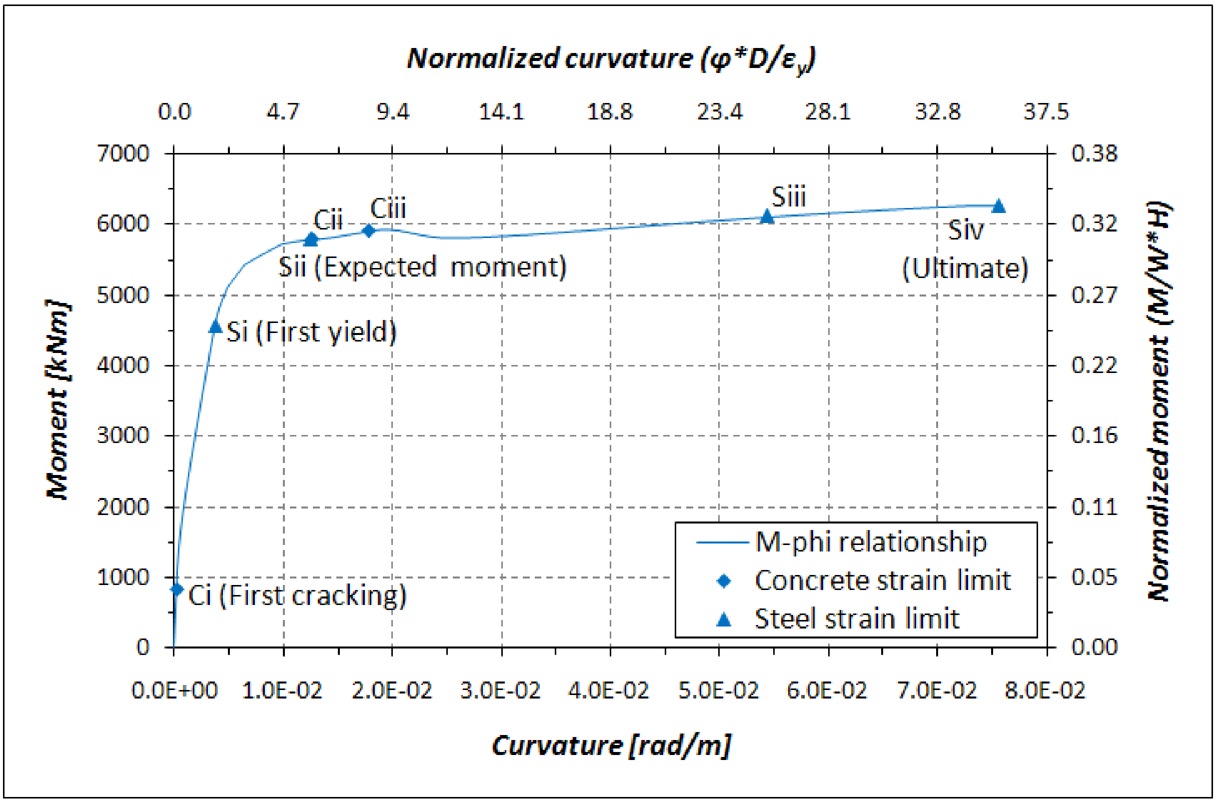

Figure 3.5: Moment-curvature relationship and strain limit states

W		***H***		***D***		ε_y
(kN)	**(kips)**	**(m)**	**(ft)**	**(m)**	**(ft)**	**(%)**
2534.9	569.7	7.31	24.0	1.22	4.0	0.26

Table 3.3: Quantities for normalizations

Concrete limit-state Ciii is successively achieved. It corresponds to deep concrete cover spalling and occurs when the compressive strain on the extreme confined concrete fiber ε_{cc} reaches a value of -0.4%.

The following limit-state Siii corresponds to the onset of longitudinal bar buckling. Since it depends on the cumulated steel strains, it is defined in terms of the difference between the tensile strain on the extreme steel fiber ε_s (positive) and the compressive strain on the extreme confined concrete fiber ε_{cc} (negative). An empirical relationship locates this limit states when:

$$\varepsilon_s - \varepsilon_{cc} = \frac{10 - \frac{s}{d_{bl}}}{100} = 5.7 \cdot 10^{-2}$$

where s is the hoop spacing and d_{bl} is the diameter of the longitudinal bars.

Finally steel limit-state Siv, corresponding to longitudinal bar fracture, is reached when:

$$\varepsilon_s - \varepsilon_{cc} = \frac{14 - \dfrac{4 \cdot s}{3 \cdot d_b}}{100} = 8.3 \cdot 10^{-2}$$

Again the, the cumulative steel strain governs this limit strain, which represents the ultimate point of the moment-curvature relationship. It is identified by moment M_u and curvature φ_u, equal to 6281.8 kNm (4633.2 kips-ft) and $7.56 \cdot 10^{-2}$ rad/m ($1.92 \cdot 10^{-3}$ rad/in), respectively.

3.1.3 Trilinear idealization

The moment-curvature relationship obtained from *Columna* was idealized whit three segments, to be given as an input for the static pushover and time-history analyses. First, the uncracked portion joins the origin to first-cracking point. The following segment links the first-cracking point with the idealized-yielding point. Idealized yield is defined as the intersection of the secant line passing through first-yield and the horizontal line passing through the expected-moment. It is identified with the moment M_y and the curvature φ_{yi}, equal to 5793.1 kN-m (4272.7 kips-ft) and $4.73 \cdot 10^{-3}$ rad/m ($1.20 \cdot 10^{-4}$ rad/in), respectively. The third inelastic segment connects the idealized-yielding point with the ultimate one.

A modified trilinear idealization was adopted to correct the incongruence of the concrete modulus of elasticity mentioned in Paragraph 3.2.1, as shown in Figure 3.6. The slope of the uncracked portion needed to be reduced, so the first-cracking point was moved to the right dividing the cracking curvature φ'_{cr} by the ratio of the two moduli. The symbol φ_{cr} will identify the modified value of the cracking curvature corresponding to $2.93 \cdot 10^{-4}$ rad/m ($7.43 \cdot 10^{-6}$ rad/in). This operation is illustrated in Figure 3.7. Table 3.4 summarizes the moment and curvature of the three significant points of the modified trilinear relationship.

	Curvature $\boldsymbol{\varphi}$		**Moment $\boldsymbol{M}$**	
	(rad/m)	**(rad/in)**	**(kNm)**	**(kip-ft)**
Modified idealized first cracking $(\boldsymbol{\varphi_{cr}}, \boldsymbol{M_{cr}})$	$2.93 \cdot 10^{-4}$	$7.43 \cdot 10^{-6}$	838.7	618.6
Idealized yield $(\boldsymbol{\varphi_{yi}}, \boldsymbol{M_y})$	$4.73 \cdot 10^{-3}$	$1.20 \cdot 10^{-4}$	5793.1	4272.7
Ultimate $(\boldsymbol{\varphi_u}, \boldsymbol{M_u})$	$7.56 \cdot 10^{-2}$	$1.92 \cdot 10^{-3}$	6281.8	4633.2

Table 3.4: Significant points of the modified trilinear idealization

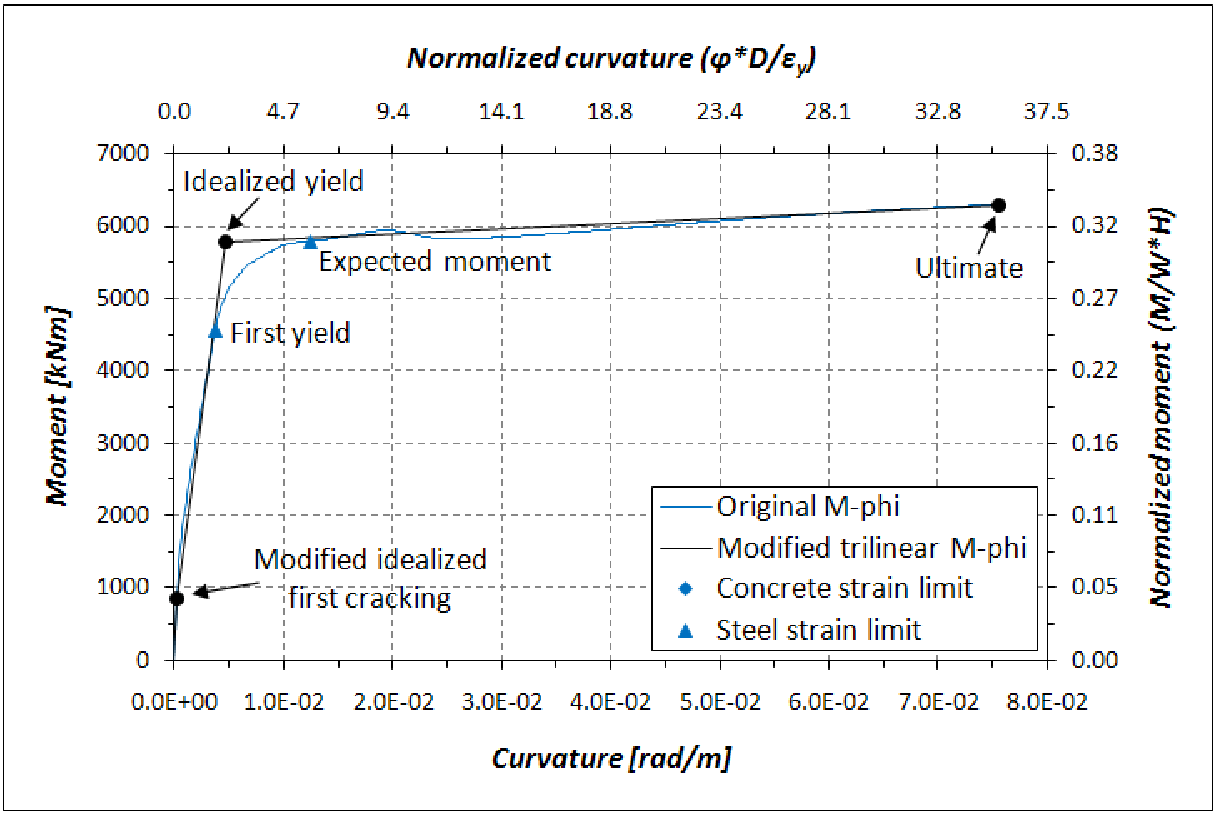

Figure 3.6: Modified trilinear idealization of the moment-curvature relationship

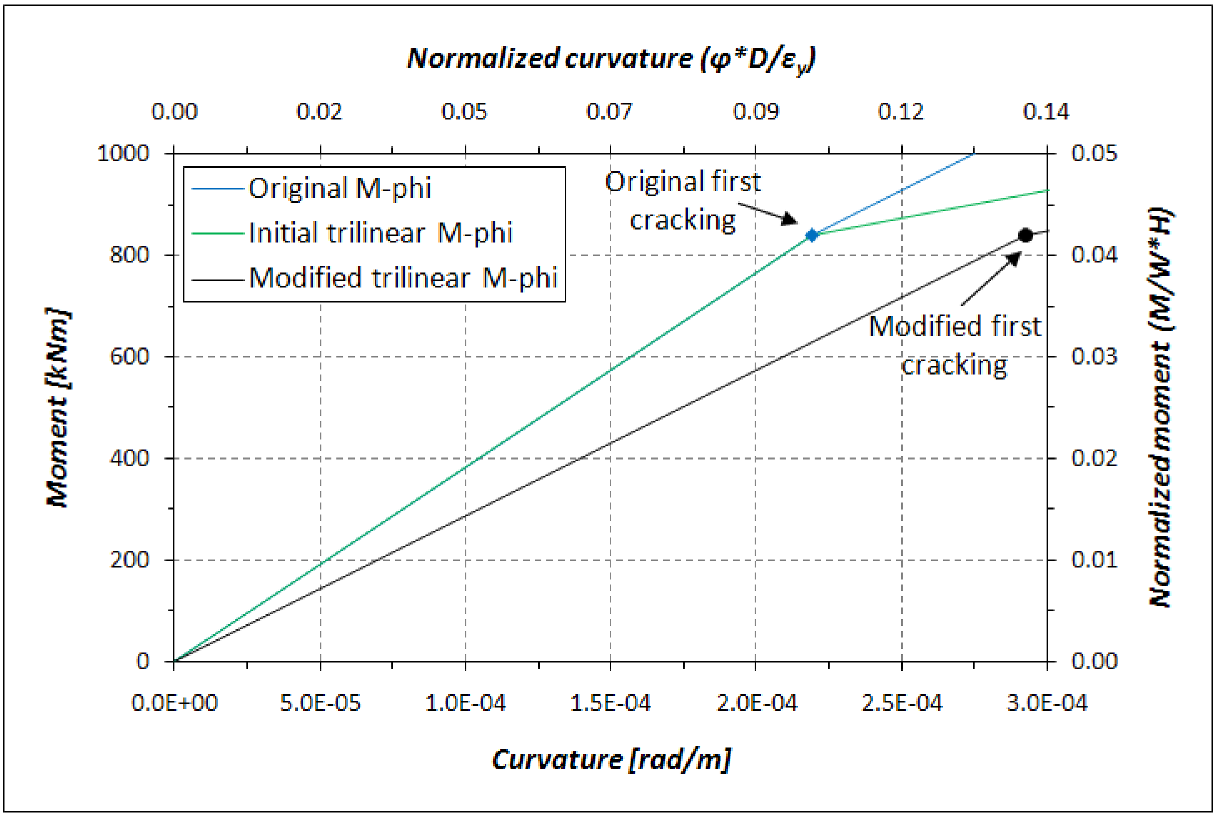

Figure 3.7: Original and modified trilinear idealization of the moment-curvature relationship

3.2 Structural analysis model

A bidimensional lumped plasticity and lumped mass model was created with the program *Ruaumoko* [Carr, 2008]. A displacement-driven pushover analysis and a non-linear time history analysis were performed to simulate the response of the specimen during testing.

3.2.1 Description of the model

Figure 3.8 shows a graphical representation of the structural model implemented in the program *Ruaumoko* [Carr, 2008].

3.2.1.1 Geometry, masses and applied loads

The footing was simply considered as a fix restraint for the column base, see Figure 3.8. The column was modeled with inelastic Giberson one-component frame elements [Giberson, 1967]. This type of element includes a central elastic portion, rigid-end blocks, and plastic hinge segment between the elastic and rigid parts, see Figure 3.8. The column was discretized into four 1.83-m (72-in) long elements. Consequently, five node evenly spaced along the column height were defined.

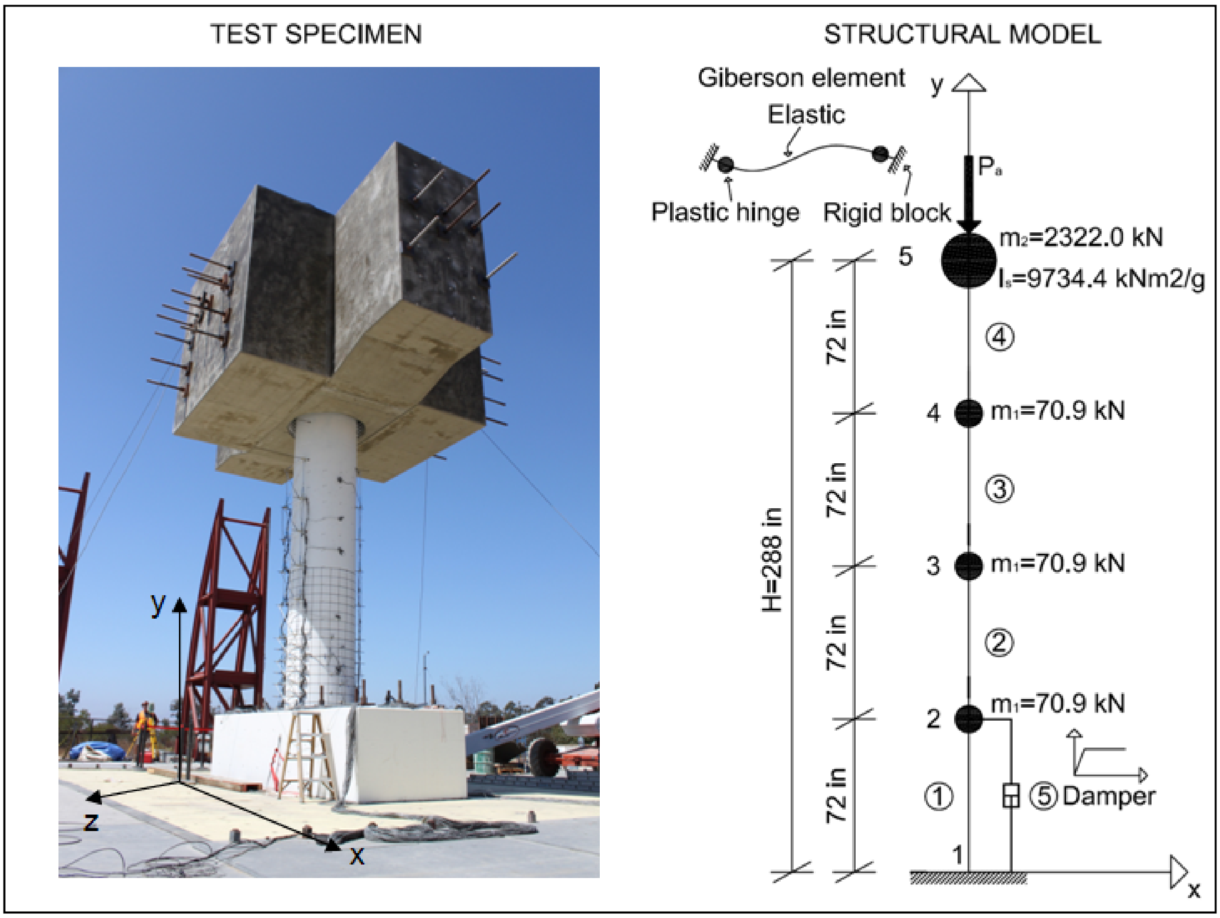

TEST SPECIMEN

STRUCTURAL MODEL

Figure 3.8: Ruaumoko structural model

One third of the column mass, corresponding to a weight of 70.9 kN (15.9 kips), was lumped at each of the three intermediate nodes, to represent the distributed seismic weight along the column height. A single lumped mass located at the top node of the column, corresponding to a weight of 2322.0 kN (522 kips), was intended to represent the superstructure. A rotational inertia of 9734.4 kNm^2/g (3391987.1kip-in^2/g) was included, where g is the gravity acceleration.

A constant vertical force P_a of 2534.9 (569.7 kips), accounting for the measured weights of the column and the superstructure, was applied at the top node of the column (see Figure 3.8).

3.2.1.2 Elastic cross-section properties

Elastic stiffness properties were assigned to the central portion of the Giberson element. A concrete modulus of elasticity $\mathrm{E_{c,avg}}$ equal to 22483.1 MPa (3260.9 ksi), obtained by averaging the values at 42 and 43 days, was assigned. The uncracked transformed moment of inertia of the cross section I_t, and the uncracked transformed area A_t, were defined as:

$$I_t = \frac{M_{cr}}{\varphi_{cr} \cdot E_{c,avg}} = 0.127\, m^4\ (306272.5\, in^4)$$

$$A_t = A_g + A_{sl} \cdot \left(\frac{E_s}{\mathrm{E_{c,avg}}} - 1 \right) = 1.307\, m^2\ (2026.3\, in^4)$$

where A_g is the area of the gross concrete section, A_{sl} is the area of the longitudinal reinforcement, and E_s is the steel modulus of elasticity (see Table 2.7). Euler-Bernoulli beam formulation was used, assuming shear deformations were negligible.

3.2.1.3 Hysteresis rule

The Schoettler-Restrepo hysteresis rule [Schoettler, 2010] was adopted to represent the inelastic cyclic moment-curvature relationship of the column plastic hinge segment, see Figure 3.9.

The idealized trilinear moment-curvature relationship derived in Section 3.1.3 was used as the backbone curve, with symmetric behavior in positive and negative bending directions (see Figure 3.9). *Ruaumoko* takes the initial stiffness K_1 as:

$$K_1 = E_{c,agv} \cdot I_t$$

The cracking moment M_{cr} is given as a fraction of the idealized yield moment M_y, assigning the coefficient F_{cr}; instead the cracking curvature φ_{cr} is automatically calculated according to elastic laws:

$$M_{cr} = F_{cr} \cdot M_y$$

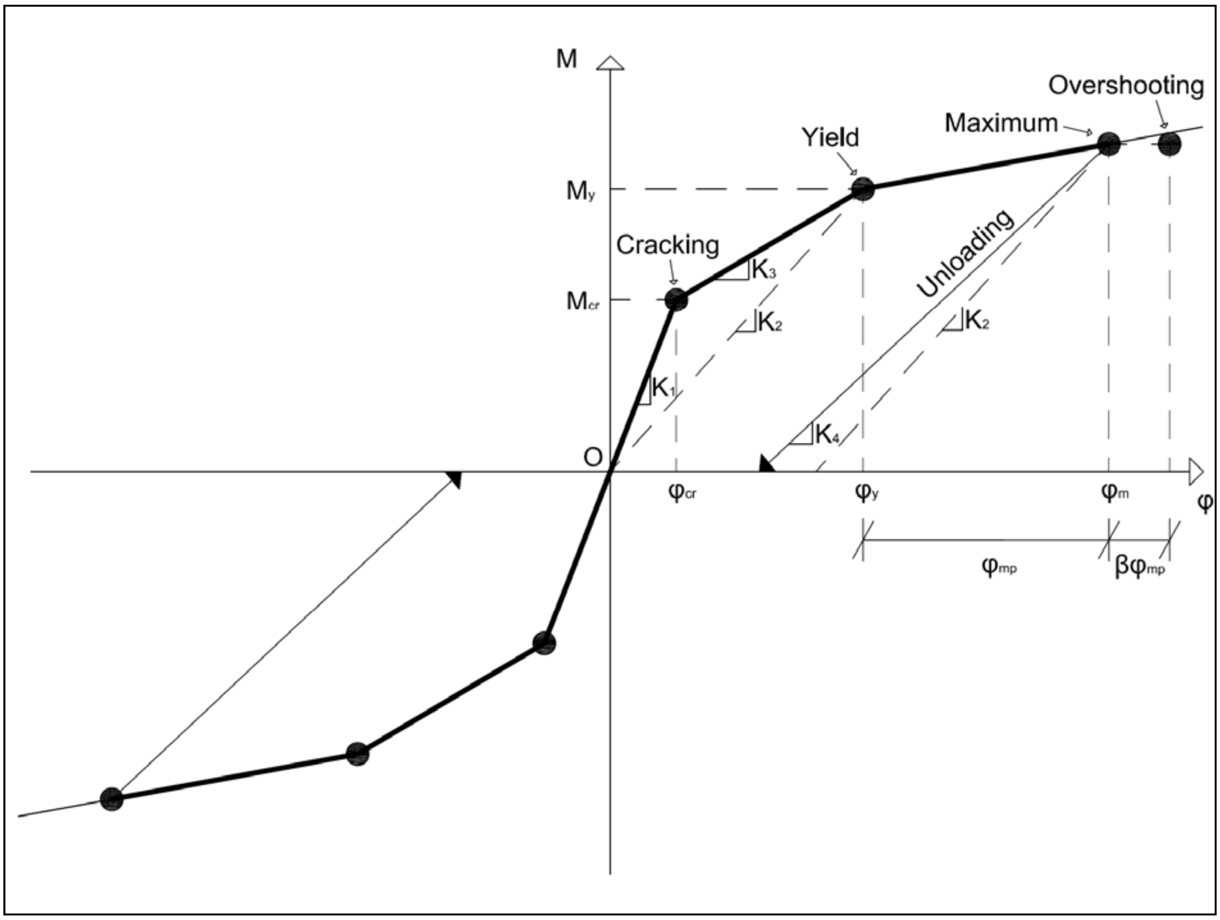

Figure 3.9: Schoettler-Restrepo hysteresis rule

$$\varphi_{cr} = \frac{M_{cr}}{K_1}$$

While the yield moment is explicitly assigned, the yield curvature is implicitly calculated through the secant stiffness K_2, defined in terms of the initial one by the coefficient ρ:

$$K_2 = \rho \cdot K_1$$

$$\varphi_y = \frac{M_y}{K_2}$$

The post-yield stiffness, that is the slope of the third branch of the backbone curve, is gived as a fraction of the initial one as well, by the parameter r:

$$K_3 = r \cdot K_1$$

Strength degradation was ignored by assigning a large curvature ductility capacity.

Three parameters define the cyclic behavior of the Schoettler-Restrepo hysteresis rule. The unloading stiffness factor α, the reloading stiffness factor β, and the pinching factor $Pinch$ were calibrated based on the experimental results of a similar reinforced concrete column and were chosen equal to 0.45, 0.20, and 1.00, respectively. The input parameter α governs the slope of the unloading branch K_4, defined as:

$$K_4 = \rho \cdot K_1 \cdot \left(\frac{\varphi_y}{\varphi_m}\right)^{\alpha}$$

where φ_m is the maximum curvature before unloading.

The factor β defines the curvature at which the hysteresis rejoins the backbone curve. It allows overshooting of the maximum curvature upon reloading, computed as:

$$\beta \cdot \varphi_{mp}$$

where φ_{mp} is the plastic component of φ_m. Pinching of the hysteresis was ignored by assuming the values 1.00 for the input parameter $Pinch$. Table 3.5 summarizes the values of all the input parameters assigned to define the Schoettler-Restrepo hysteresis rule.

3.2.1.4 Plastic hinge length

A plastic hinge length L_p of 989 mm (38.94 in.), corresponding to 0.8 times the column diameter, was adopted at the bottom end of the lowest column element. This value was obtained from an equation proposed by Priestley [Priestley et al, 2007] and included in Caltrans *Seismic Design Criteria* [Caltrans, 2006 a]:

$$L_p = 0.08 \cdot H + 0.15 \cdot f_y \cdot d_{bl} \geq 0.3 \cdot f_y \cdot d_{bl}$$

where H is the column height, f_y is the yield strength of the longitudinal reinforcement (Table 2.6) and d_{bl} is the diameter of the longitudinal bars. A plastic hinge length of 839 mm (33.05 in.) was assigned at the other end, thus obtaining a total potential plastic extent equal to the full element length. This configuration was used for all four column elements.

3.2.1.5 Structural damping

Initial stiffness Rayleigh classical damping formulation [Chopra, 1995 and Carr, 2002] was adopted, assigning 1% damping ratio to the first two modes.

Under low-intensity input ground motions, the structural model response obtained from time-history analyses showed an unlikely long duration of free vibration. Increasing the damping ratio until a value of 5% did not solve this problem. For this reason, an elasto-plastic Giberson [Giberson, 1967] element was added in parallel to the base segment, to simulate the frictional energy dissipation along crack interfaces. In Figure 3.8 this element is represented

M_y		r	ρ	F_{cr}	α	β	$Pinch$
(kNm)	**(kip-ft)**	**(-)**	**(-)**	**(-)**	**(-)**	**(-)**	**(-)**
5793.1	4272.7	$2.41 \cdot 10^{-3}$	0.427	0.145	0.45	0.20	1.00

Table 3.5: Schoettler-Restrepo hysteresis rule parameters

as a damper to stress its purpose: introducing dissipation without influencing the global strength and the stiffness of the structure.

This goal was achieved by taking the flexure stiffness of this element equal to one third, the axial stiffness equal to 1/1000 and yield moment equal to 1/100, of the values assigned to each column segment (see Table 3.6).

3.2.2 Displacement-driven pushover analysis

A monotonic increasing horizontal displacement was applied to the uppermost node of the structural model. The ultimate displacement was set at 559 mm (22.0 in.). A sufficiently small time step was chosen to simulate a pseudo-static loading of the structure, minimizing the contribution of the inertia forces. Second order effects were included by performing a large displacement analysis [Carr, 2008].

3.2.2.1 Results

The information obtained from the pushover analysis can be summarized in the base shear versus top displacement diagram, shown in Figure 3.11. The base shear V_b is normalized by the total weight of column and superstructure W to obtain the base shear coefficient C_h, and the top displacement Δ was normalized by the column height H to obtain the drift ratio δ. The quantities used for normalization are already shown in Table 3.3.

Idealized yield can be easily recognized on the pushover curve as the sharp knee point. It is identified with the shear $V_{b,y}$ and displacement Δ_{yi}, equal to 781.8 kN (175.8 kips) and 88 mm (3.47in.), respectively. Figure 3.11 shows also the points corresponding to strain limit state at the column base; normalized curvatures, drift ratios, and ductilities for these limit states are summarized in Table 3.7.

The uncracked and fully-cracked fundamental period of the structure, $T_{1,u}$ and $T_{1,c}$ respectively, were determined from the pushover results of the model without elasto-plastic damper. An uncracked stiffness, K_u, of 19894.4 kN/m (113.6 kip/in) was computed as the slope of the uncracked branch and a fully-cracked one, K_c, of 8834.0 kN/m (50.4 kip/in) was taken equal to the slope of a secant line passing to the idealized yield point. Assuming these

I_t		A_t		M_y	
(m^4)	**(in^4)**	**(m^2)**	**(in^2)**	**(kNm)**	**(kip-ft)**
0.042	102090.8	$1.31 \cdot 10^{-3}$	2.03	57.9	42.7

Table 3.6: Substituted cross-section properties for damper element

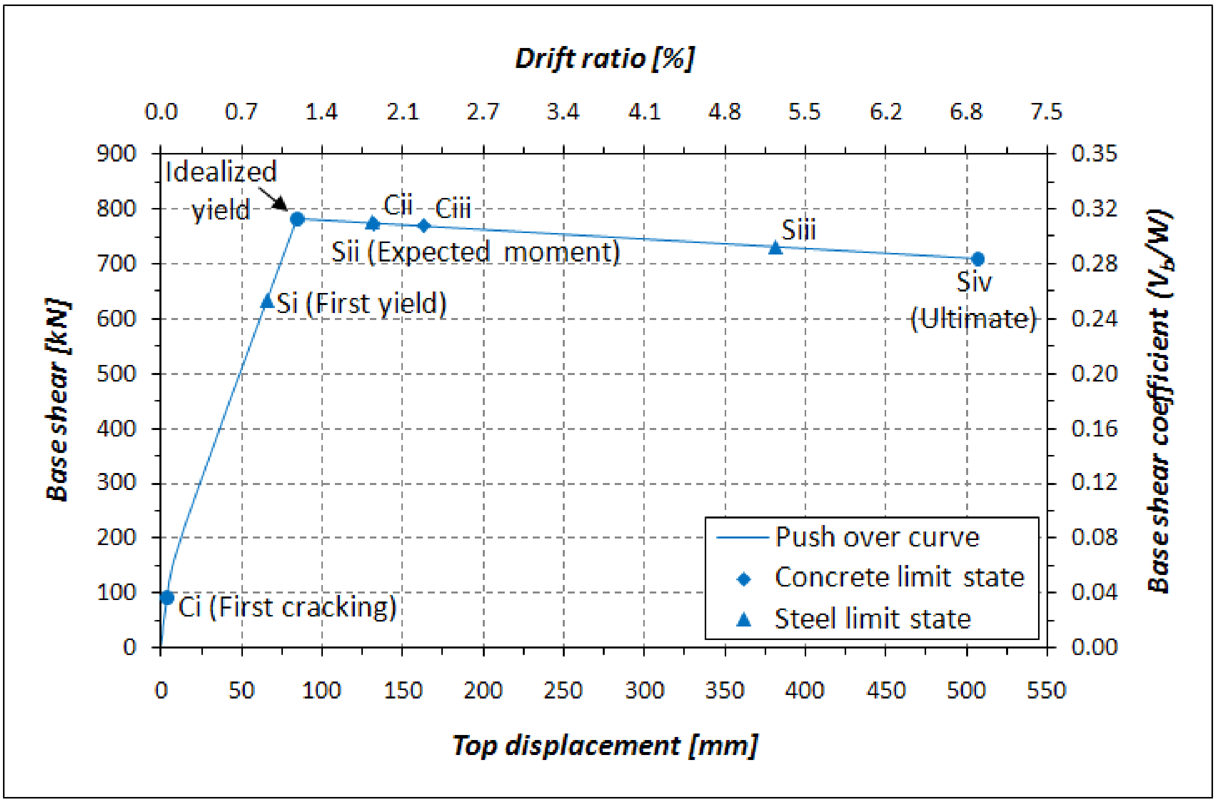

Figure 3.11: Base shear-top displacement from the push over analysis

	$\varphi \cdot \frac{D}{\varepsilon_y}$	$\mu_\varphi = \frac{\varphi}{\varphi_{yi}}$	δ (%)	$\mu_\Delta = \frac{\Delta}{\Delta_{yi}}$
Ci (First cracking)	0.10	0.05	0.06	0.05
Si (First yield)	1.72	0.79	0.90	0.75
Sii (Expected moment)	5.72	2.62	1.79	1.49
Cii	5.82	2.67	1.81	1.50
Ciii	8.20	3.76	2.23	1.85
Siii	25.09	11.51	5.21	4.32
Siv (Ultimate)	34.86	15.99	6.93	5.75

Table 3.7: Normalized curvatures, drift ratios and ductilities of the strain limits state

quantities, the two fundamental periods are equal to:

$$T_{1,u} = 2 \cdot \pi \cdot \sqrt{\frac{K_u}{M}} = 0.72\ sec$$

$$T_{1,c} = 2 \cdot \pi \cdot \sqrt{\frac{K_c}{M}} = 1.07\ sec$$

where M is the total mass of column and the superstructure. A good agreement can be observed between the analytical uncracked period $T_{1,u}$ and the experimental one obtained from the first with noise, which was 0.78 sec.

3.2.3 Non-linear time history analysis

A non-linear time history analysis was performed to simulate the specimen response. The dynamic equation of equilibrium was integrated by Ruaumoko through the unconditionally stable implicit Newmark Constant Average Acceleration method [Clough 1993].

The dynamic excitation was applied as a horizontal ground acceleration history at the fixed base. The ground motions reproduced by the table during testing were considered, thus including the effect of the specimen-table interaction on the input time-histories. In particular, they were run in series to account for the residual deformation following each earthquake (see Figure 3.12).

3.2.3.1 Results

The peak response parameters obtained from the non-linear time history analysis after each earthquake are shown in Figures 3.13 to 3.18. The analytical idealized values of yield curvature φ_{yi} and displacement Δ_{yi} are used to compute the ductilities shown in Table 3.8.

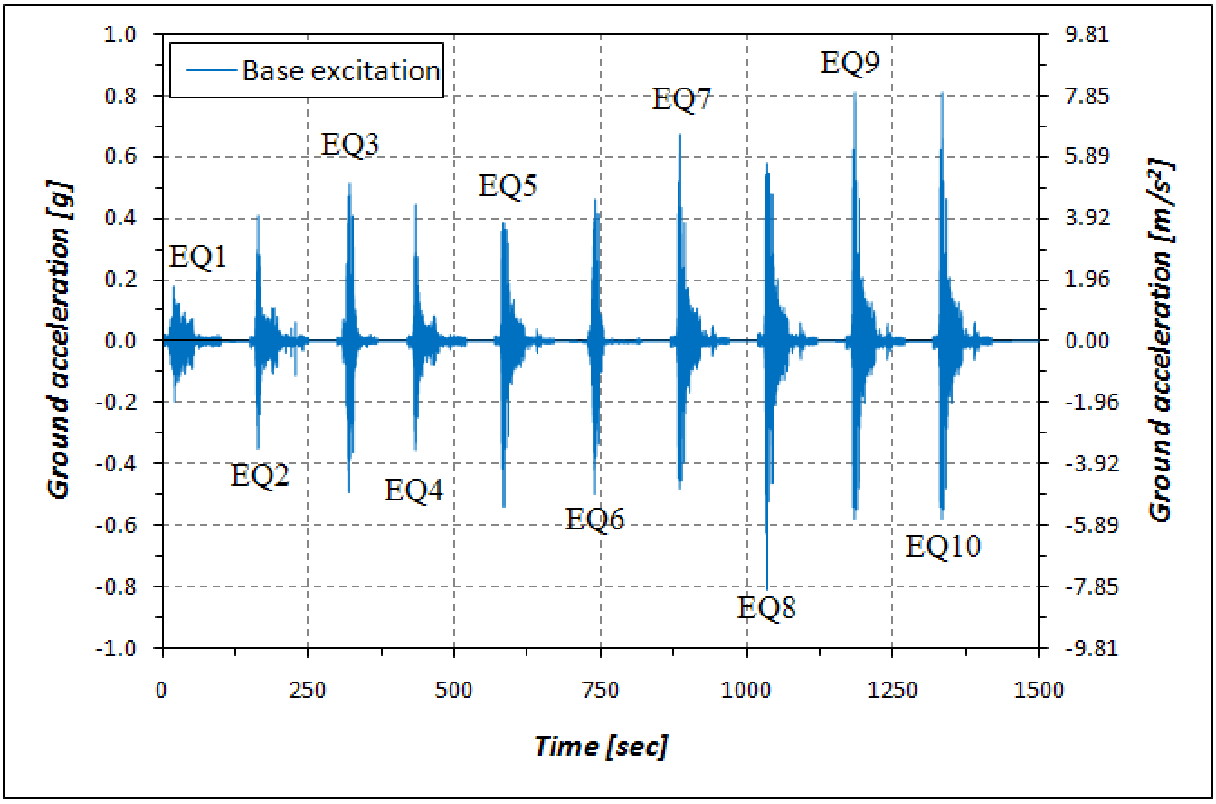

Figure 3.12: Input analysis ground motions

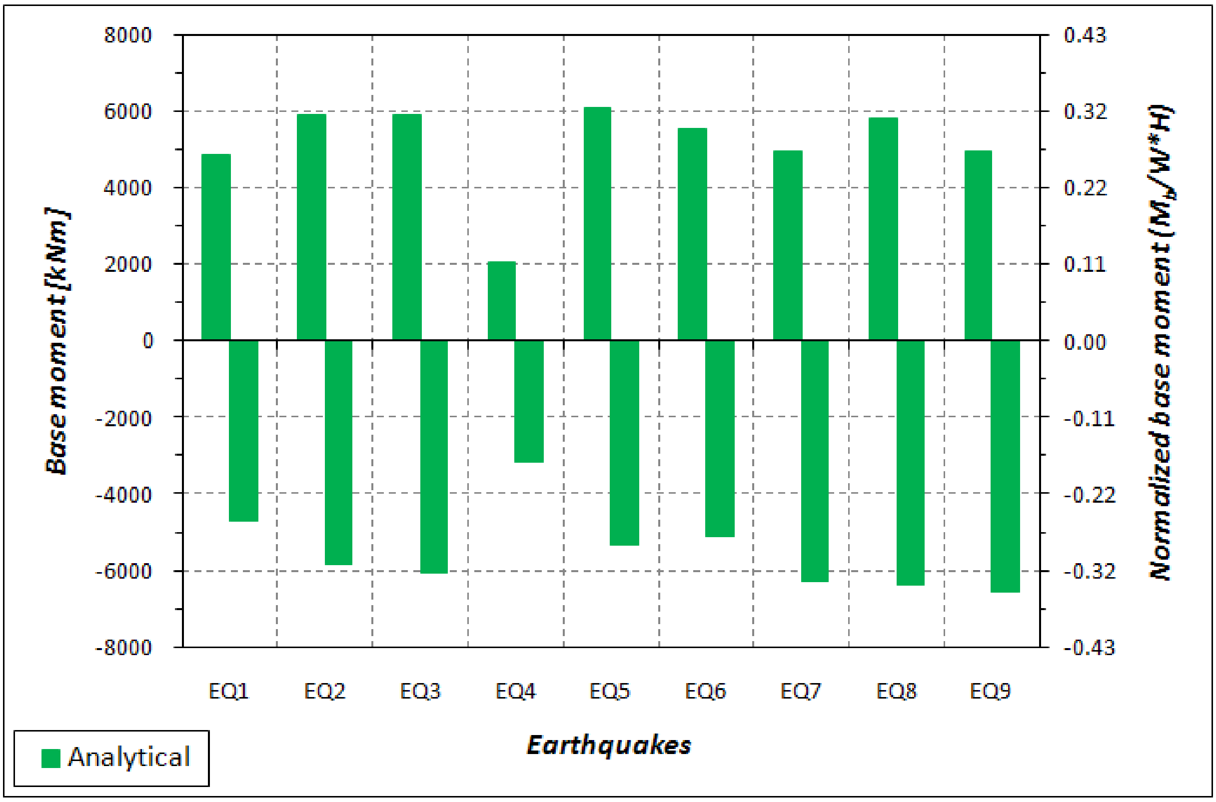

Figure 3.13: Analytical peak base moment

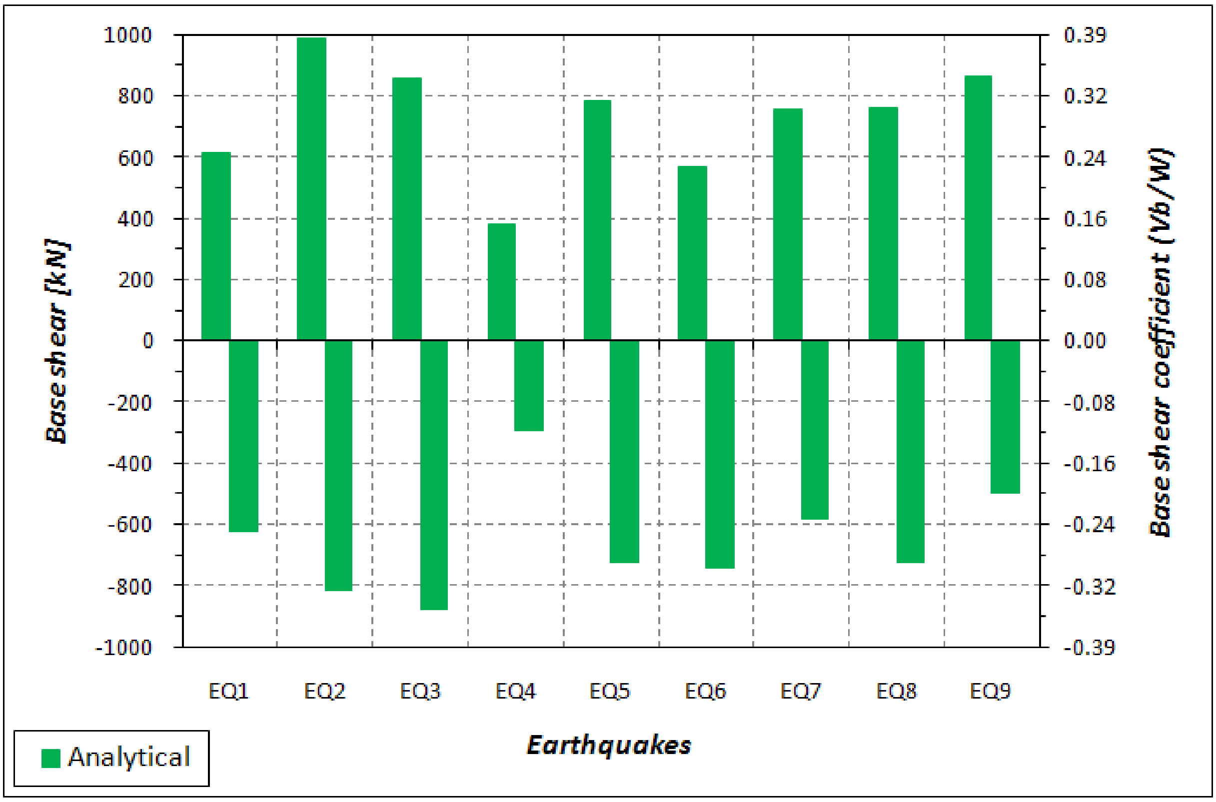

Figure 3.14: Analytical peak base shear

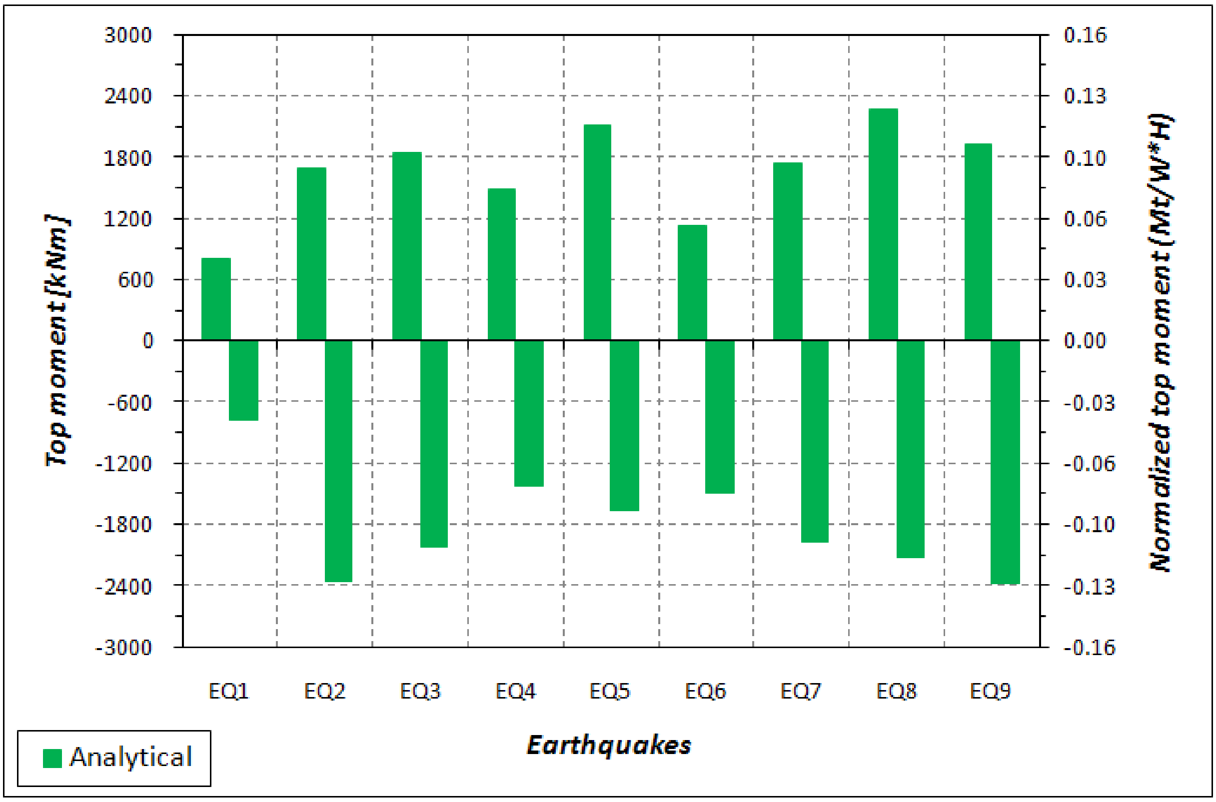

Figure 3.15: Analytical peak top moment

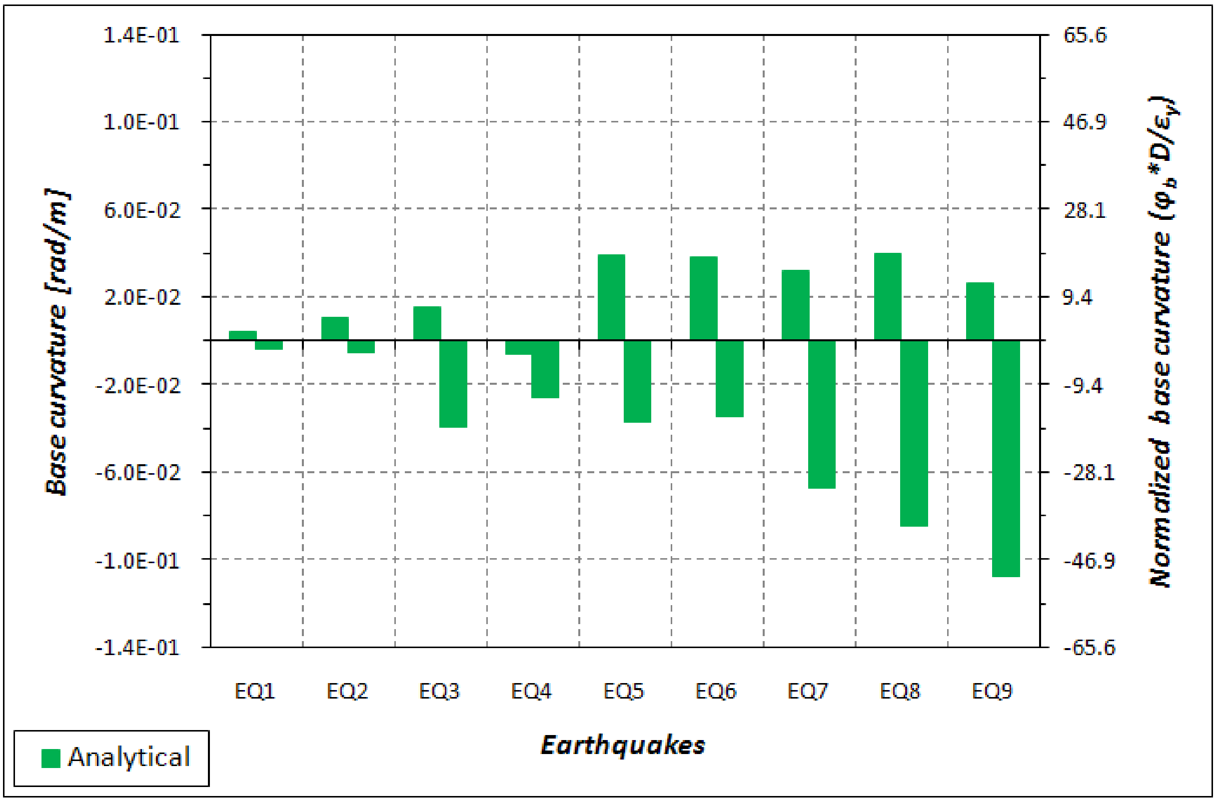

Figure 3.16: Analytical peak base curvature

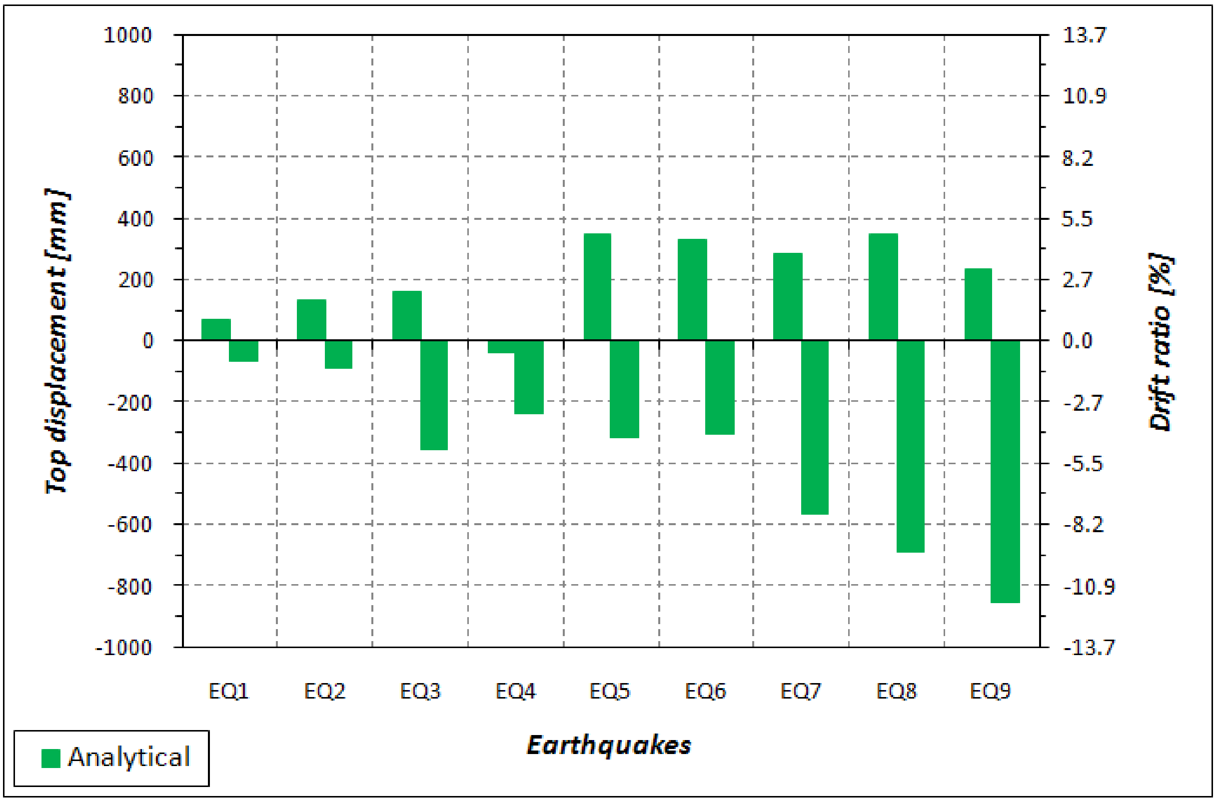

Figure 3.17: Analytical peak top displacement

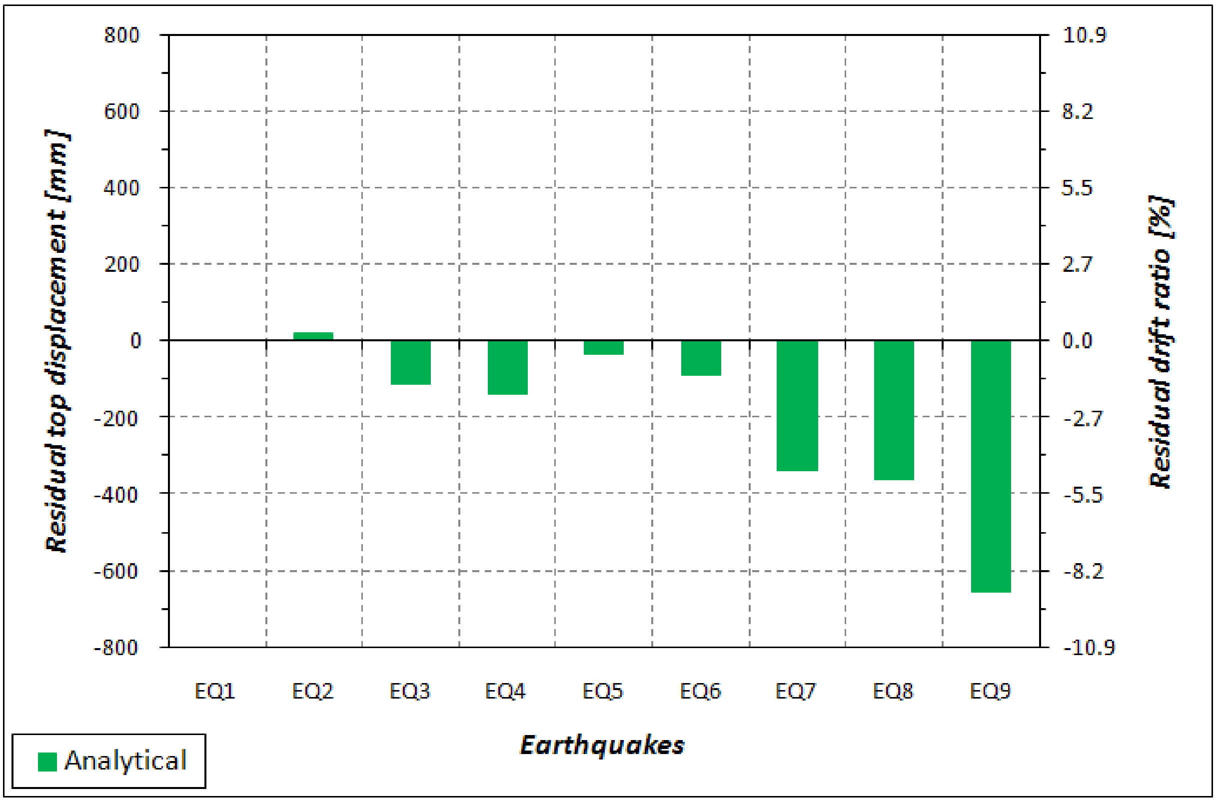

Figure 3.18: Analytical residual top displacement

Earthquake	**Curvature ductility**	**Displacement ductility**
EQ1	0.80	0.80
EQ2	2.16	1.51
EQ3	8.41	4.06
EQ4	5.50	2.68
EQ5	8.18	3.90
EQ6	8.14	3.76
EQ7	14.14	6.61
EQ8	17.82	7.82
EQ9	22.81	9.66
EQ10	50.78	20.53

Table 3.8: Analytical curvature and displacement ductilities

4. Experimental results

As mentioned in Section 2.1.3, the specimen was instrumented with strain gauges, linear potentiometers, and GPS to measure internal, local, and global deformations during testing. Accelerometers were also installed to compute the inertia forces. This chapter presents the experimental data recorded during testing and the procedure used to determine them.

4.1 Post-processing of recorded data

4.1.1 Data filtering

Recorded data were filtered to eliminate spurious response outside the shake table's reproducible frequency content. Accelerometer measurements were band pass filtered with a high order FIR filter with cutoff frequencies of 0.25 and 25 Hz. All other measurements were low pass filtered with a high order FIR filter with a cutoff frequency of 25 Hz. Hamming type filters of order of 5000 were used.

4.1.2 Displacement measurement

Relative displacements between the column and the shake table were directly measured using string potentiometers. The same quantities can be determined by summing flexure, shear and fix end rotation displacement components obtained from curvature and shear LVDT measurements. Note that positive displacement is toward the East.

4.1.2.1 Flexural displacement component

The flexural displacement component was determined from the deformations measured by vertical LVDTs within each column segment, on both the North and the South faces. A segment of the column is identified as the part of the column between two adjacent instrumentation levels, see Figure 2.15 and 2.16.

First, the measured relative displacements between consecutive instrumentation level, on both the North and the South face of the column, were divided by the initial gauge lengths to obtain the strains on the East and the West end. Curvatures on both the North and the South faces were determined as the algebraic difference of the strains on the East end minus the ones on the West end, divided by the horizontal distance between the curvature LVDTs.

As shown in Figure 4.1a-b, for the South face, the curvature within the generic column segment was computed as:

$$\varphi_s = \frac{\frac{v_{sw}}{h} - \frac{v_{se}}{h}}{l}$$

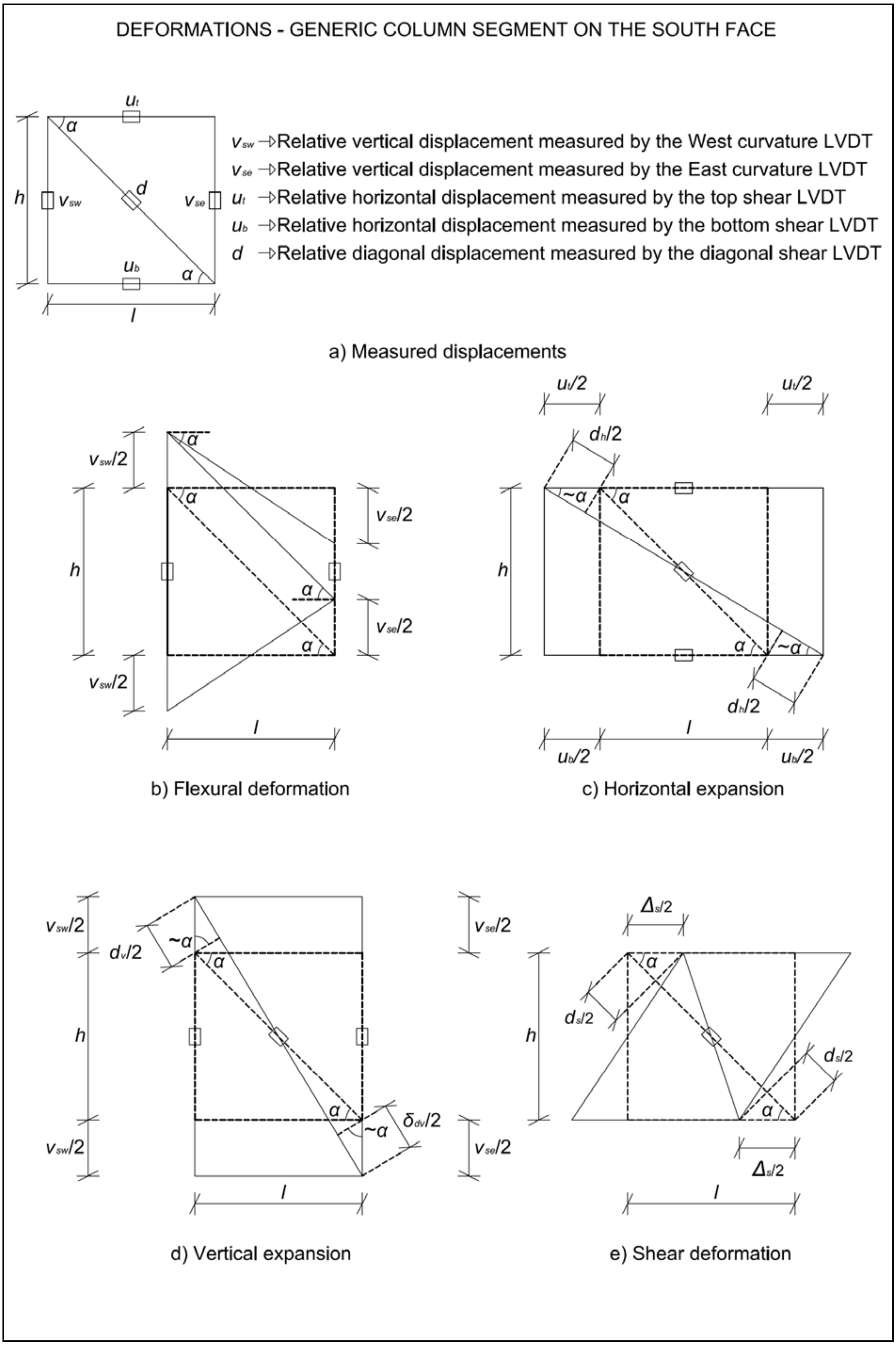

Figure 4.1:Deformations of the generic column segment on the South face

$$\varphi_n = \frac{\frac{v_{ne}}{h} - \frac{v_{nw}}{h}}{l}$$

where φ_s and φ_n are the curvature on the South and North side, v_{sw} and v_{se} are the relative vertical displacements between adjacent curvature rods measured by the West and East curvature LVTDs on the South face, v_{nw} and v_{ne} are the relative vertical displacements between adjacent curvature rods measured by the West and East curvature LVTDs on the North face, h is the height of the column segment (also initial gauge length) and l is the horizontal distance between the two sensors. The average curvature within each column segment was computed as the mean of the ones obtained for the North and the South side. In particular, the base curvature, φ_b, was calculated over a 406 mm (16 in.) gauge length, corresponding to 1/3 of the column diameter, from 51 mm (2 in.) to 457 mm (18 in.) above the footing.

The flexural displacement component was obtained by integrating the computed curvatures along the column height. Above the uppermost instrumentation level, the curvature was assumed to vary linearly from the last measured values to zero at the column top.

4.1.2.2 Shear displacement component

The shear displacement component was determined from the relative displacements measured by the shear LVDTs within each column segment on the South face, see Figure 2.15. The displacements measured by the diagonal LVDTs contains components due to horizontal expansion, vertical expansion and shear deformation; flexural deformation does not produce relative diagonal displacement as can be seen in Figure 4.1b.

As shown in Figure 4.1c, the relative diagonal displacement due to the horizontal expansion, d_h, was evaluated as:

$$d_h = \frac{u_t}{2} \cdot \cos \alpha + \frac{u_b}{2} \cos \alpha$$

where u_t and u_b are relative horizontal displacements between the curvature rods in the top and bottom instrumentation level measured by the horizontal LVDTs; α is the angle formed by the diagonal LVDT on the horizontal, which can be computed as:

$$\alpha = \arctan\left(\frac{h}{l}\right)$$

where h is the height of the column segment and l is the horizontal distance between the two rods in a level.

As shown in Figure 4.1d, the relative diagonal displacement due to the vertical expansion, d_v, was computed as:

$$\delta_{dv} = \frac{v_{sw}}{2} \cdot \sin\alpha + \frac{v_{se}}{2} \sin\alpha$$

where v_{sw} and v_{se} are the relative vertical displacements between the adjacent curvature rods measured by West and East vertical LVTDs respectively.

The relative diagonal displacement due to shear deformation, d_s, was obtained as the displacement measured by the diagonal LVDT minus the ones due to the horizontal, d_h, and vertical, d_v, expansion:

$$d_s = d - d_h - d_v$$

As shown in Figure 3.1e, the shear displacement component, Δ_s, was evaluated as:

$$\Delta_s = \frac{d_s}{\cos\alpha}$$

4.1.2.3 Fix-end rotation displacement component

The fix-end rotation displacement component is due to bond slip between the longitudinal bars and the concrete of the footing, and the strain penetration of the longitudinal steel developing into the footing. This displacement component was determined from the displacement measured by four vertical spring potentiometers located at the bottom instrumentation level, see Figure 2.15 and 2.16. These instruments had a gauge length of 51 mm (2 in.). Although the deformation measured by these sensors included the change in flexural curvature within the first 51 mm (2 in.) of the column, it was presumed that its effect would be negligible compared to the one of strain penetration and bond slip. The method used to obtain the displacement component due to fix-end rotation is similar to the one used for obtaining the flexural displacement component. First, the differences in magnitudes between the East and West measured displacements were evaluated on both the North and the South side. These differences were divided by the horizontal distance between the East and West LVDTs to obtain the average rotation on the two sides. The computed rotations were averaged and, assuming a column rigid rotation about its centroidal axis at the base, the horizontal displacement component was obtained by multiplying the rotation by the column length.

4.1.3 Inertia forces and moments

The inertia forces were computed using the data from the accelerometers located as already shown in Figure 2.22 and 2.23. Only the accelerometers represented in Figure 4.2 were used for this calculation.

The horizontal accelerations along the column height were measured by accelerometers installed on the East and West faces at six levels. First, the two accelerations at each level were averaged. In the absence of a pair of working accelerometers, the value from a single sensor was used. The resulting acceleration was multiplied by the weight of the corresponding segment, to obtain the horizontal inertia force at that level. The tributary weights, for the pairs of horizontal accelerometers located along the column height at the same level, were taken from segments bounded by horizontal planes cutting the column between consecutive sensors, see Figure 4.2. At the two uppermost column accelerometers were assigned half of the weight of the segment embedded in the central block; the remaining segment weight was considered part of the top block.

Two accelerometers were placed on the North and the South faces of the side blocks to measure the horizontal accelerations of the top block center of mass. The average value of these measurements, multiplied by the mass accounting for the superstructure and one half of the embedded segment, gave the block horizontal inertia force.

In the calculation of the bending moments, the rotational acceleration and the inertia of the superstructure were also considered. The acceleration was derived from the measurements of two vertical accelerometers located on the end blocks. The resulting moment was obtained by multiplying the rotational acceleration by the rotational inertia of the superstructure, equal to 9734.4 kNm^2/g (3391987.1 kip-in^2/g). $P - \Delta$ effects were included by multiplying, step by step, the superstructure weight by the horizontal displacement of its center of mass.

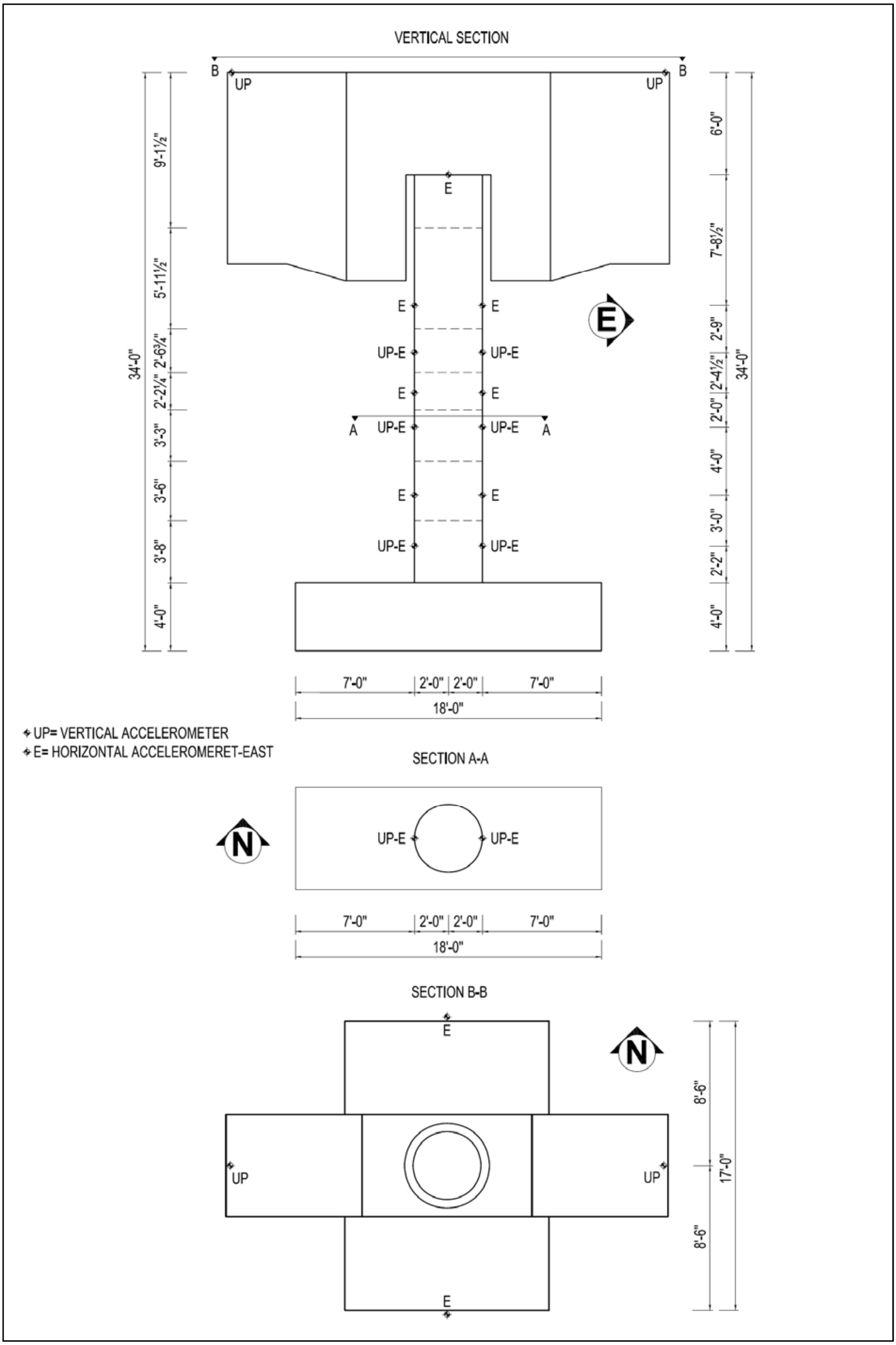

Figure 4.2: Accelerometer tributary weights (scale 1:100)

4.2 Tests results

4.2.1 EQ1 – Agnew State Hospital

Agnew State Hospital record was intended to represent a low-intensity earthquake with high probability of occurrence. Under EQ1, the column was expected to reach the analytical idealized yield displacement, Δ_{yi}, equal to 88 mm (3.47 in.) and corresponding to a 1.20% yield drift ratio δ_{yi}. The purpose of this test was to induce in the specimen a displacement ductility demand of 1.0.

There was no observable post-test damage in the column. A hairline crack, defined here as less than 0.1 mm (0.004 in.), was found at the column-footing interface. The crack was discontinuous on the East, South, and West faces of the column. No other cracks were identified in the test specimen after EQ1. A post-test view of the East face of the column base is shown in Figure 4.3.

The overall column response during EQ1, in terms of base moment versus base curvature, is shown in Figure 4.4. The base moment, M_b, is normalized by the product $W \cdot H$, where W is the total weight of column and superstructure, and H is the column height. The base curvature, φ_b, is normalized by the ratio ε_y/D, where D is the diameter of the cross-

Figure 4.3: Column base post-EQ1

section and ε_y is the yield strain of the longitudinal reinforcement obtained from the experimental stress-strain relationship, see Figure 2.25. The analytical idealized moment-curvature relationship and the idealized yield moment, M_y, equal to 5793.1 kNm (4272.7 kip-ft), are also shown in this plot.

As can be seen in Figure 4.4, the analytical idealized moment-curvature relationship is globally stiffer than the experimental one. For this reason, to compute curvature ductilities, an experimental idealized yield curvature, φ_{ye}, was defined as:

$$\varphi_{ye} = \frac{M_y}{EI_{e,1}} = 8.36 \cdot 10^{-3} \frac{rad}{m} \left(2.12 \cdot 10^{-4} \frac{rad}{in}\right)$$

where $EI_{e,1}$ is the average of the slopes of two secant lines passing through the origin and the positive and negative peak moment. φ_{ye} corresponds to 1.77 times the analytical value φ_{yi}, which is equal to $4.73 \cdot 10^{-3}$ rad/m ($1.20 \cdot 10^{-4}$ rad/in). The adjective “idealized” stresses that φ_{ye} definition is based on the analytical idealized yield moment, M_y, and not on an experimental one.

An essentially linear elastic and symmetric behavior can be observed in the moment-curvature response of the column base. Very small hysteresis loops demonstrate negligible energy dissipation under EQ1. A peak moment of 3934.1 kNm (2901.7 kip-ft), corresponding to $0.68 \cdot M_y$, and a peak curvature of $6.80 \cdot 10^{-3}$ rad/m ($1.73 \cdot 10^{-4}$ rad/in), corresponding to $0.81 \cdot \varphi_{ye}$ were reached.

The overall column response during EQ1, in terms of base shear versus top displacement, is shown in Figure 4.5. The base shear, V_b, is normalized by the weight of column and superstructure, W, to obtain the base shear coefficient C_h. The top displacement, Δ, is normalized by the column height, H, to obtain the drift ratio δ. The analytical idealized base-shear relationship and the base shear corresponding to the idealized yield, $V_{b,y}$, equal to 781.8 kN (175.8 kips), are also shown in this diagram.

Good agreement between the analytical idealized shear-displacement relationship and the experimental one can be appreciated in Figure 4.5. Nevertheless, an experimental idealized yield displacement, Δ_{ye}, was defined as:

$$\Delta_{ye} = \frac{V_{b,y}}{K_{e,1}} = 90\ mm\ (3.54\ in)$$

where $K_{e,1}$ is the average of the slopes of two secant lines passing through the origin and the positive and negative peak shear. Δ_{ye} corresponds to 1.02 times the analytical one Δ_{yi}, which is equal to 88 mm (3.47 in.). The adjective “idealized” stresses that Δ_{ye} definition is based on the analytical base shear corresponding to the idealized yield, $V_{b,y}$, and not on an experimental one.

A nearly linear elastic and symmetric behavior can be observed in the shear-displacement response of the column. Higher modes are responsible for the wiggles on this curve. These effects have larger influence on the shear-displacement response than on the moment-curvature response, which appears to be smoother. A peak displacement of 62 mm (2.44 in.) or a 0.85% drift ratio, corresponding to $0.69 \cdot \Delta_{ye}$, was measured at the top of the column. A negligible residual displacement of 1 mm (0.03 in.) or 0.01% residual drift ratio demonstrates an essentially linear elastic response. A peak shear of 499.9 kN (112.4 kips), corresponding to $0.64 \cdot V_{b,y}$ and a base shear coefficient of 0.20, was reached during this test.

An essentially trapezoidal moment envelope along the column height in both negative and positive bending direction can be seen in Figure 4.6. The base moment, M_b, is normalized by $W \cdot H$ as before, and the elevation form the top of the footing, y, is normalized with respect to the column diameter D. The analytical idealized yield moment M_y is also plotted for reference. Deviation from the exact trapezoidal shape is due to the distributed mass of the column.

A nonzero moment can be observed at the top of the column. A peak value of 696.5 kNm (513 .7 kip-ft), corresponding to 18% of the peak moment recorded at the column base, was reached during this test. This fact is due to the non-negligible rotational inertia of the superstructure mass, which generates a significant moment at the top.

The positive and negative curvature envelopes along the column height are shown in Figure 4.7. The average curvature values determined within each column segment are plotted in correspondence of each segment midpoint and they are linearly interpolated. The curvature locally exceeded the experimental idealized yield one in the negative bending direction. This is principally due to the unpredictable crack pattern: the curvature LVDTs located on column segments interested by cracks opening showed very large curvature, whereas the ones included between two cracks, which propagated along the rods, gave a very small value of curvature.

The positive and negative envelopes of the relative displacement between column and table (solid lines) together with the post-test residual configuration (dashed line), are shown in Figure 4.8. The displacements are derived from the string potentiometer measurements, located as already shown in Figure 2.21. A flexural-dominated behavior can be deduced from the different peak displacement components: 44 mm (1.72 in.) from flexure, 1 mm (0.03 in.) from shear, and 10 mm (0.39 in.) from fix end rotation.

The longitudinal strain envelopes along the four monitored bars are plotted in Figures 4.9 to 4.12. The strains are obtained by averaging the measurement of two strain gauges, installed on the exterior and interior face of each bar, at the same elevation (see Figure 2.14a). The peak strains are normalized with respect to the experimental yield value ε_y, and the elevation from the top of the footing y is divided by the column diameter D.

A peak strain of 0.22% in tension, corresponding to $0.85{\cdot}\varepsilon_y$, was reached on the North bar of the West side (Figure 4.11). Localized yielding in tension may have occurred since recorded strain from a single strain gauge reached 0.24%, corresponding to $0.92{\cdot}\varepsilon_y$. A peak strain of -0.17% in compression was achieved on the South bar of the East side (Figure 4.10).

The envelope of the strains, recorded with the strain gauges on the exterior face of the hoops at the East and West sides of the column, are shown in Figures 4.13 and 4.14. The strains are normalized with respect to an approximated yield strain ε_{yh} of 0.23%. This value is taken as the average of the strains corresponding to 300.0 MPa (40.5 ksi) in the two experimental stress-strain curves already shown in Figure 2.26; Conventional yielding is adopted because no yield plateau can be identified on these curves.

A peak strain of 0.19% in tension, corresponding to $0.83{\cdot}\varepsilon_y$, was recorded on the West side of the second hoop above the column-footing interface. A strain of 0.16%, corresponding to $0.69{\cdot}\varepsilon_y$, occurred at the same side one hoop above, see Figure 4.14.

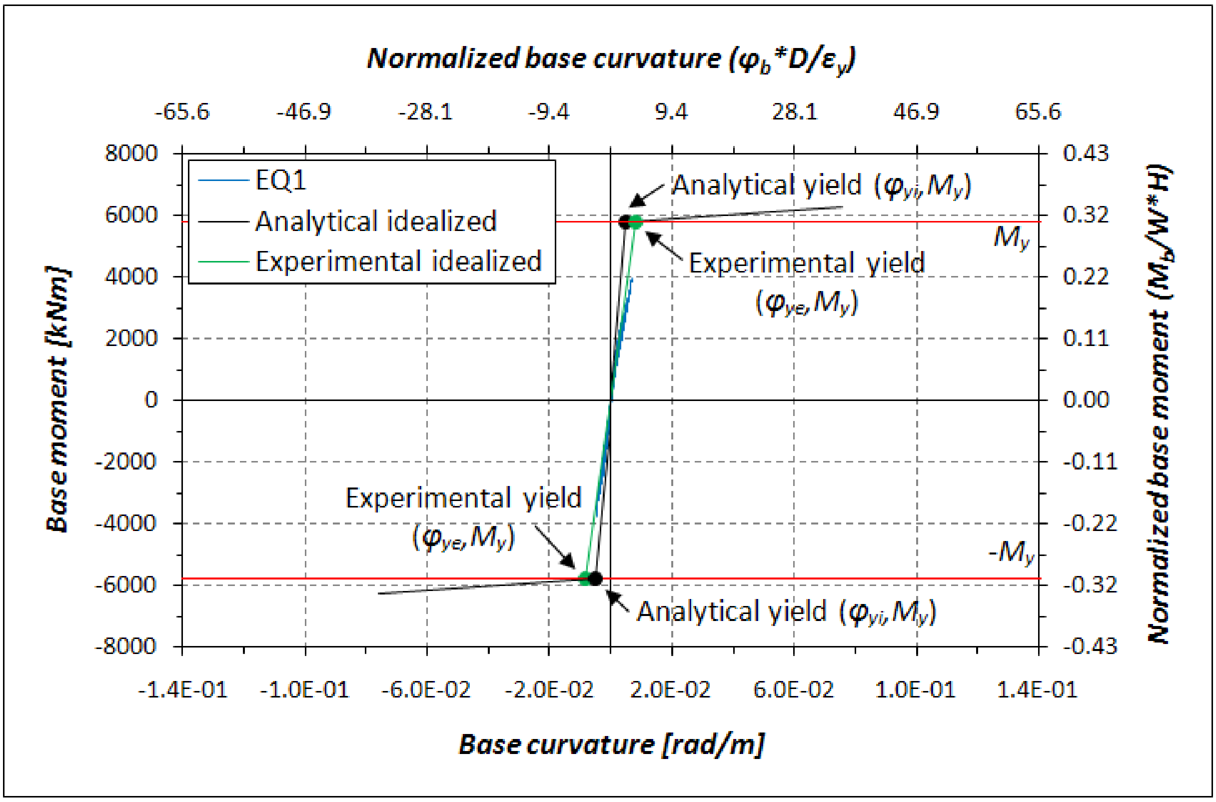

Figure 4.4: Base moment-base curvature response for EQ1

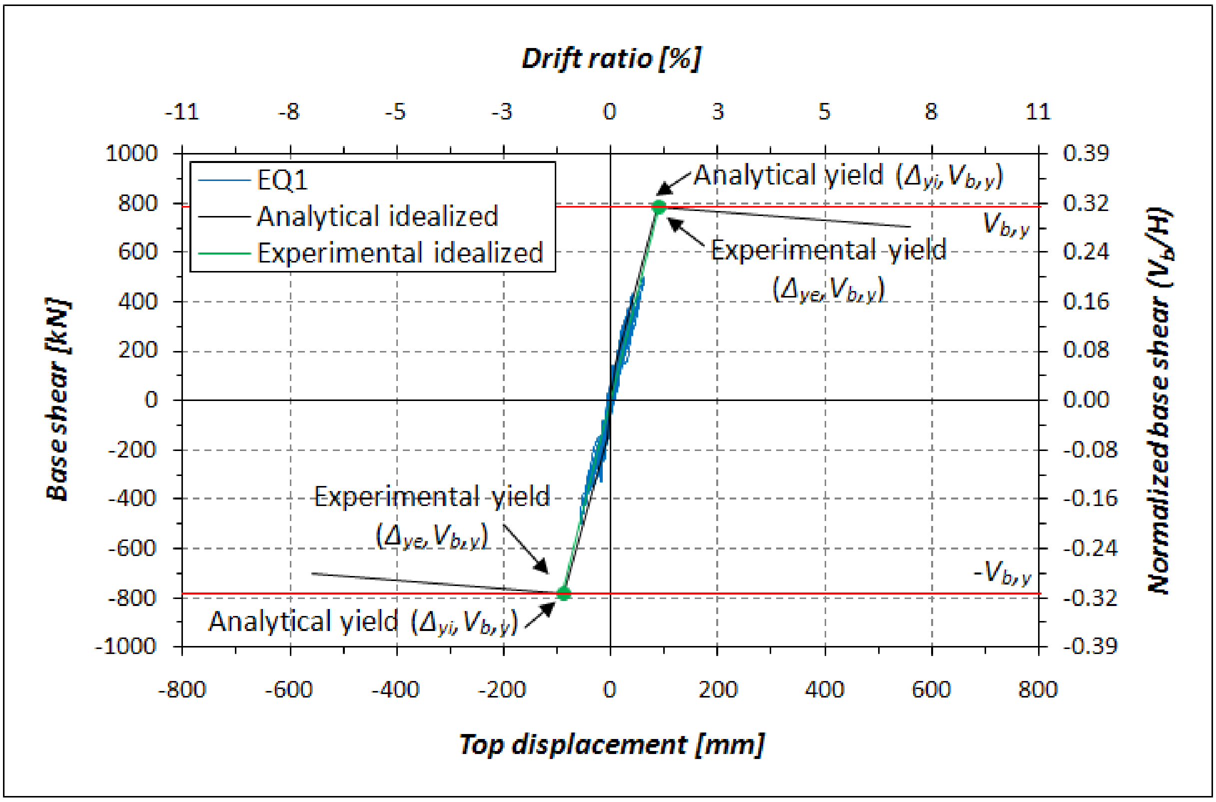

Figure 4.5 Base shear-top displacement response for EQ1

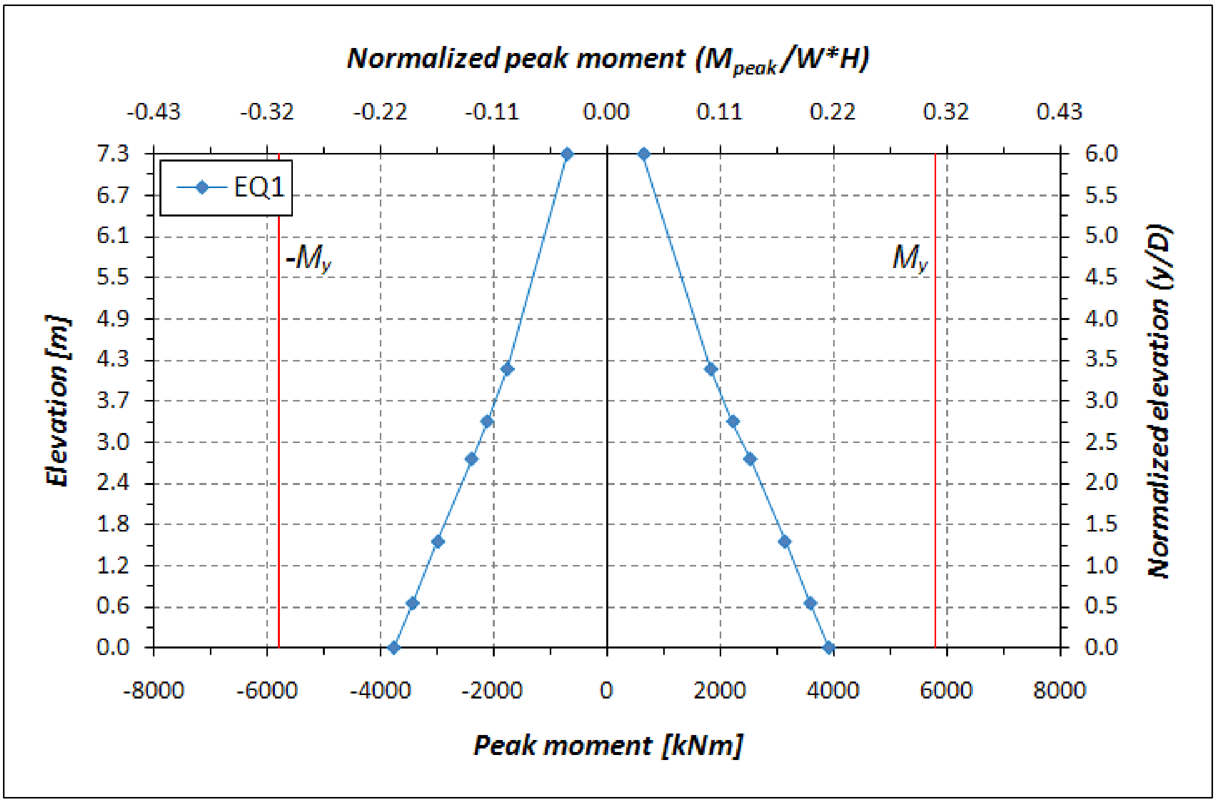

Figure 4.6: Moment envelops along the column height for EQ1

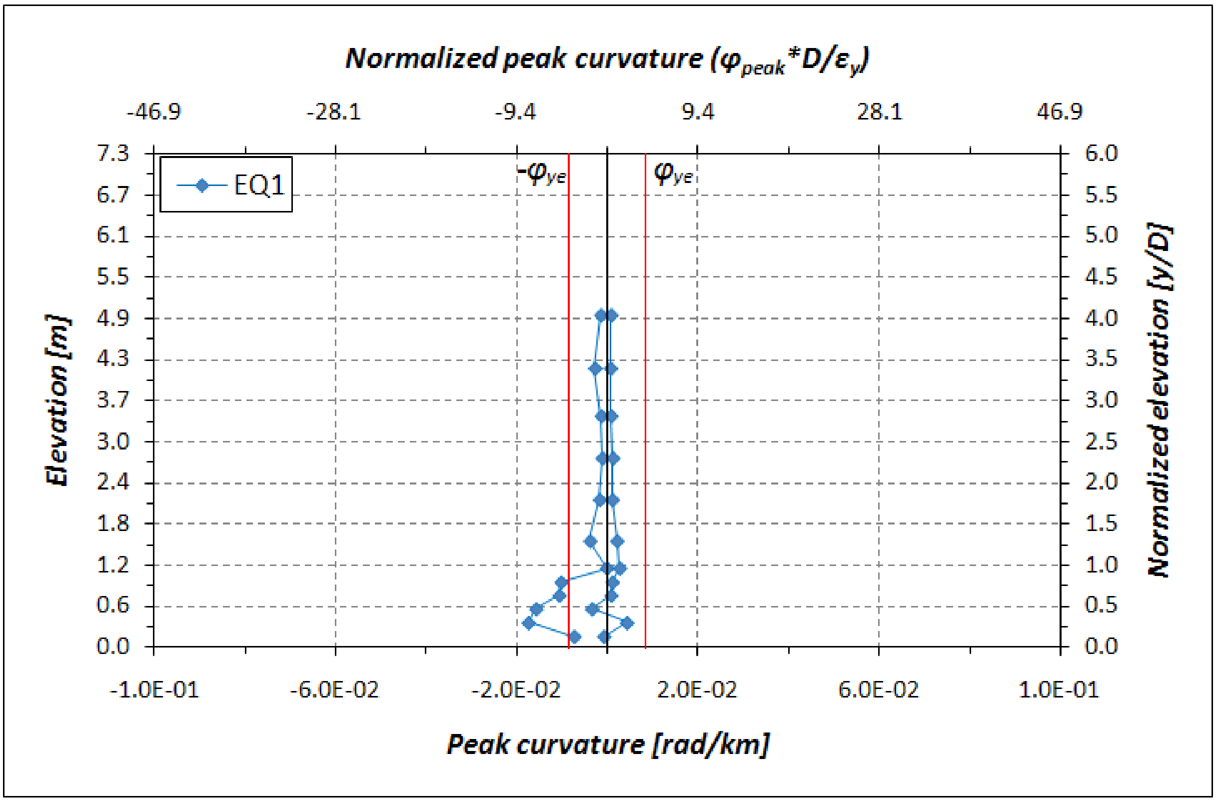

Figure 4.7: Curvature envelops along the column height for EQ1

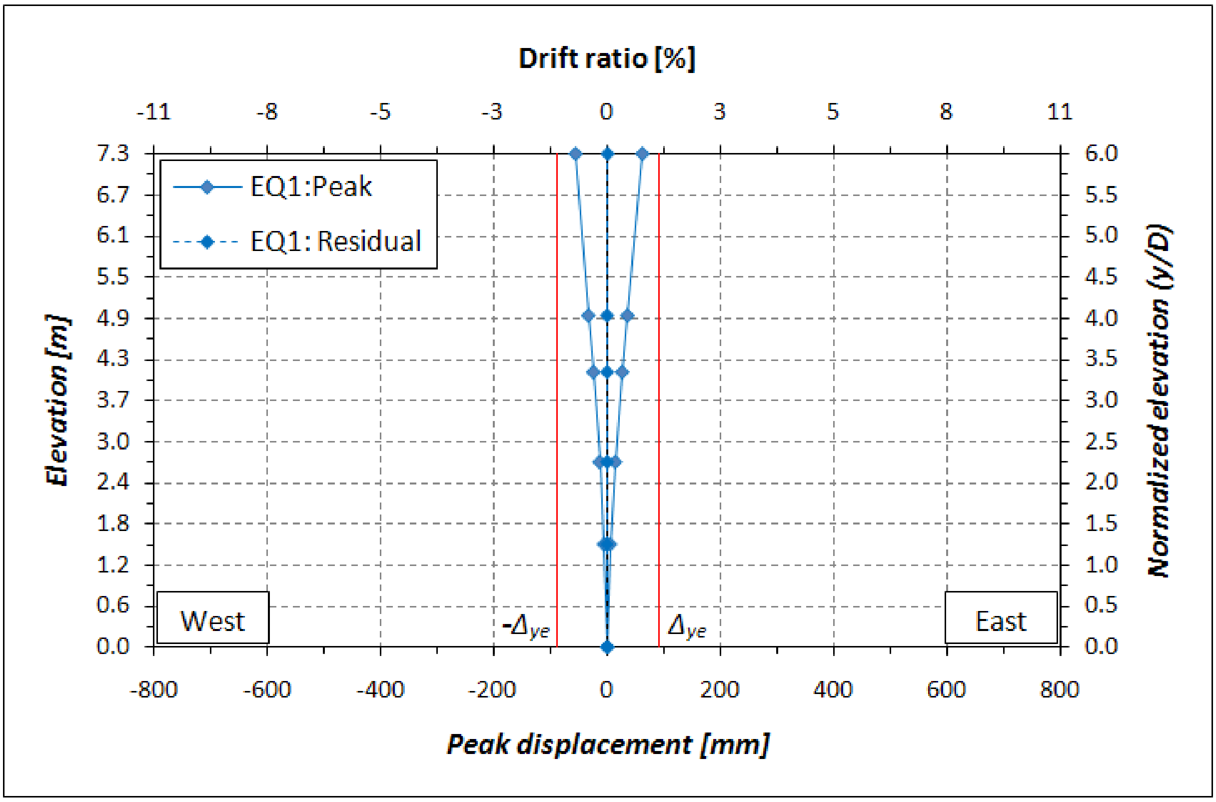

Figure 4.8: Displacement and displacement components envelops along the column height for EQ1

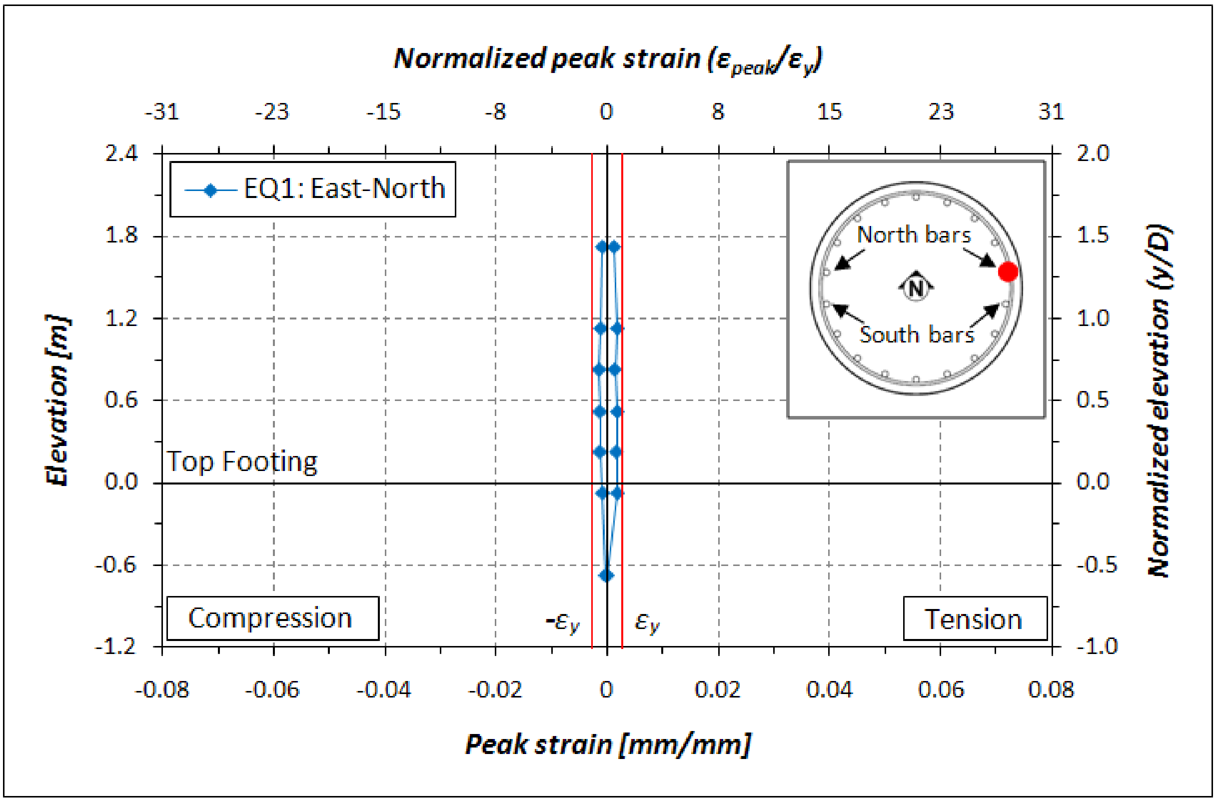

Figure 4.9: Longitudinal bar strain profile for EQ1: East side North bar

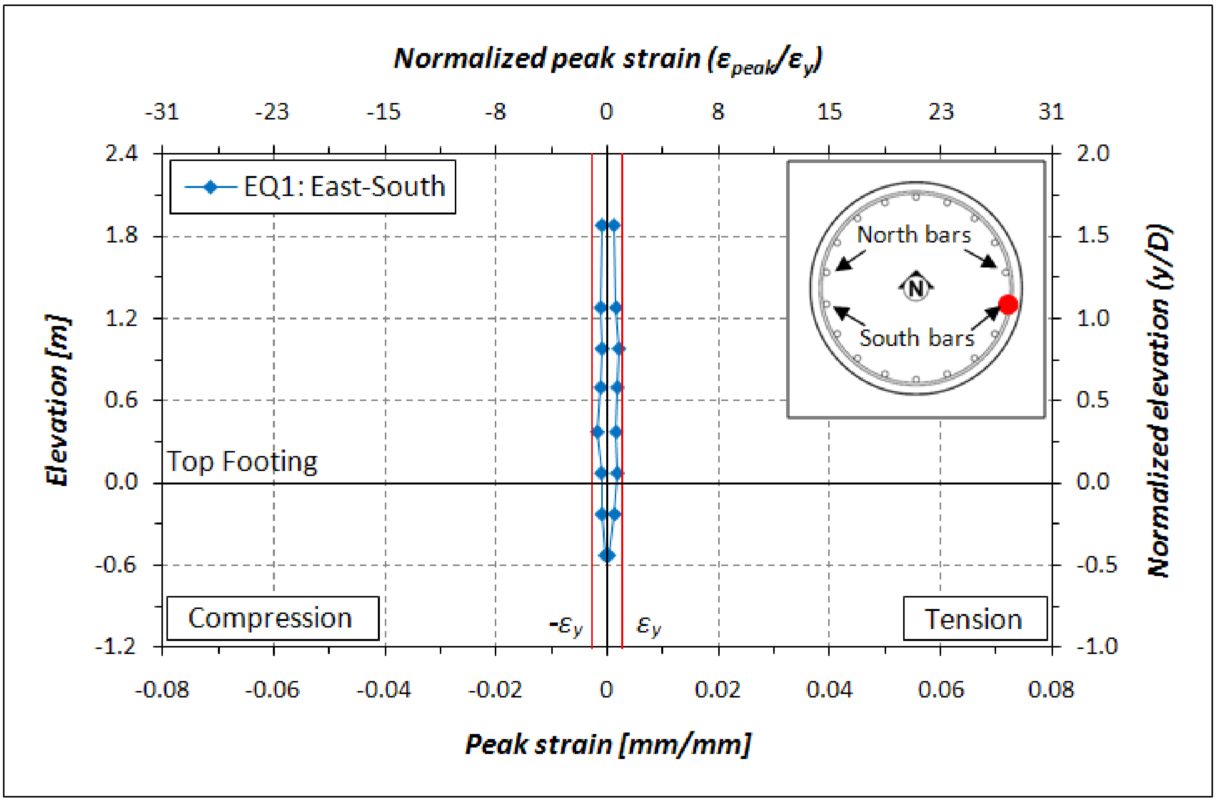

Figure 4.10: Longitudinal bar strain profile for EQ1: East side South bar

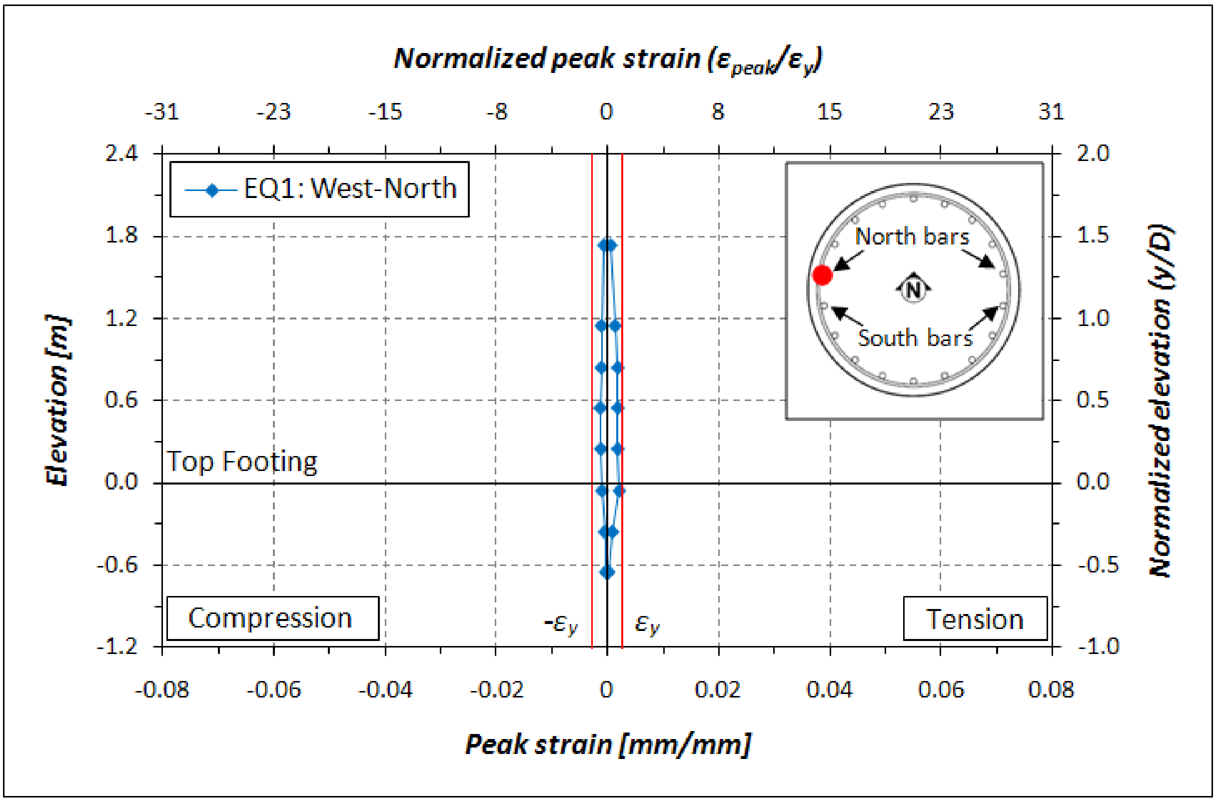

Figure 4.11: Longitudinal bar strain profile for EQ1: West side North bar

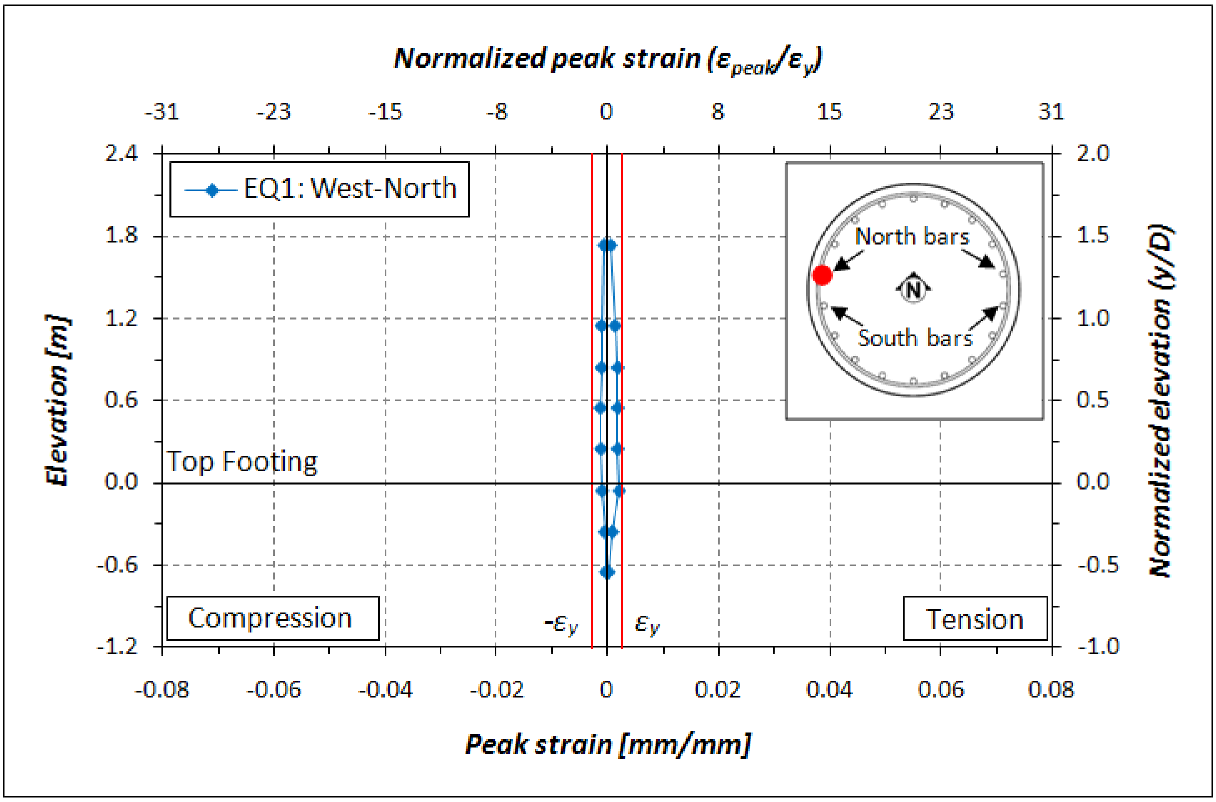

Figure 4.12: Longitudinal bar strain profile for EQ1: West side South bar

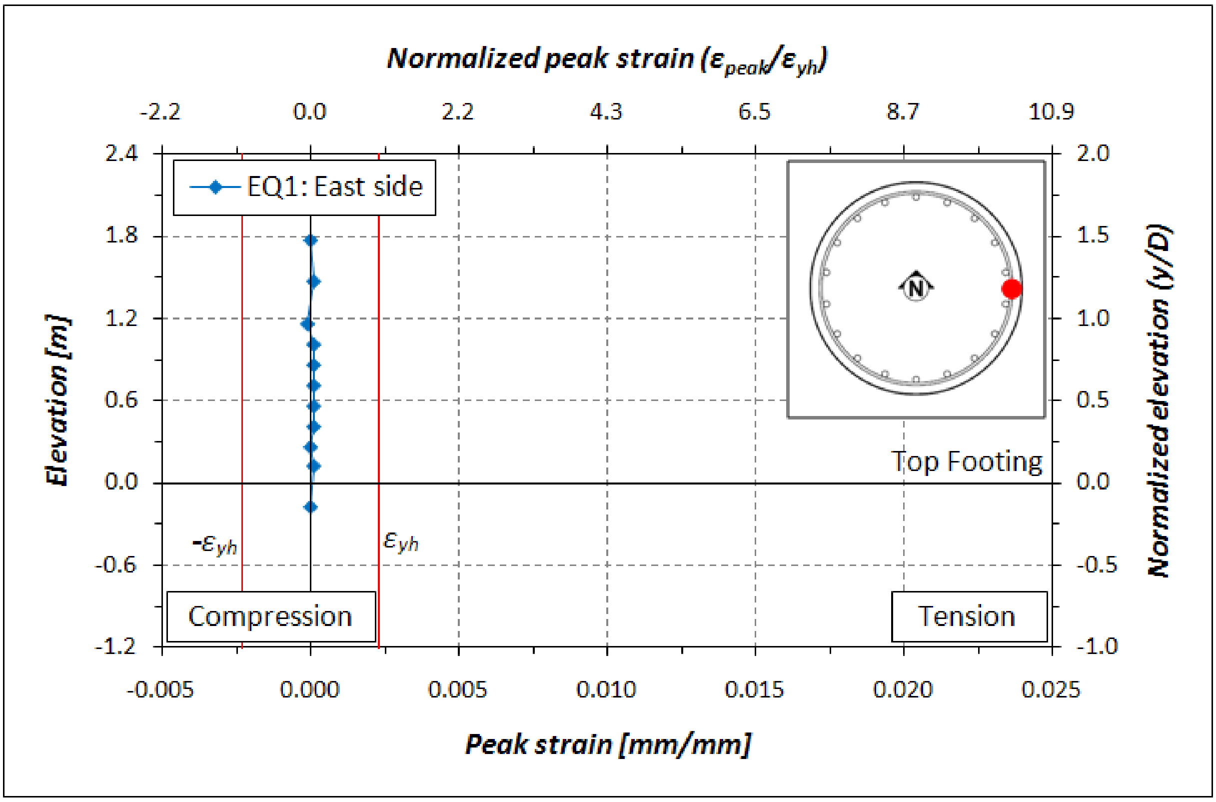

Figure 4.13: Hoops strain profile for EQ1: East side

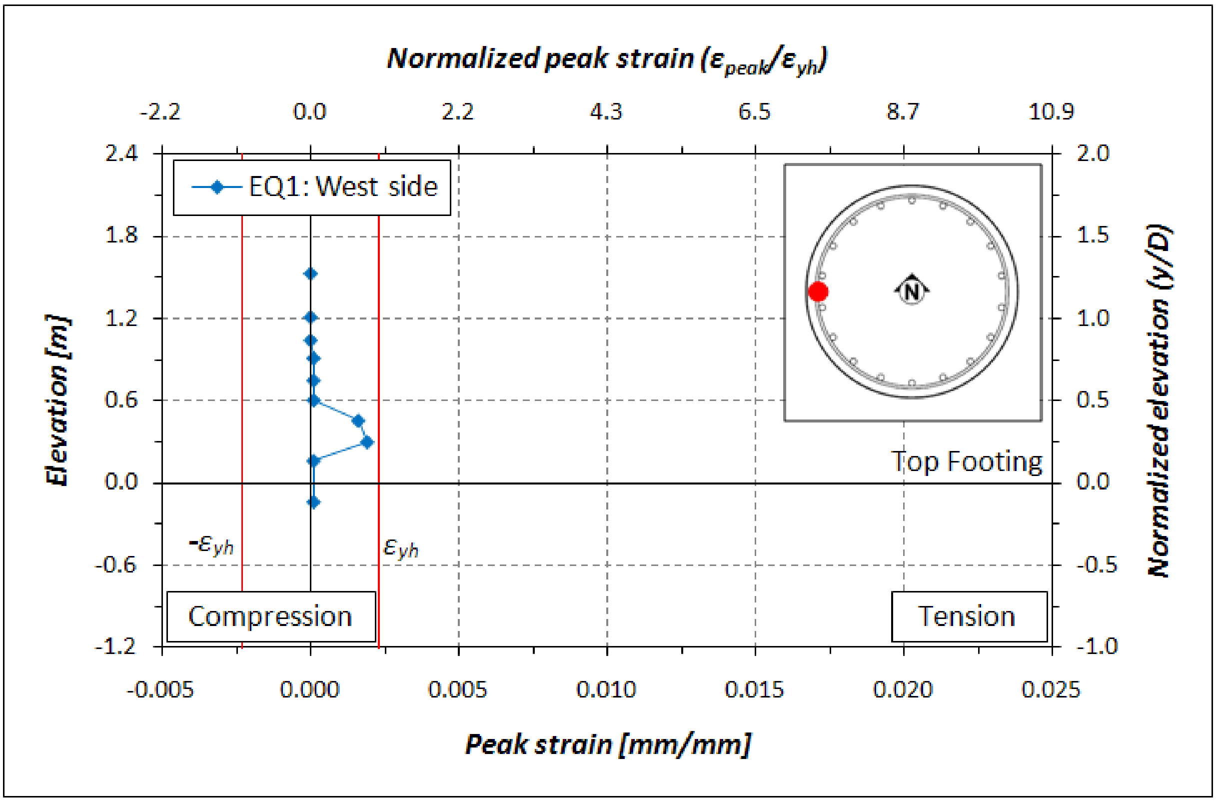

Figure 4.14: Hoops strain profile for EQ1: West side

4.2.2 EQ2 – Corralitos

The Corralitos ground motion was reproduced as EQ2 to simulate a medium-intensity earthquake. The objective of this test was to induce in the specimen a displacement ductility of 2.0.

No signs of concrete spalling were observed. Crack propagation occurred at the column-footing interface and additional cracks opened. Discontinuous and no thicker than 0.1 mm (0.004 in.) cracks were identified at the base and at the upper visible part of the column. The cracks were located on both the East and West side of the column and they were essentially horizontal, demonstrating a flexural-dominated behavior of the specimen. Cracks spaced between 152 mm (6 in.) and 305 mm (12 in.) were found in the column from its base to about 1.68 m (5.5 ft) and additional ones were observed between 3.91 m (12.5 ft) and 4.97 m (16.3 ft). A post- test view of the East face of the column base is shown in Figure 4.15. The video snapshot was taken before crack marking, so the cracks are not visible in this figure.

A nonlinear response can be observed in the moment-curvature relationship of the column base, see Figure 4.16. A good agreement between analytical and experimental yield moment can be deduced from the drastic change of the slope in the positive quadrant: the knee branch occurs approximately at a moment equal to M_y. A peak moment of 5865.8 kNm

Figure 4.15: Column base post-EQ2

(4326.4 kip-ft), corresponding to $1.01{\cdot}M_y$, and a peak curvature of $1.56{\cdot}10^{-2}$ rad/m ($3.96{\cdot}10^{-4}$ rad/in), corresponding to $1.87{\cdot}\varphi_{ye}$, were reached during EQ2.

No further linear elastic and symmetric behavior can be identified in the base shear versus top displacement response, see Figure 4.17. Higher mode effects becomes more apparent in this plot. A peak displacement of 133 mm (5.24 in.) or a 1.82% drift ratio, corresponding to $1.48{\cdot}\Delta_{ye}$, was recorded at the top of the column. A residual displacement of 4 mm (0.16 in.) or 0.05% residual drift ratio, demonstrates the onset of inelastic behavior. A peak shear of 697.6 kN (156.8 kips), corresponding to $0.89{\cdot}V_{b,y}$ and a base shear coefficient of 0.28, was achieved during this test.

The positive and negative moment envelopes along the column height are shown in Figure 4.18. A peak top moment of 1411.1 kNm (1040.8 kip-in), corresponding to 24% of the peak moment recorded at the column base, was reached during EQ2. The first cracking moment M_{cr}, which is equal to 838.7 kNm (618.6 kip-ft), was abundantly overcame.

The average curvature locally exceeded the experimental idealized yield one in both positive and negative bending directions. The average flexural rotation, which is represented by the area underlying the average curvature envelopes, propagated along the column height and a large concentration of curvature was not located at the column base, see Figure 4.19.

The positive and negative envelopes of the relative displacement between column and table (solid line) and the post-test residual configuration (dashed line) are shown in Figure 4.20. A flexural-dominated behavior can be inferred from the different peak displacement components: 91 mm (3.58 in.) from flexure, 4 mm (0.14 in.) from shear, and 26 mm (1.02 in.) from fix end rotation.

The strains envelopes along the instrumented longitudinal bars are plotted in Figures 4.21 to 4.24. Three of the four monitored bars reached the yield strain in tension near the column-footing interface. Only the South bar on the East side remained elastic. A relevant peak strain of 1.32% in tension, corresponding to $5.08{\cdot}\varepsilon_y$, was recorded on the North bar of the West side (Figure 4.23). Although localized yielding occurred, plasticity did not fully developed. Yielding in compression occurred on the South bar of the East side, where a peak strain of -0.27%, corresponding to $1.04{\cdot}\varepsilon_y$, was recorded (Figure 4.22).

The hoop strain envelopes on the East and West side of the column are shown in Figures 4.25 and 4.26. The second and the third hoops above the column-footing interface yielded in tension. A peak strain of 0.29%, corresponding to $1.26{\cdot}\varepsilon_{sh}$, was recorded on the West side of the second hoop.

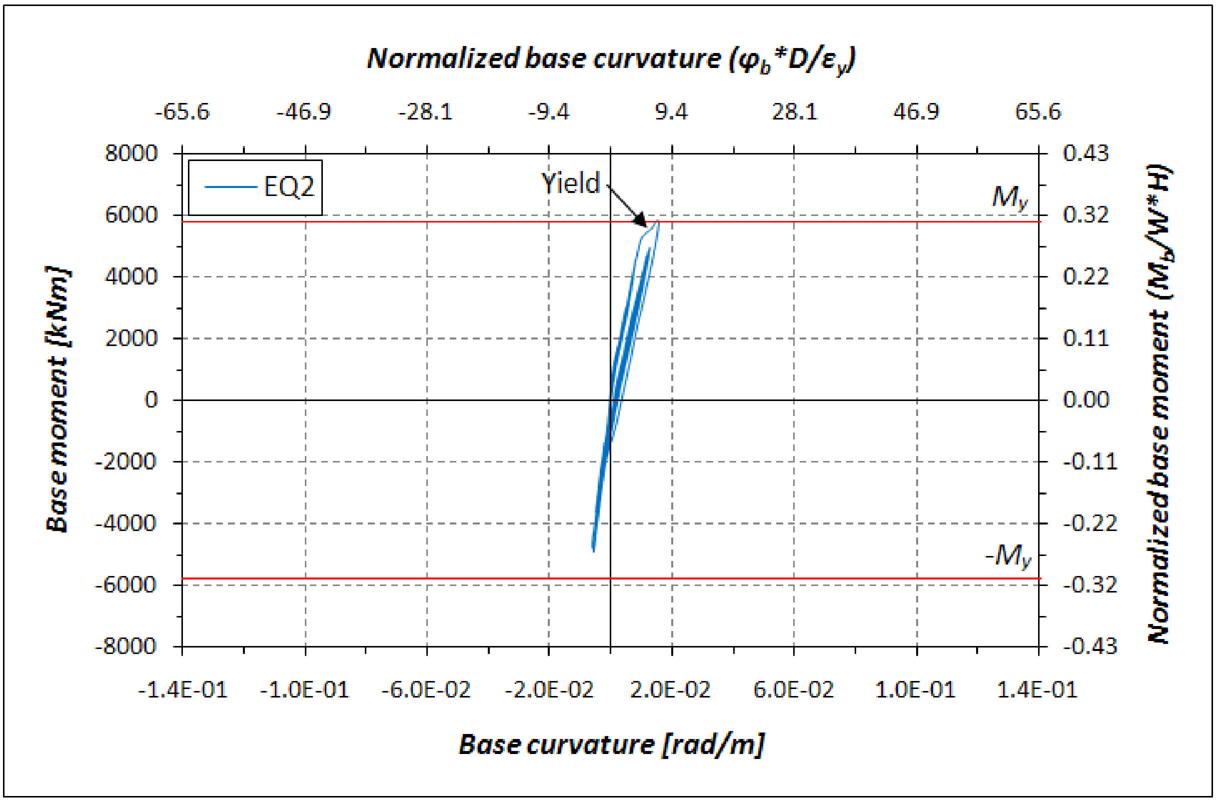

Figure 4.16: Base moment-base curvature response for EQ2

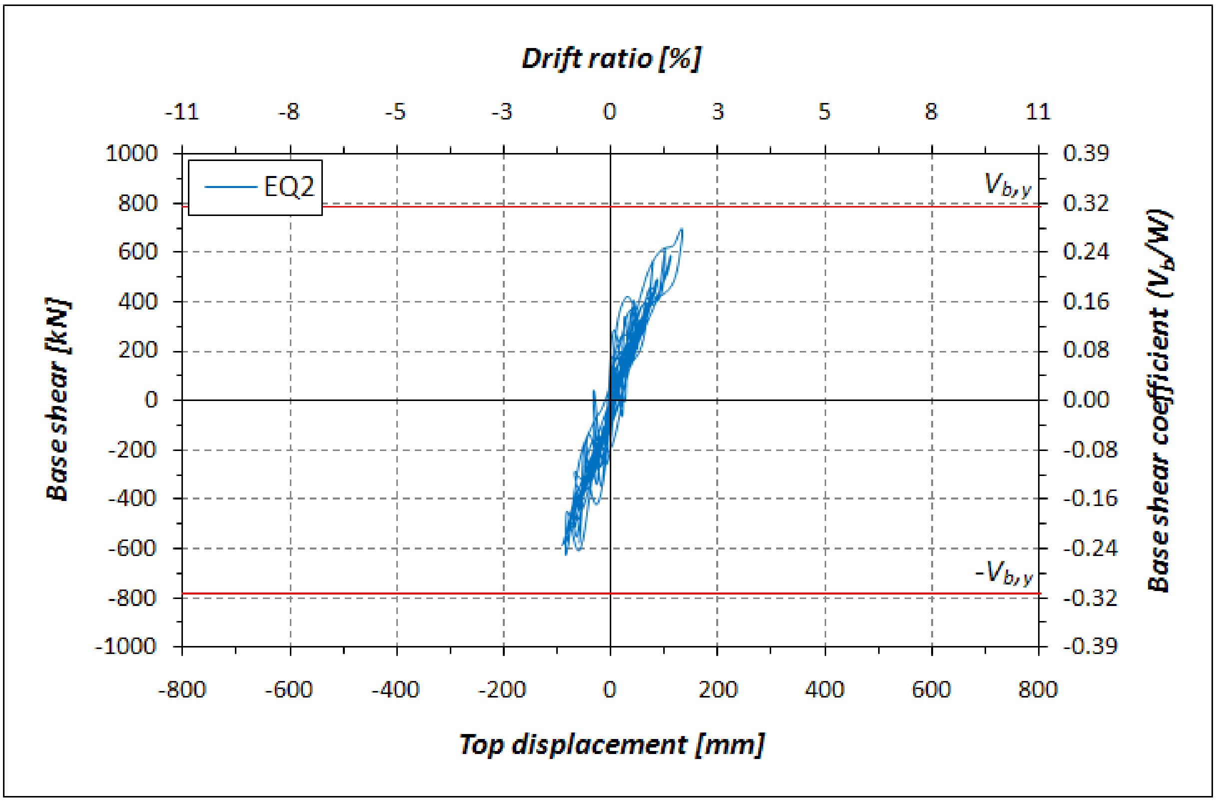

Figure 4.17 Base shear-top displacement response for EQ2

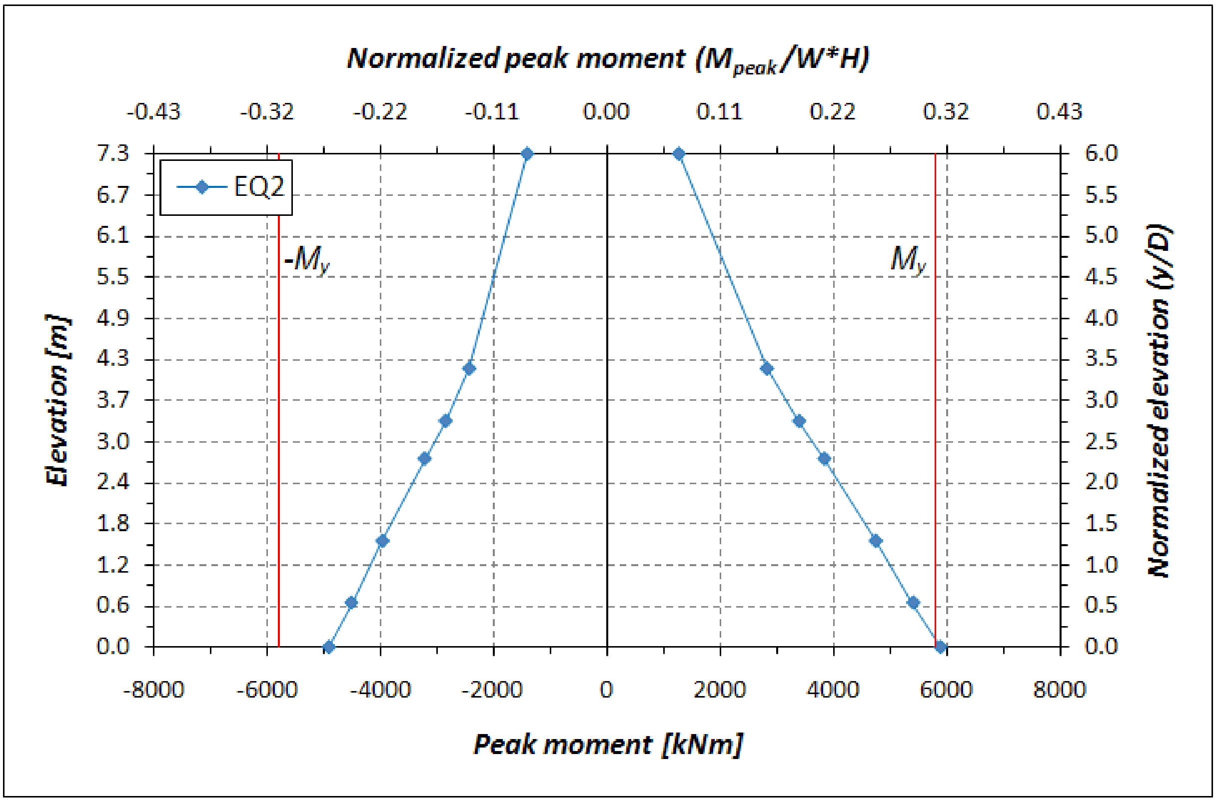

Figure 4.18: Moment envelops along the column height for EQ2

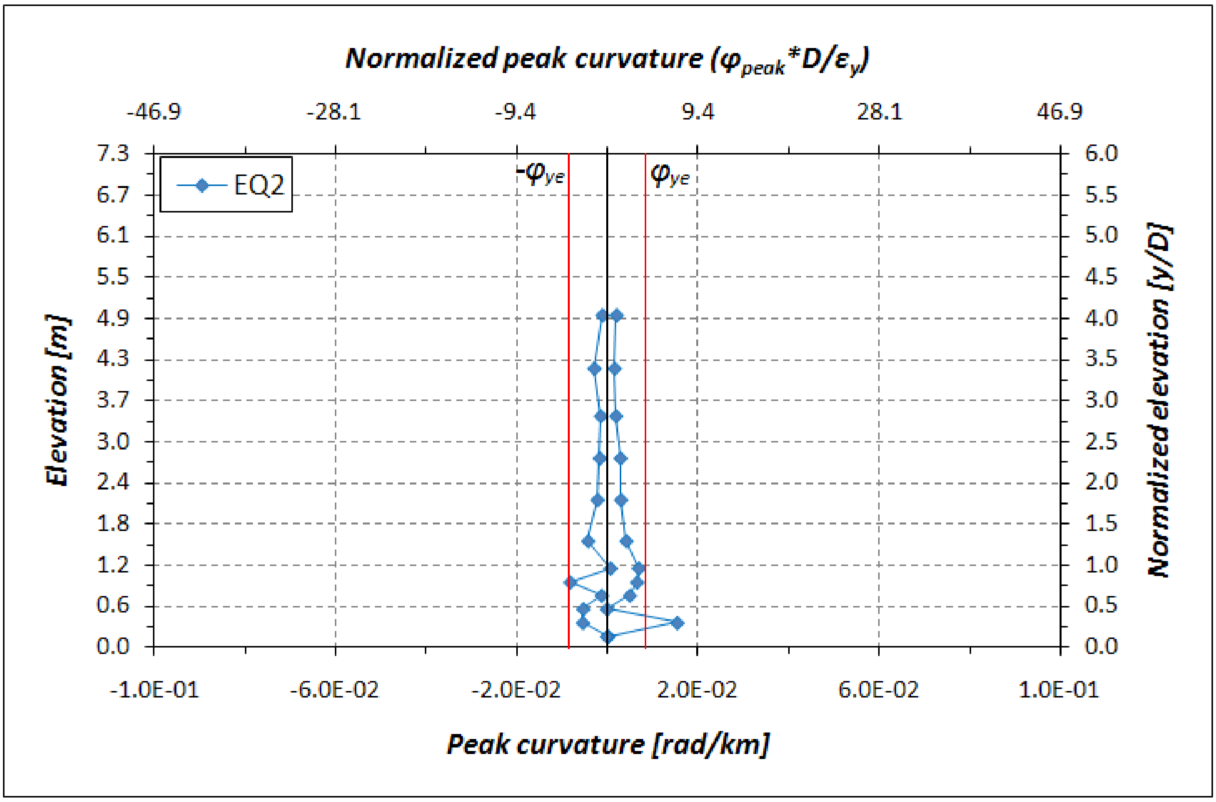

Figure 4.19: Curvature envelops along the column height for EQ2

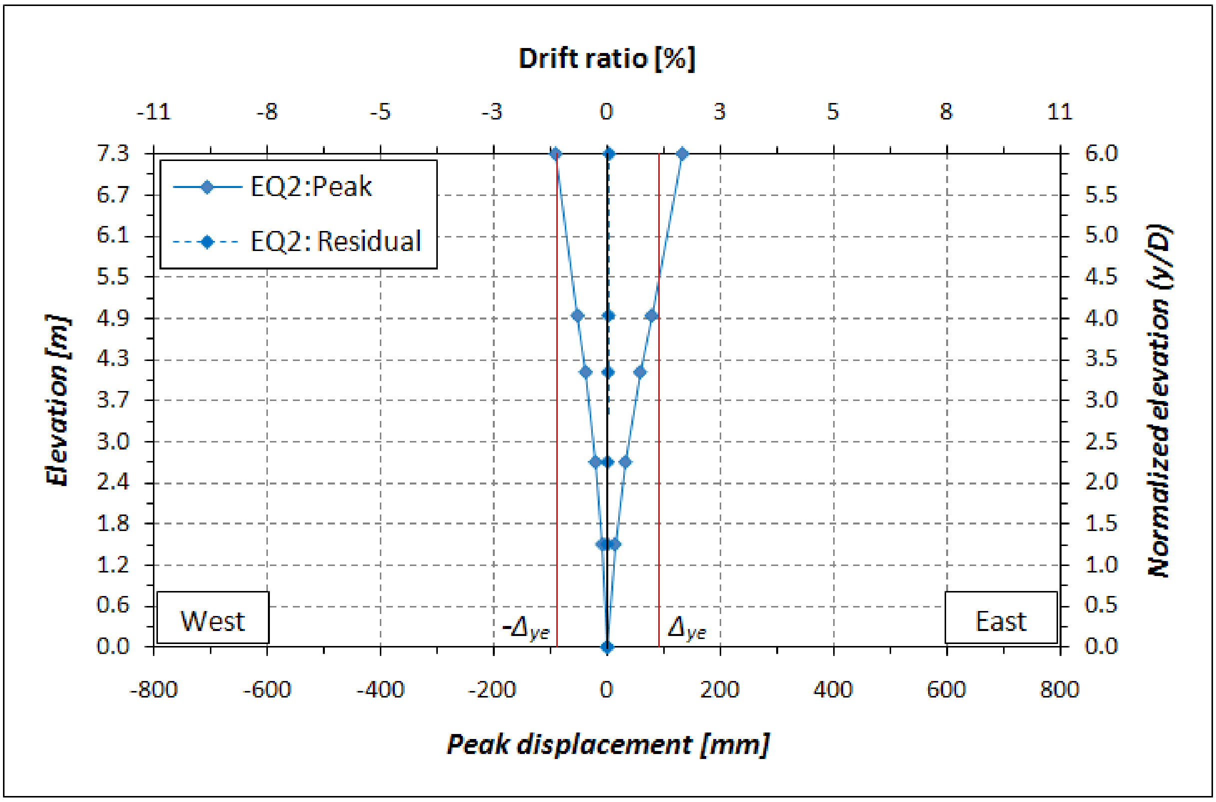

Figure 4.20: Displacement and displacement components envelops along the column height for EQ2

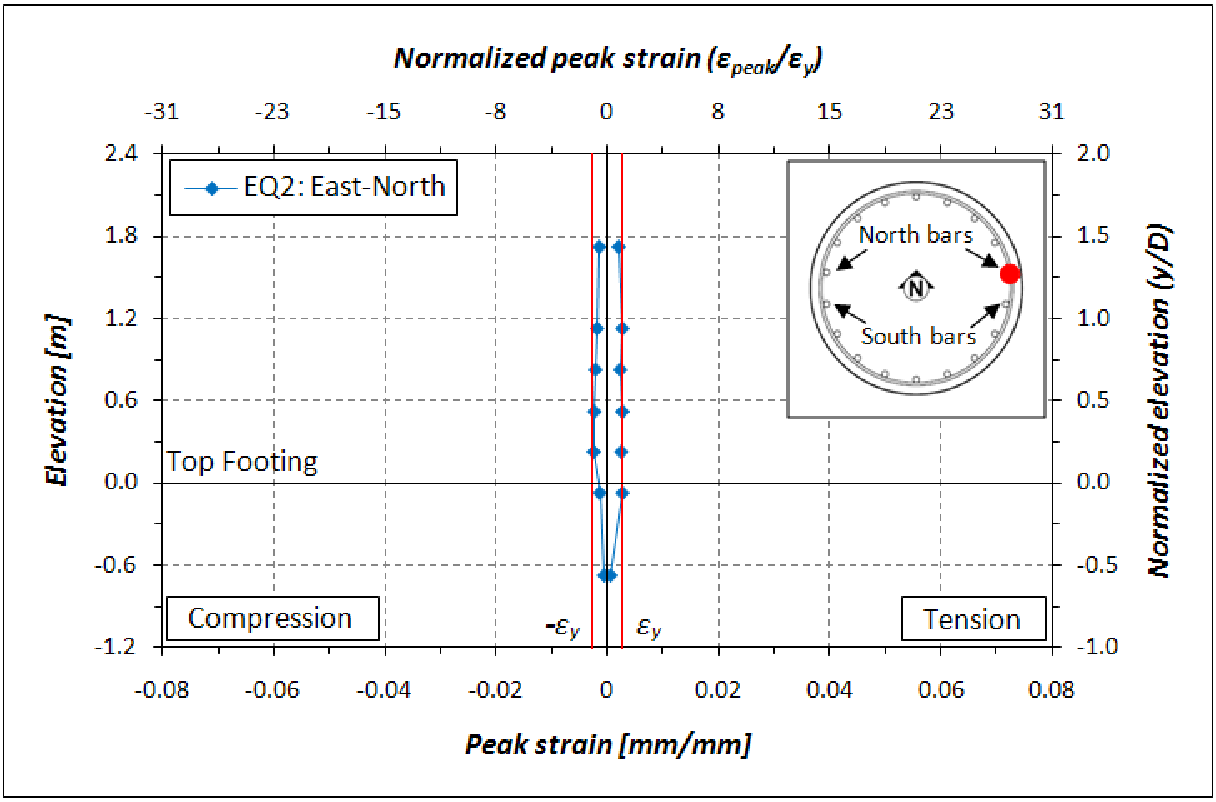

Figure 4.21: Longitudinal bar strain profile for EQ2: East side North bar

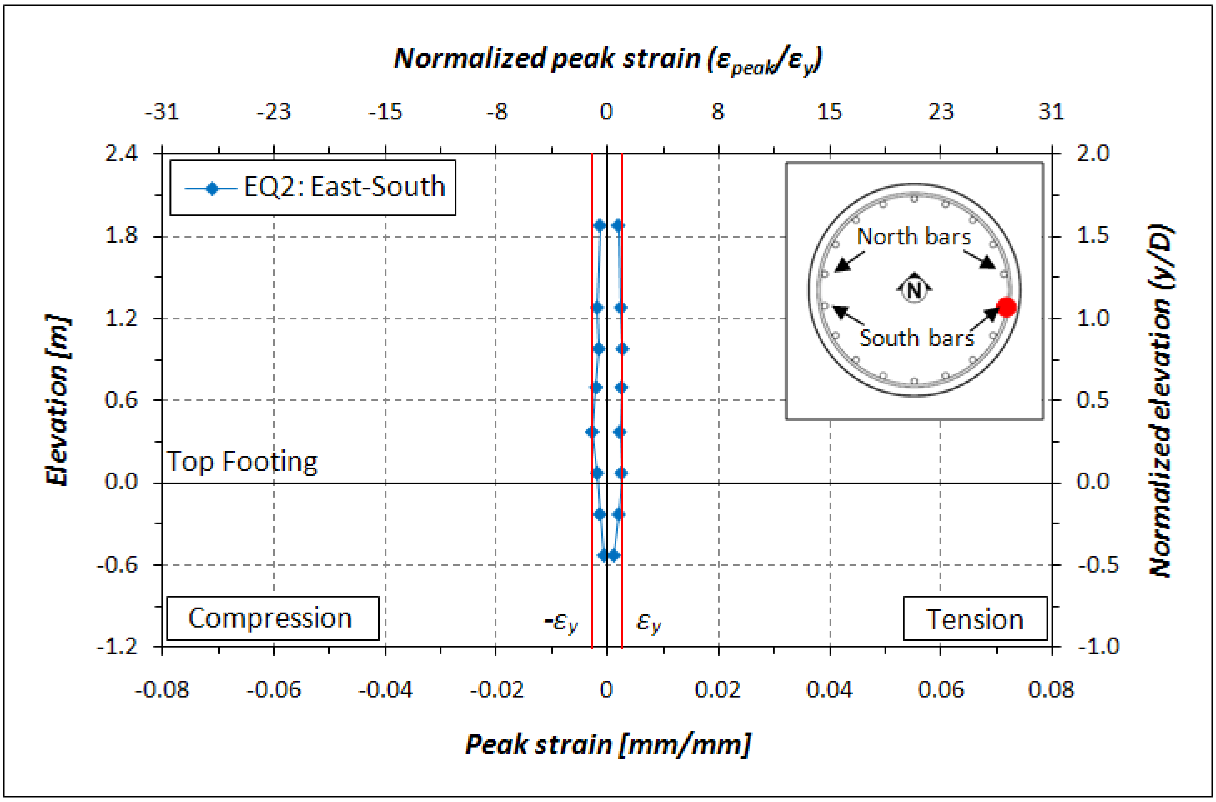

Figure 4.22: Longitudinal bar strain profile for EQ2: East side South bar

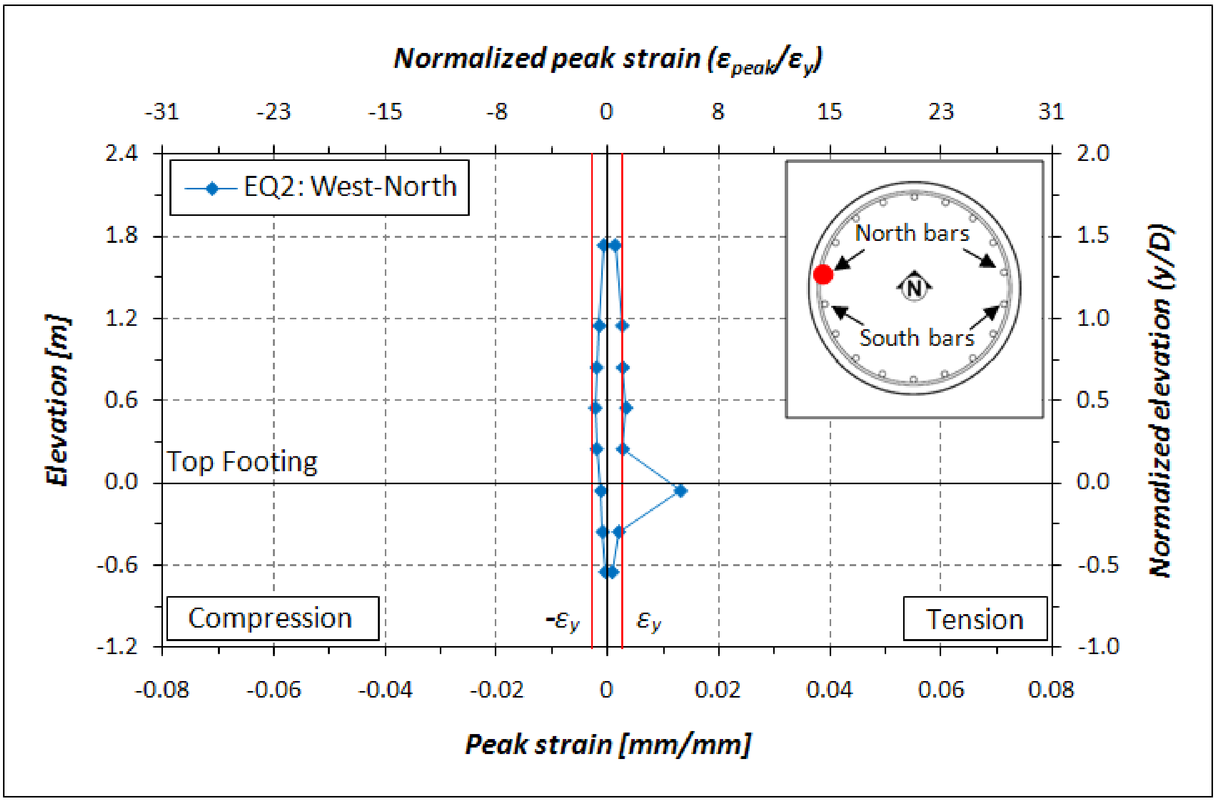

Figure 4.23: Longitudinal bar strain profile for EQ2: West side North bar

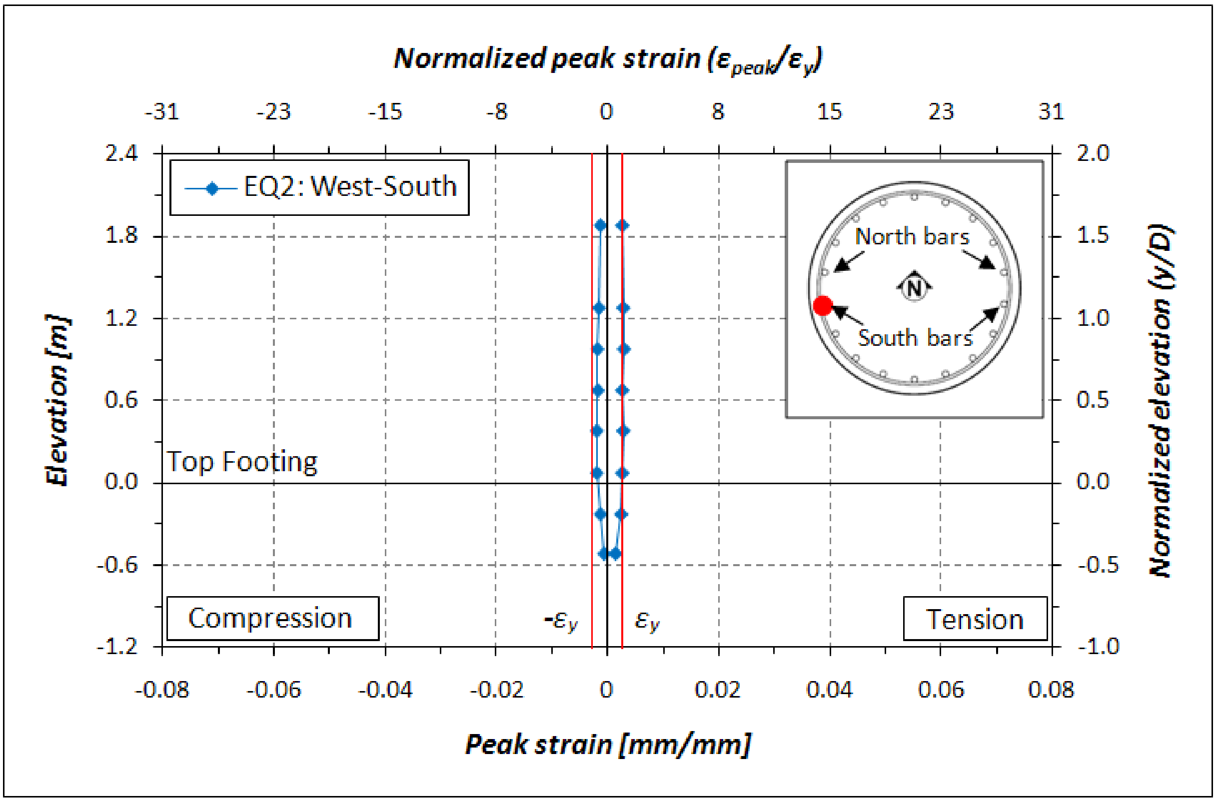

Figure 4.24: Longitudinal bar strain profile for EQ2: West side South bar

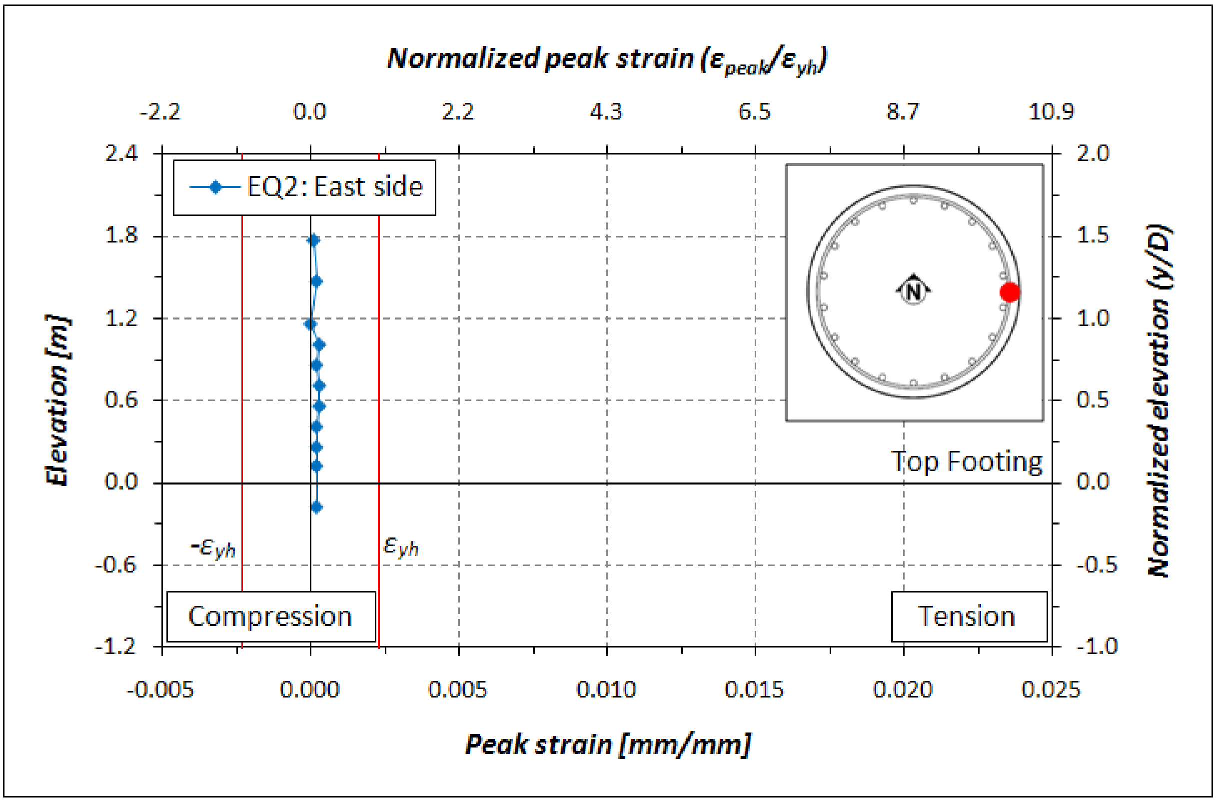

Figure 4.25: Hoops strain profile for EQ2: East side

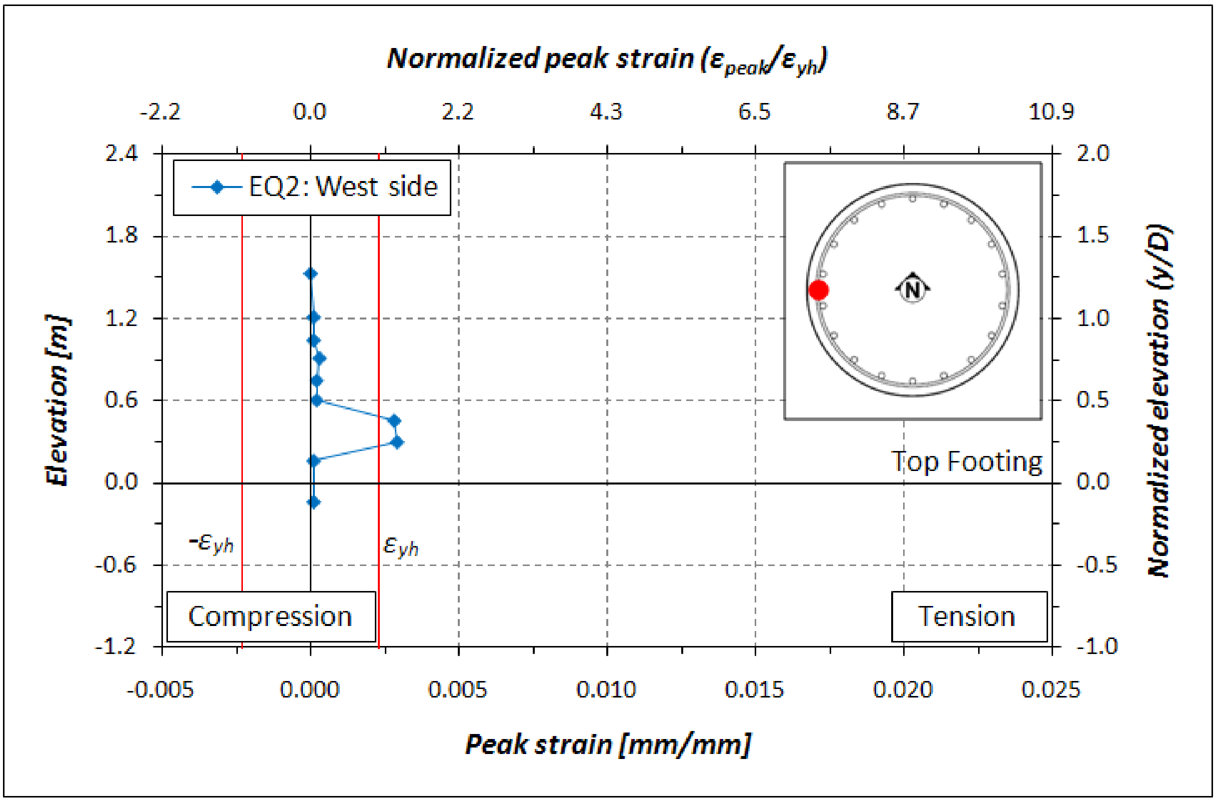

Figure 4.26: Hoops strain profile for EQ2: West side

4.2.3 EQ3 – Los Gatos Presentation Center

Los Gatos Presentation Center ground motion was performed as EQ3 to simulate an earthquake with 5% probability of exceedance in 50 years according to Caltrans *Seismic Design Criteria* [Caltrans, 2006 a]. For such earthquake the column was expected to undergo a displacement ductility demand of 4.0 and fully maintained its vertical load carrying capacity.

Concrete spalling was observed on both the East and West sides of the column base. It was accentuated on West side, where the excitation produced maximum compression. A maximum spalling height of about 1.143 m (3.75 ft), corresponding to almost one column diameter, occurred in the extreme West side. A spalling height of about 914 mm (3.0 ft) characterized the surrounding area. The spalled concrete was measured to be approximately 51-mm (2-in.) tick, corresponding to the thickness of the entire concrete cover. The exterior face of some hoops were visible behind the spalled concrete. Onset of spalling was observed on the East face of the column, with a maximum height of about 381 mm (15 in.).

The horizontal cracks formed during the previous tests increased in length. The ones located at the column base started to wrap around the column. They also increased their thickness with a maximum residual value of 1.4 mm (0.055 in.). New flexural cracks were observed on both the East and the West side of the column. They were principally located at the column base, but cracks spaced at approximately 305 mm (12 in.) were identified on the East side along the entire height of the column. Vertical and diagonal cracks were observed on both the North and South face at the column base. They did not propagate above one column diameter and their thickness never exceeded a value of 1 mm (0.04 in.). The cracks pattern demonstrates a flexural-dominated behavior with a negligible shear contribute. As can be seen in the post-test view of the East face of the column base shown in Figure 4.27, only cosmetic damage was observed. The snap shot in this figure was taken before cracks had been marked, but the crack pattern and concrete flaking are visible.

A ductile behavior and distinct hysteresis loops can be observed in the base moment versus base curvature response, see Figure 4.28. Again, a good agreement between analytical and experimental yield moment can be deduced from the drastic change of the slope in the negative quadrant: the knee branch occurs approximately at a moment equal to M_y. The analytical idealized elastic limit is exceeded twice in both the positive and negative quadrant: the first time with a similar slope of EQ2 and the second time with a smaller one due to the induced damages from the first pulse of EQ3. Stiffness degradation occurred during this test:

Figure 4.27: Column base post-EQ3

the initial slope of the moment curvature relationship is greater than the one recorded during the free vibration of ending test. A peak moment of 6597.8 kNm (4866.3 kip-ft), corresponding to 1.14·M_y, and a peak curvature of 6.08·10^{-2} rad/m (1.54·10^{-3} rad/in), corresponding to 7.27·φ_{ye} were reached.

Large loops, affected by higher mode effects, can be found in the base shear versus top displacement response, see Figure 4.29. The column reached the base shear corresponding to idealized yield, $V_{b,y}$, in both positive and negative quadrant, preserving its vertical load carrying capacity. A peak shear of 887.4 kN (199.5 kips), corresponding to 1.14·$V_{b,y}$ and a base shear coefficient of 0.35, was reached during EQ3. This value was the largest shear force obtained in any test. A peak displacement of 361 mm (14.20 in.) or a 4.93% drift ratio, corresponding to 4.01·Δ_{ye}, was measured at the top of the column. A residual displacement of -63 mm (-2.49 in.) or -0.87% residual drift ratio remained post-test. The column was inclined in the West side at the end of the test.

A top moment of 1525.6 kNm (1125.2 kip-ft), corresponding to 23% of the peak moment reached at the base of the column, can be identified in the positive moment envelope along the column height, see Figure 4.30.

The average curvature envelopes exceeds the experimental idealized yield value at the column base in both the positive and negative bending directions, see Figure 4.31. Large values of curvature were expected at the column base, but the lowest set of LVDTs measured a very small curvature due to the absence of cracks in this lower segment of the column. Larger values were recorded starting from 203 mm (8 in.) above the column-footing interface. The flexural rotation started to concentrate at the column base and did not propagate along its height. Although significant values of curvature and flexural rotation were measured nearly the column base, no appreciable concentration of damage were observed.

The positive and negative envelopes of the relative displacement between column and table (solid line) and the post-test residual configuration (dashed line) are shown in Figure 4.32. A flexural-dominated behavior can be deduced from the different peak displacement components: 267 mm (10.50 in.) from flexure, 17 mm (0.67 in.) from shear, and 74 mm (2.90 in.) from fix end rotation. The shear component is not negligible as in the previous test and the fix end one assumes a significant value.

The strains envelopes along the instrumented longitudinal bars are plotted in Figures 4.33 to 4.36. All the four monitored bars yielded in tension showing a large post-elastic deformation. The two bars located on the East side showed a 1.5 column diameter yield-length: one diameter above the column-footing interface and one half below it. One column diameter yield-length located above the column-footing interface can be identified on the West side bars. The average strain measured by a pair of strain gauges reached a peak value of 2.98% in tension, corresponding to $11.46 \cdot \varepsilon_y$, on the South bar of the East side (Figure 4.34). Yielding in compression occurred in all the four monitored bars, but only the two on the West side showed a large post-elastic deformation. A peak average strain of -1.47%, corresponding to $5.65 \cdot \varepsilon_y$, occurred on the South bar of the West side (Figure 4.36).

A regular change can be found in the recorded strains measuring hoop dilation, see Figures 4.37 and 4.38. Test EQ3 produced a small strain increase on almost all the monitored hoops. This effect was probably due to the confinement pressure, which the concrete core applied on the hoops, and not to an onset of longitudinal bars buckling, as buckling deformation was not observed. The only two hoops that yielded during EQ2 exceeded the elastic limit after this test. In particular, a peak strain of 0.29% in tension, corresponding to $1.26 \cdot \varepsilon_{yh}$, was recorded at the West side on both the second and the third hoop above the column-footing interface.

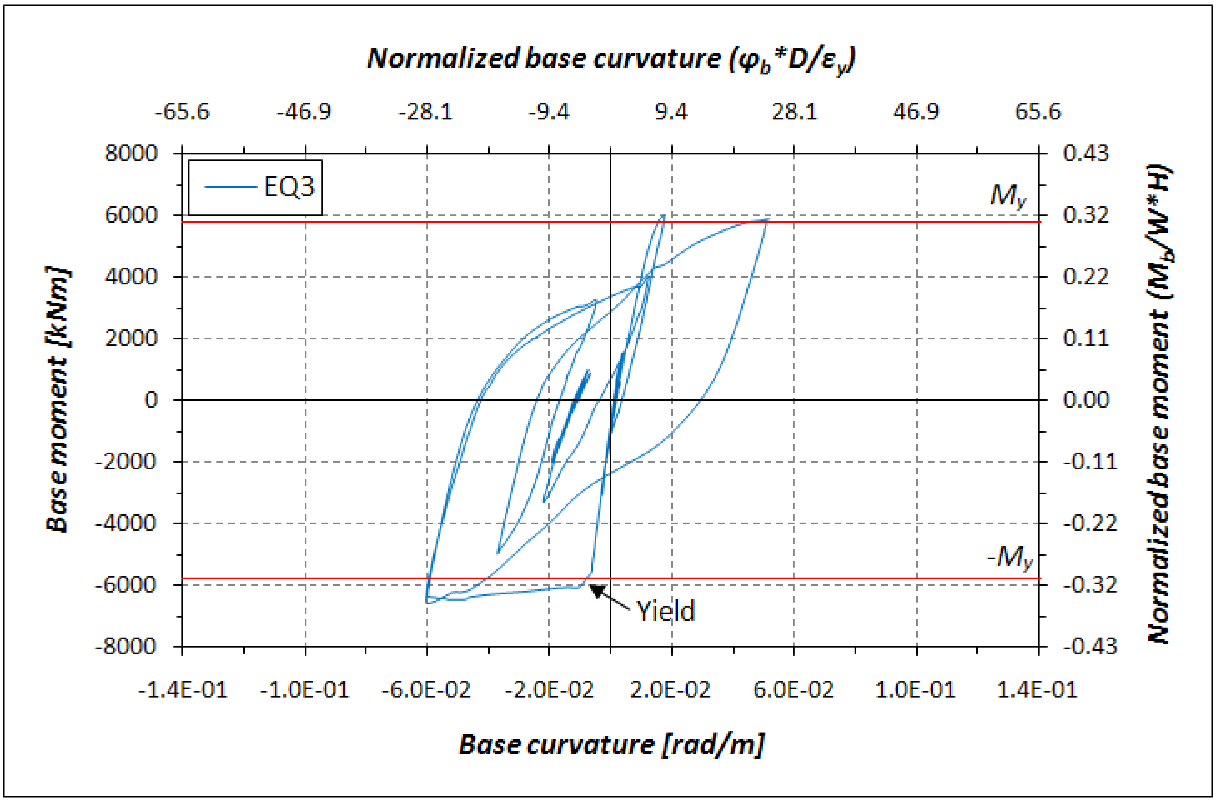

Figure 4.28: Base moment-base curvature response for EQ3

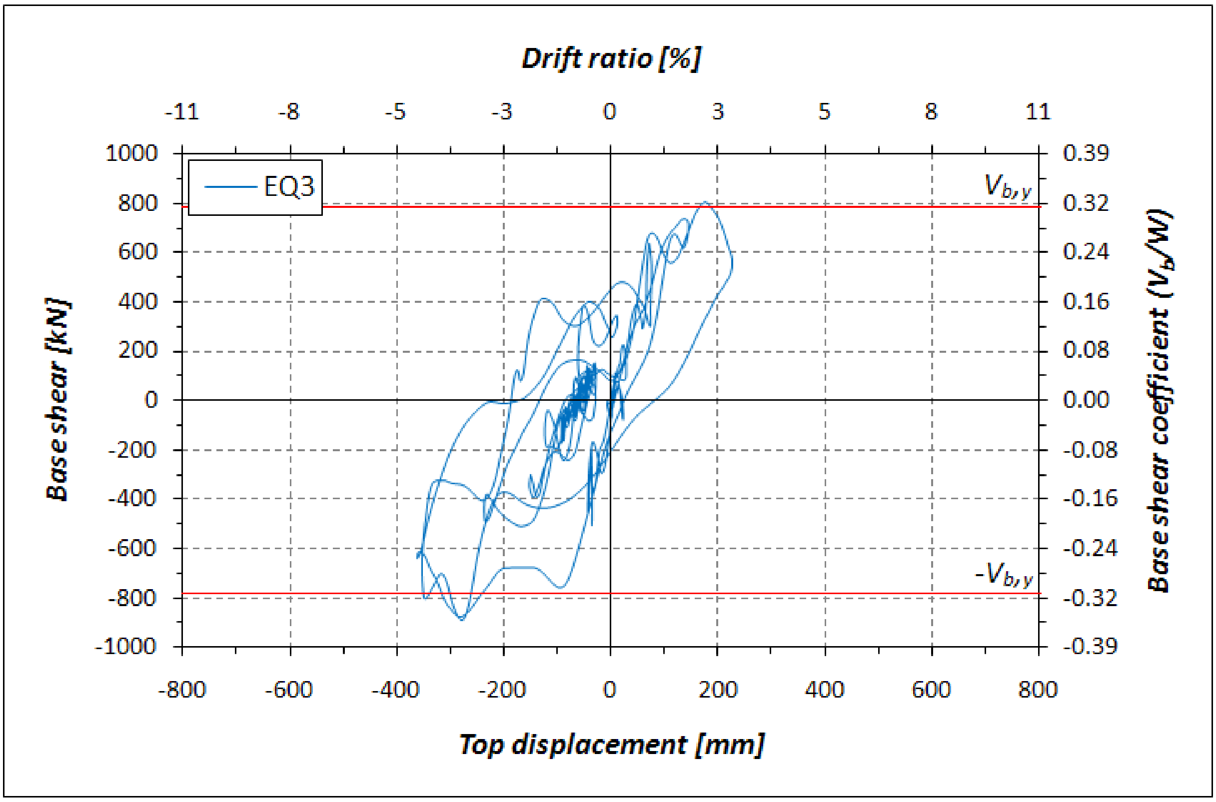

Figure 4.29 Base shear-top displacement response for EQ3

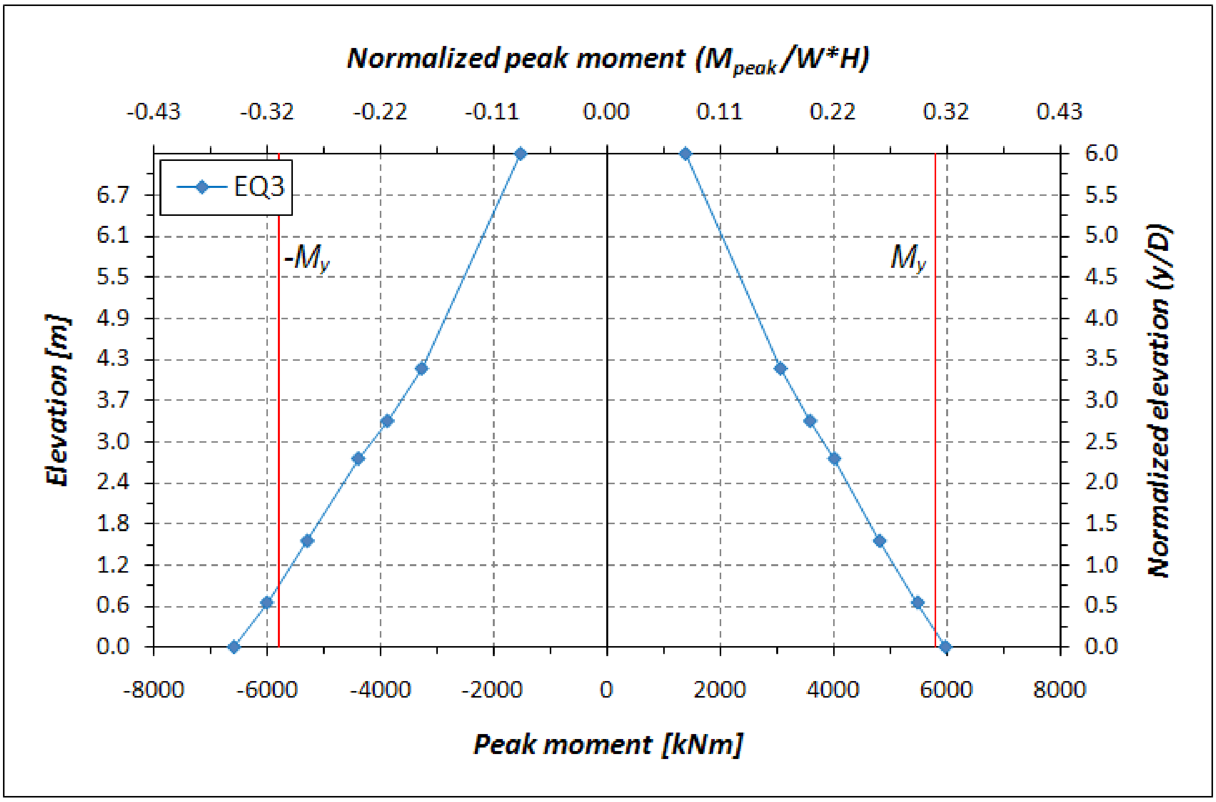

Figure 4.30: Moment envelops along the column height for EQ3

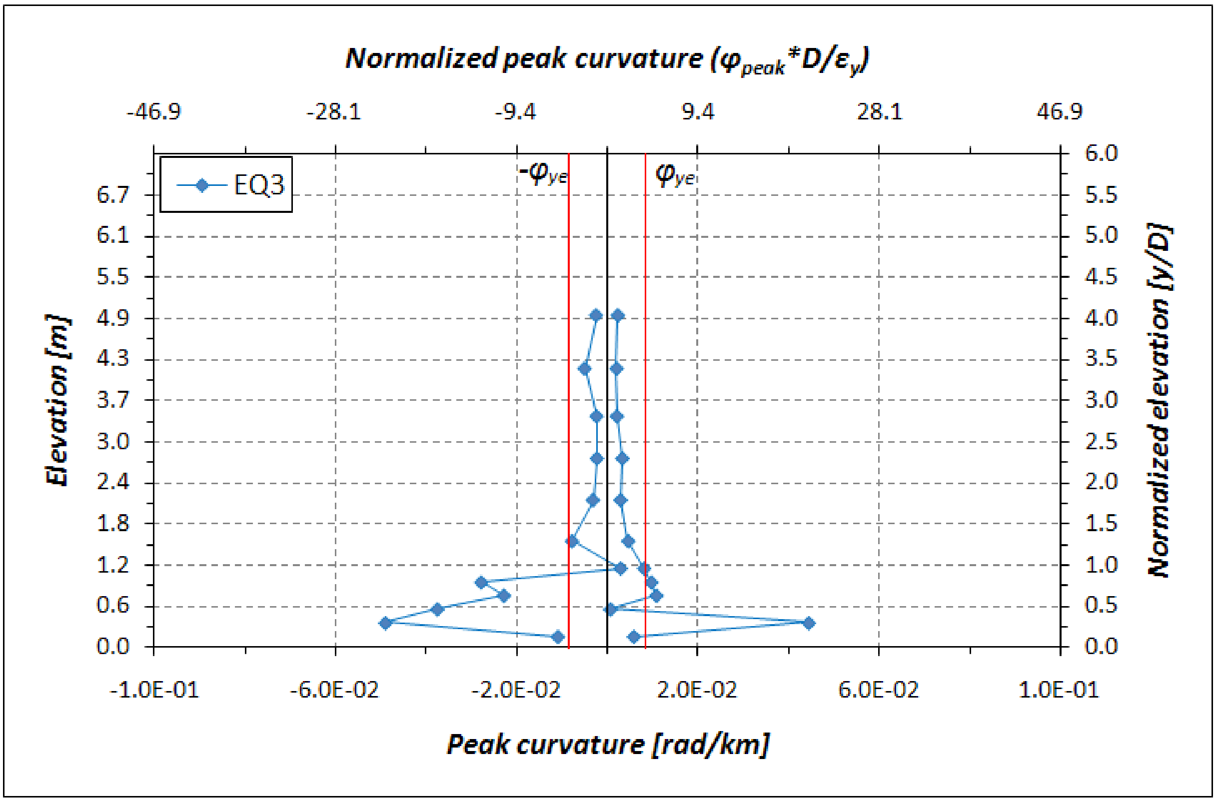

Figure 4.31: Curvature envelops along the column height for EQ3

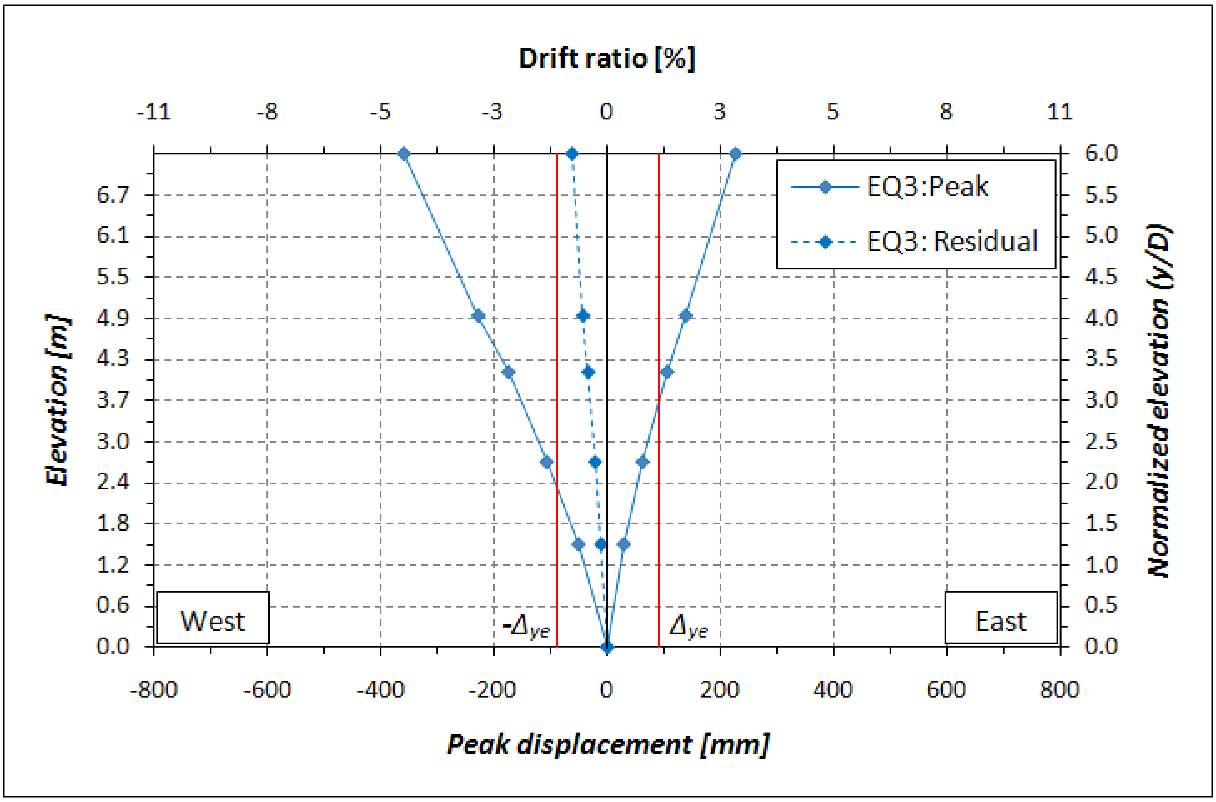

Figure 4.32: Displacement and displacement components envelops along the column height for EQ3

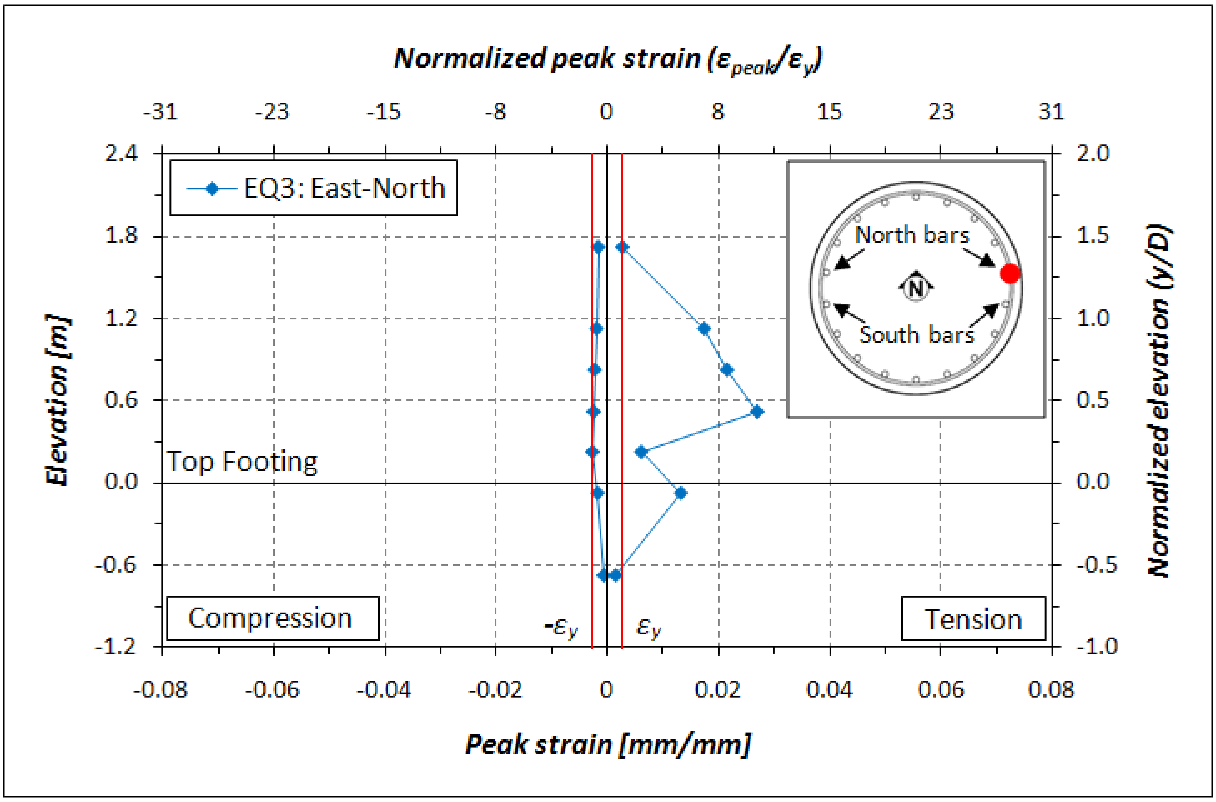

Figure 4.33: Longitudinal bar strain profile for EQ3: East side North bar

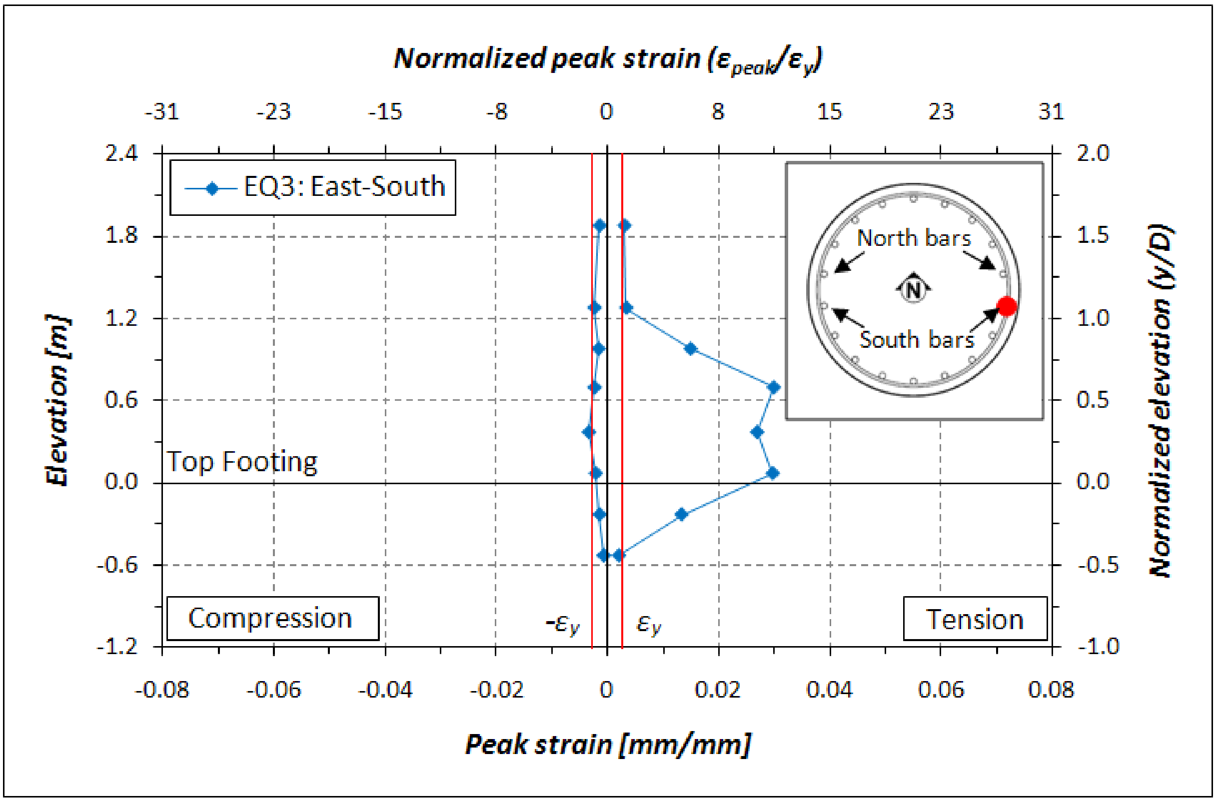

Figure 4.34: Longitudinal bar strain profile for EQ3: East side South bar

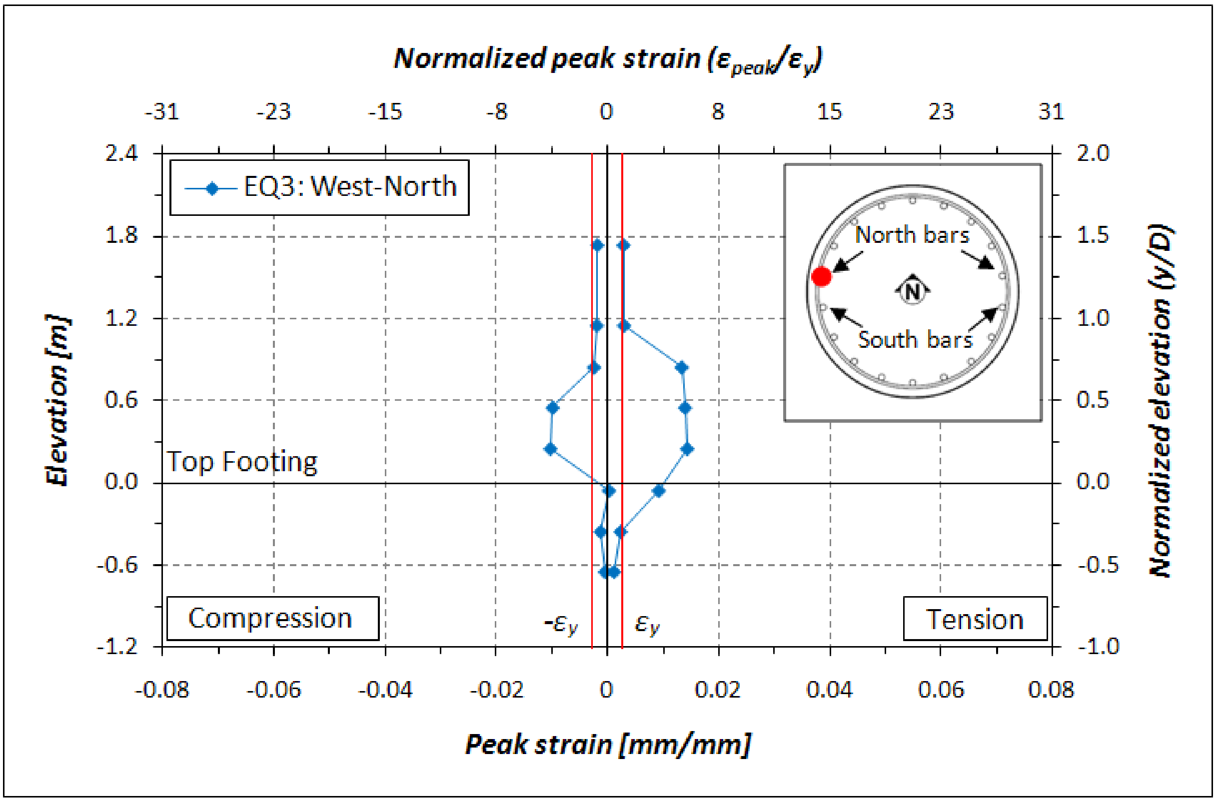

Figure 4.35: Longitudinal bar strain profile for EQ3: West side North bar

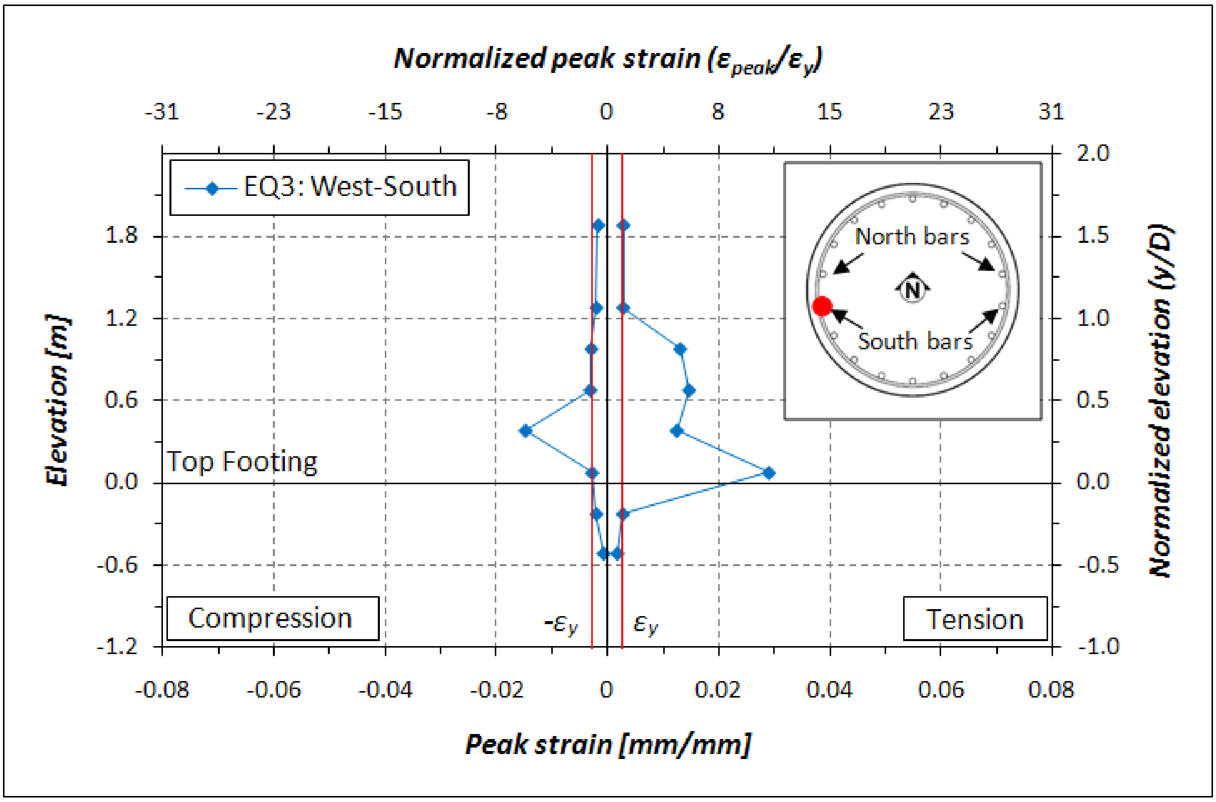

Figure 4.36: Longitudinal bar strain profile for EQ3: West side South bar

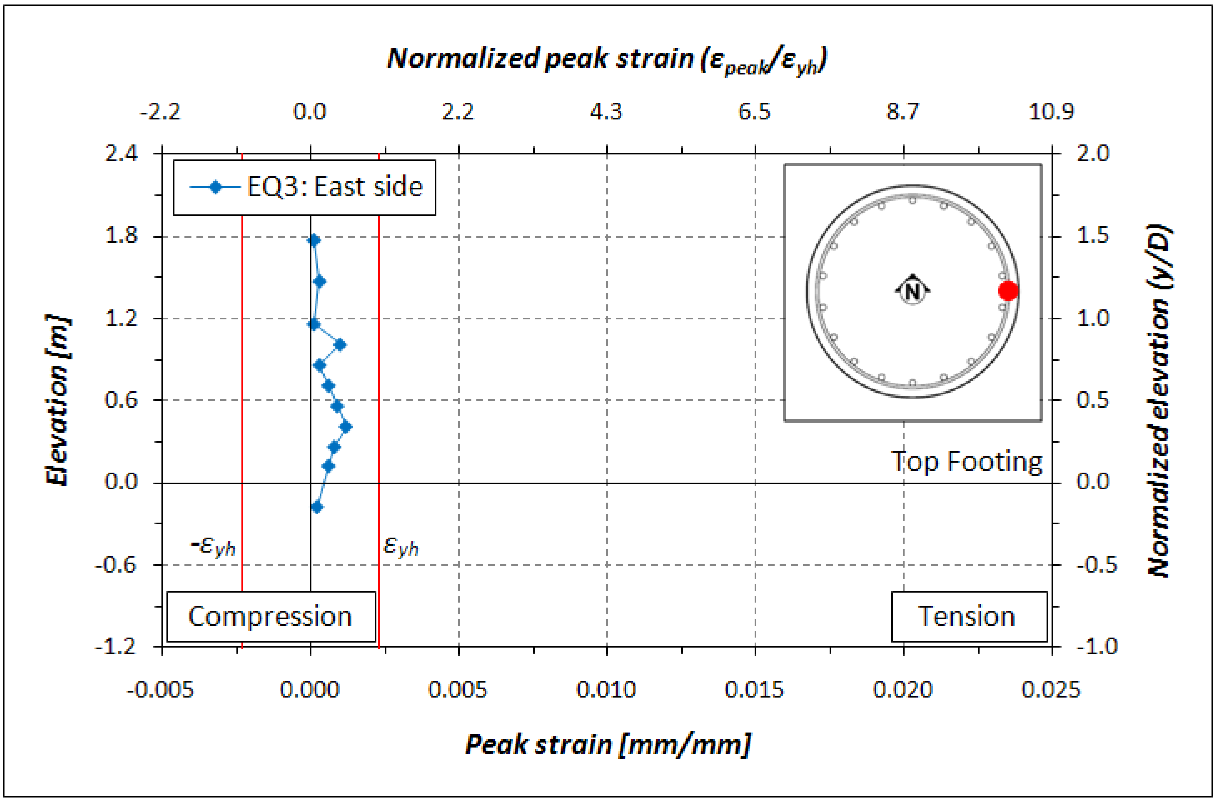

Figure 4.37: Hoops strain profile for EQ3 and EQ2: East side

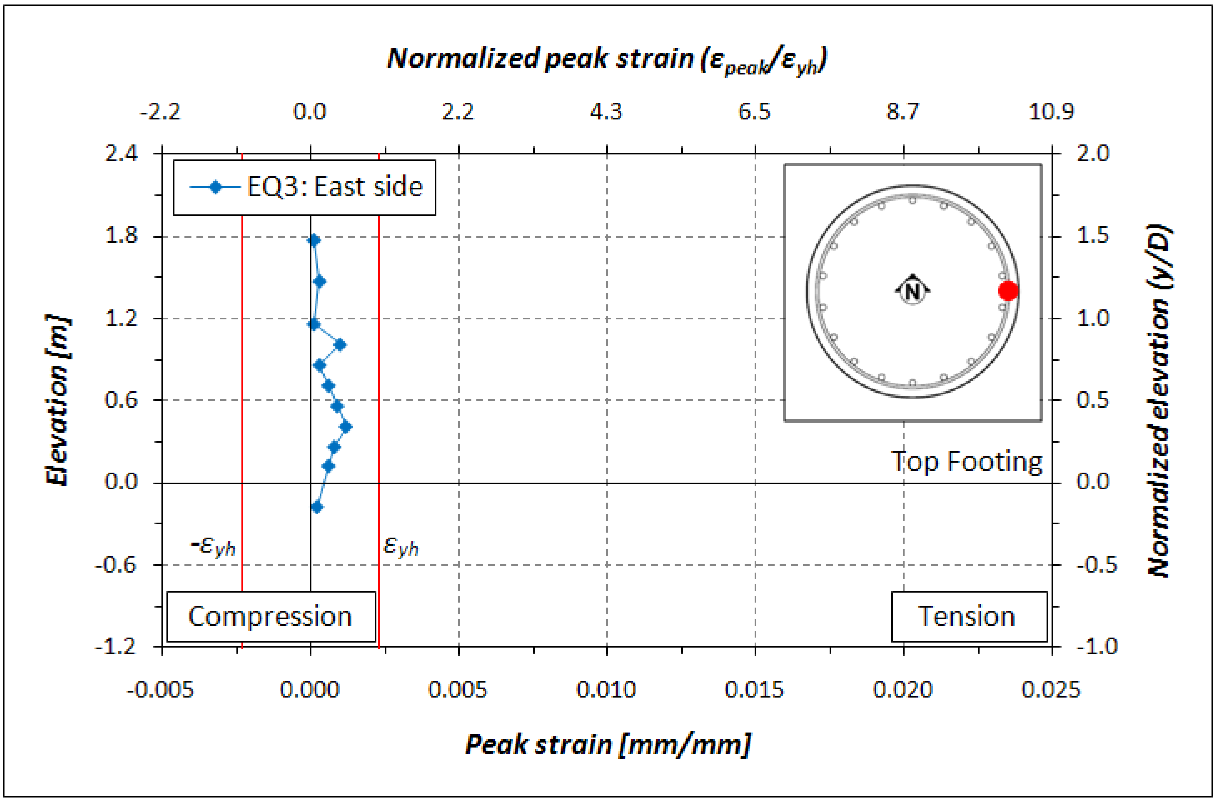

Figure 4.38: Hoops strain profile for EQ3 and EQ2: West side

4.2.4 EQ4 – Corralitos

The Corralitos ground motion was repeated as EQ4 to simulate a medium-intensity aftershock. The objective of this test was to observe the effects of an earthquake on damage structures. The succession of ground motions from EQ1 to EQ3 induced in the test specimen damages modifying its dynamic properties. Reproducing Corralitos record again, allowed comparison of the column response before and after the induced damage.

A significant residual displacement after test EQ3 denotes that target displacement ductilities are not relevant to subsequent tests. Target displacement ductilities used in the ground motion selection process were based on the cracked section properties and zero initial displacement. No attempts were made to straighten or repair the column between tests.

Cracks were not marked post EQ4 due to testing time constraints. Regions with spalling caused by the previous test barely enlarged. A post-test view of the East face of the column base is shown in Figure 4.39. As can be observed from the comparison of the post-test views of the East face of the column base after EQ3 (Figure 4.27) and after EQ4 (Figure 4.39), no significant damaged was induced by EQ4 excitation.

The base moment versus base curvature response of the column during EQ4 is plotted together with the one obtained during EQ2 in Figure 4.40. A nearly linear elastic behavior can

Figure 4.39: Column base post-EQ4

be observed in the moment-curvature response obtained from this test. Very small hysteresis loops demonstrate negligible energy dissipation during EQ4. Stiffness degradation due to the induced damage from the previous earthquakes can be observed comparing the response of Corralitos record as EQ2 with EQ4, see Figure 4.40. A peak moment of 3698.1 kNm (2727.6 kip-ft) was reached under EQ4 excitation. It corresponds to 63% of the peak moment measured during EQ2. This demonstrates that the same earthquake can produce different effects in structures with different dynamic properties. Principally due to a residual curvature accumulated during the previous tests, a peak curvature 61% larger than the one obtained in test EQ2 was reached during this test. A values of $2.51 \cdot 10^{-2}$ rad/m ($6.38 \cdot 10^{-4}$ rad/in) gives a curvature ductility of 3.0.

Stiffness degradation and the decrease of the horizontal inertial forces can be appreciate in the comparison of the base shear versus top displacement response recorded during EQ2 and EQ4, see Figure 4.41. A peak shear of 399.3 kN (89.8 kips), or 0.16 base shear coefficient, corresponding to 57% of the one obtained in EQ2 was reached during this test. A peak displacement of 170 mm (6.71 in.), corresponding to a 2.33% drift ratio, induced in the specimen a displacement ductility demand of 1.89. A residual displacement of -59 mm (-2.33 in.), corresponding to -0.81% residual drift ratio, was essentially the same of the one accumulated after EQ3.

The positive and negative moment envelopes along the column height for EQ4 and EQ2 are plotted together in Figure 4.42. A top moment of 1457.0 kNm (1074.7 kip-ft), 3% larger than the one measured under EQ2, was reached in this test.

The average curvature at the base of the column in the negative quadrant is larger than the one obtained during EQ2, see Figure 4.43. This is principally due to the previous test's induced damages, which are identifiable by the residual West inclination of the column. The column oscillated around the inclined configuration during this test.

The oscillation of the column around the inclined configuration can be observed in the two hysteretic responses already shown in Figures 4.40 and 4.41, where the EQ4 ones present a clear eccentricity due to the plastic deformations, and also in the displacement envelopes along the column height, see Figure 4.44. The displacement in the West direction is larger than the one obtained during EQ2, even if the forces generated during EQ4 are lower. A flexural-dominated behavior can be deduced from the different peak displacement components: 122 mm (4.81 in.) from flexure, 3 mm (0.11 in.) from shear, and 32 mm (1.26 in.) from fix end rotation.

A comparison of the longitudinal strain obtained during test EQ4 and EQ2 can be found in Figures 4.45 to 4.48. The recorded strains were influenced from the plastic deformation accumulated during the previous tests. Large strains can be observed in both the bars located on the East side. The average strain reached a peak value of 1.44% in tension, corresponding to 5.54·ε_y, on the South bar of the East side (Figure 4.46). Few changes can be appreciated in the average strain profile of the bars located on the West side. A peak average strain of -0.59% in compression, corresponding to 2.27·ε_y, occurred on the South bar of the West side (Figure 4.48).

A comparison of the hoop strain envelopes obtained during test EQ4 and EQ2 can be found in Figures 4.49 to 4.50. An essentially identical strain envelope for both the earthquakes can be seen on the East side. Smaller strains can be found in the first and the second hoop above the column-footing interface on the West side. A peak strain of 0.16% in tension, corresponding to 0.69·ε_{yh}, was recorded on the second hoop of the West side.

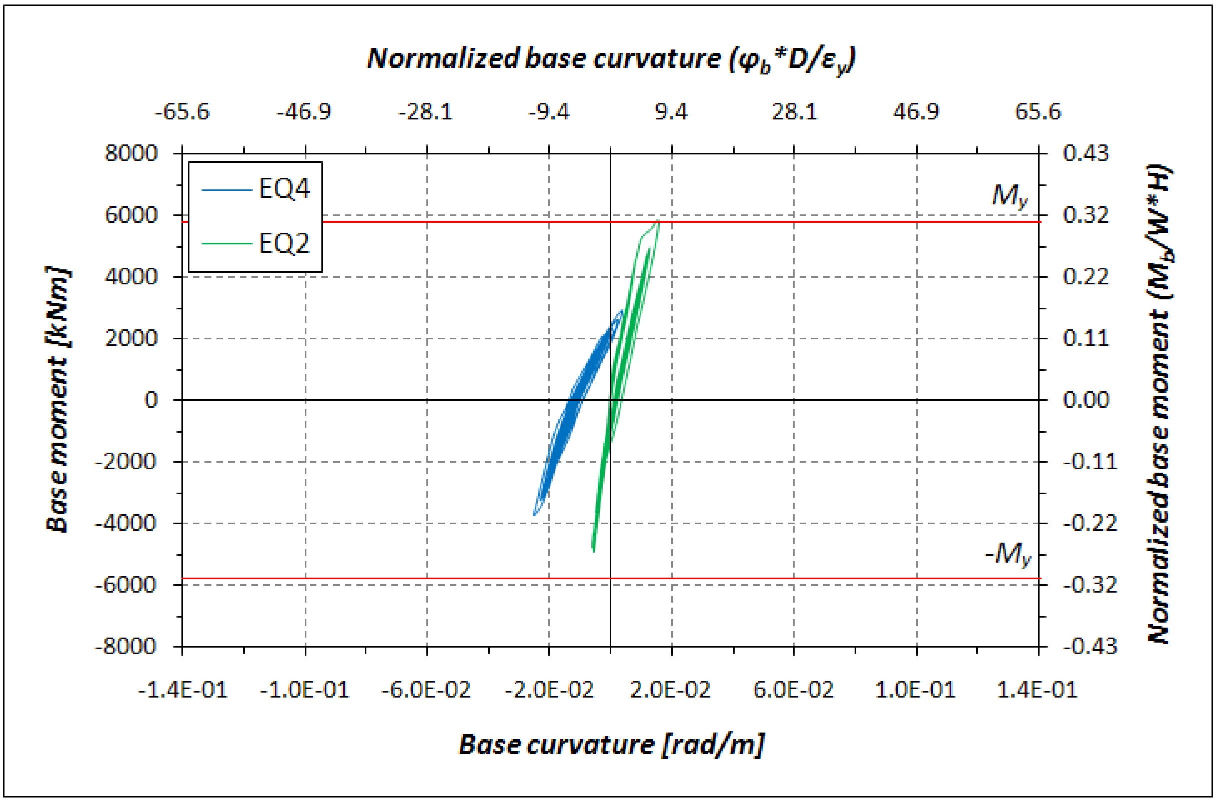

Figure 4.40: Base moment-base curvature response for EQ4 and EQ2

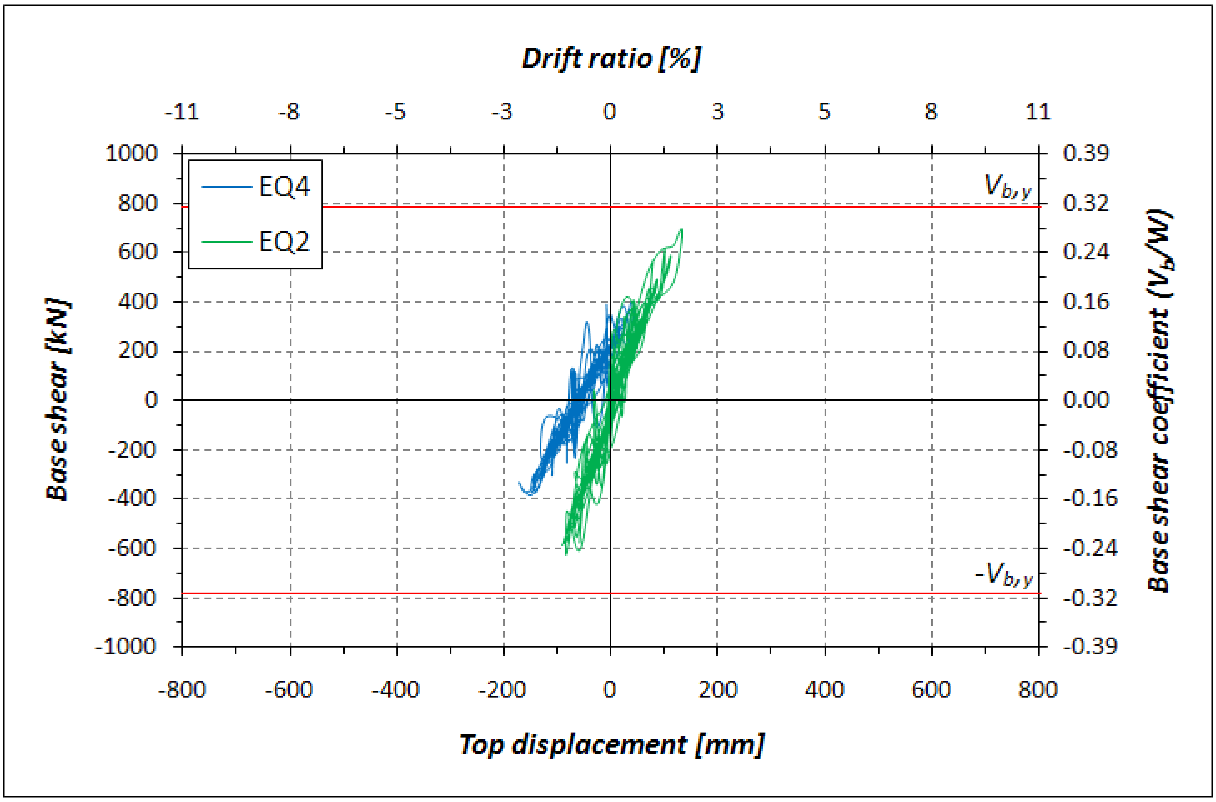

Figure 4.41 Base shear-top displacement response for EQ4 and EQ2

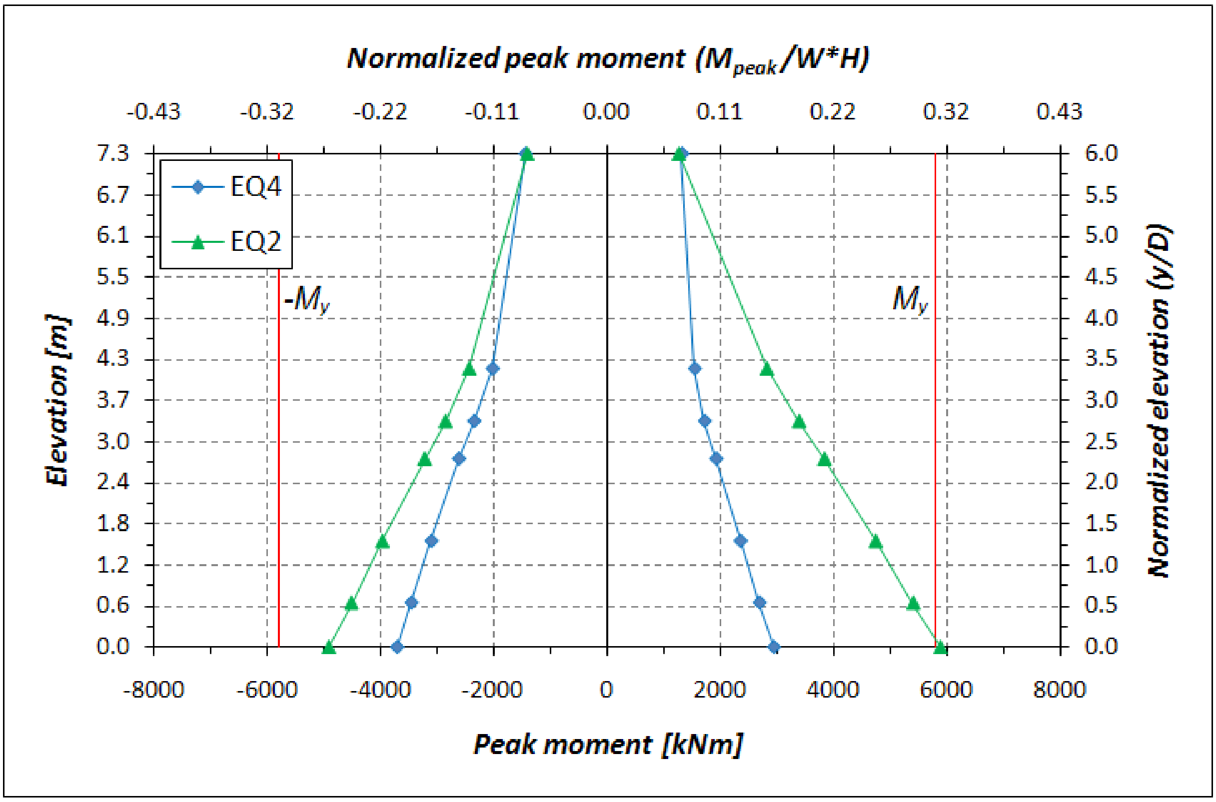

Figure 4.42: Moment envelops along the column height for EQ4 and EQ2

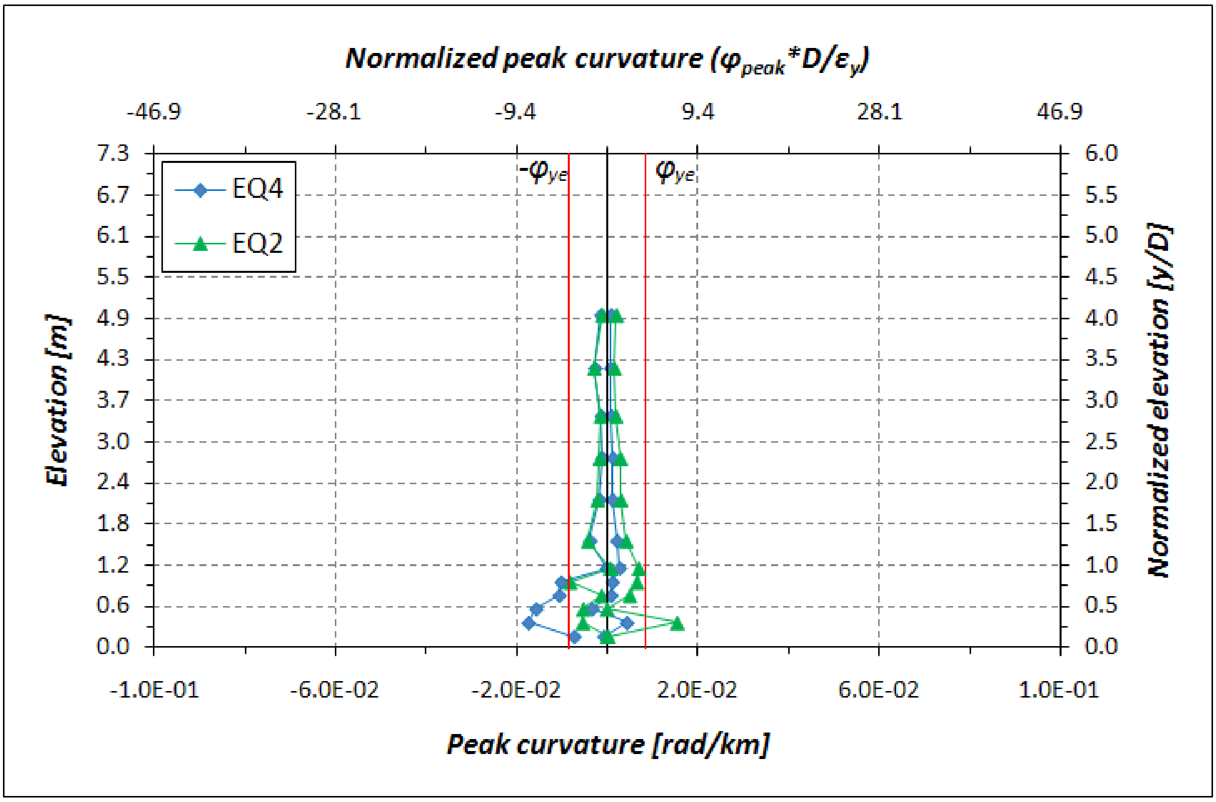

Figure 4.43: Curvature envelops along the column height for EQ4 and EQ2

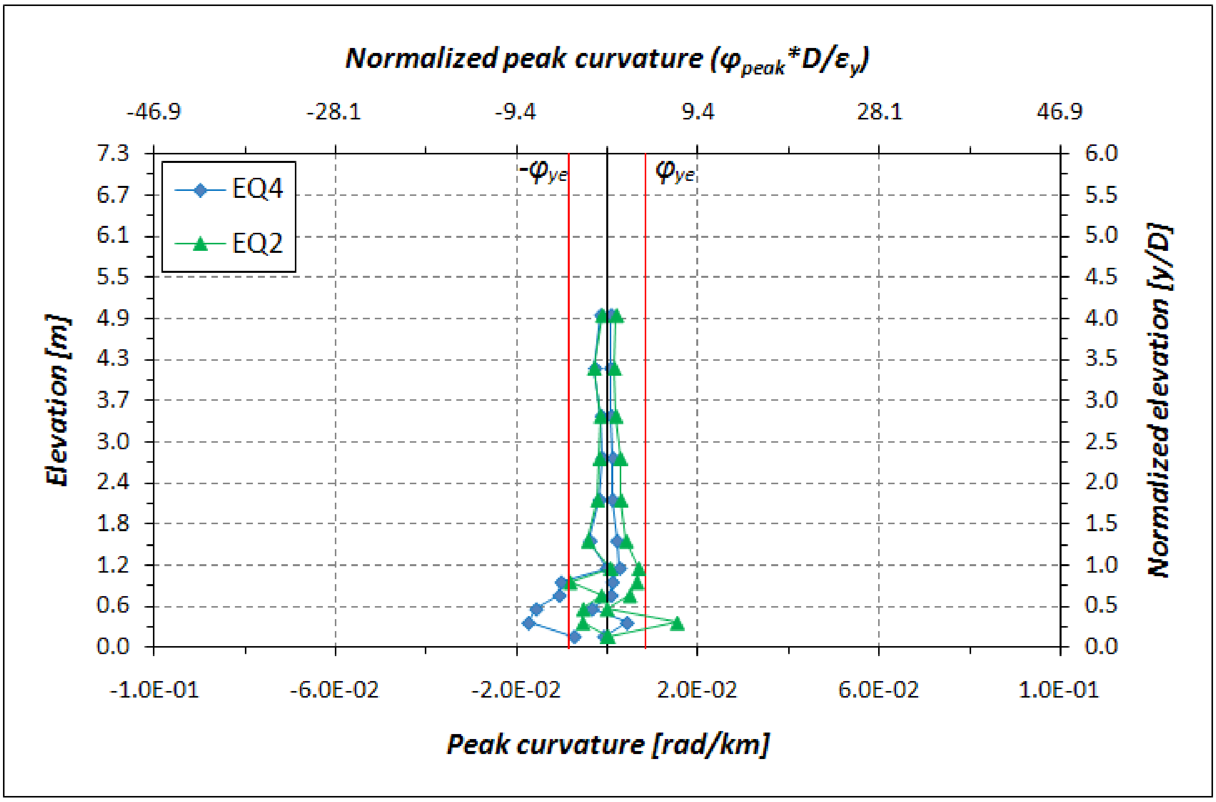

Figure 4.44: Displacement and displacement components envelops along the column height for EQ4 and EQ2

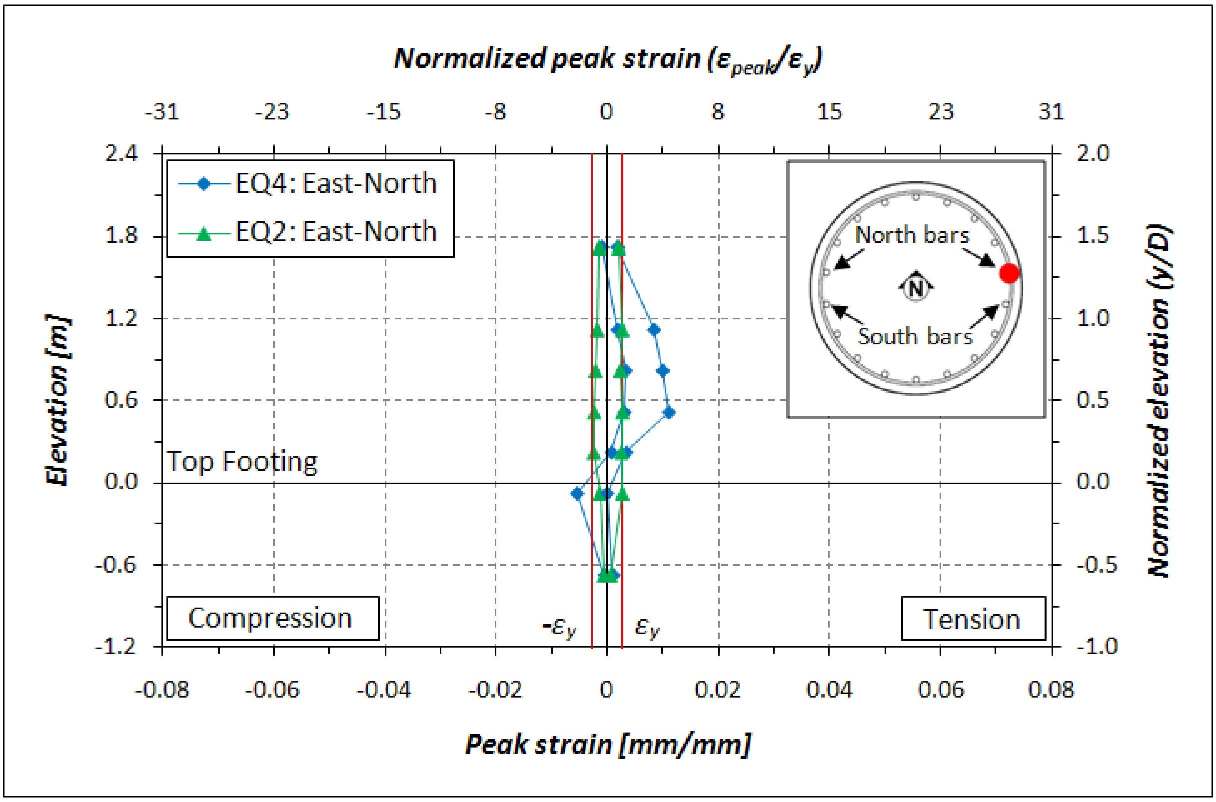

Figure 4.45: Longitudinal bar strain profile for EQ4 and EQ2: East side North bar

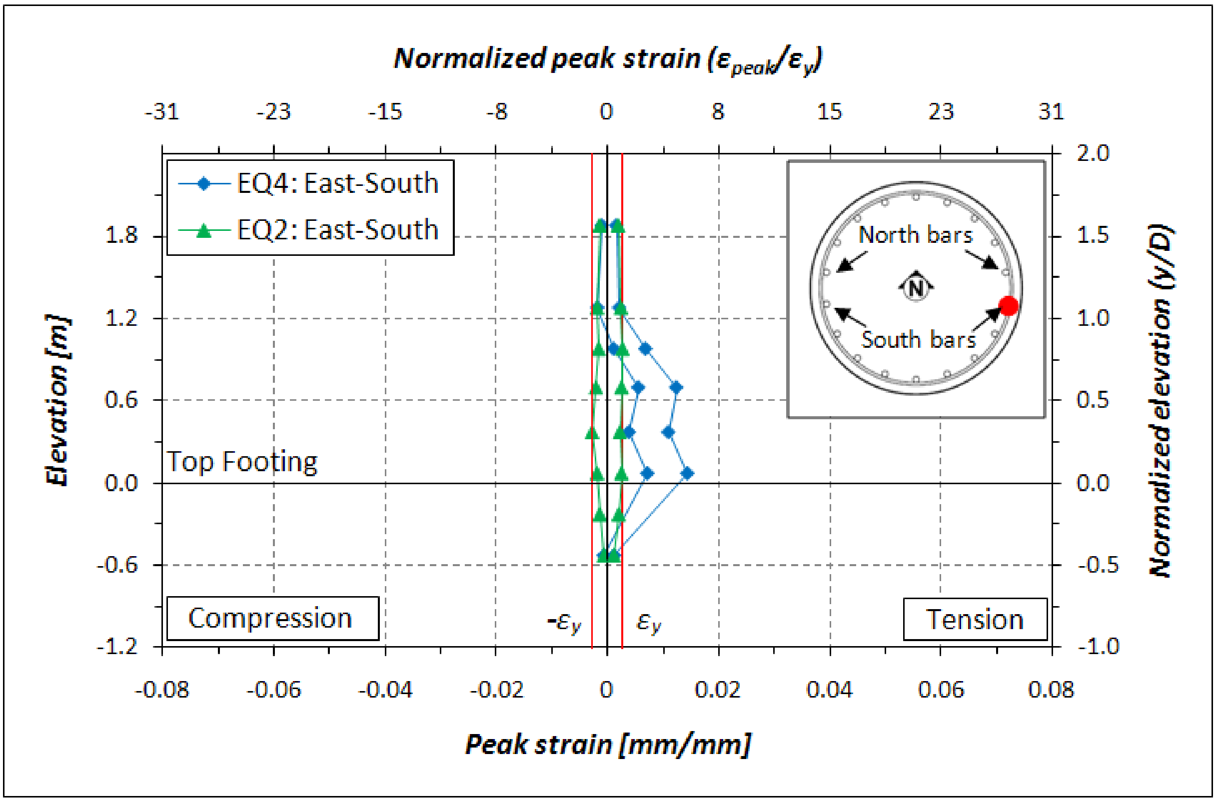

Figure 4.46: Longitudinal bar strain profile for EQ4 and EQ2: East side South bar

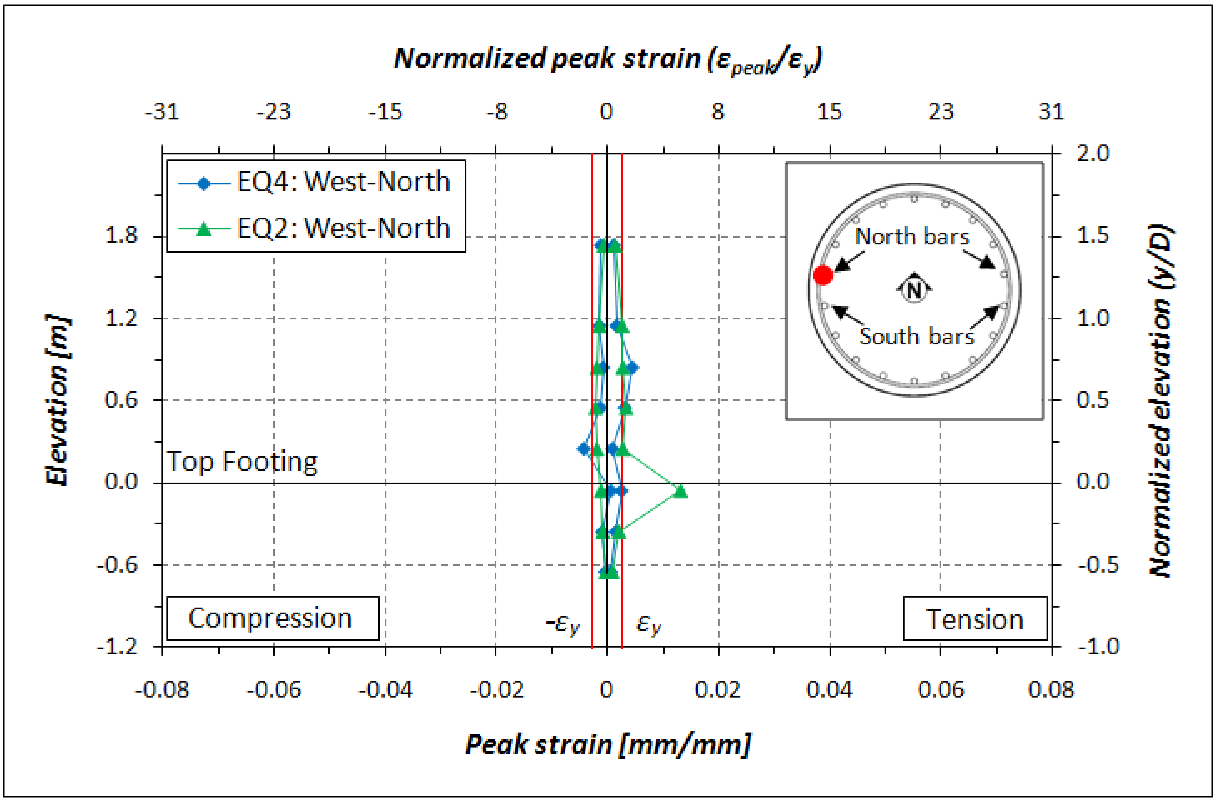

Figure 4.47: Longitudinal bar strain profile for EQ4 and EQ2: West side North bar

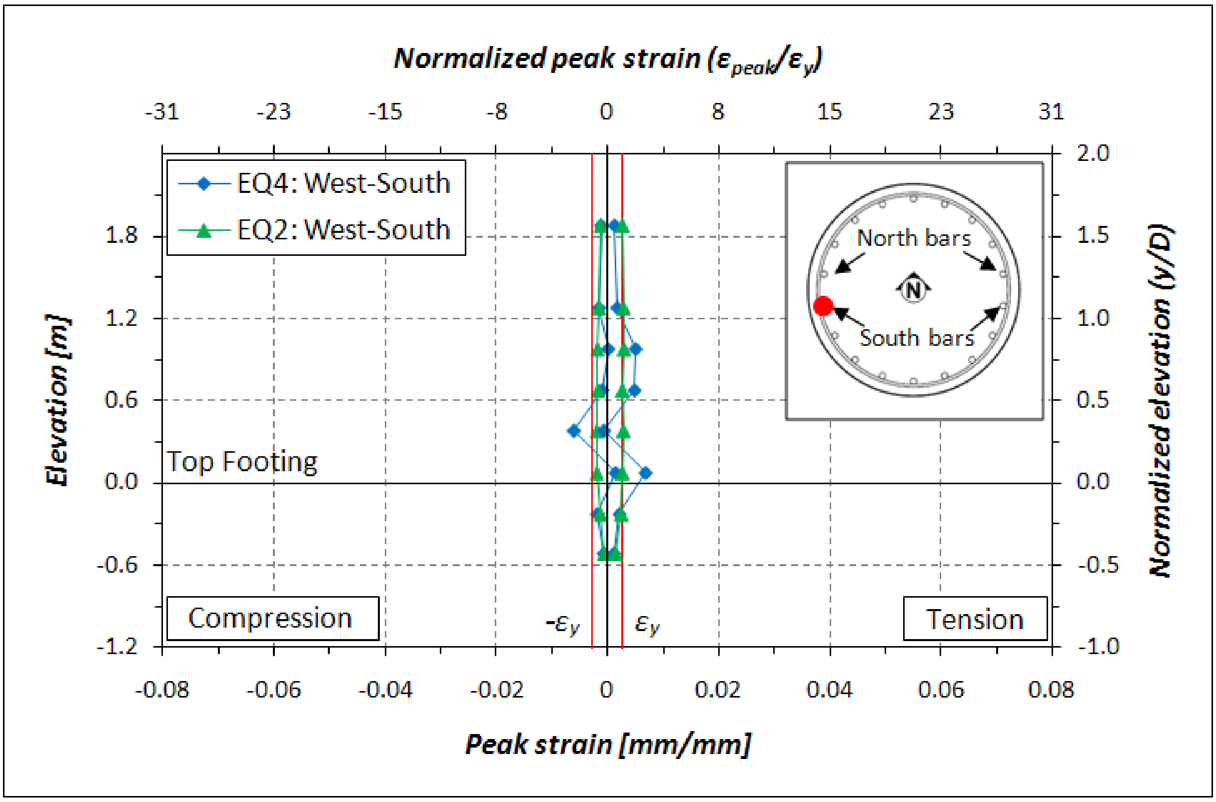

Figure 4.48: Longitudinal bar strain profile for EQ4 and EQ2: West side South bar

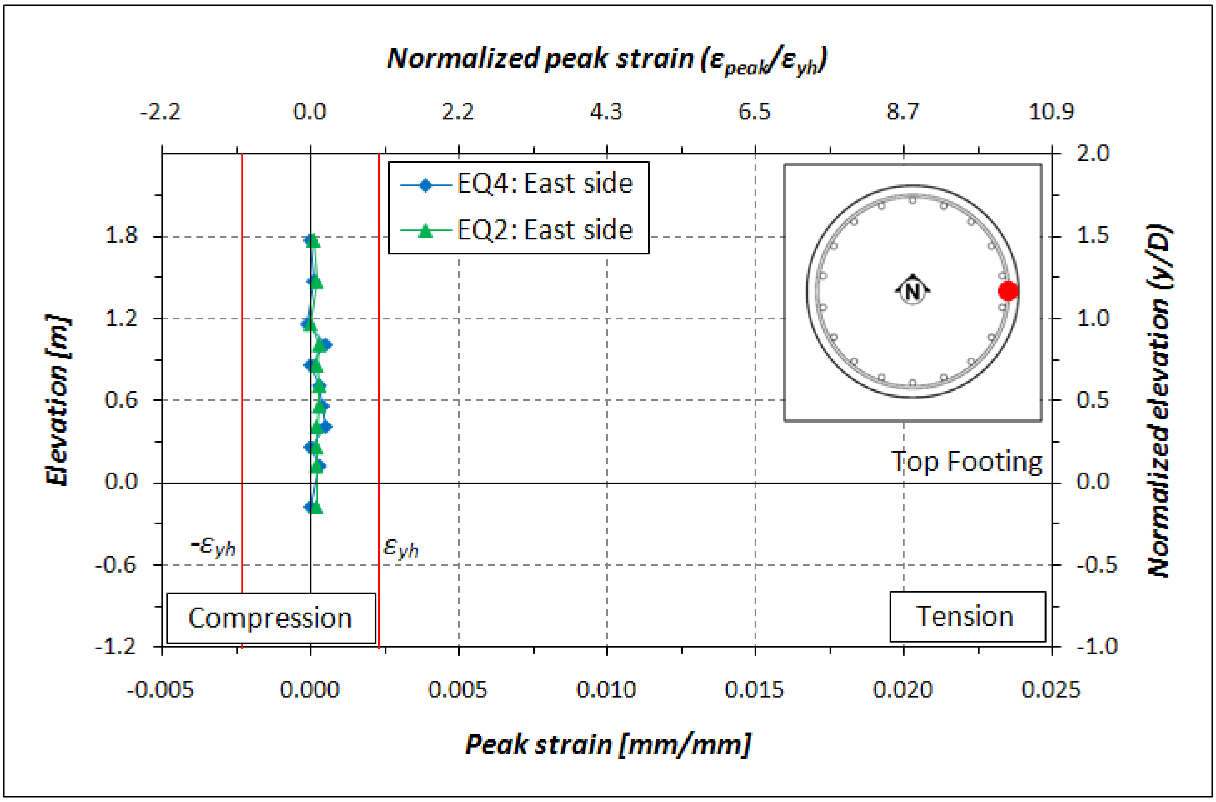

Figure 4.49: Hoops strain profile for EQ4 and EQ2: East side

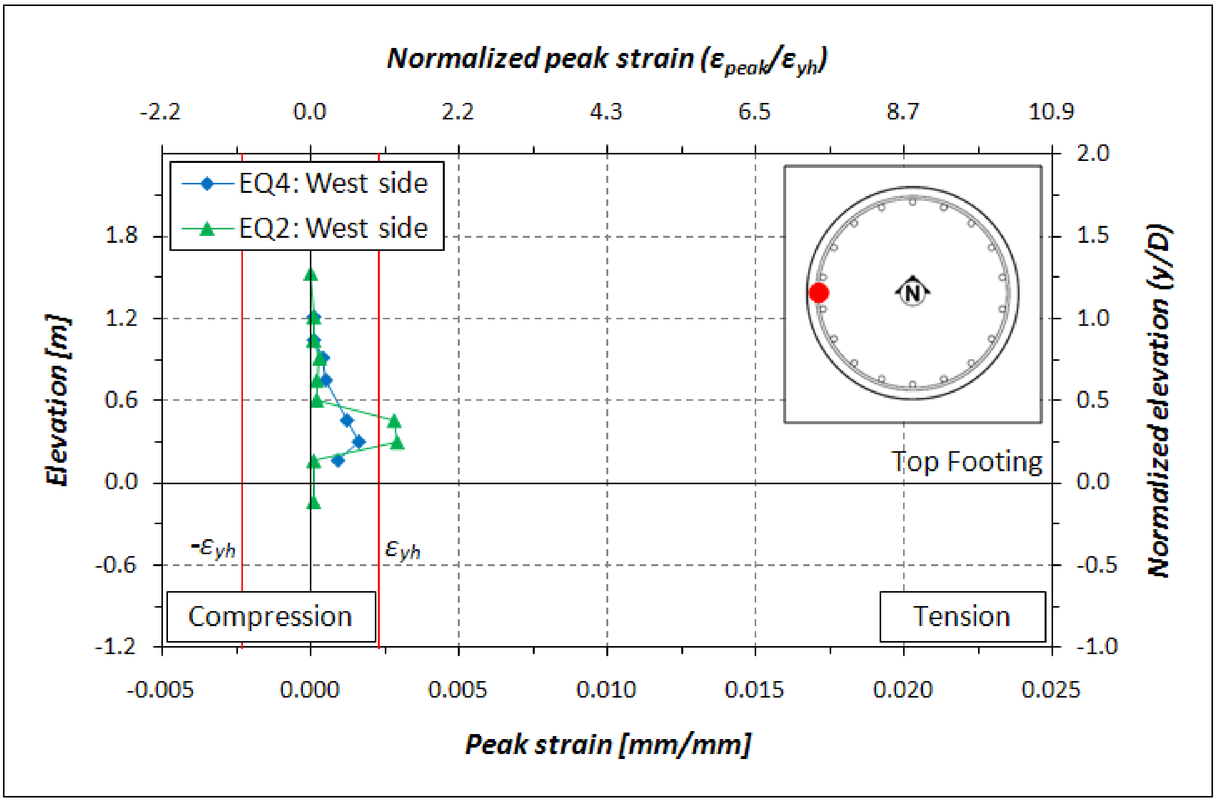

Figure 4.50: Hoops strain profile for EQ4 and EQ2: West side

4.2.5 EQ5 – Takatori 80% scaled

Takatori record 80% scaled with an inverted polarity of the original ground motion was reproduced as EQ5. The objective of this test was to induced in the specimen a very large nonlinear demand, identifiable with an expected displacement ductility of 8.0.

More than 51-mm (2-in.) deep concrete spalling was observed on both the East and West side of the column. The spalling area laterally increased at the West side conserving the same maximum height of 1.143 m (3.75 ft) obtained at the end of EQ3. The spalling started to enter the confined concrete making visible many hoops and some longitudinal bars, which did not show buckling on this side.

Spalling with similar features was identified on the East side of the column. The maximum spalling height was smaller than the one observed on the West side, and equal to 762 mm (30 in.). Onset of longitudinal bar buckling was observed on this side. At least two of the visible bars were barely bent between the first and the third hoops above the column-footing interface. An appreciable deformation of the second and the third hoop above the column-footing interface was observed.

New horizontal, vertical and diagonal cracks was principally observed on the column base. The existing cracks increased their length, but their residual width was not much affected as this was generally less than 1 mm (0.04 in.). However, thicker cracks can be identified in the spalled area with a residual thickness of about 2 mm (0.08 in.). The pre-existing flexural cracks located on both the East and the West side along the entire column height increased their length wrapping around the column and new horizontal cracks opened between them. A post-test view of the East face of the column base is shown in Figure 4.51.

A ductile response and relative stable hysteresis loops can be observed in the base moment versus base curvature relationship, see Figure 4.52. Large hysteresis loops indicate significant energy dissipation during this test. The analytical idealized yield moment M_y is reached in the positive quadrant: previous tests generated a degradation of stiffness but not a degradation of moment carrying capacity. A peak moment of 7214.6 kNm (5321.2 kip-ft), corresponding to $1.25 \cdot M_y$ and a peak curvature of $1.05 \cdot 10^{-1}$ rad/m ($2.67 \cdot 10^{-3}$ rad/in), corresponding $12.60 \cdot \varphi_{ye}$, were achieved during this test.

Large loops can be found in the base shear versus top displacement response with visible higher mode effects, see Figure 4.53. The base shear reaches again the value corresponding to analytical idealized yield, $V_{b,y}$, in the positive quadrant. This denotes that the column still preserved its force carrying capacity. A peak shear of 812.6 kN (182.7 kips), corresponding to

Figure 4.51: Column base post-EQ5

$1.04{\cdot}V_{b,y}$ and a base shear coefficient of 0.32, was reached. A peak displacement of 569 mm (22.40 in.), or a 7.78% drift ratio, corresponding to $6.33{\cdot}\Delta_{ye}$, was measured at the top of the column. The negative residual displacement accumulated during the previous tests was completely recovered and a new positive one of 104 mm (4.11 in.) or 1.43% residual drift ratio remained after test.

A top moment of 1220.1 kNm (899.9 kip-ft), corresponding to 17% of the peak moment reached at the base of the column, can be identified in the positive moment envelope along the column height, see Figure 4.54.

Significant values of average curvature lumped at the column base denote a concentration of damage in this location, see Figure 4.55. The flexural rotation along the column height started to be less significant than the one recorded at the column base.

The positive and negative envelopes of the relative displacement between column and table (solid line) and the post-test residual configuration (dashed line) are shown Figure 4.56. The deformed configuration of the column was essentially due to a flexure rotation lumped at the column base; the displacement envelopes vary nearly linear from about one column diameter above the footing to the column top. A flexural-dominated behavior can be deduced from the different peak displacement components: 416 mm (16.36 in.) from flexure, 31 mm (2.21 in.) from shear, and 82 mm (3.24 in.) from fix end rotation.

The strain envelopes along the instrumented longitudinal bars are plotted in Figures 4.57 to 4.60. All the four monitored bars showed a large post-elastic elongation. In particular, the South bar of the West side was stretched until a peck strain of 4.66%, corresponding to 17.92$\cdot\varepsilon_y$ (Figure 4.60). Large compressive strains were recorded with the strain gauges installed on the East side bars, proving the observed onset of buckling of some longitudinal bars. The average strain reached a peak value of -1.55% in compression, corresponding to 5.96$\cdot\varepsilon_y$, on the North bar of the East side, (Figure 4.57). A similar strain in compression of 1.50%, corresponding to 5.77$\cdot\varepsilon_y$, was recorded on the South bar of the same side (Figure 4.58).

Two large peaks can be identified in the hoop strain profiles, see Figure 4.61 and 4.62. The third hoop above the column-footing interface showed on the East side a peak strain in tension of 0.81%, corresponding to 3.52$\cdot\varepsilon_{yh}$. The second hoop above the column-footing interface showed a very large peak strain on the West side due to a probable longitudinal bars buckling, which were hidden by the loose concrete cover. A peak strain of 2.46%, corresponding to 10.5$\cdot\varepsilon_{yh}$, was recorded.

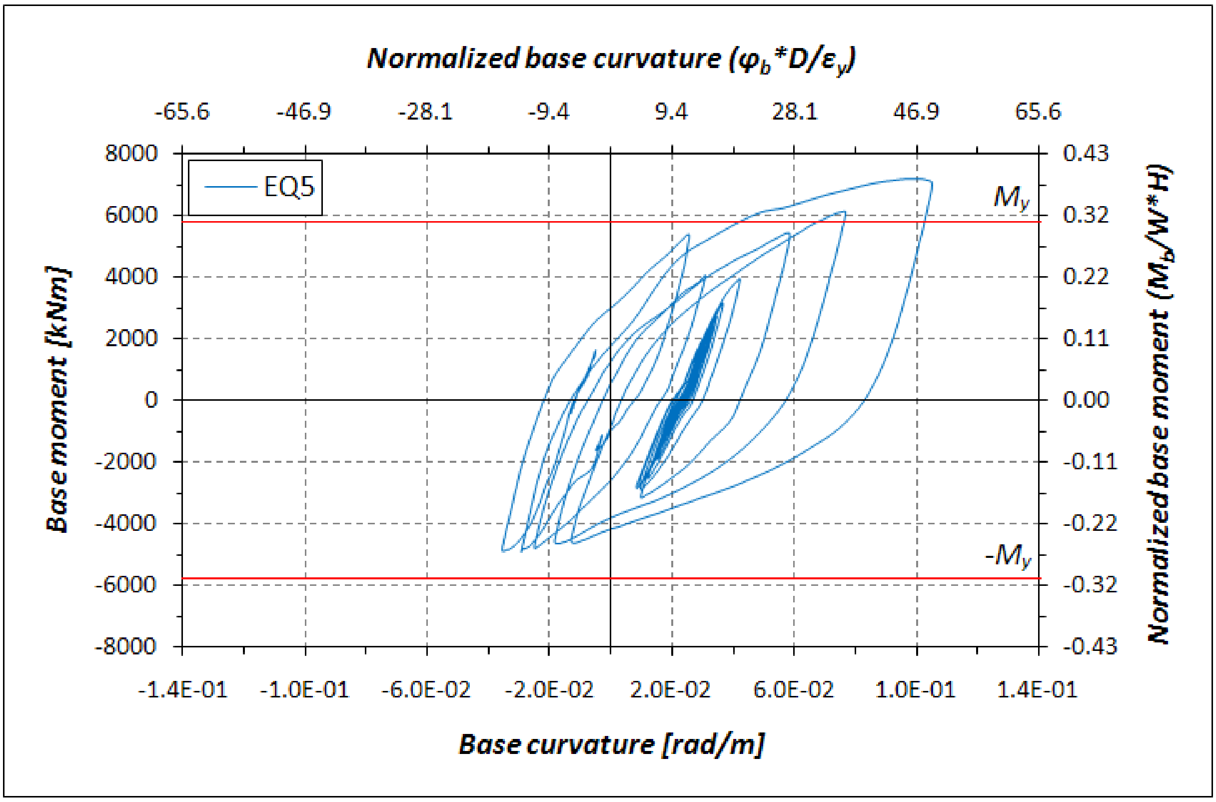

Figure 4.52: Base moment-base curvature response for EQ5

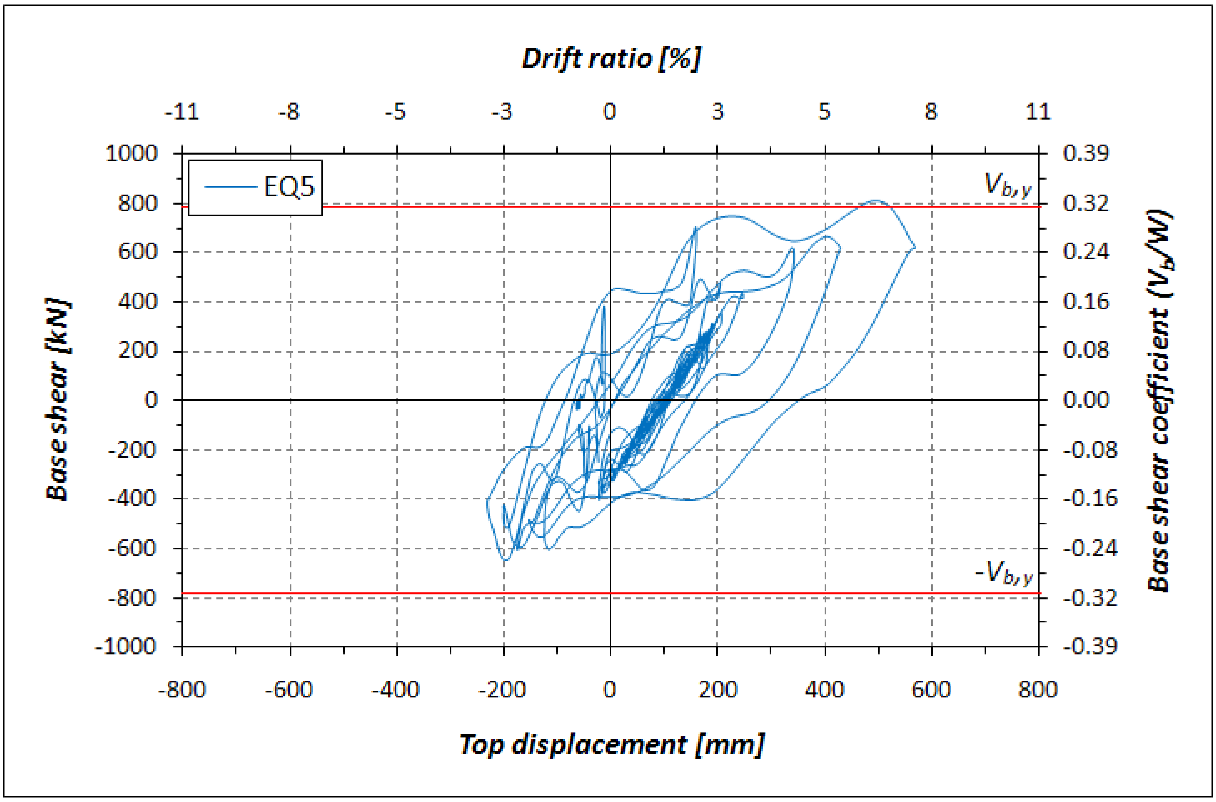

Figure 4.53 Base shear-top displacement response for EQ5

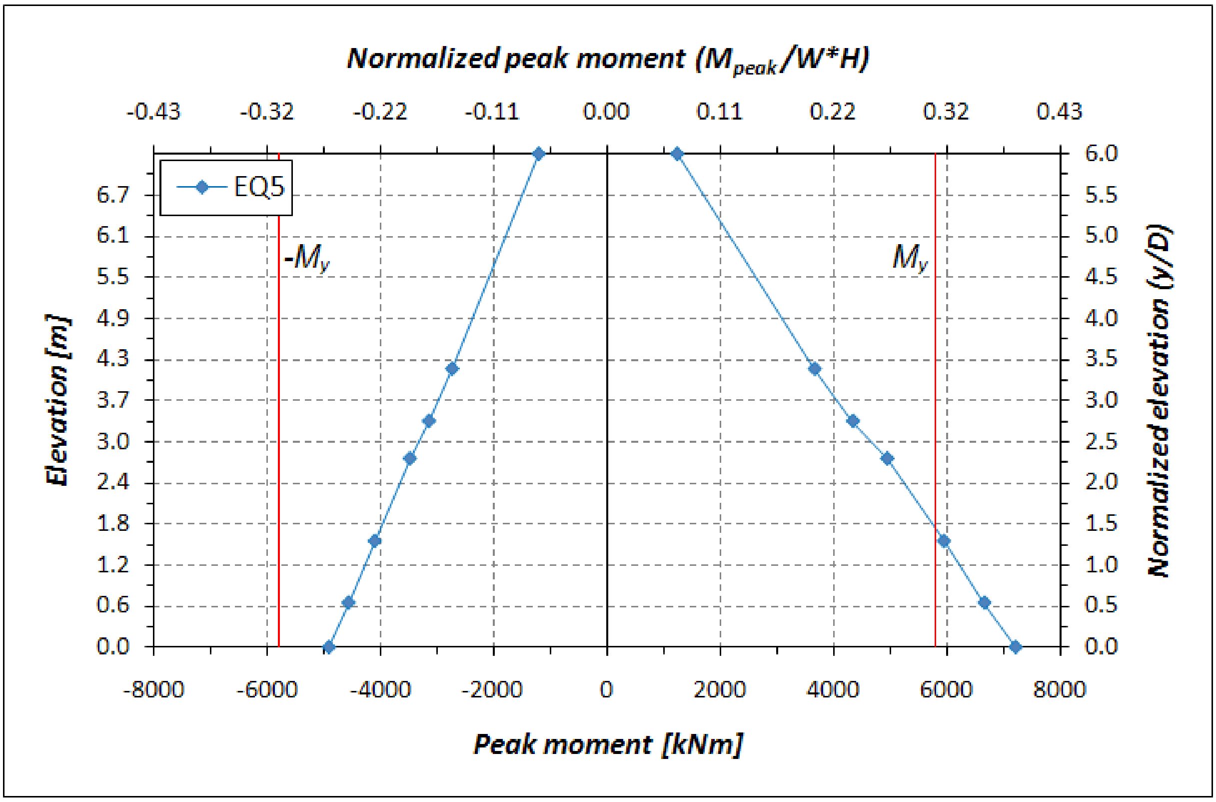

Figure 4.54: Moment envelops along the column height for EQ5

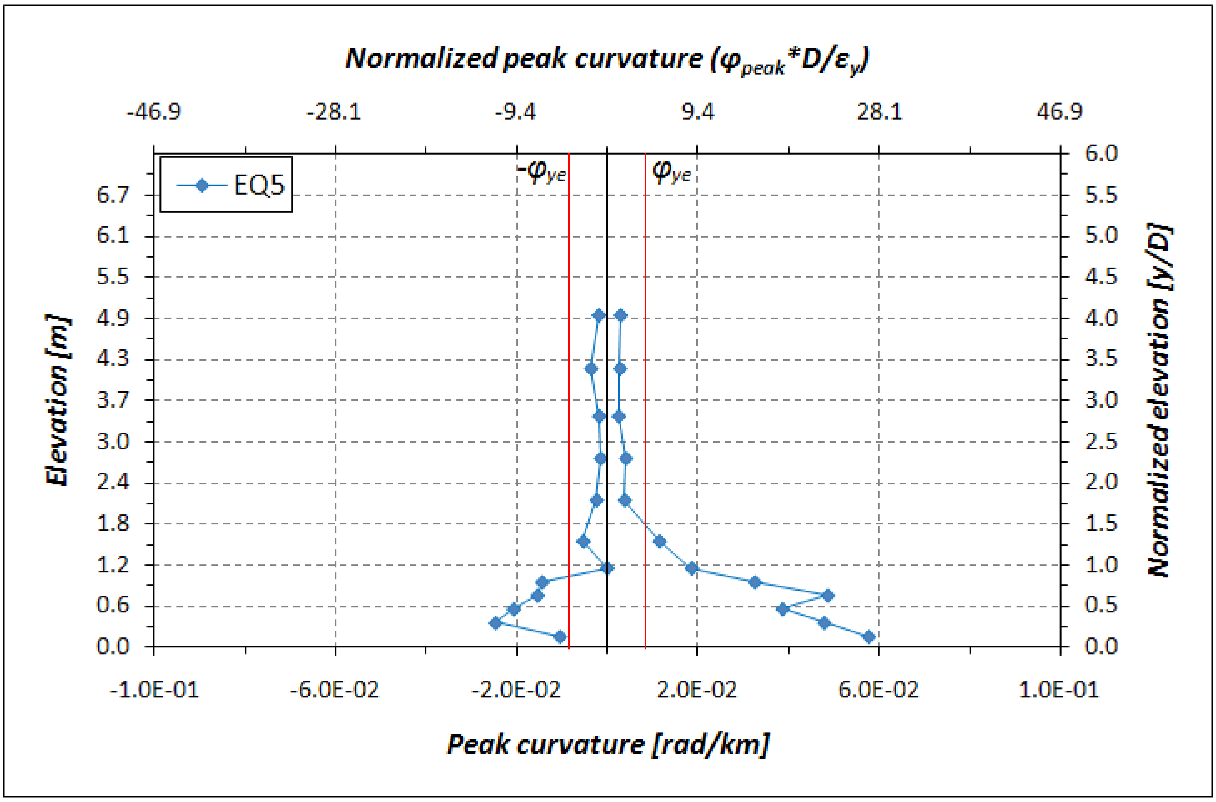

Figure 4.55: Curvature envelops along the column height for EQ5

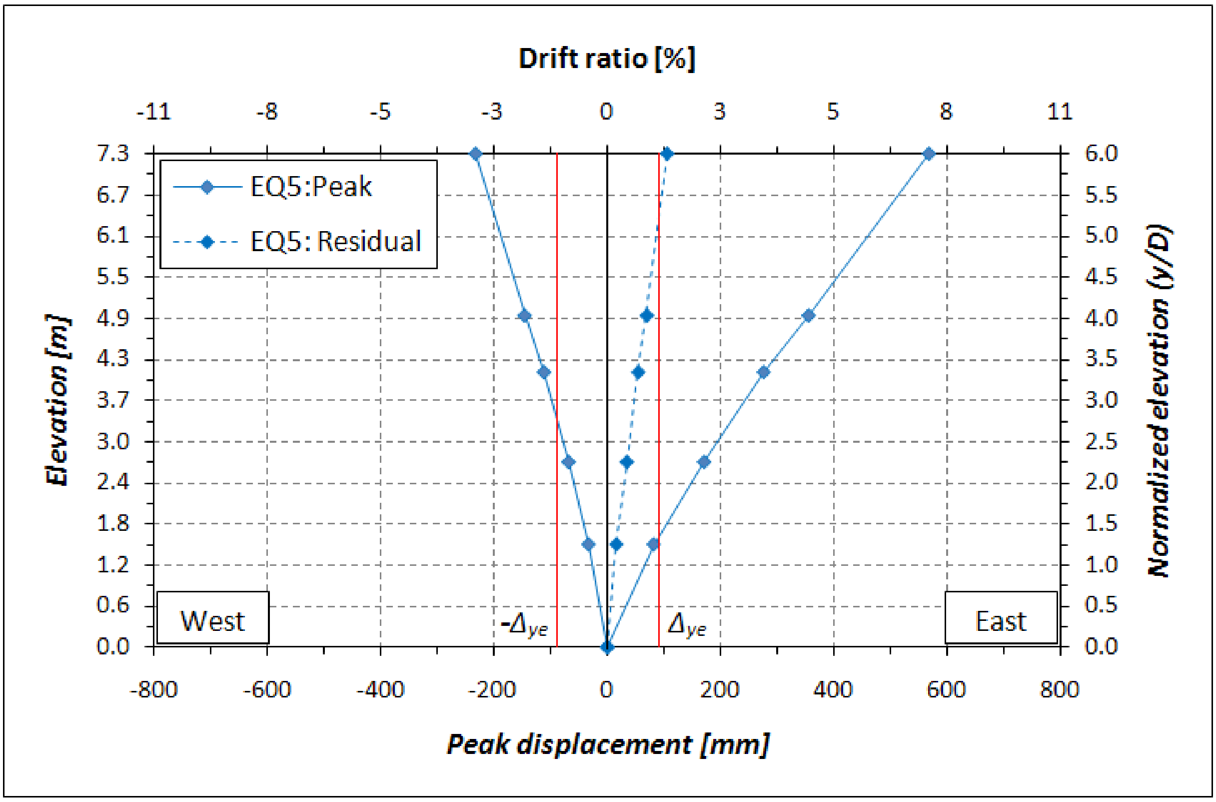

Figure 4.56: Displacement and displacement components envelops along the column height for EQ5

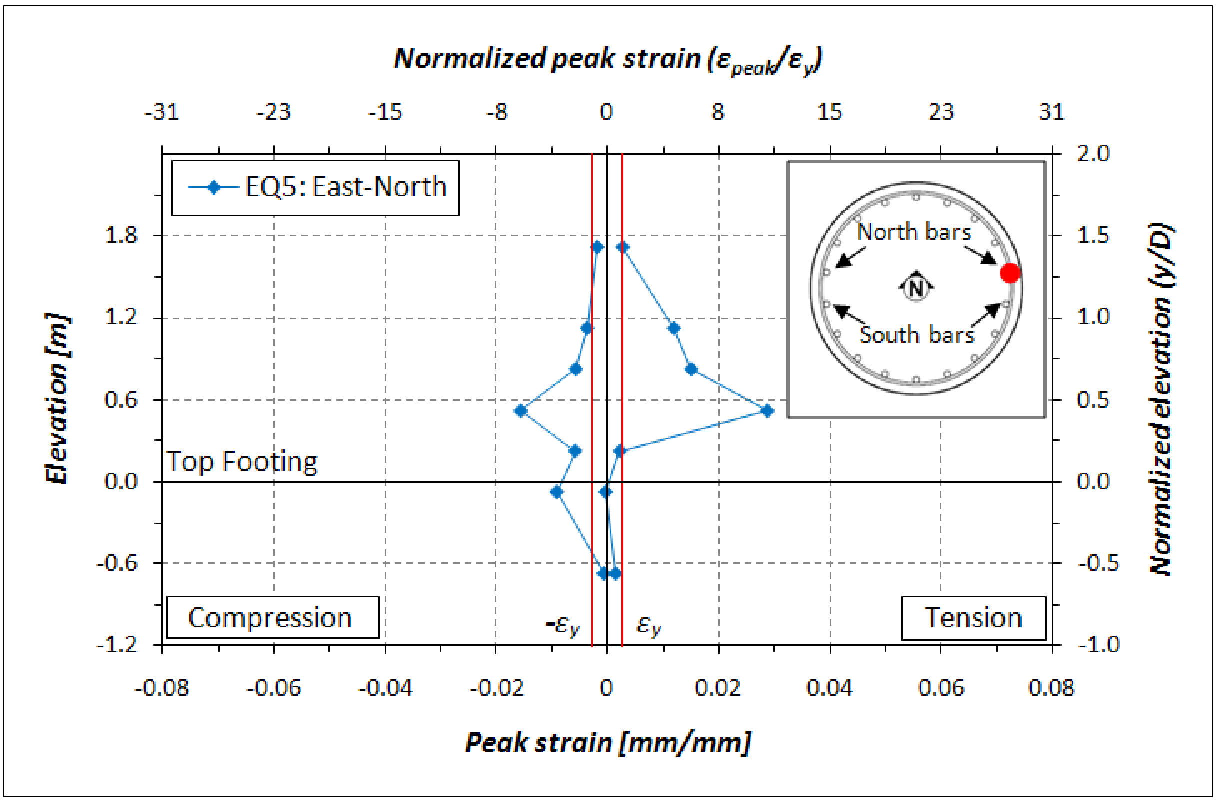

Figure 4.57: Longitudinal bar strain profile for EQ5: East side North bar

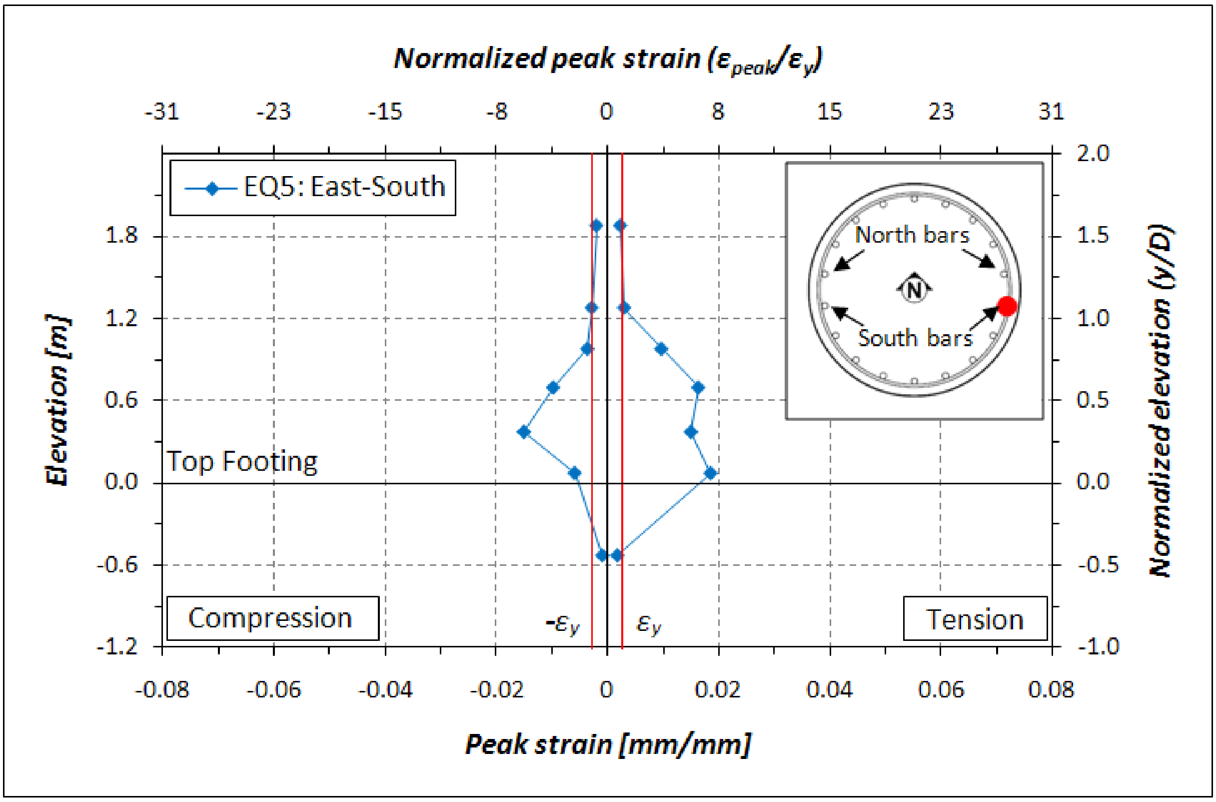

Figure 4.58: Longitudinal bar strain profile for EQ5: East side South bar

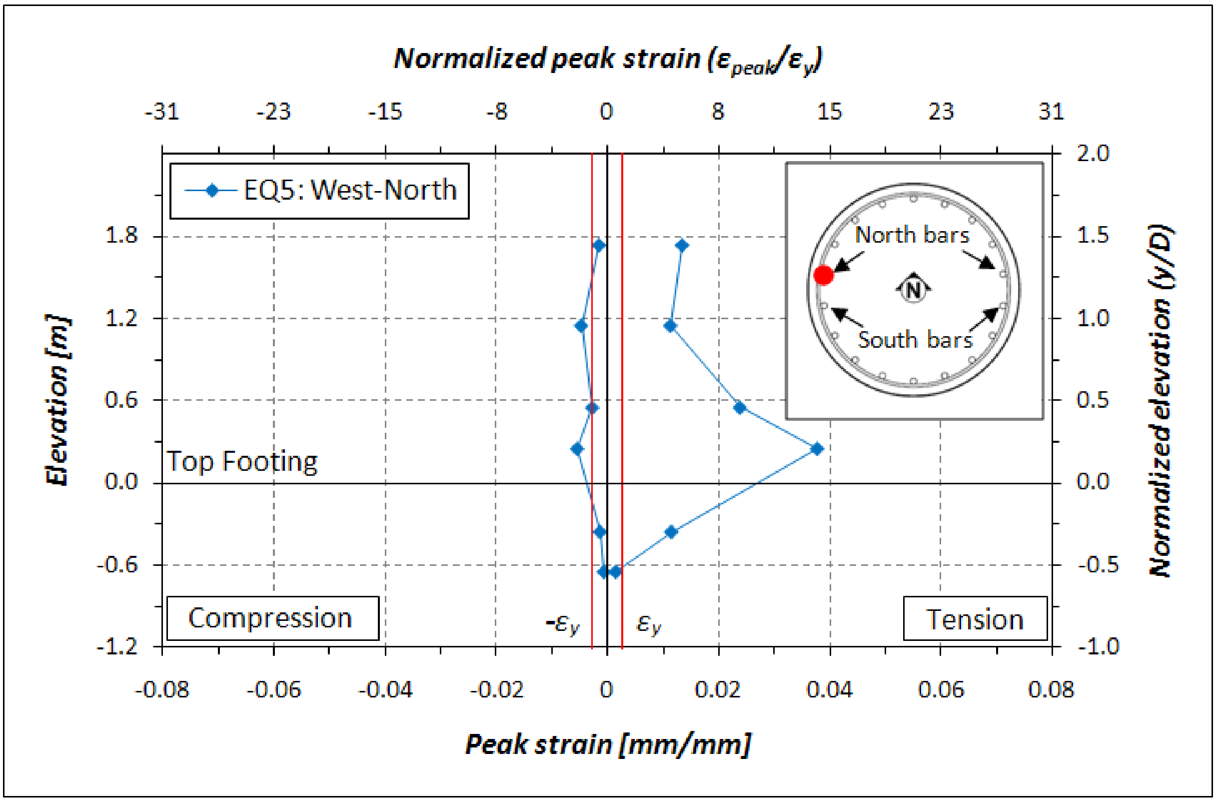

Figure 4.59: Longitudinal bar strain profile for EQ5: West side North bar

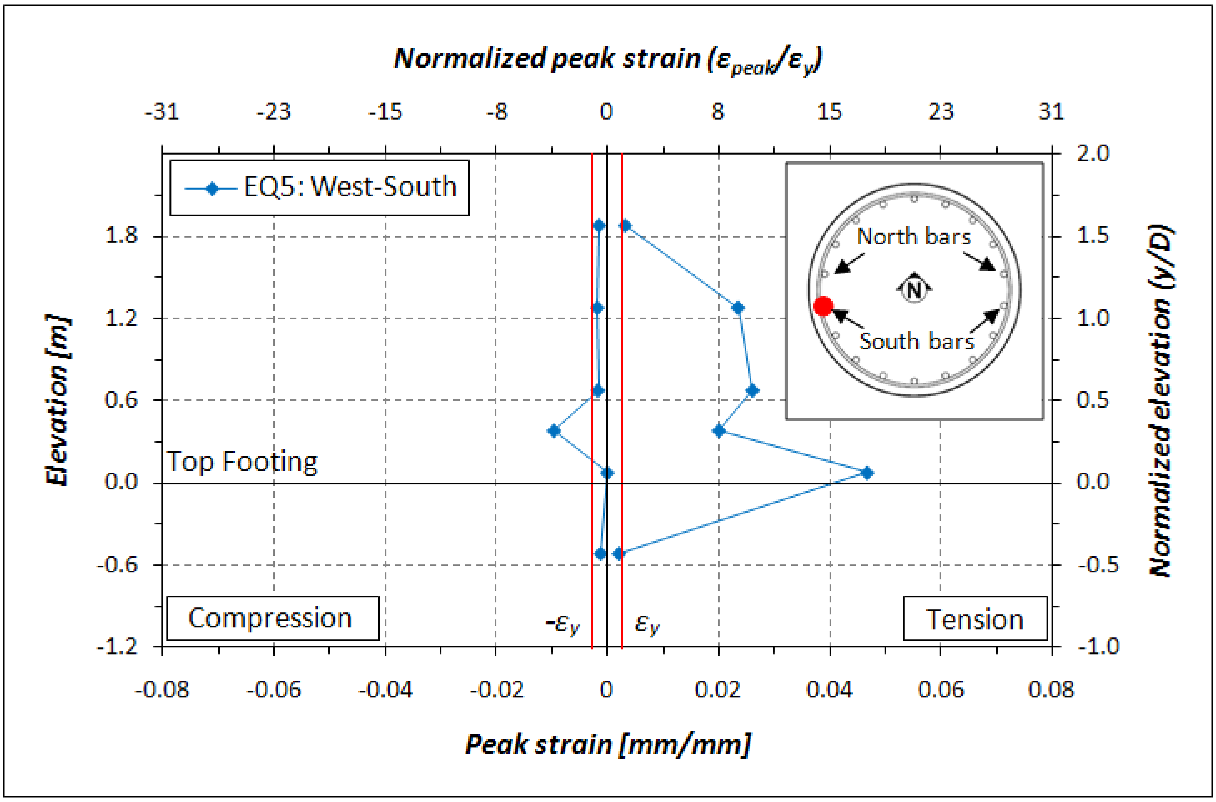

Figure 4.60: Longitudinal bar strain profile for EQ5: West side South bar

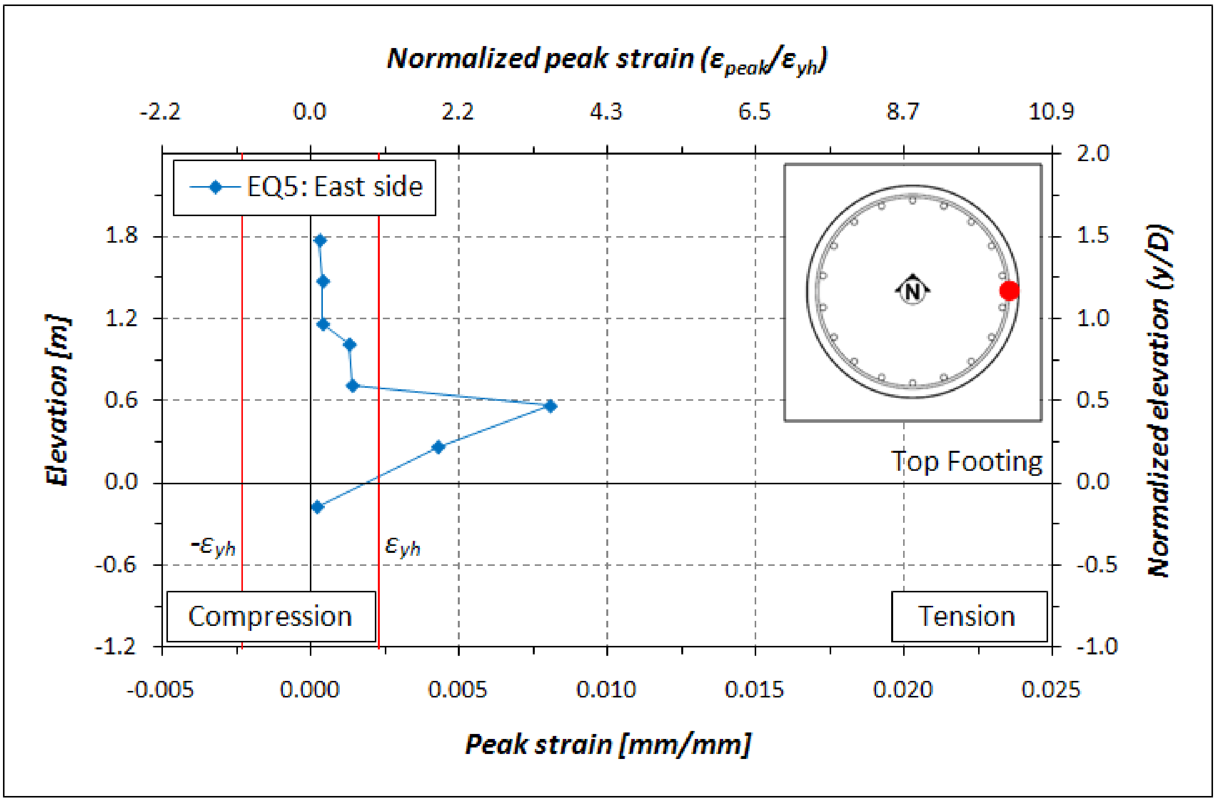

Figure 4.61: Hoops strain profile for EQ5: East side

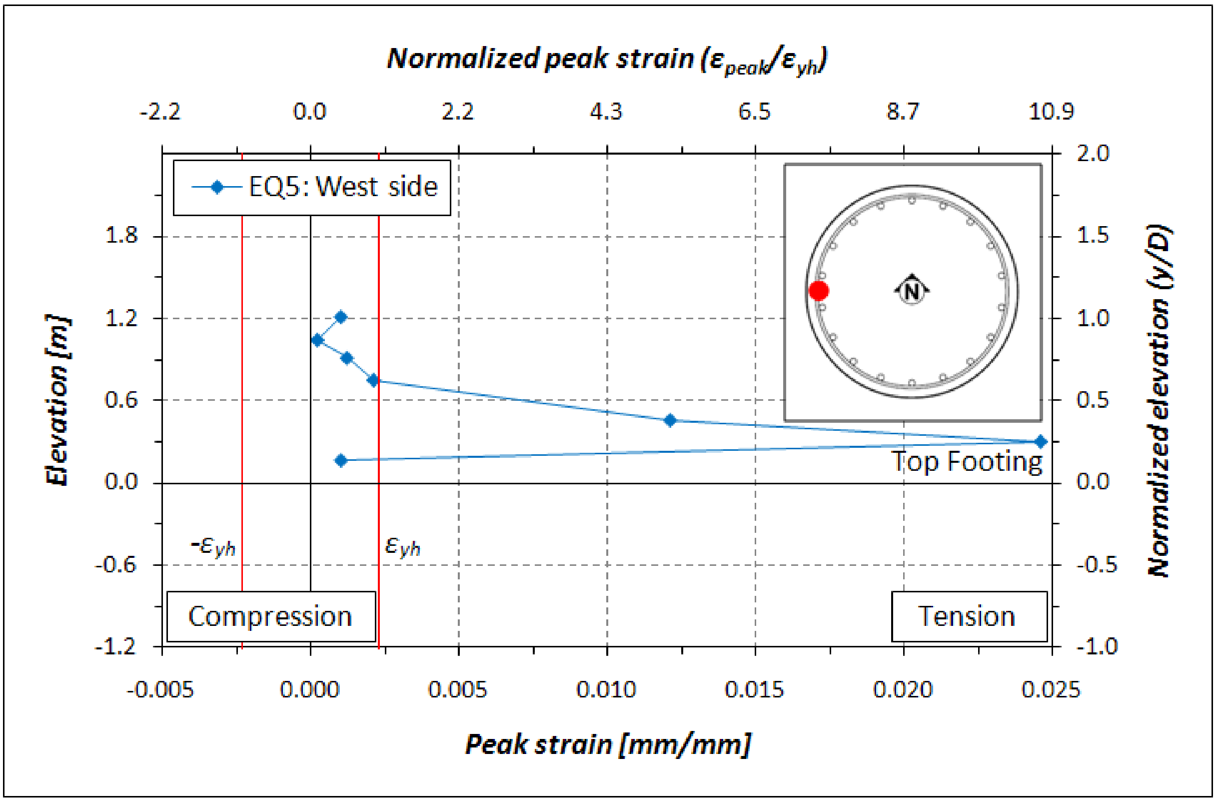

Figure 4.62: Hoops strain profile for EQ5: West side

4.2.6 EQ6 – Los Gatos Presentation Center

The design level earthquake was repeated as EQ6 to simulate an aftershock of Takatori 80% scaled (EQ5). As already done for EQ2 and EQ4, the results of EQ6 will be compared with the EQ3 ones to highlight the differences in the response of the structure before and after the induced damages from the previous earthquakes.

No significant damage was induced in the specimen during this test. Concrete spalling was visible, but did not extend beyond the damage occurred in EQ5. Removal of lose spalled concrete occurred between EQ5 and EQ6. For this reason, apparent difference can be observed in the two post-test views of the East face of the column base, compare Figure 4.51 and Figure 4.63. The column essentially conserved the same extent of spalling and cracks occurred during the previous test.

Test EQ6 was the last intended earthquake simulation in the test protocol. However, damage to this point was limited to concrete spalling and a local onset of longitudinal bar buckling. This provided the opportunity to extended the scope of testing, adding ground motions to the loading protocol.

The base moment versus base curvature response of the column during EQ6 is plotted together with the one obtained during EQ3 in Figure 4.64. Similar moment-curvature

Figure 4.63: Column base post-EQ6

relationships with stable hysteretic loops can be observed in this plot. Relevant stiffness but not strength degradation occurred between these two tests. A peak moment of 6505.5 kNm (4798.2 kip-ft) can be identified in the positive quadrant. Its value is nearly the same as the one measured during EQ3 in the opposite bending direction. Very large hysteresis loops demonstrate considerable energy dissipation under EQ6. Principally due to a residual curvature accumulated during the previous tests, a peak curvature 51% larger than the one obtained in EQ3 was reached during EQ6. A value of $9.16 \cdot 10^{-2}$ rad/m ($2.33 \cdot 10^{-3}$ rad/in) induced in the specimen a curvature ductility of 10.96.

Even if local onset of longitudinal bar bucking was observed in the previous test, the column globally preserved its force carrying capacity. This can be deduced by observing the base shear versus top displacement response shown in Figure 4.65. The base shear increased again until the value corresponding to analytical idealized yield, $V_{b,y}$, in both the positive and negative quadrant. A peak shear of 766.1 kN (172.2 kips), corresponding to a base shear coefficient of 0.30, was reached during this test. This value is 14% less than the one obtained in test EQ3. A peak displacement of 490 mm (19.28 in.), corresponding to a 6.69% drift ratio, was induced in the specimen. When normalized, this is a displacement ductility demand of 5.44. A residual displacement of 50 mm (1.97 in.), corresponding to 0.68% residual drift ratio, was measured at the end of this test.

The positive and negative moment envelopes along the column height for EQ6 and EQ3 are plotted together in Figure 4.42. A top moment of 1798.1 kNm (1326.2 kip-ft), 18% larger than the one measured under EQ3, was reached in this test.

The average curvature at the base of the column in the positive bending direction was larger than the one obtained during EQ3, see Figure 4.67. This is principally due to the previous test, which induced in the specimen a relevant positive residual displacement, identifiable with a residual East inclination of the column. Significant values of curvature lumped at the base demonstrate the presence of a plastic region extending about one column diameter above the column-footing interface.

The residual deformation due to this test can be observed in the two hysteretic responses already shown in Figures 4.64 and 4.65, where the EQ6 ones present a clear eccentricity due to the plastic deformations, and also in the displacement envelopes along the column height, see Figure 4.68. The peak displacements in the East direction recorded during EQ6 are much larger than the ones obtained in EQ3. A substantially rigid rotation of the upper part of the column respect its base can be observed in this diagram. This observation is made by the nearly linear displacement envelopes above 20% of the column height. A flexural-dominated behavior can be deduced from the different peak displacement components: 352 mm (6.85 in.) from flexure, 20 mm (0.78 in.) from shear, and 73 mm (2.87 in.) from fix end rotation.

A comparison of the longitudinal strains obtained during test EQ6 and EQ3 can be found in Figures 4.69 to 4.72. The recorded strains were influenced from the plastic deformation accumulated during the previous tests. Larger strains were recorded in all the monitored bars during this test. The average strain reached a peak value of 4.23% in tension, corresponding to 16.27·ε_y, on the South bar of the West side (Figure 4.72). A peak strain of -1.63% in compression, corresponding to 5.96·ε_y, occurred on the South bar of the East side (Figure 4.70).

Two large peaks in tension can be identified in the hoop strain profiles, see Figures 4.73 and 4.74. The third hoop above column-footing interface presented on the East side a peak strain of 0.81% in tension, corresponding to 3.52·ε_{yh}. The second hoop above the column-footing interface showed a peak strain in tension of 1.03% on the West side, corresponding to 4.48·ε_{yh}.

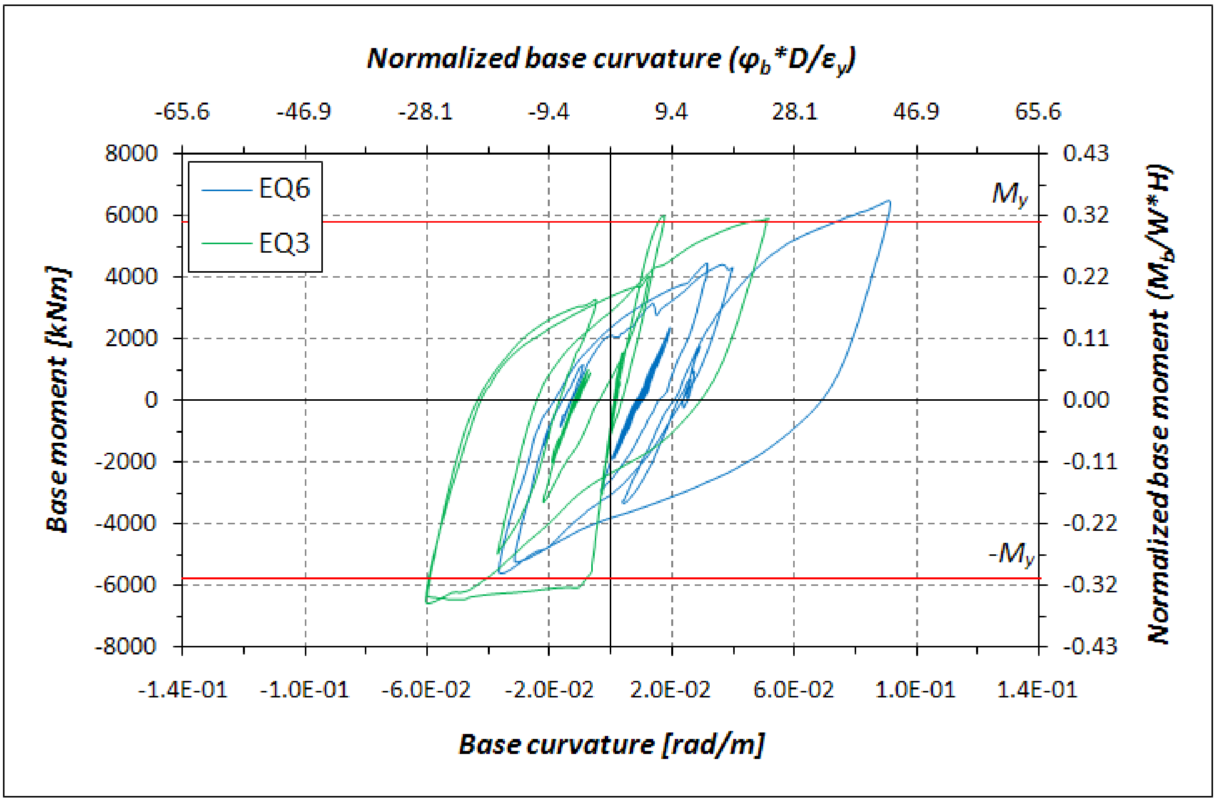

Figure 4.64: Base moment-base curvature response for EQ6 and EQ3

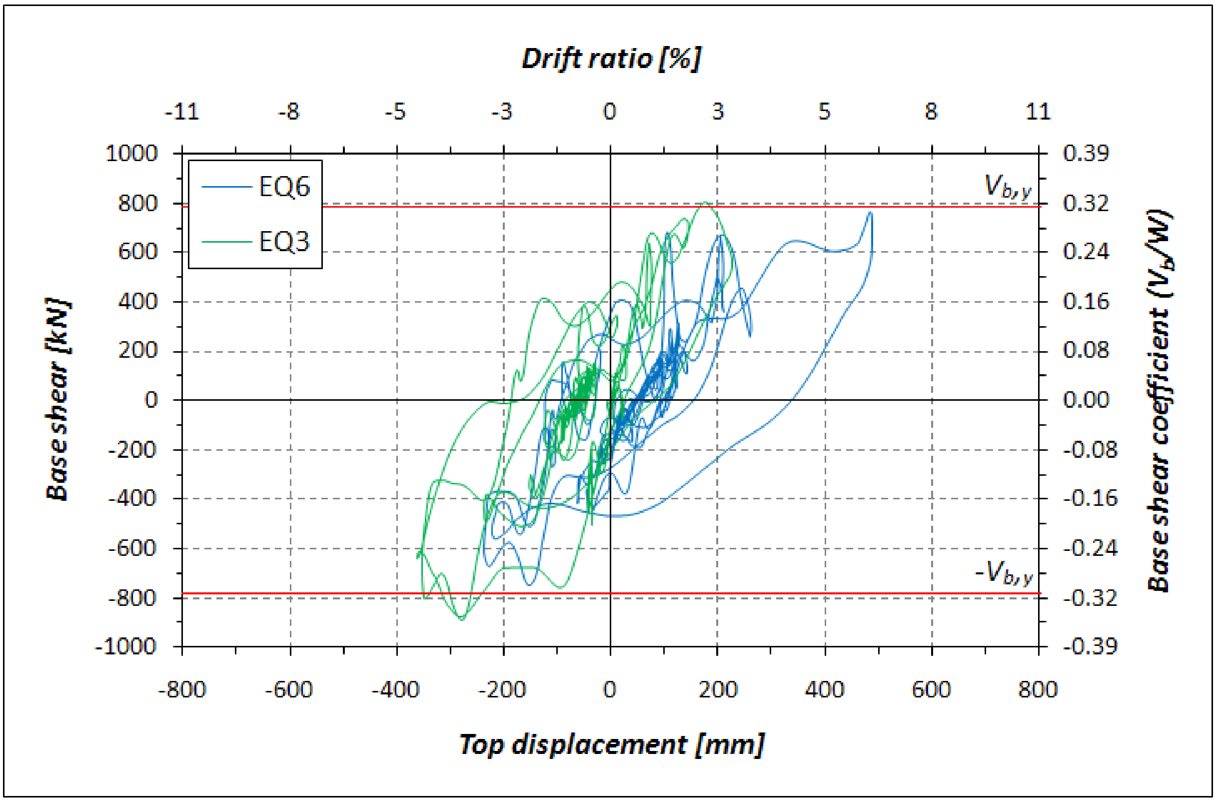

Figure 4.65 Base shear-top displacement response for EQ6 and EQ3

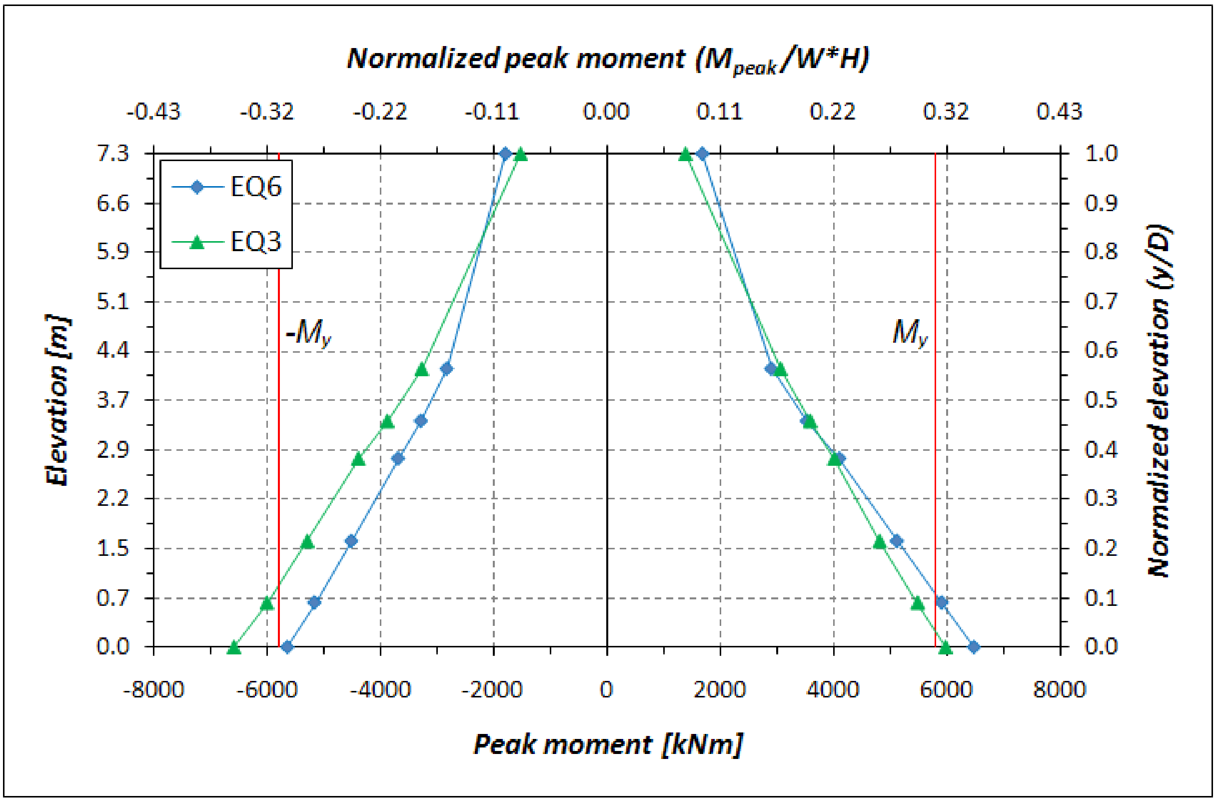

Figure 4.66: Moment envelops along the column height for EQ6 and EQ3

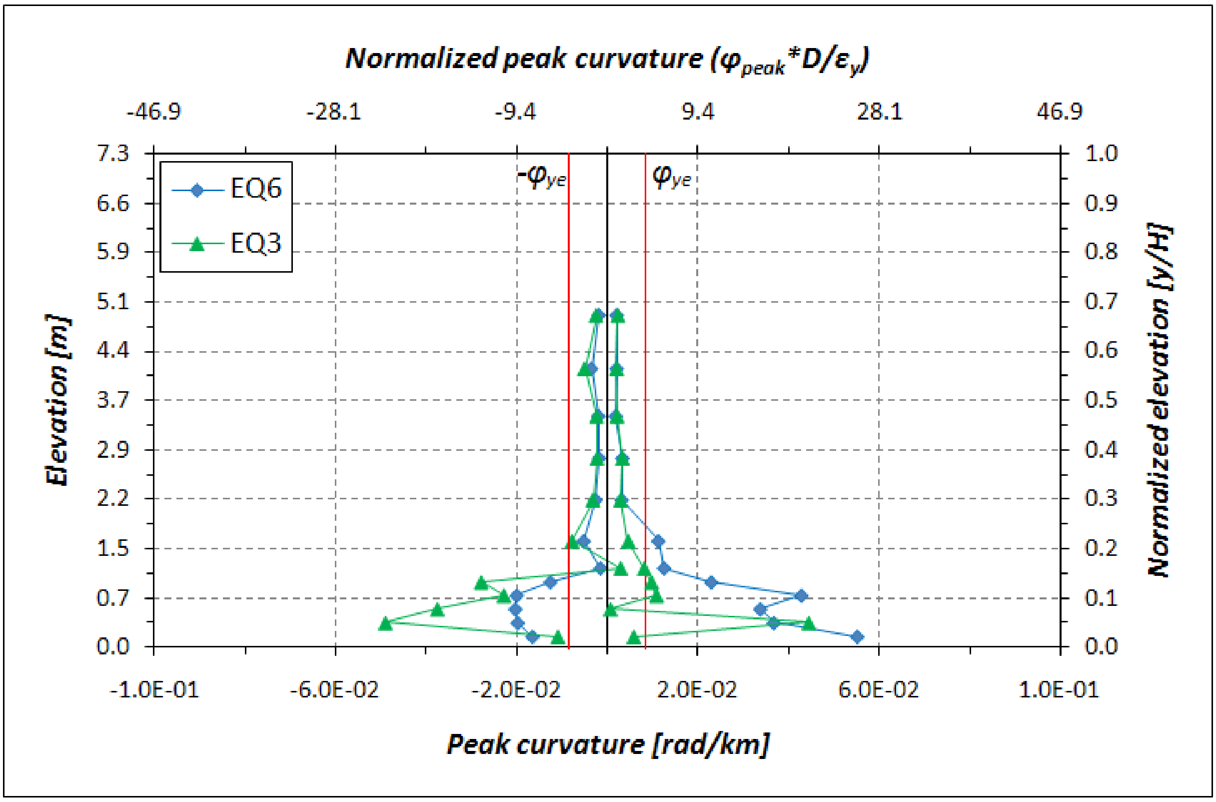

Figure 4.67: Curvature envelops along the column height for EQ6 and EQ3

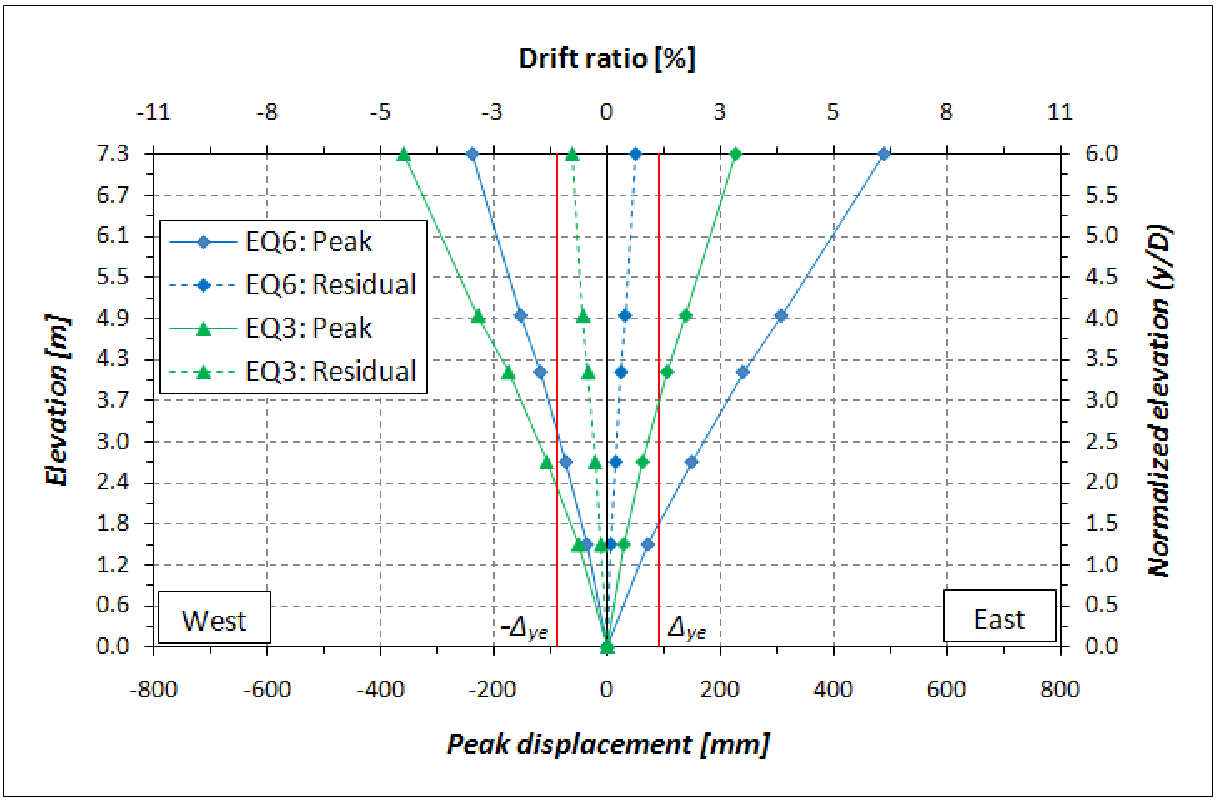

Figure 4.68: Displacement and displacement components envelops along the column height for EQ6 and EQ3

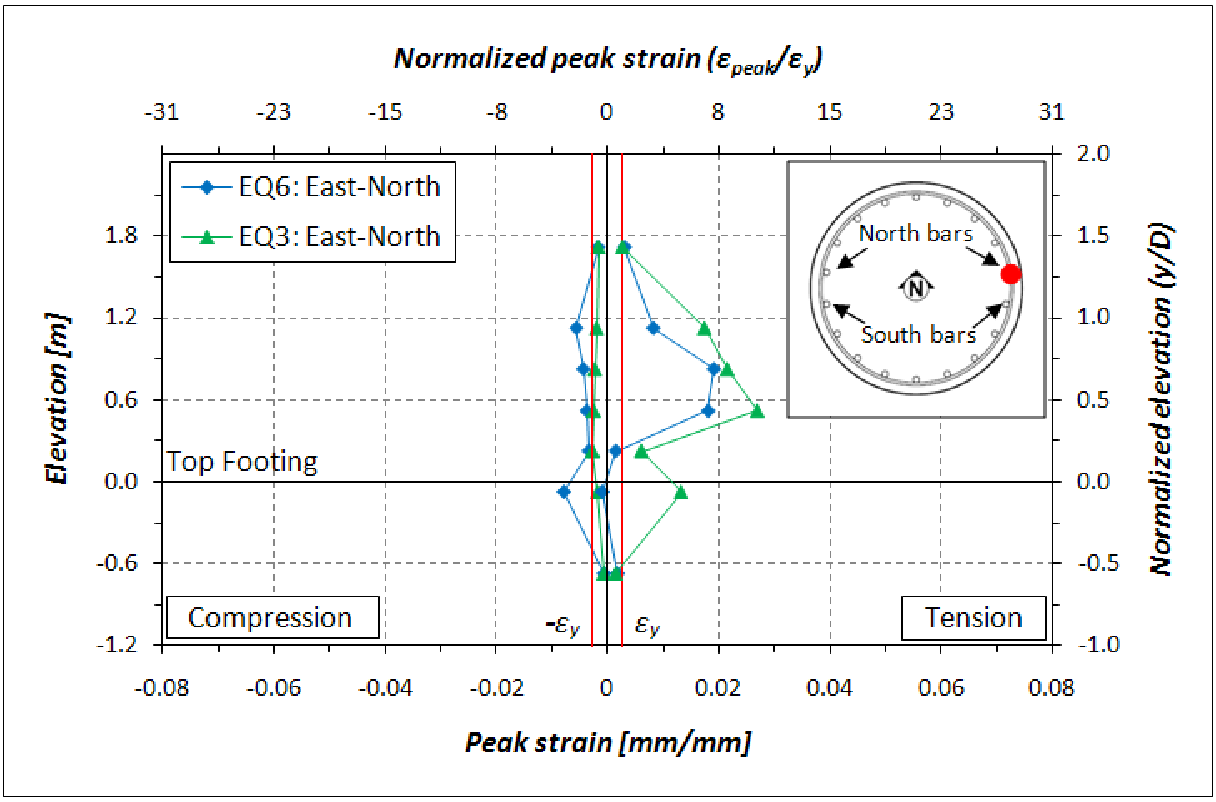

Figure 4.69: Longitudinal bar strain profile for EQ6 and EQ3: East side North bar

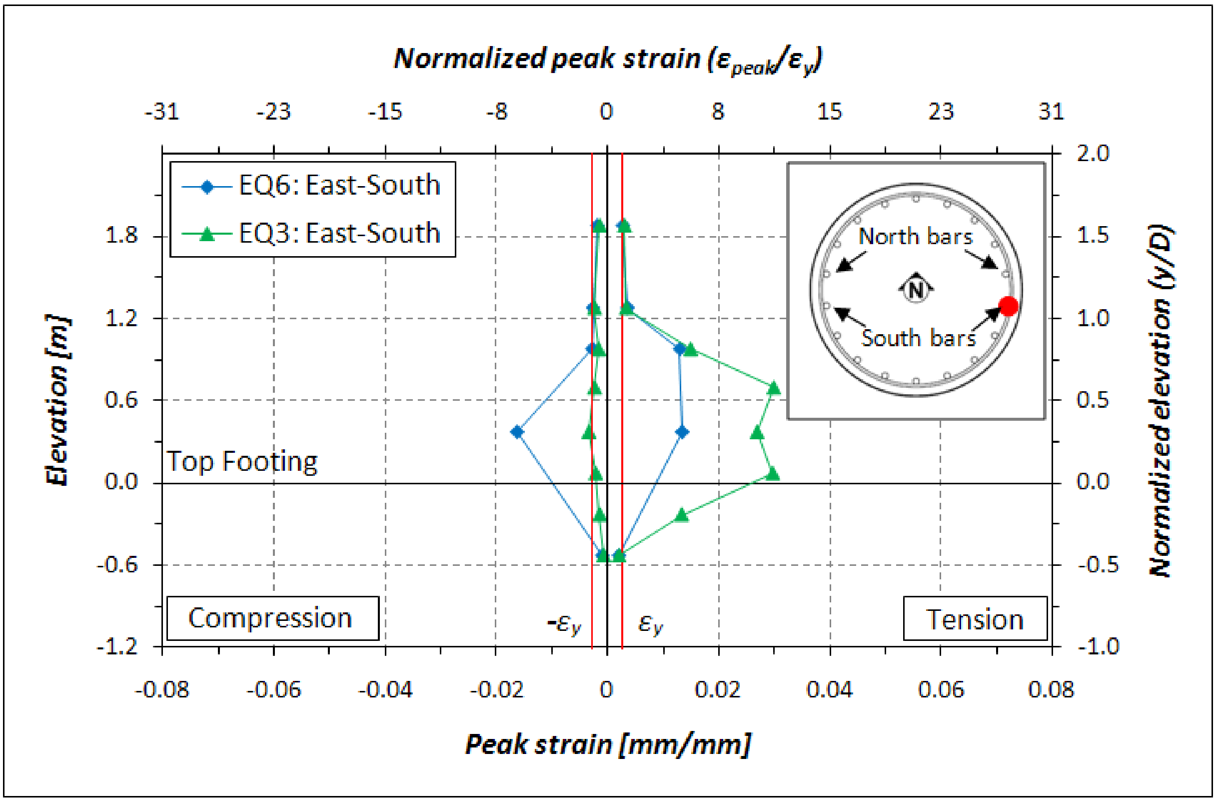

Figure 4.70: Longitudinal bar strain profile for EQ6 and EQ3: East side South bar

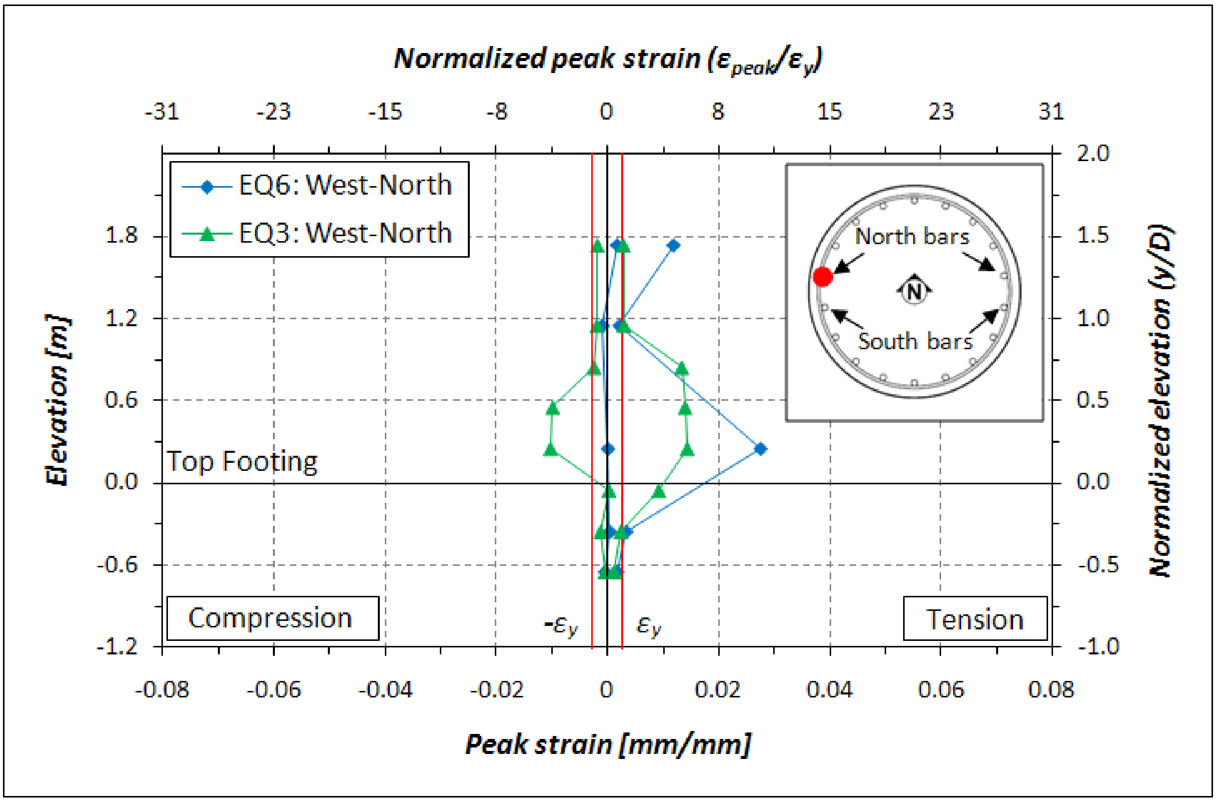

Figure 4.71: Longitudinal bar strain profile for EQ6 and EQ3: West side North bar

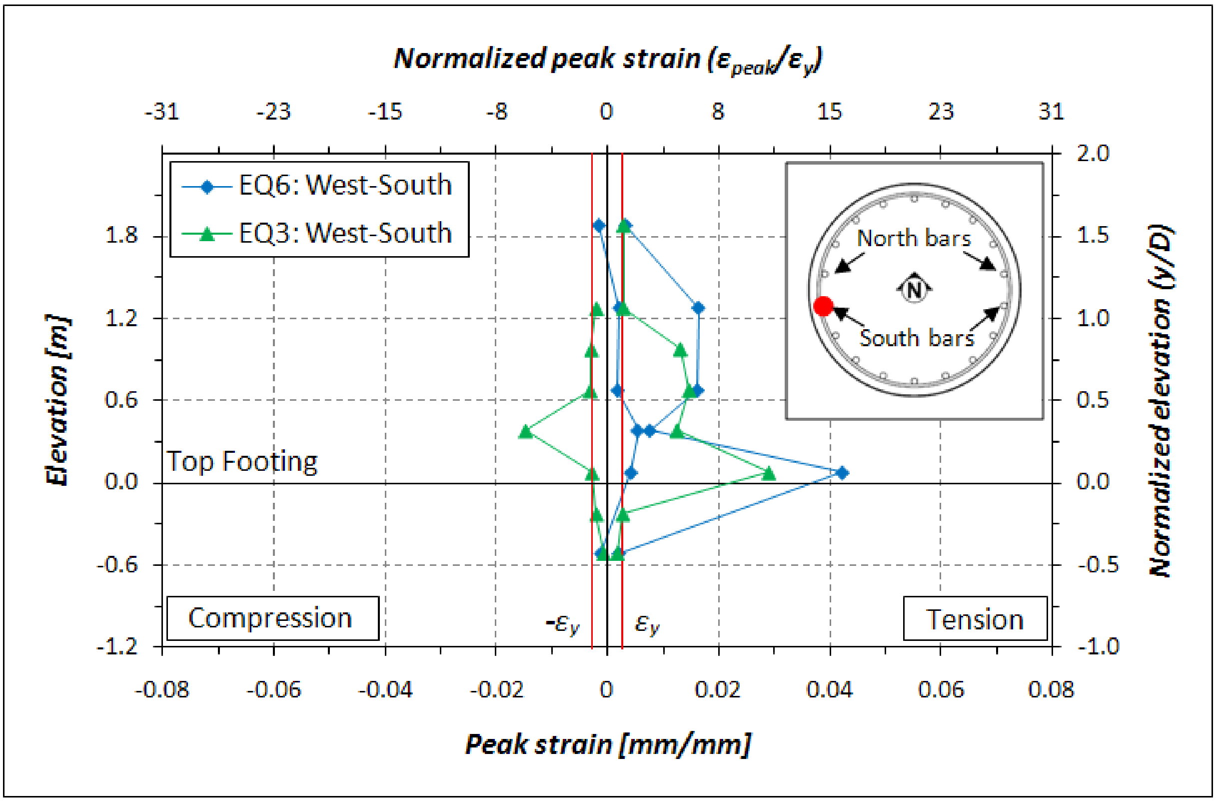

Figure 4.72: Longitudinal bar strain profile for EQ6 and EQ3: West side South bar

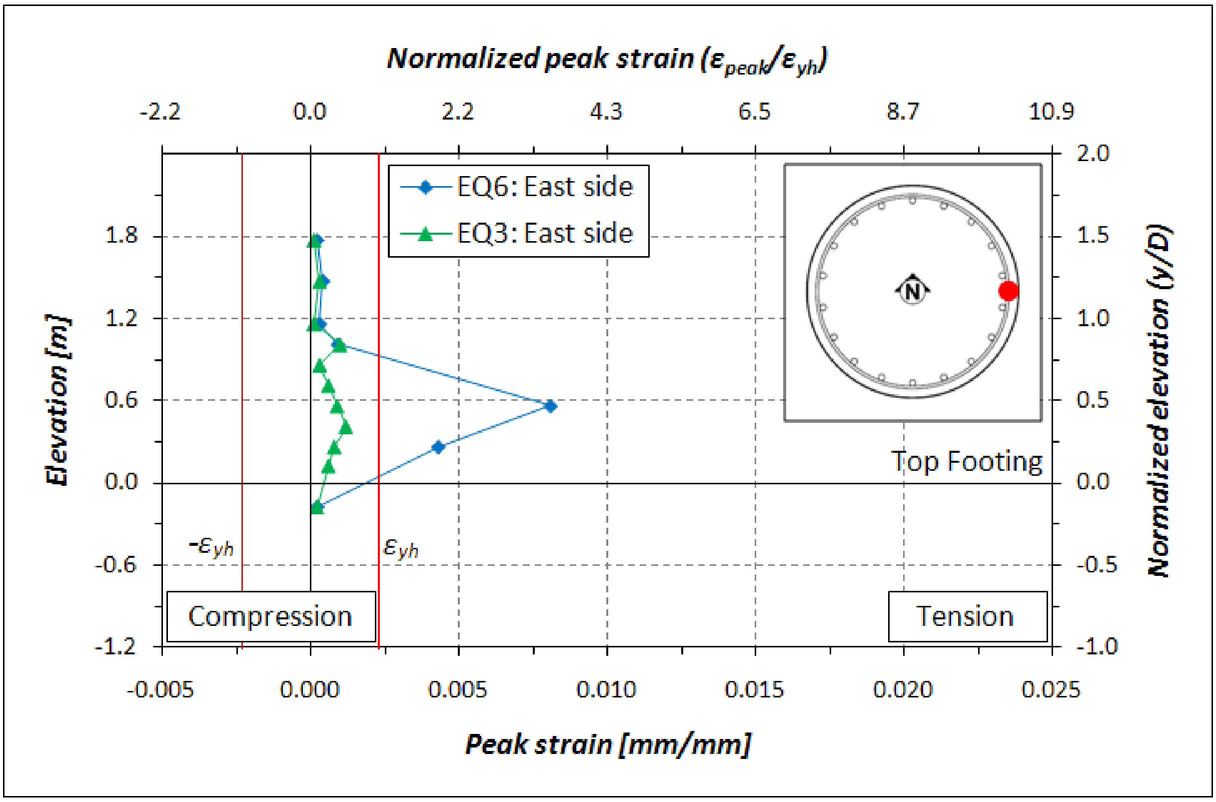

Figure 4.73: Hoops strain profile for EQ6 and EQ3: East side

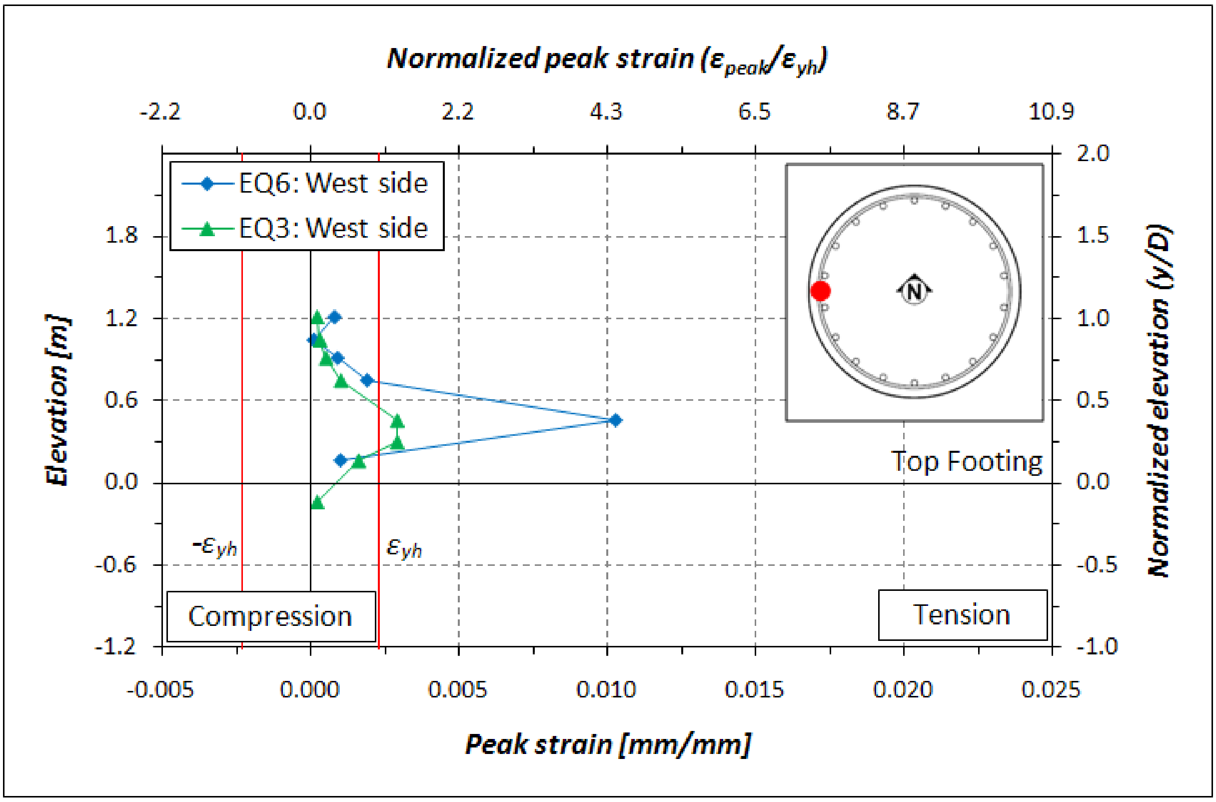

Figure 4.74: Hoops strain profile for EQ6 and EQ3: West side

4.2.7 EQ7 – Takatori

For extended testing, the original and unscaled Takatori record was utilized at different amplitudes to bring the column to a near collapse conditions. This ground motion was reproduced as EQ7 with a scale factor of 1.0 and the original polarity.

Further concrete spalling occurred on both the East and West sides of the column base. Some differences from the previous test can be found on the West side where unstable spalled concrete detached from the column during this test. Buckling of numerous longitudinal reinforcing bars occurred during EQ7, but none fractured. The concrete core start to suffer superficial crushing in proximity of the buckled bars. A post-test view of the East face of the column base is shown in Figure 4.75.

A ductile response with relatively stable hysteresis loops can be observed in the base moment versus base curvature relationship recorded during EQ7, see Figure 4.76. Large hysteresis loops demonstrate large energy dissipation. The idealized yield moment M_y is reached in the negative quadrant, proving that previous tests did not generate significant moment carrying capacity degradation in the specimen. A peak moment of 7378.0 kNm (5441.7 kip-ft), corresponding to $1.27 \cdot M_y$, and a peak curvature of $1.05 \cdot 10^{-1}$ rad/m ($2.66 \cdot 10^{-3}$ rad/in), corresponding to $12.55 \cdot \varphi_{ye}$, were reached during EQ7.

Figure 4.75: Column base post-EQ7

Large loops with visible higher mode effects can be found in the base shear versus top displacement response, see Figure 4.77. The base shear reaches again the value corresponding to the analytical idealized yield, $V_{b,y}$, in the negative quadrant. This demonstrates that the column still preserved its shear carrying capacity. A peak shear of 816.9 kN (183.6 kips), corresponding to 1.04·$V_{b,y}$ and a base shear coefficient of 0.32, was reached during this tests. A peak displacement of 553 mm (21.78 in.) or a 7.56% drift ratio, corresponding to 6.15·Δ_{ye}, was measured at the top of the column. The positive residual displacement accumulated during the previous tests was recovered and a new residual displacement of -145 mm (-5.70 in.), or -1.98% residual drift ratio, was observed at the end of this test.

A peak top moment of 1460.0 kNm (1076.8 kip-ft), corresponding to 20% of the peak moment reached at the base of the column, can be identified in the negative bending direction, see Figure 4.78.

Large average curvatures lumped at the column base, demonstrate a stable presence of a plastic region. The plastic length did not extend during this earthquake remaining about one column diameter above the footing. The flexural rotation along the column height is negligible with respect to the one recorded at the column base, see Figure 4.79.

The positive and negative envelopes of the relative displacement between column and table (solid line) and the post-test residual configuration (dashed line) are potted together in Figure 4.80. A flexural-dominated behavior with a significant fix-end rotation contribute can be deduced from the different peak displacement components: 439 mm (17.27 in.) from flexure, 29 mm (1.15 in.) from shear, and 100 mm (3.95 in.) from fix end rotation.

The strains envelopes along the instrumented longitudinal bars are plotted in Figures 4.81 to 4.84. Significant post-elastic elongation can be observed in three of the four monitored bar. In particular, the South bar of the East side reached a peak strain of 4.28% corresponding to 16.46·ε_y (Figure 4.82). The average strain reached a peak value of -0.91% in compression, corresponding to 3.50·ε_y, on the South bar of the East side (Figure 4.82).

The hoop strain envelopes on the East and West side of the column are shown in Figures 4.85 and 4.86. The same hoops as in the EQ6 test, second and third above the footing, were the most stretched on the West side. Although they generally showed smaller strains than the ones recorded during the previous test, they were visibly deformed. In this case a peak strain of 0.81% in tension, corresponding to 3.52·ε_{yh}, was recorded at the West side of the second hoop above the column-footing interface.

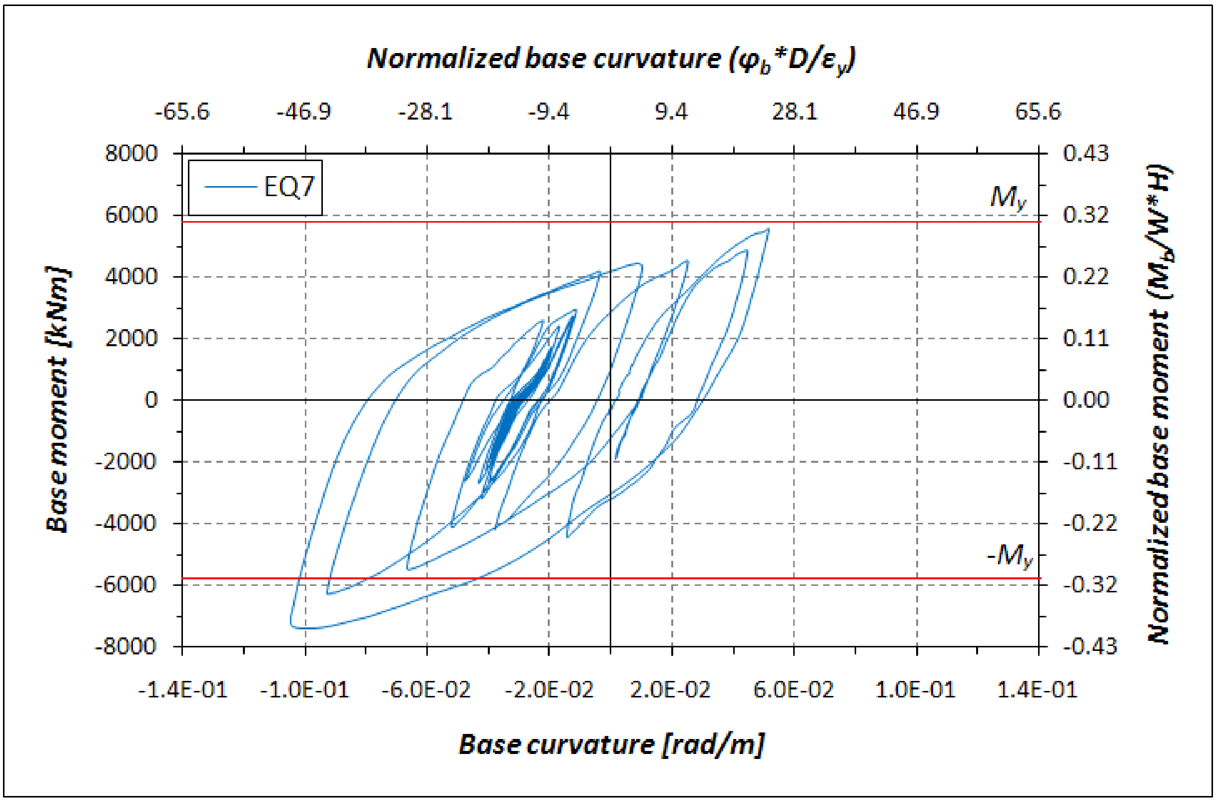

Figure 4.76: Base moment-base curvature response for EQ7

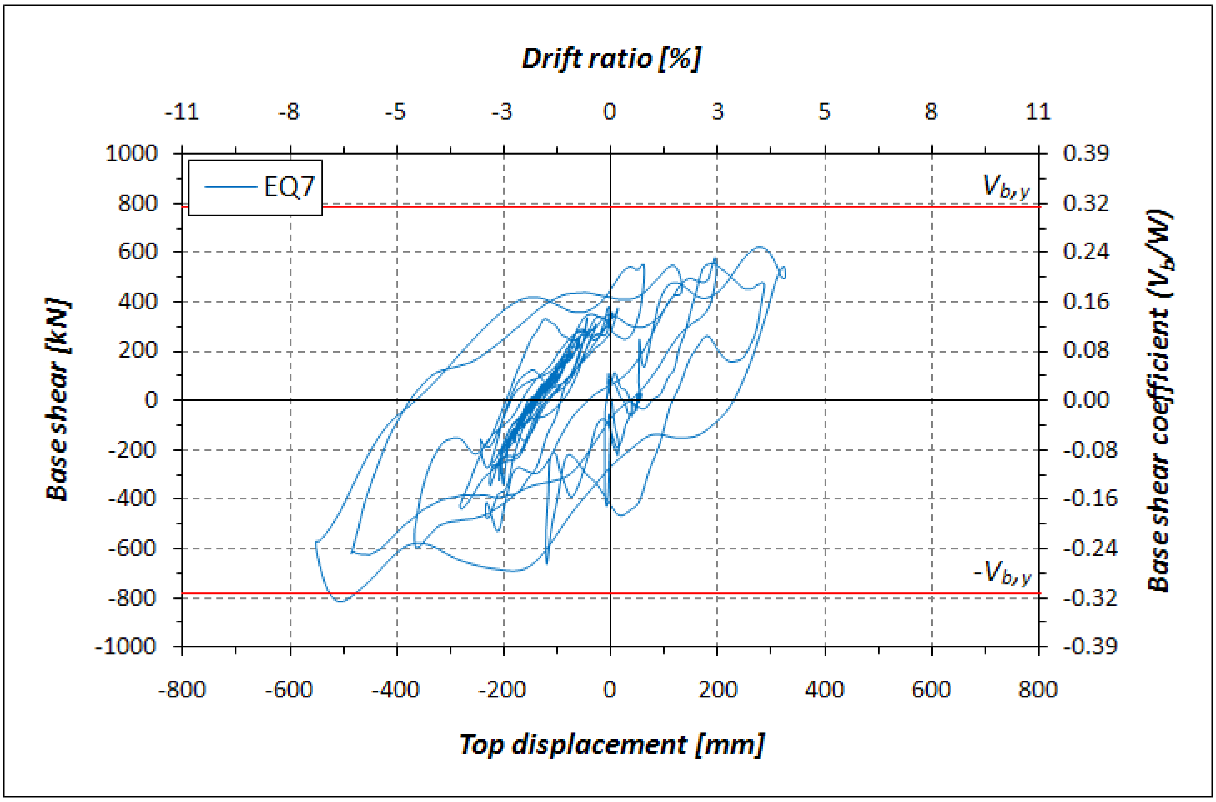

Figure 4.77 Base shear-top displacement response for EQ7

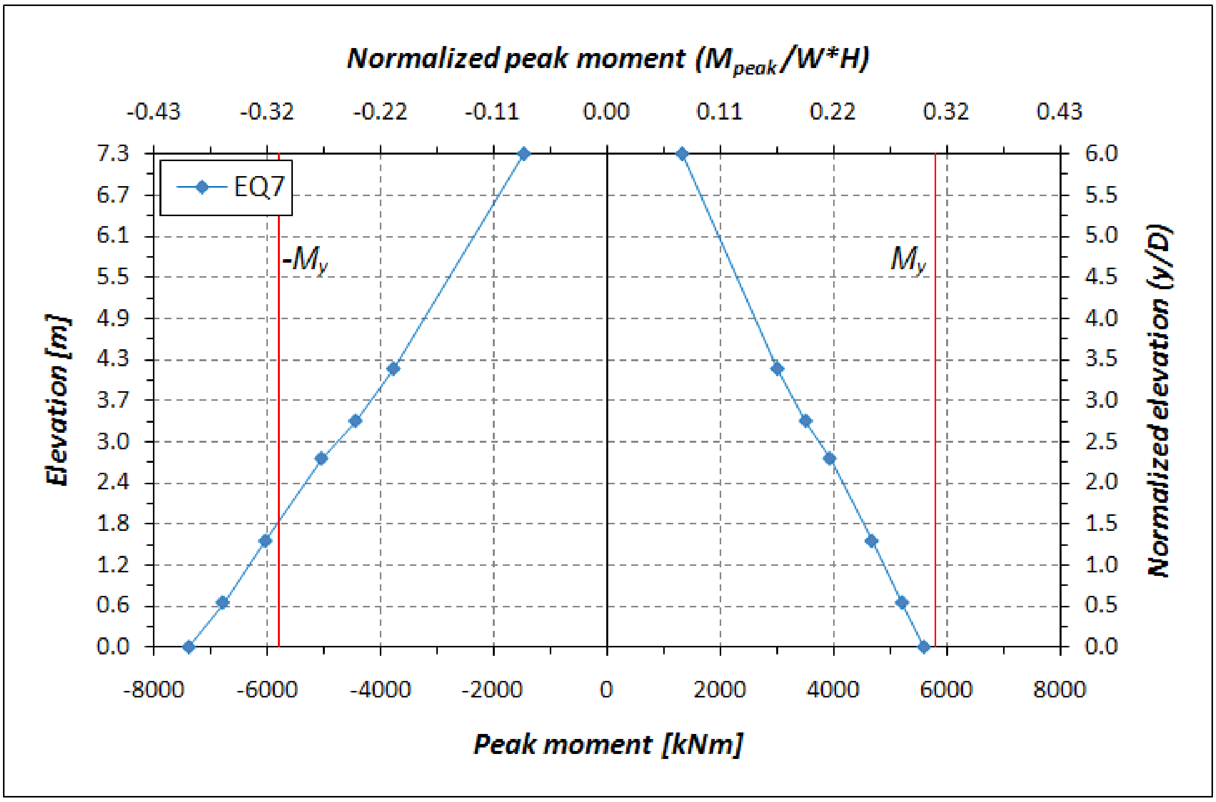

Figure 4.78: Moment envelops along the column height for EQ7

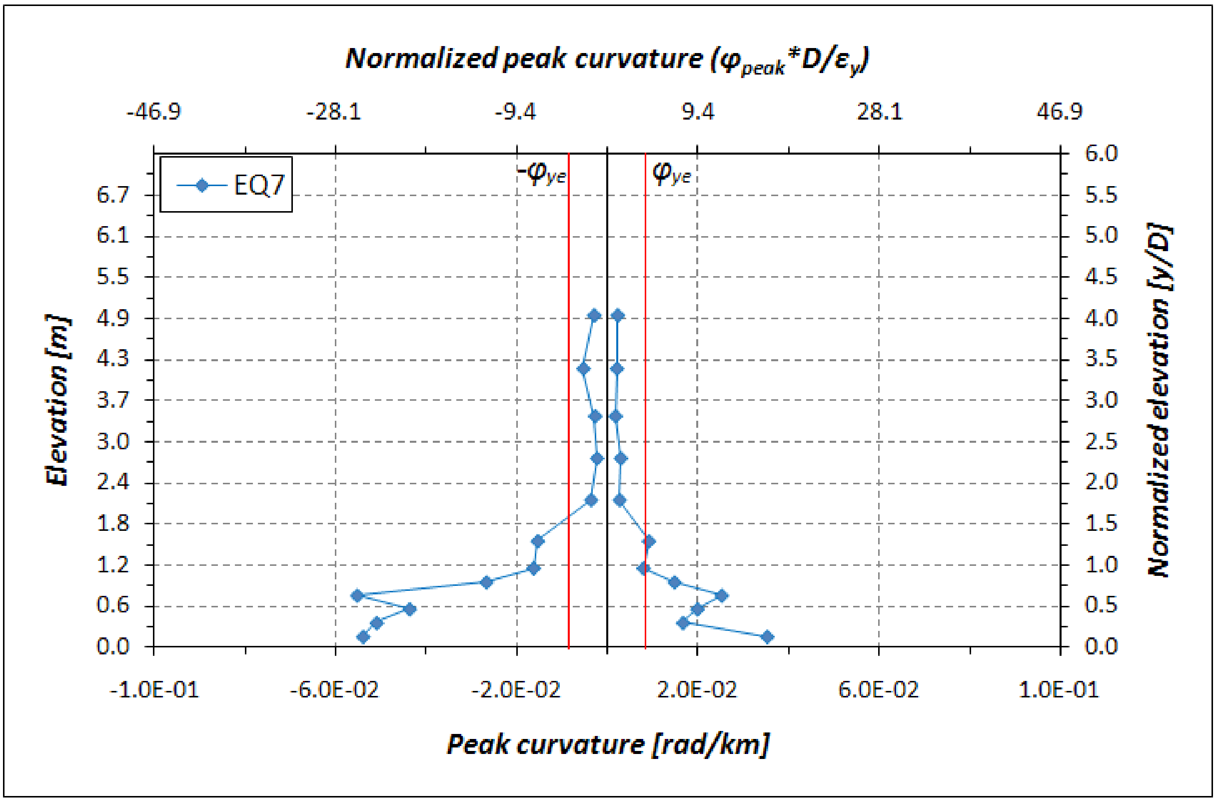

Figure 4.79: Curvature envelops along the column height for EQ7

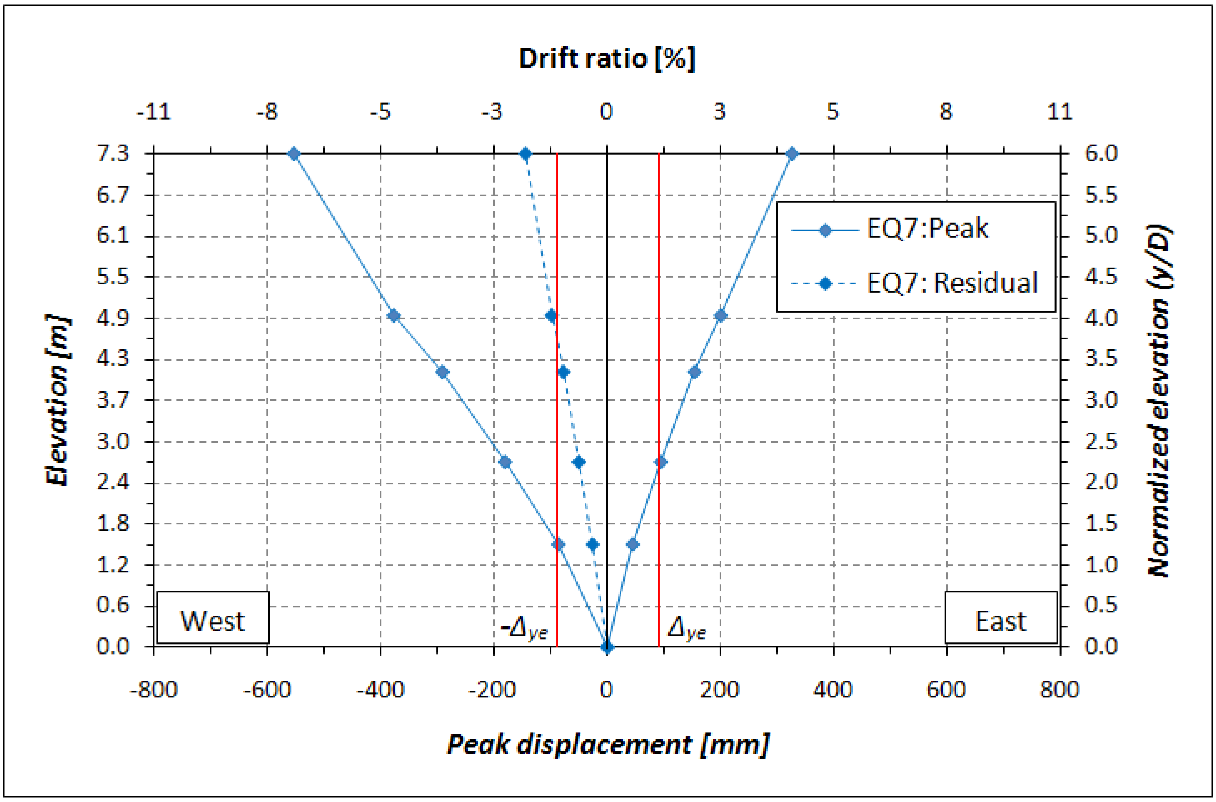

Figure 4.80: Displacement and displacement components envelops along the column height for EQ7

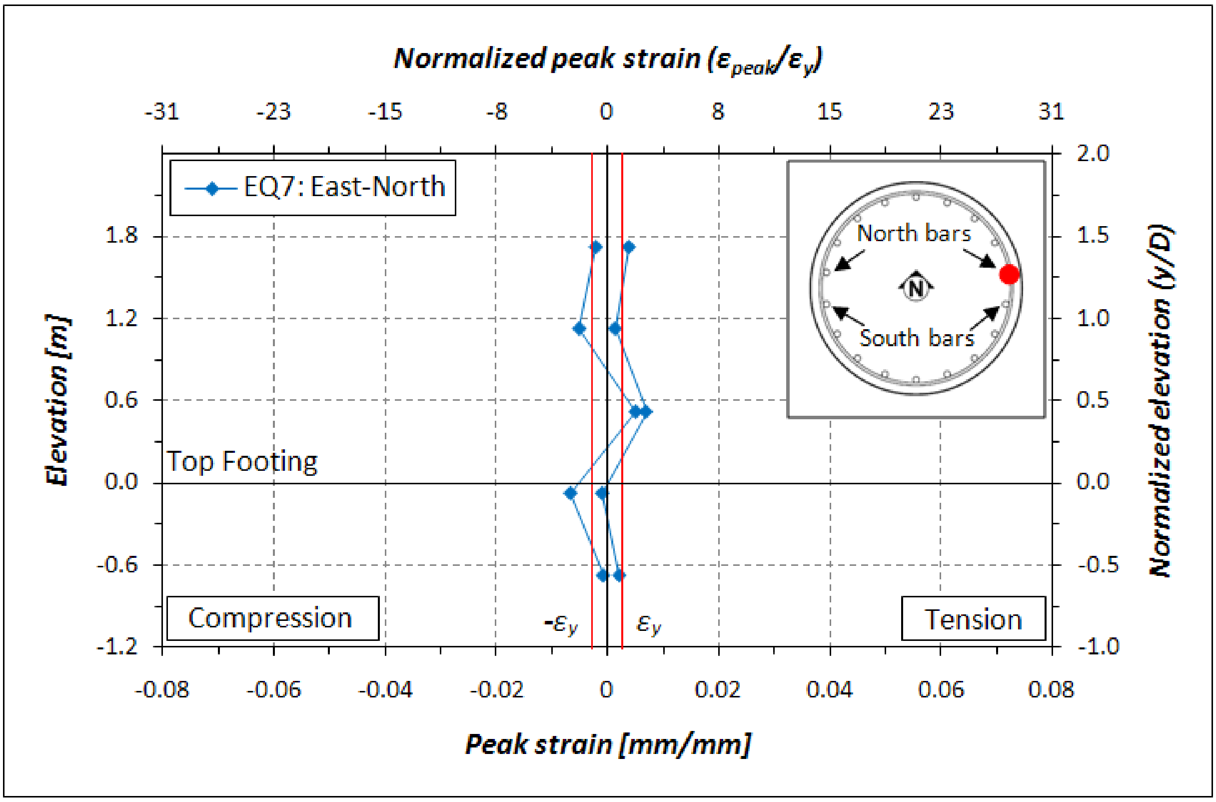

Figure 4.81: Longitudinal bar strain profile for EQ7: East side North bar

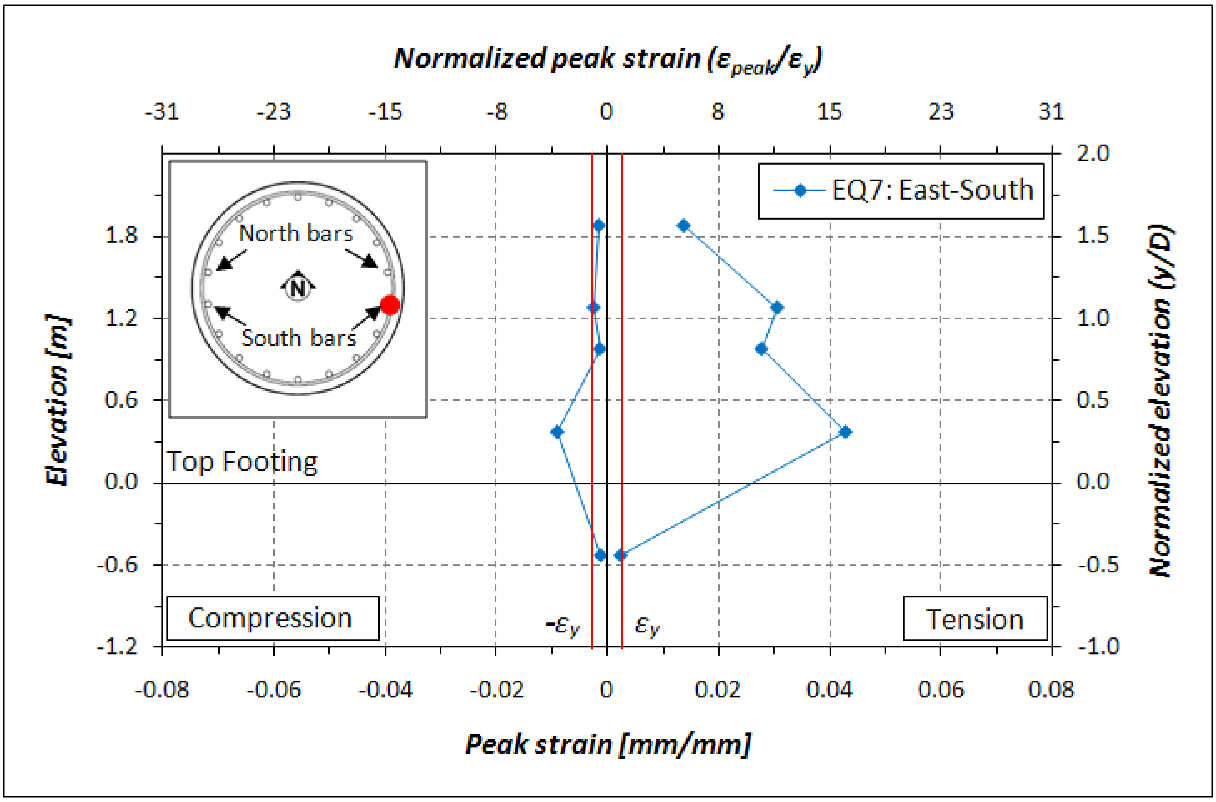

Figure 4.82: Longitudinal bar strain profile for EQ7: East side South bar

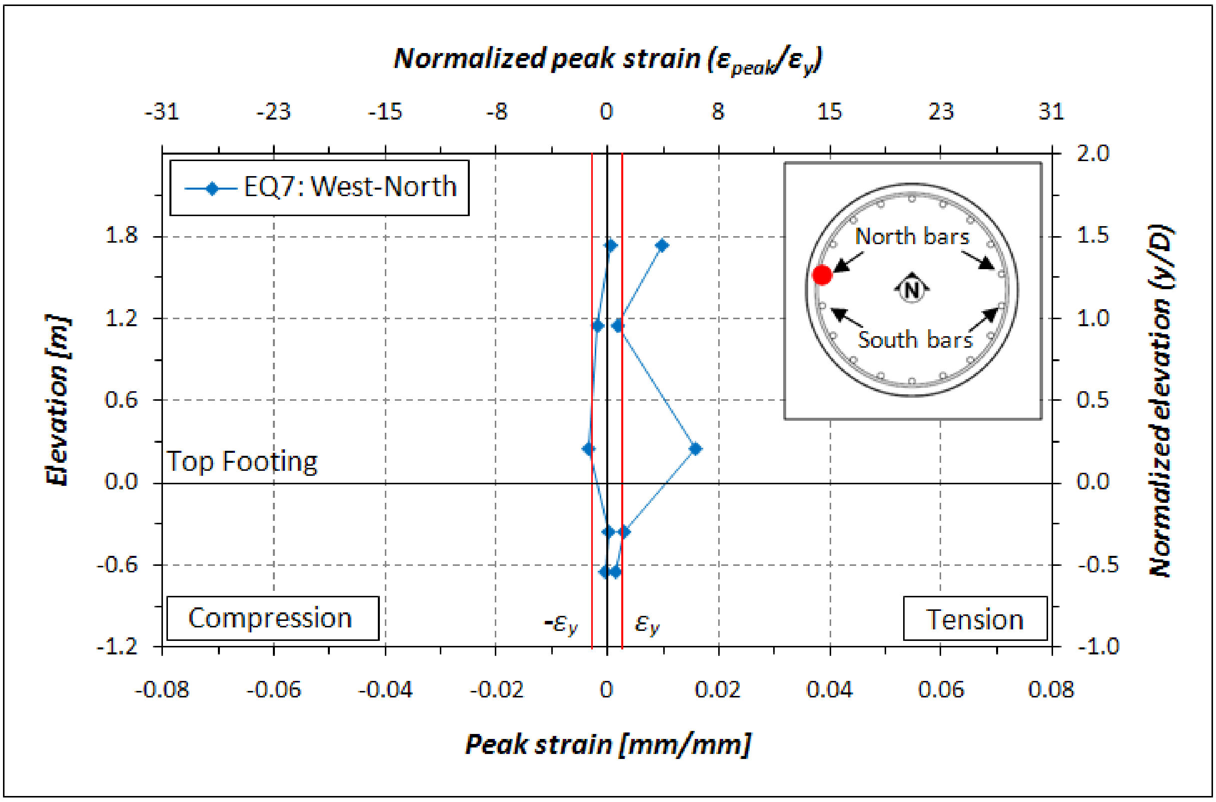

Figure 4.83: Longitudinal bar strain profile for EQ7: West side North bar

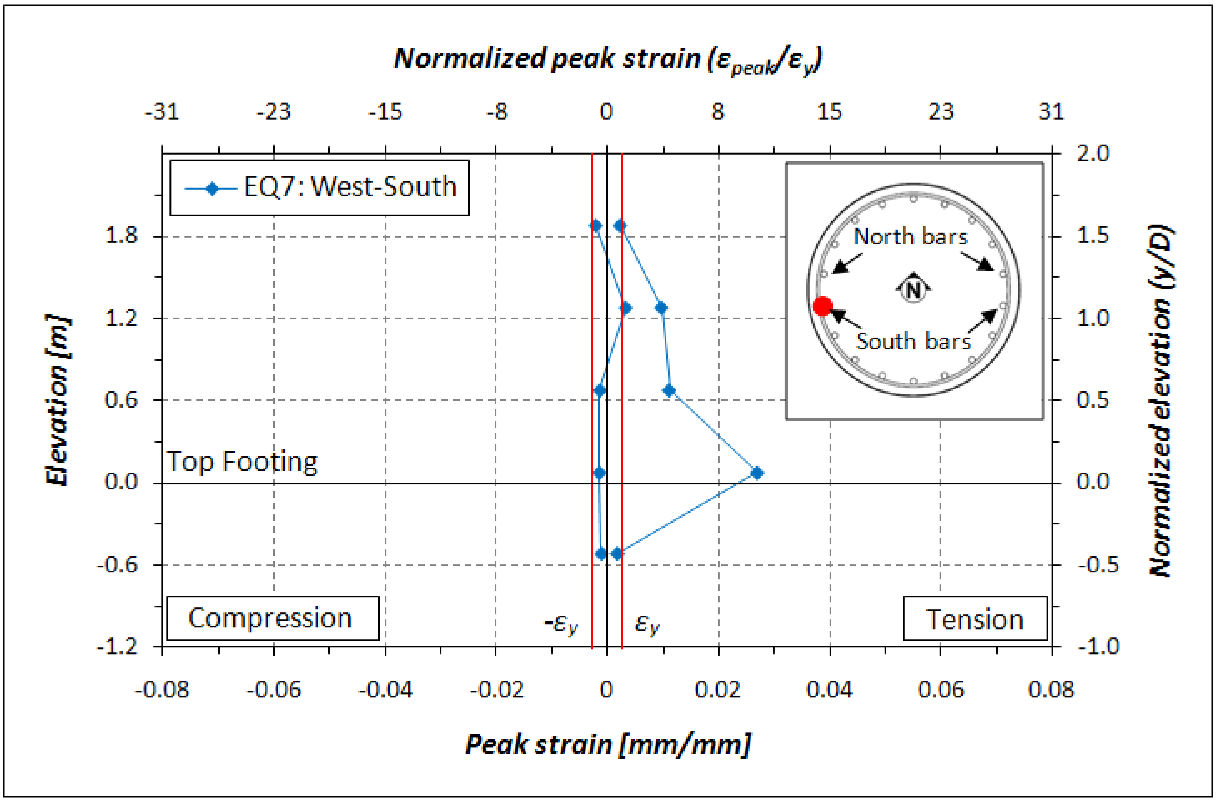

Figure 4.84: Longitudinal bar strain profile for EQ7: West side South bar

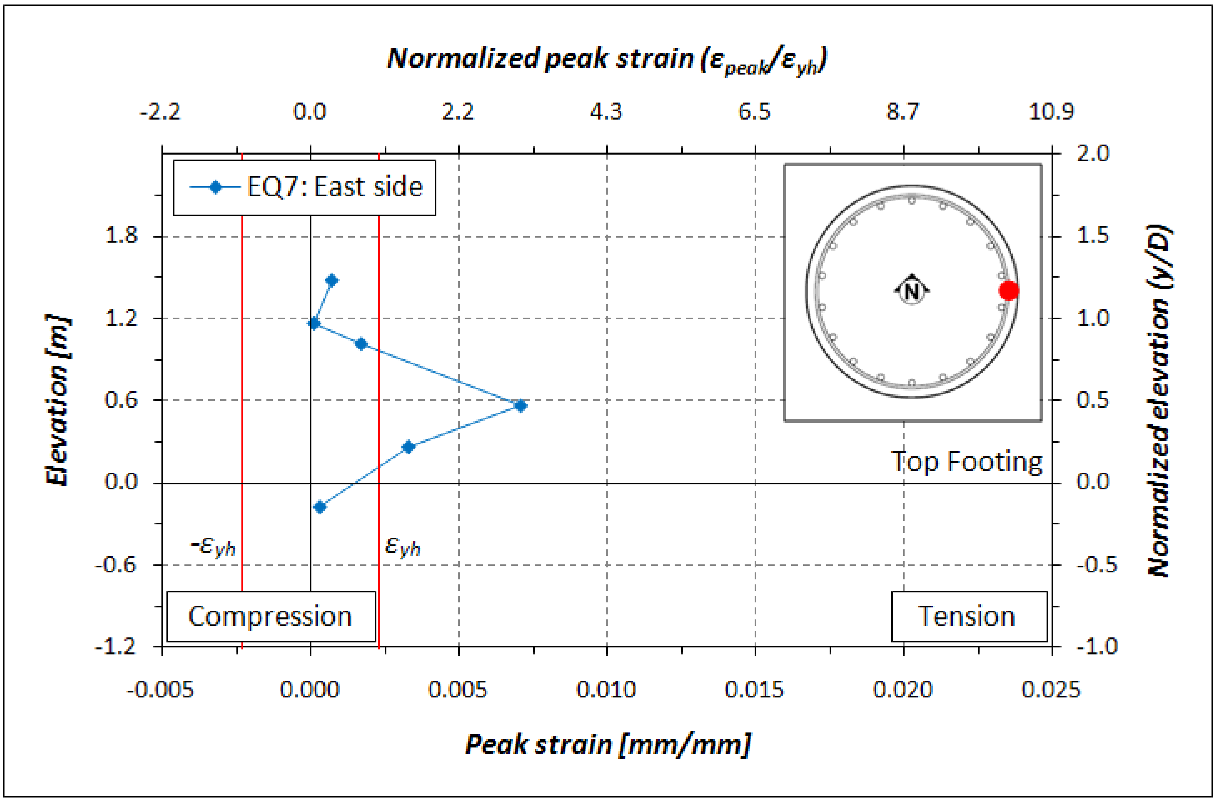

Figure 4.85: Hoops strain profile for EQ7: East side

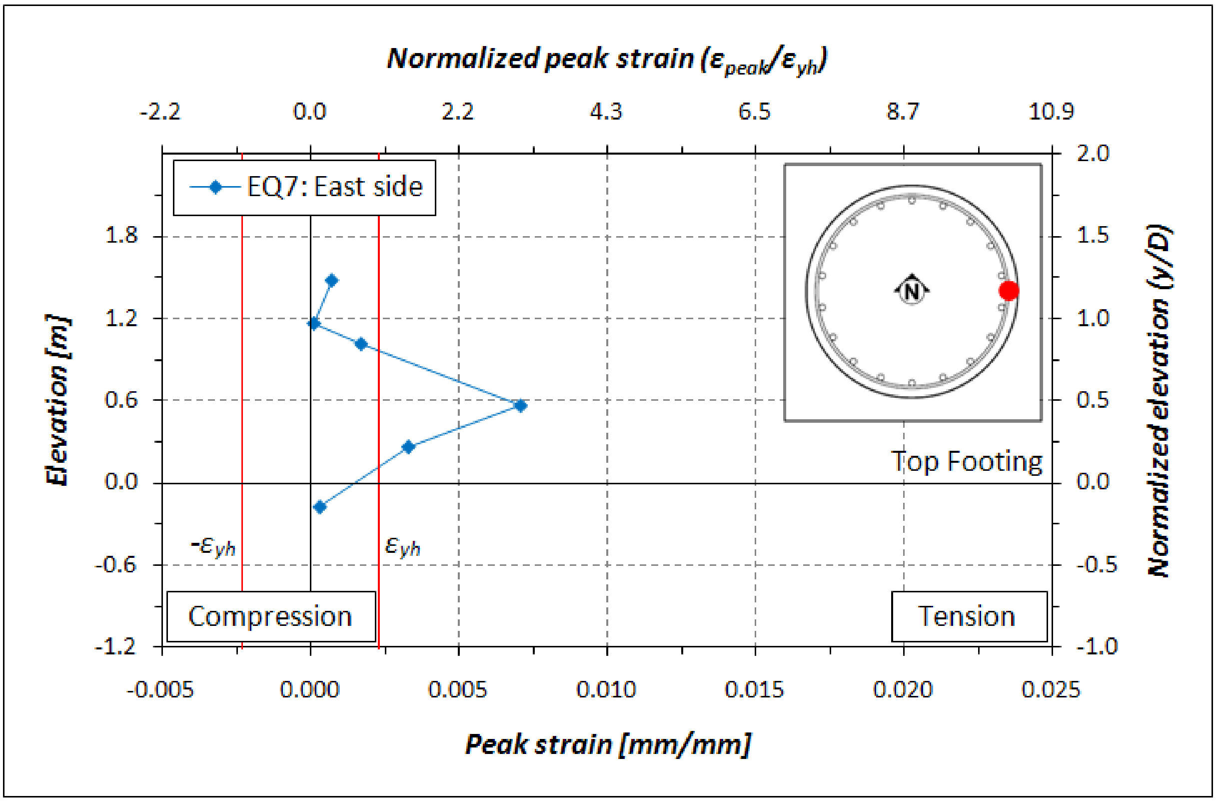

Figure 4.86: Hoops strain profile for EQ7: West side

4.2.8 EQ8 – Takatori 120% scaled

The Takatori record was reproduced as EQ8 with a scale factor of 1.2 and an opposite polarity of the previous test. The objective of this test was to bring the specimen to near-collapse conditions.

Longitudinal bar buckling and fracture occurred during this test. The two exposed bars on the East face located on the North side of the column central line had fractured. One of those bars was monitored with strain gauges. The noise of bar fracture was clearly heard twice during this test. Lose concrete cover did not allow clear visibility of the longitudinal reinforcement on the West side, so that no sign of bar fracture were visible on the this side. A post-test view of the East face of the column base is shown in Figure 4.87.

The previous earthquakes did not have a significant influence on the moment carrying capacity of the specimen. As can be seen in the moment-curvature response of the column base (Figure 4.88), the base moment exceeds again the idealized yield value, M_y, in both the positive and negative quadrants. A ductile response with significant energy dissipation can be observed in this diagram, which evidences large hysteresis loops. A peak moment of 7116.8 kNm (5249.1 kip-ft), corresponding to $1.23 \cdot M_y$ and only 4% smaller than the one obtained in the previous test, was reached during EQ8. A peak curvature of $1.23 \cdot 10^{-1}$ rad/m ($3.13 \cdot 10^{-3}$

Figure 4.87: Column base post-EQ8

rad/in), corresponding to $14.75 \cdot \varphi_{ye}$ and 15% larger than the one obtained in the previous test was achieved. Principally due to damages accumulation at the column base, EQ8 produced a smaller moment and a larger curvature demands compared with the ones obtained in EQ7.

The base shear versus top displacement response can be found in Figure 4.89. The base shear did not reach the one corresponding to analytical idealized yield, $V_{b,y}$, but the positive and negative peak values were very close to it. This demonstrates a small shear carrying capacity degradation, which did not compromise the vertical load carrying capacity of the column. A peak shear of 744.6 kN (167.4 kips), corresponding to $0.95 \cdot V_{b,y}$ and a base shear coefficient of 0.29, occurred in this test. A peak displacement of 606 mm (23.85 in.) or 8.28% drift ratio, corresponding to $6.74 \cdot \Delta_{ye}$, and 6% larger than the one obtained during the previous test, was measured at the top of the column. The negative residual displacement accumulated during the previous tests was recovered and new residual displacement of 97 mm (3.83 in.), or 1.33% residual drift ratio, remained post test.

A peak top moment of 1740.8 kNm (1284.0 kip-ft), corresponding to 24% of the peak moment reached at the base of the column, can be identified in the positive moment envelope along the column height, see Figure 4.90.

The positive and negative curvature envelopes along the column height are shown in Figure 4.91. The average curvatures recorded during EQ8 are generally larger than the ones obtained in the previous test and essentially lumped at the column base.

The positive and negative envelopes of the relative displacement between column and table (solid line) and the post-test residual configuration (dashed line) are potted together in Figure 4.92. A flexural-dominated behavior can be deduced from the different peak displacement components: 438 mm (17.23 in.) from flexure, 32 mm (1.27 in.) from shear, and 96 mm (3.78 in.) from fix end rotation.

The strains envelopes along the instrumented longitudinal bars are plotted in Figures 4.93 to 4.96. Numerous strain gauges were lost, so that few measurements are available. A significant plastic elongation can be observed in one of the four monitored bar. The South bar of the West side reached a peak average strain of 5.84% corresponding to $22.46 \cdot \varepsilon_y$ (Figure 4.96). The average strain reached a peak value of -0.40% in compression, corresponding to $1.54 \cdot \varepsilon_y$, on the South bar of the East side (Figure 4.94).

The hoop strain envelopes on the East and West side of the column are shown in Figures 4.97 and 4.98. A relevant tensile strain was recorded at the West side of the third hoop above the column-footing interface. The average strain on this hoop reached a peak value of 1.13% corresponding to $4.91 \cdot \varepsilon_{yh}$.

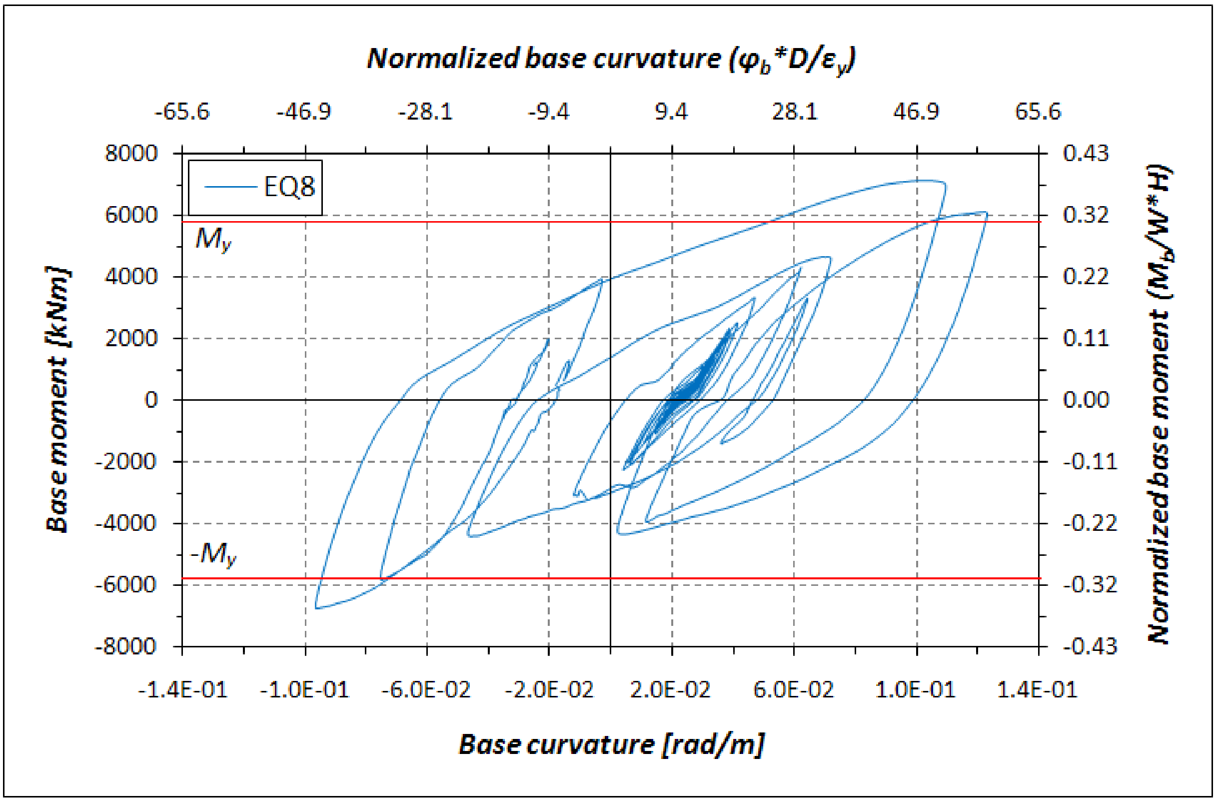

Figure 4.88: Base moment-base curvature response for EQ8

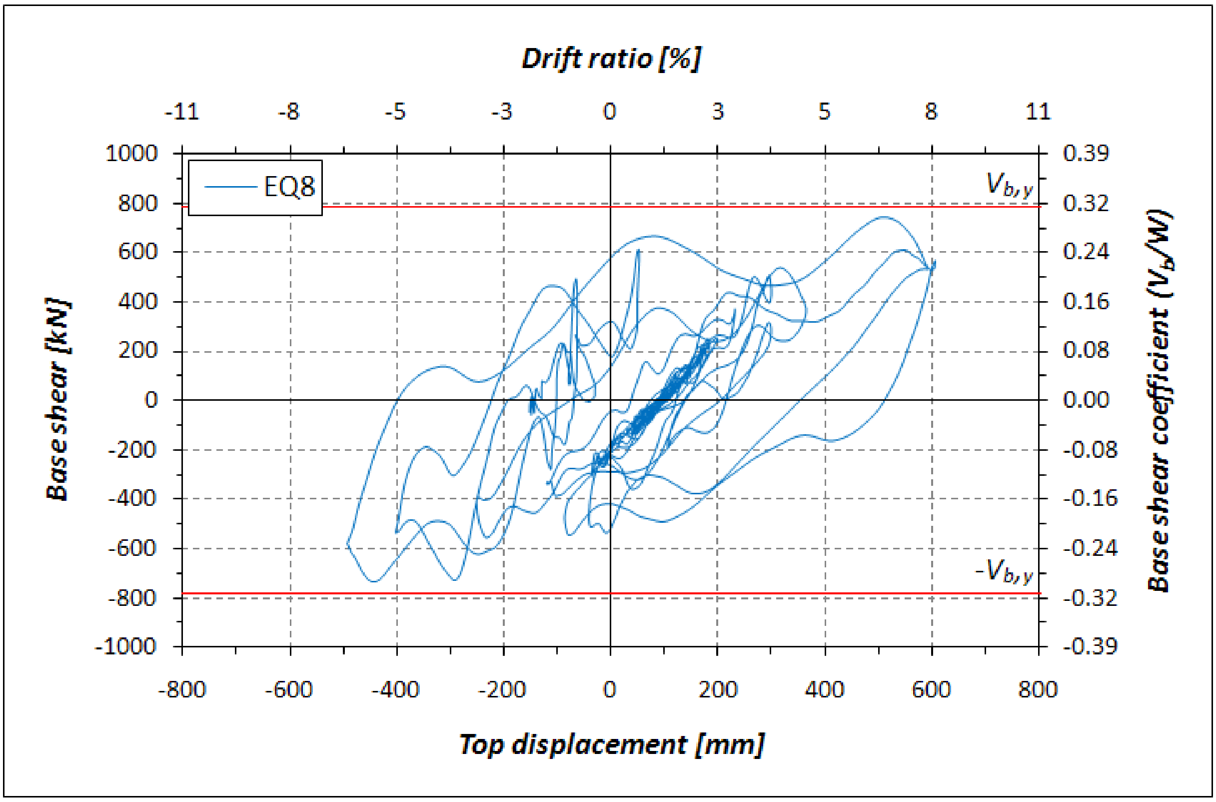

Figure 4.89 Base shear-top displacement response for EQ8

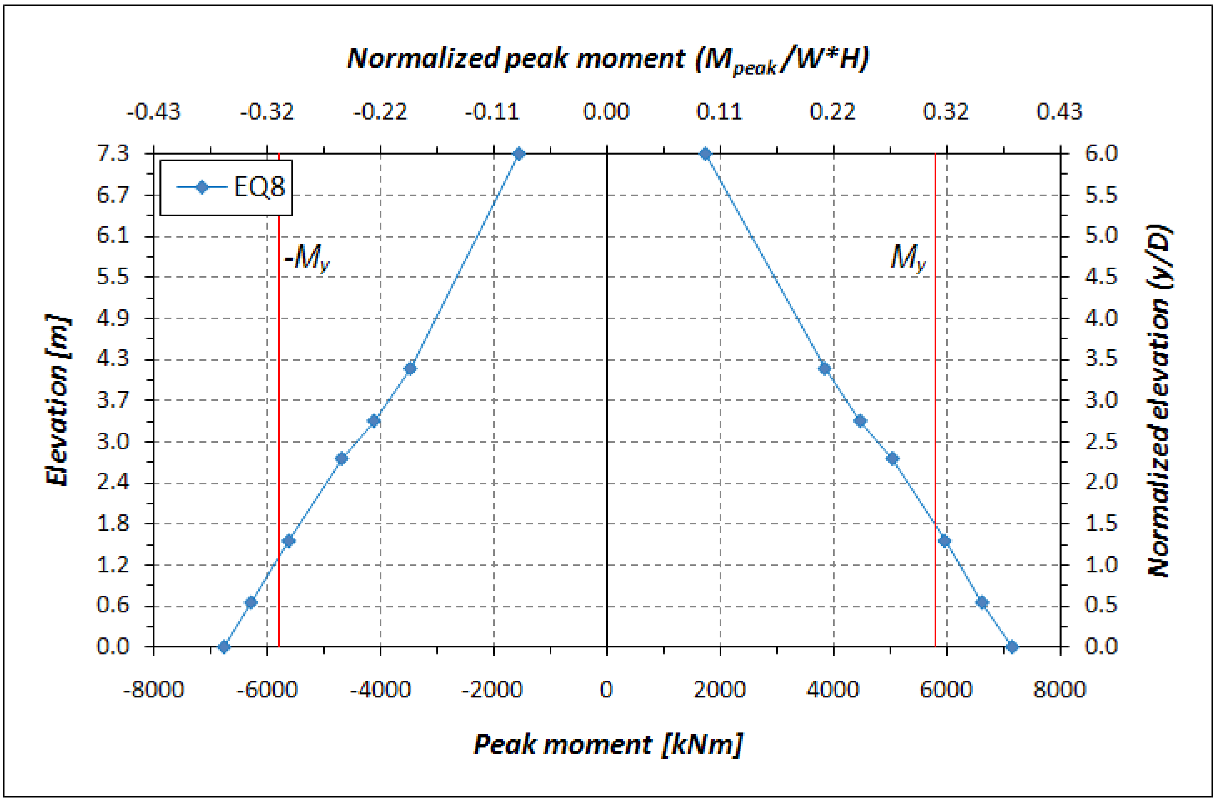

Figure 4.90: Moment envelops along the column height for EQ8

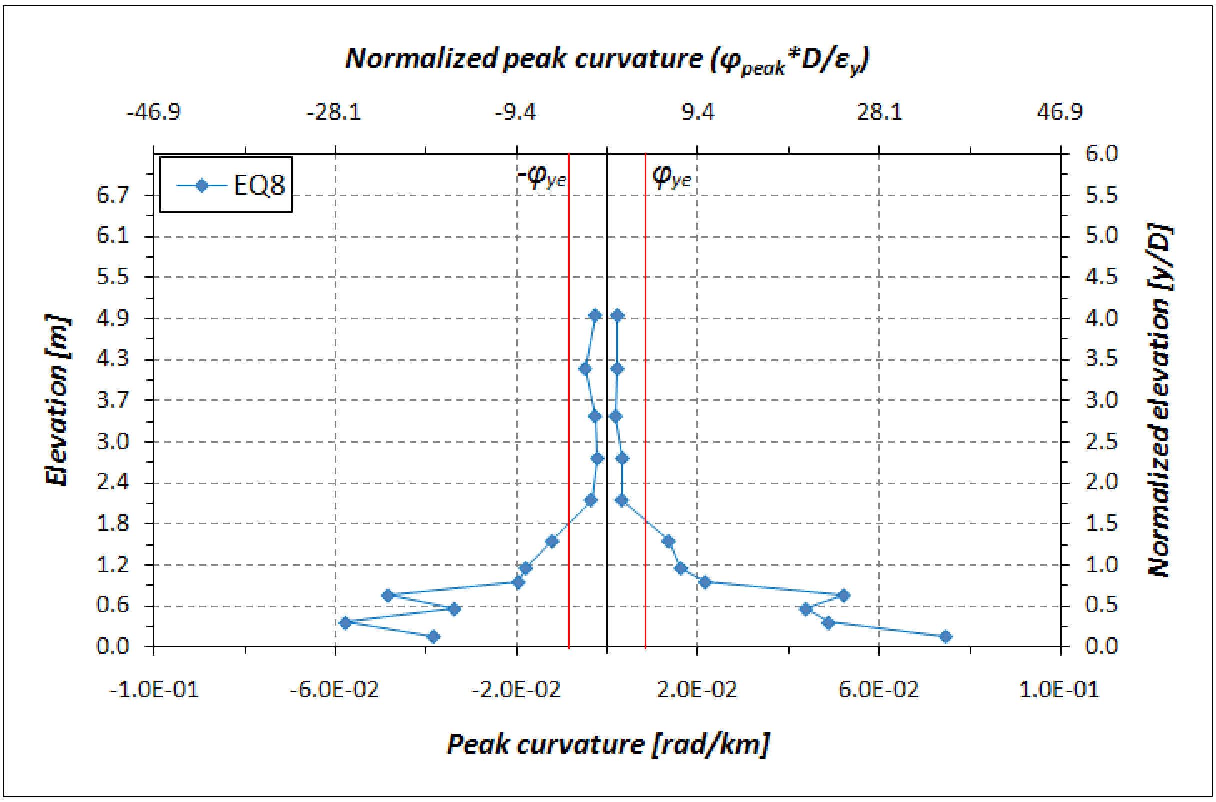

Figure 4.91: Curvature envelops along the column height for EQ8

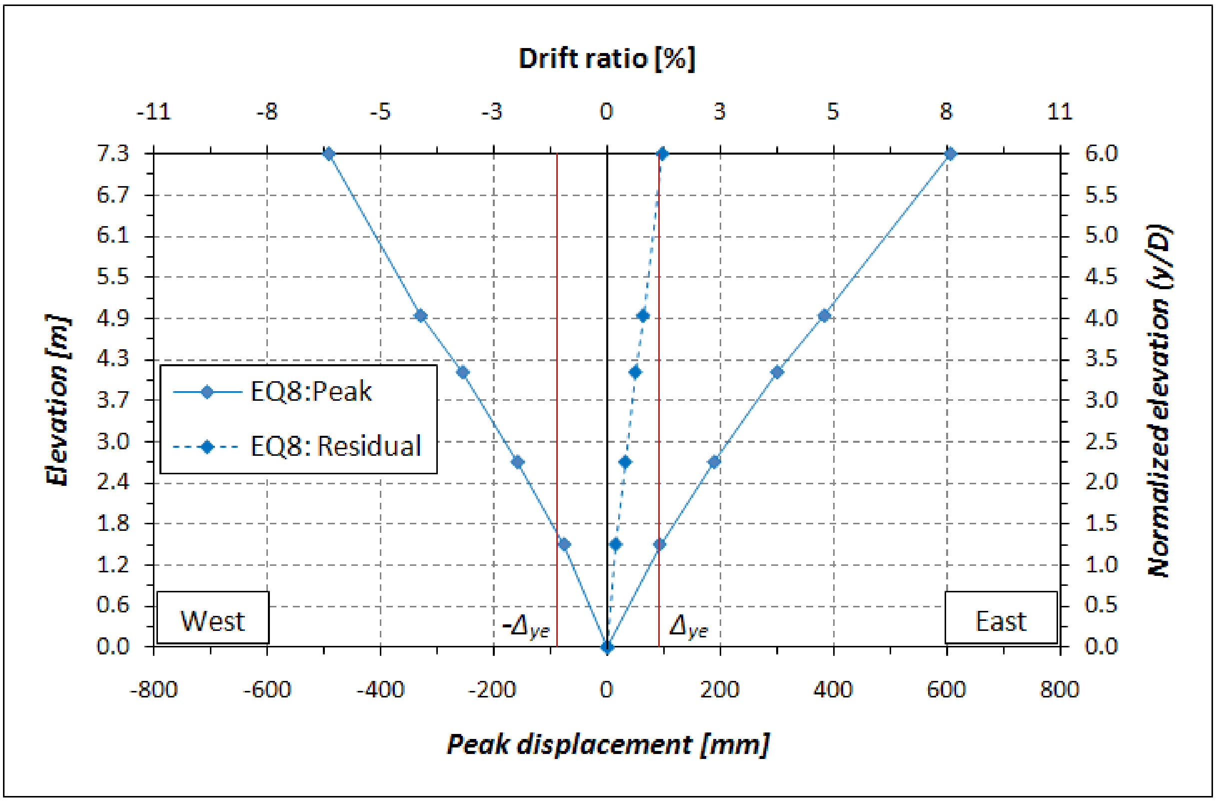

Figure 4.92: Displacement and displacement components envelops along the column height for EQ8

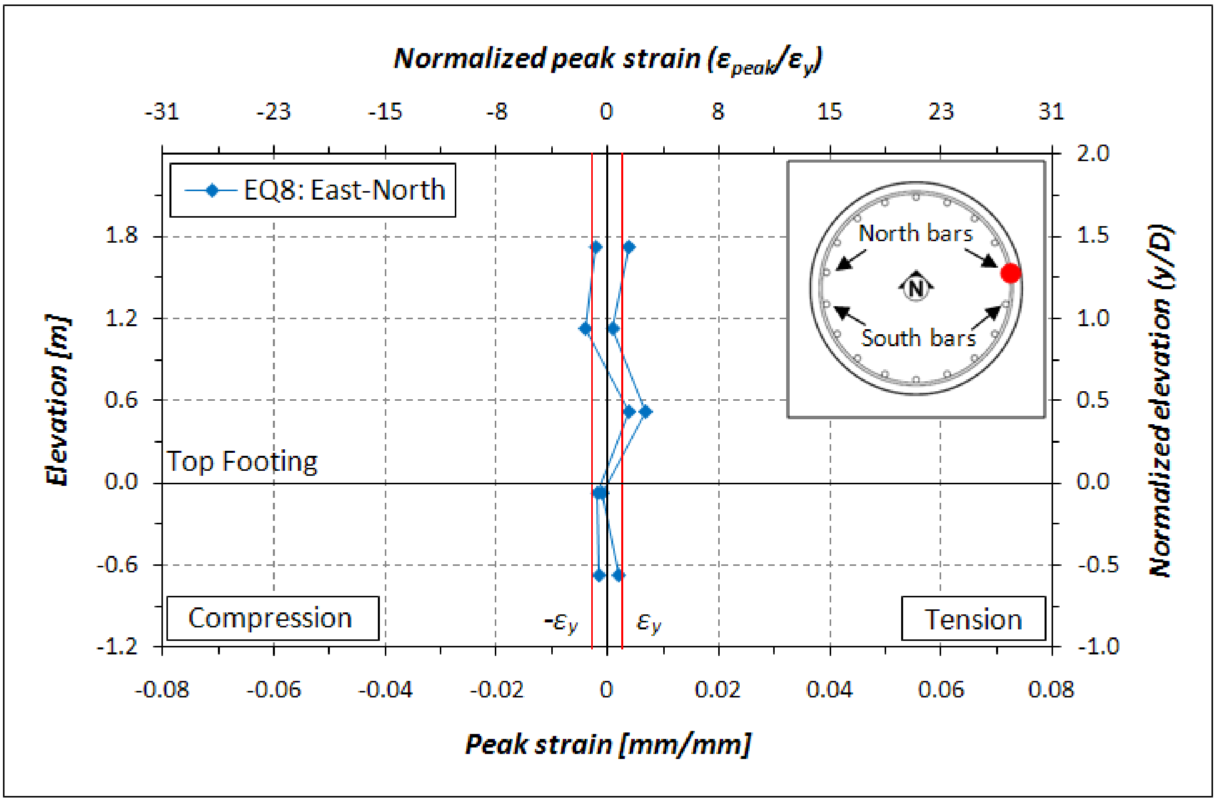

Figure 4.93: Longitudinal bar strain profile for EQ8: East side North bar

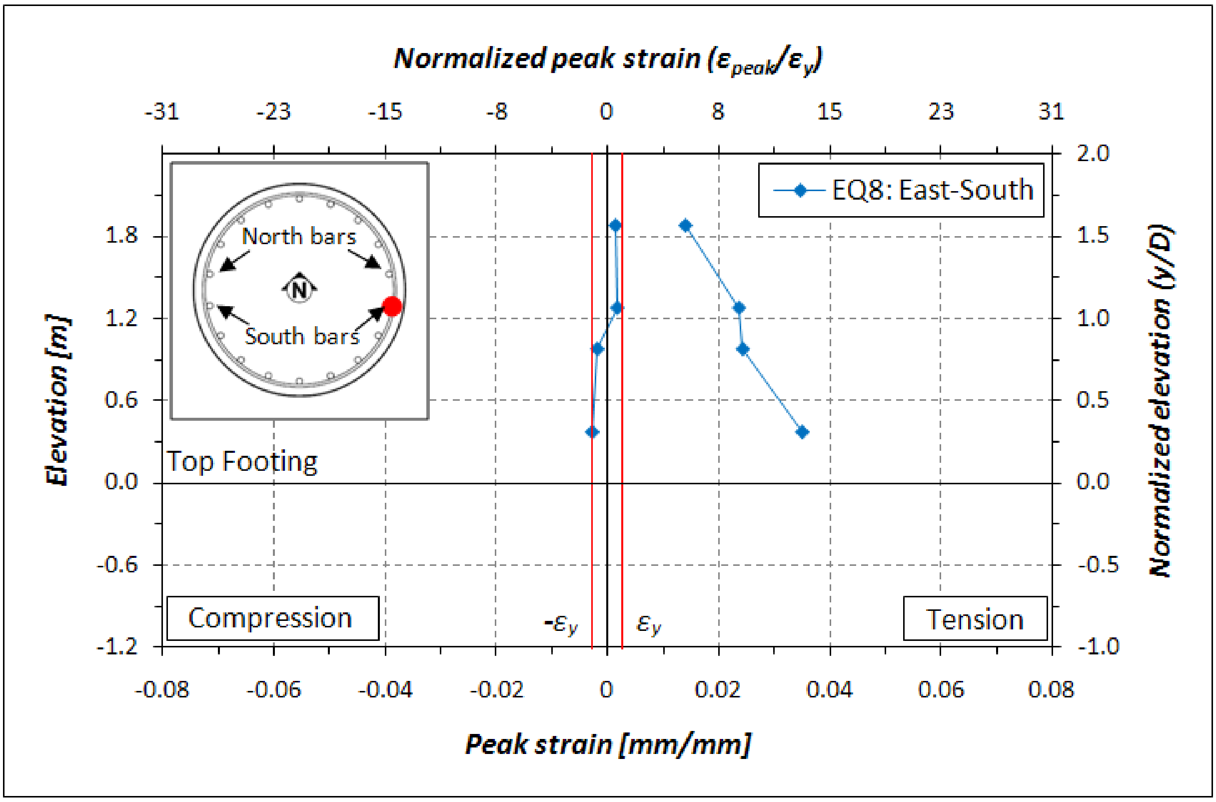

Figure 4.94: Longitudinal bar strain profile for EQ8: East side South bar

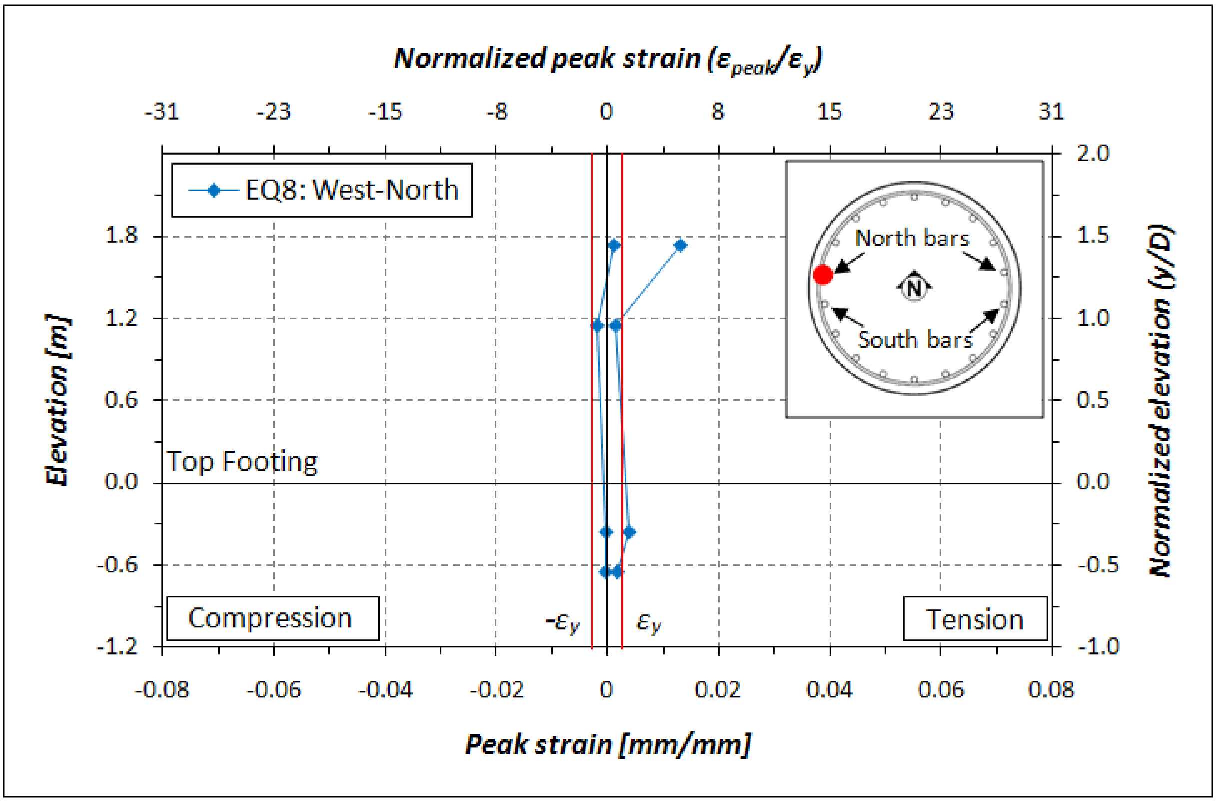

Figure 4.95: Longitudinal bar strain profile for EQ8: West side North bar

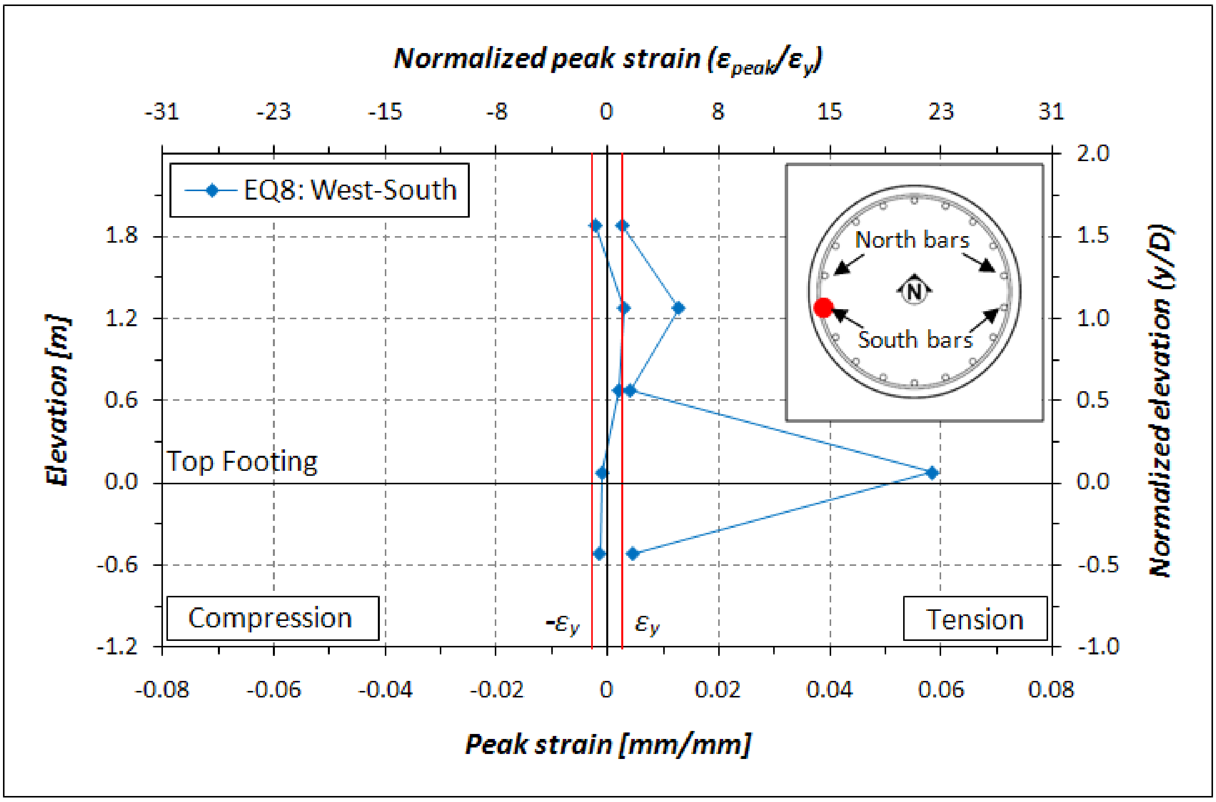

Figure 4.96: Longitudinal bar strain profile for EQ8: West side South bar

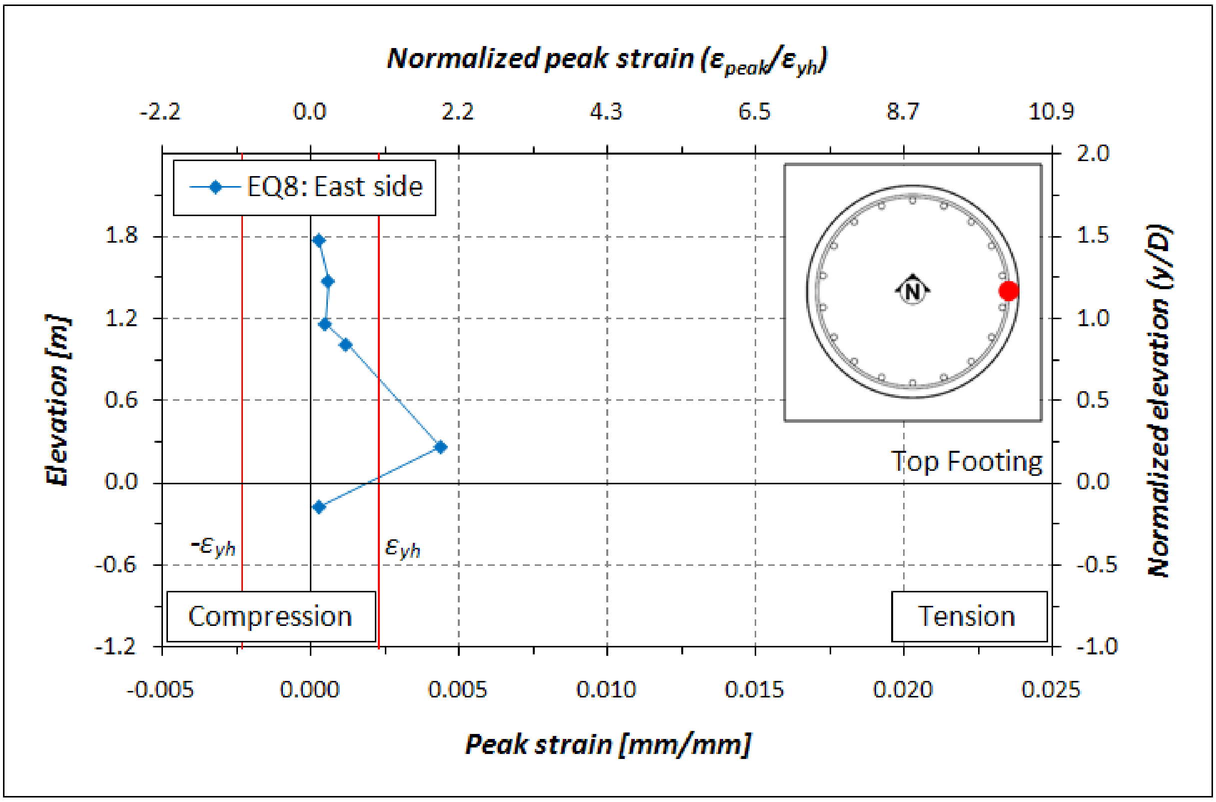

Figure 4.97: Hoops strain profile for EQ8: East side

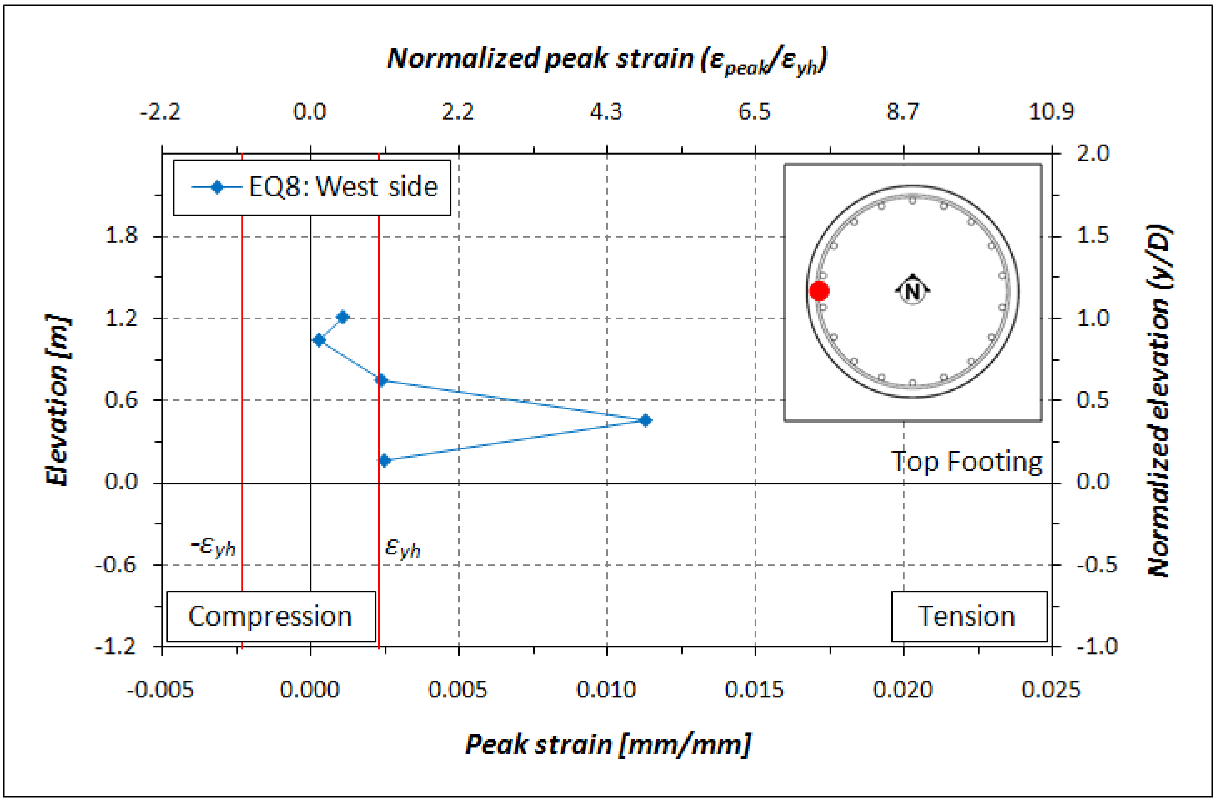

Figure 4.98: Hoops strain profile for EQ8: West side

4.2.9 EQ9 – Takatori 120% scaled

Reversing the polarity of the previous test, a scale factor of 1.2 was used with the original Takatory record for test EQ9.The objective of this test is to bring the specimen to near-collapse conditions.

Three distinct noises of bar fracture were heard during this test. Early in the time history, a third longitudinal reinforcing bar fractured on the East face of the column. The other two noises heard, were two reinforcing bars fracturing on the West side of the column. This is evident as a drop in moment capacity at about 110 rad/km (68.75 rad/mil) in the moment curvature relationship shown in Figure 4.100. Bar fractures can be clearly observed in the videos recorded with the cameras mounted on the specimen. Superficial crushing of the concrete core occurred on both the East and West face of the column. It was accentuated on the East side where two longitudinal bars fractured in the previous test. A post-test view of the East face of the column base is shown in Figure 4.99

The fracture of two longitudinal reinforcing bars occurred in the previous test had a significant influence on the column stiffness, but a less one on its moment carrying capacity. The base moment reaches again the idealized yielding value M_y in the positive quadrant with a smaller slope than the one observed in EQ8, see Figures 4.100 and 4.88. The successive bar fractures occurred during this test produced a relevant stiffness degradation, which can be

Figure 4.99: Column base post-EQ9

identified from the reduced slope characterizing the last hysteresis loops. A ductile response with significant energy dissipation can be observed in the moment-curvature response, which shows large hysteresis loops. A peak moment of 6110.8 kNm (4507.1 kip-ft), corresponding to 1.05·M_y, and a peak curvature of 1.40·10^{-1} rad/m (3.55·10^{-3}), corresponding to 16.70·φ_{ye}, were achieved during EQ9.

A small strength degradation with shear carrying capacity preservation can be appreciated in the base shear versus top displacement response, see Figure 4.101. The base shear does not reach the one corresponding to the analytical idealized yield, but the positive peak value is very close to it. A value of 742.2 kN (166.8 kips), corresponding to 0.95·$V_{b,y}$ and a base shear coefficient of 0.29, was reached during this test. A peak displacement of 635 mm (25.01 in.) or 8.69% drift ratio, corresponding to 7.06·Δ_{ye}, was measured at the top of the column. The same sign polarity of this earthquake with the previous one (EQ8) produced the largest positive residual displacement, equal to 225 mm (8.85 in.) or 3.07% residual drift ratio.

The largest moment at the top of the column was measured during this test. A peak value of 1901.0 kNm (1402.1 kip-ft), corresponding to 31% of the peak moment reached at the column base, can be observed in the negative moment envelope along the column height, see Figure 4.102.

The positive and negative curvature envelopes along the column height are shown in Figure 4.103. Significant curvature values are located from the column base to half column diameter above the footing. This demonstrates that the flexural rotation was primarily lumped to the column base. Reduced curvature with respect to the previous test can be observed in the upper part of the column.

The deformed configuration of the column was essentially a rigid rotation around the plastic region located at the column base, see displacement envelopes in Figure 4.104. A flexural-dominated behavior can be deduced from the different peak displacement components: 463 mm (18.24 in.) from flexure, 23 mm (0.92 in.) from shear, and 97 mm (3.80 in.) from fix end rotation.

The strains envelopes along the instrumented longitudinal bars are plotted in Figures 4.105 to 4.108. Numerous strain gauges had been lost, so that few data are available. No appreciable peak strain changes, with respect to the previous test, can be observed in the North bar of both the East and the West sides. The one at the East side fractured in test EQ8 whereas the one on the West side fractured during this test. A sensible decrease in peak strain, with respect to the previous test, can be seen in the South bar of the East side due to its fracture due to EQ9. A considerable elongation was measured in the South bar of the West side. A peak strain of 6.83% in tension, corresponding to $24.55 \cdot \varepsilon_y$, was reached in this bar (Figure 4.108).

The hoop strain envelopes on the East and West side of the column are shown in Figures 4.109 and 4.110. A strain smaller than the previous test can be observed on both the East and the West envelopes. A peak strain of 0.95% in tension, corresponding to $4.13 \cdot \varepsilon_{yh}$, was recorded on the West side in the third hoop above the column-footing interface.

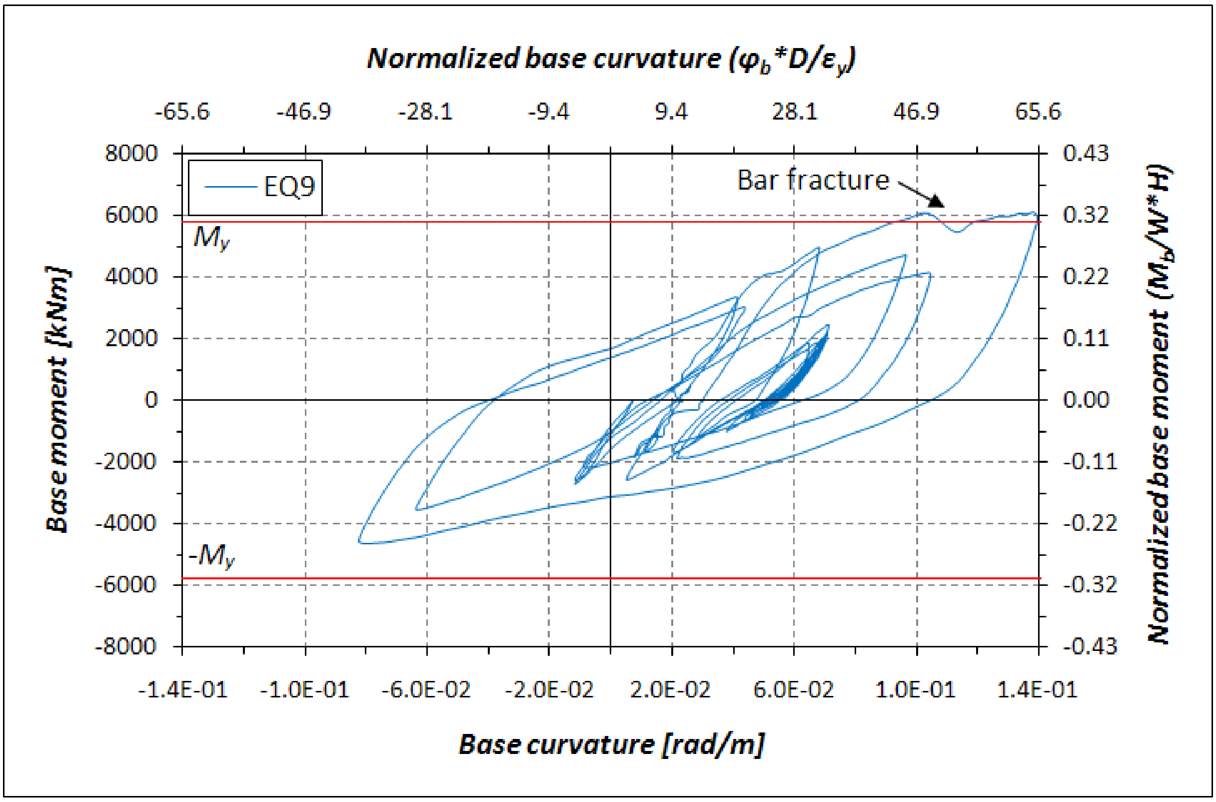

Figure 4.100: Base moment-base curvature response for EQ9

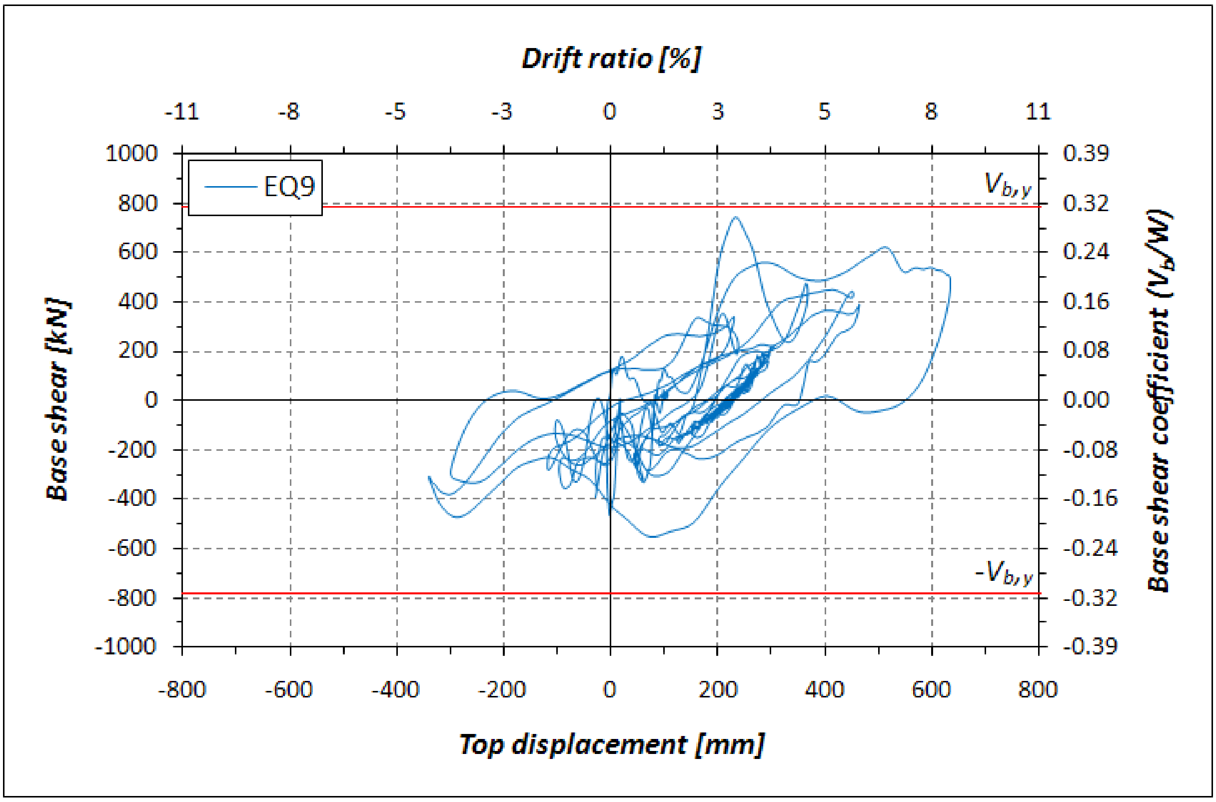

Figure 4.101 Base shear-top displacement response for EQ9

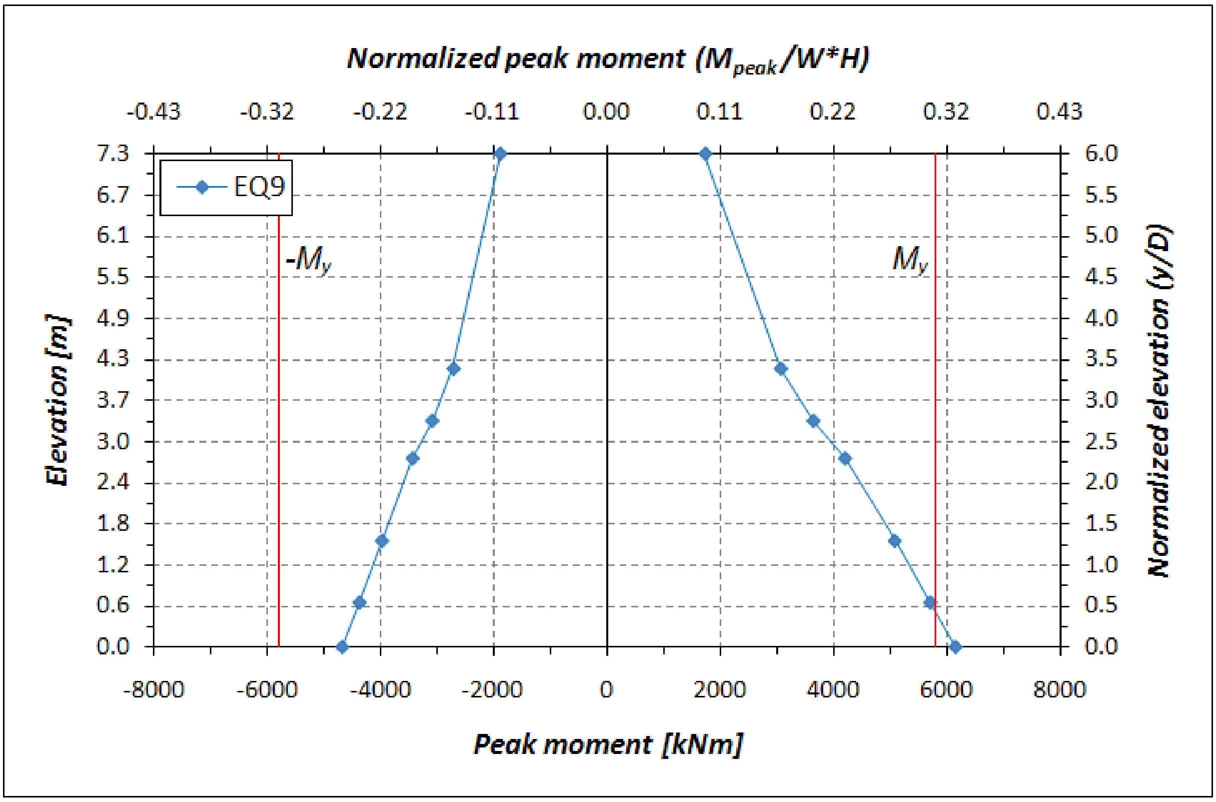

Figure 4.102: Moment envelops along the column height for EQ9

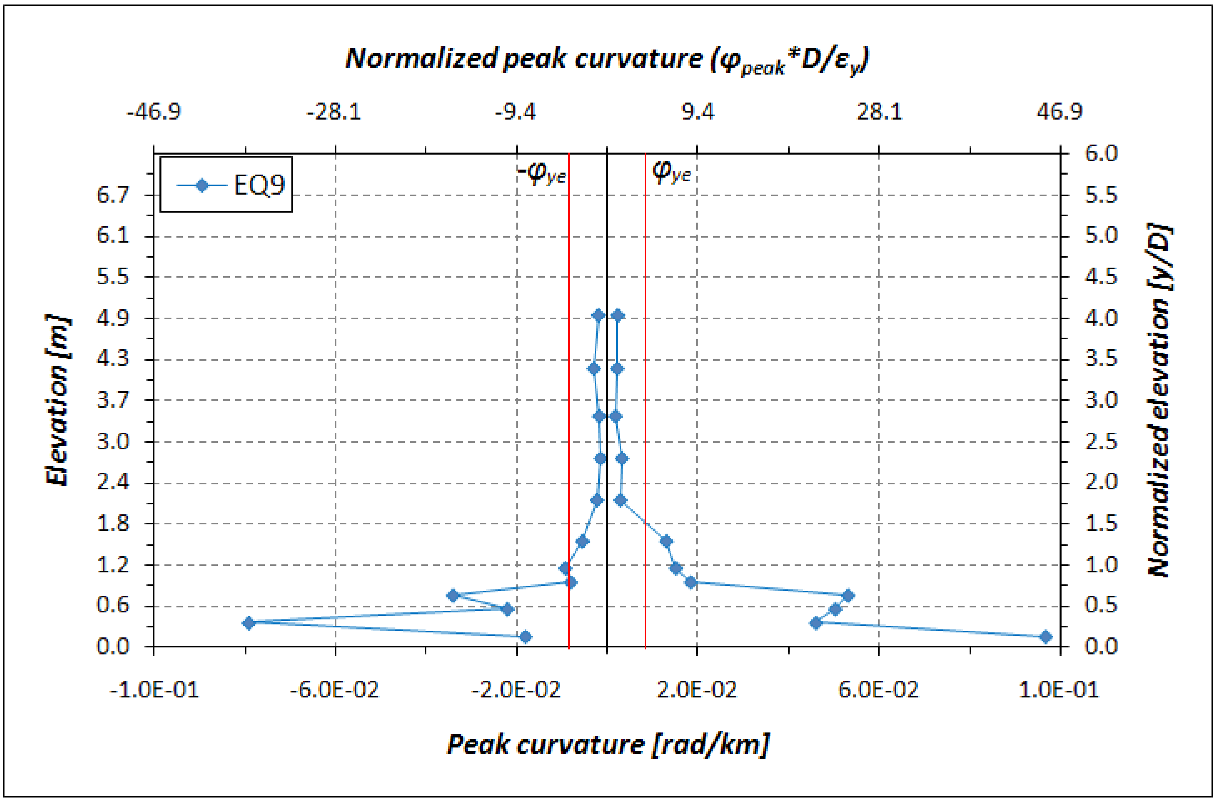

Figure 4.103: Curvature envelops along the column height for EQ9

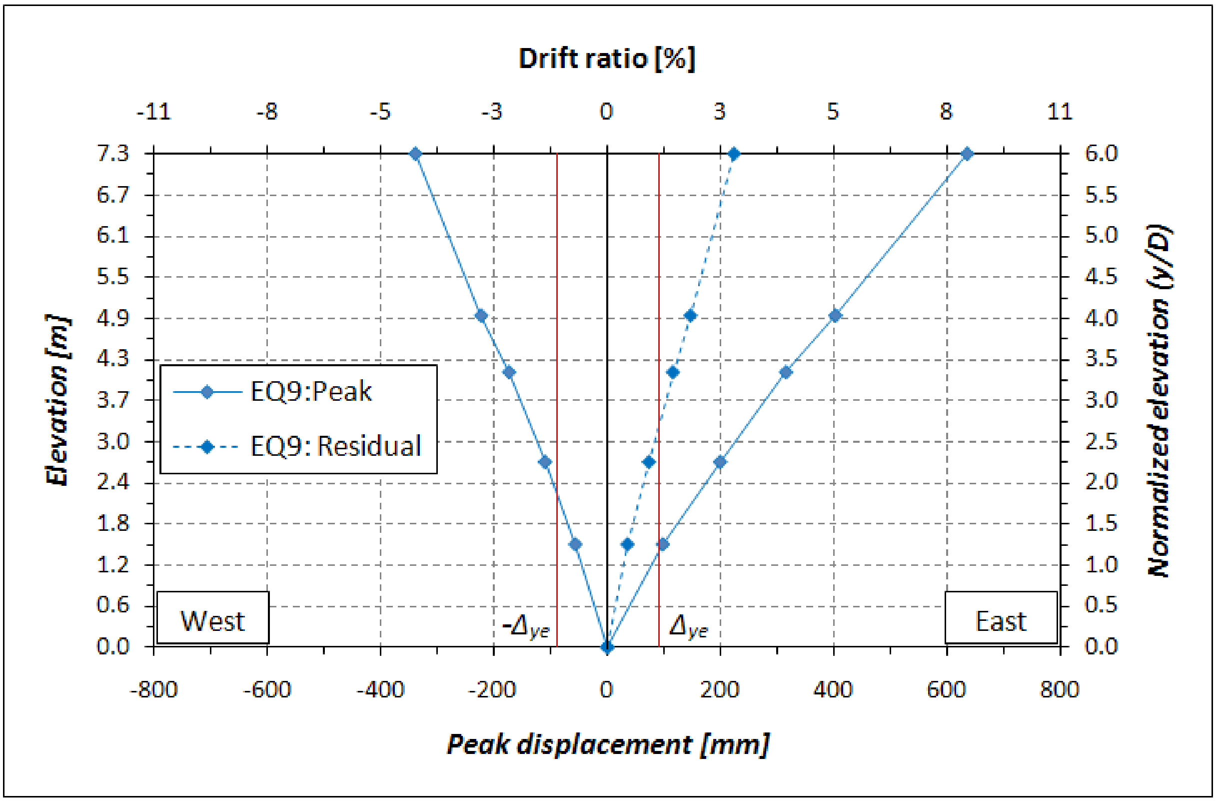

Figure 4.104: Displacement and displacement components envelops along the column height for EQ9

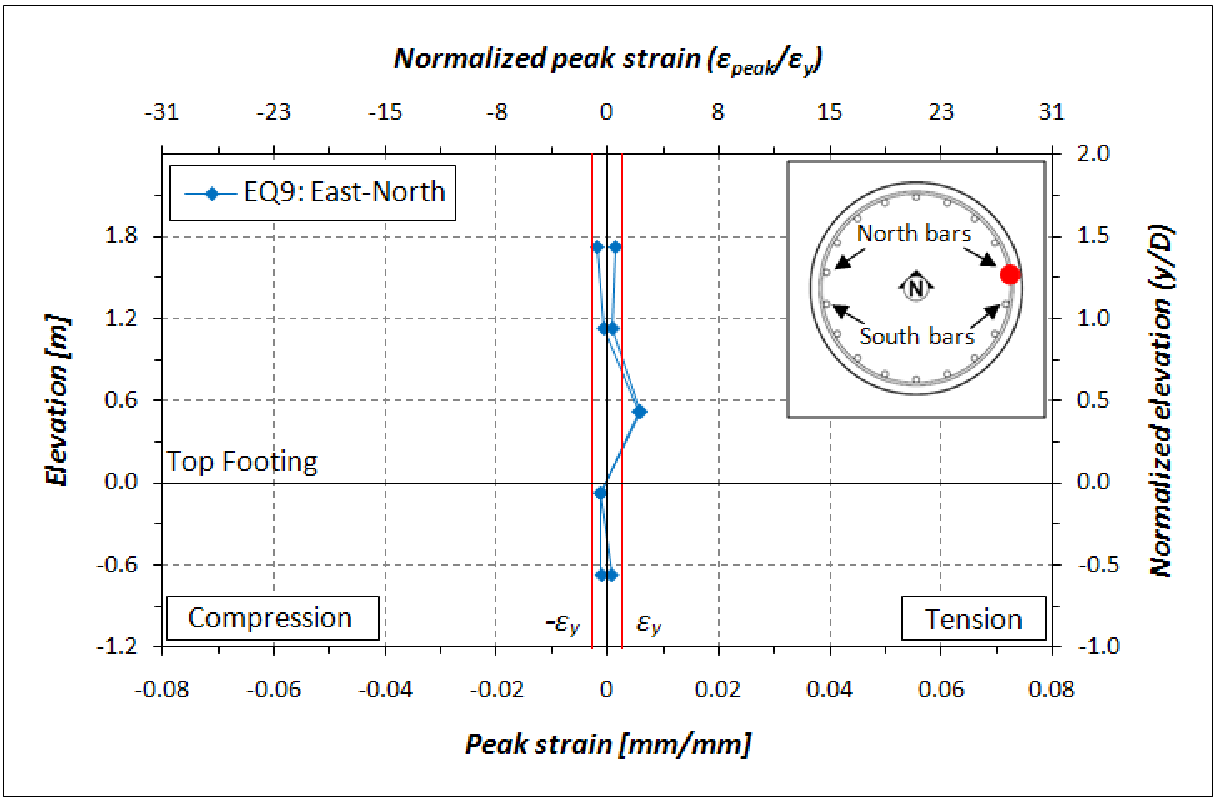

Figure 4.105: Longitudinal bar strain profile for EQ9: East side North bar

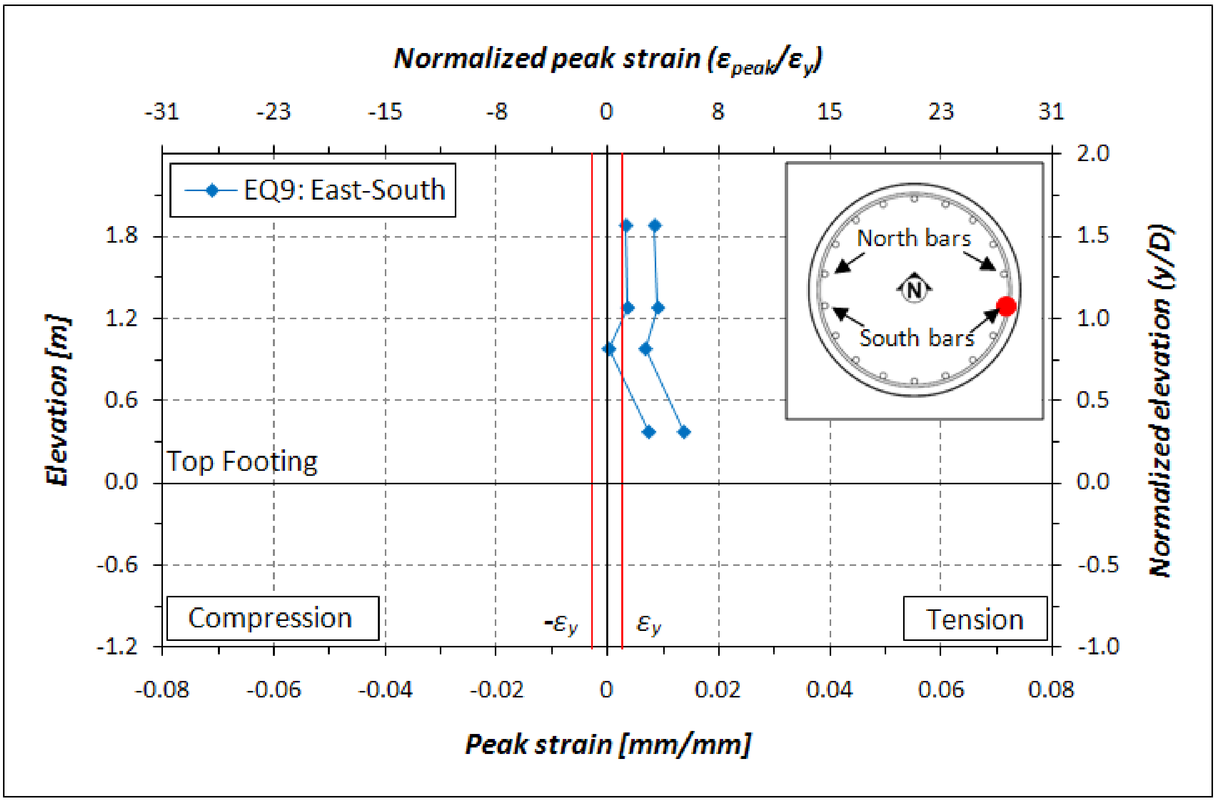

Figure 4.106: Longitudinal bar strain profile for EQ9: East side South bar

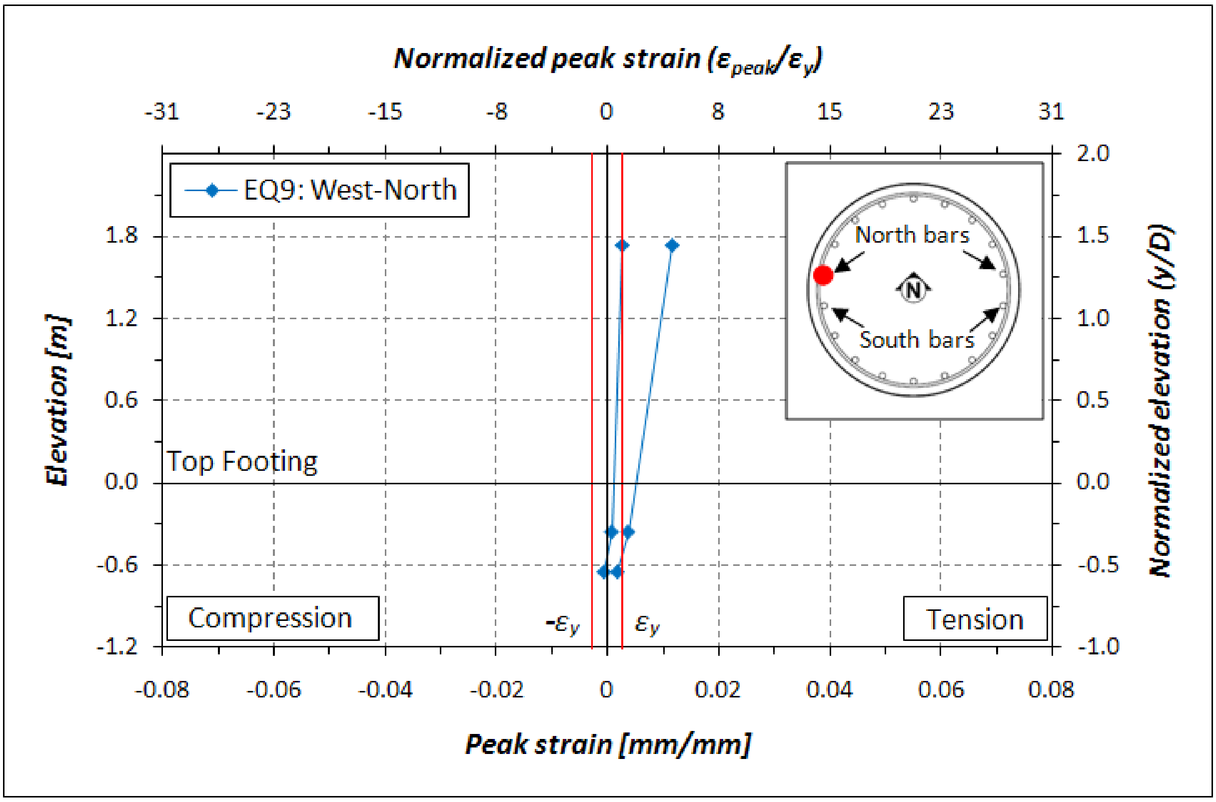

Figure 4.107: Longitudinal bar strain profile for EQ9: West side North bar

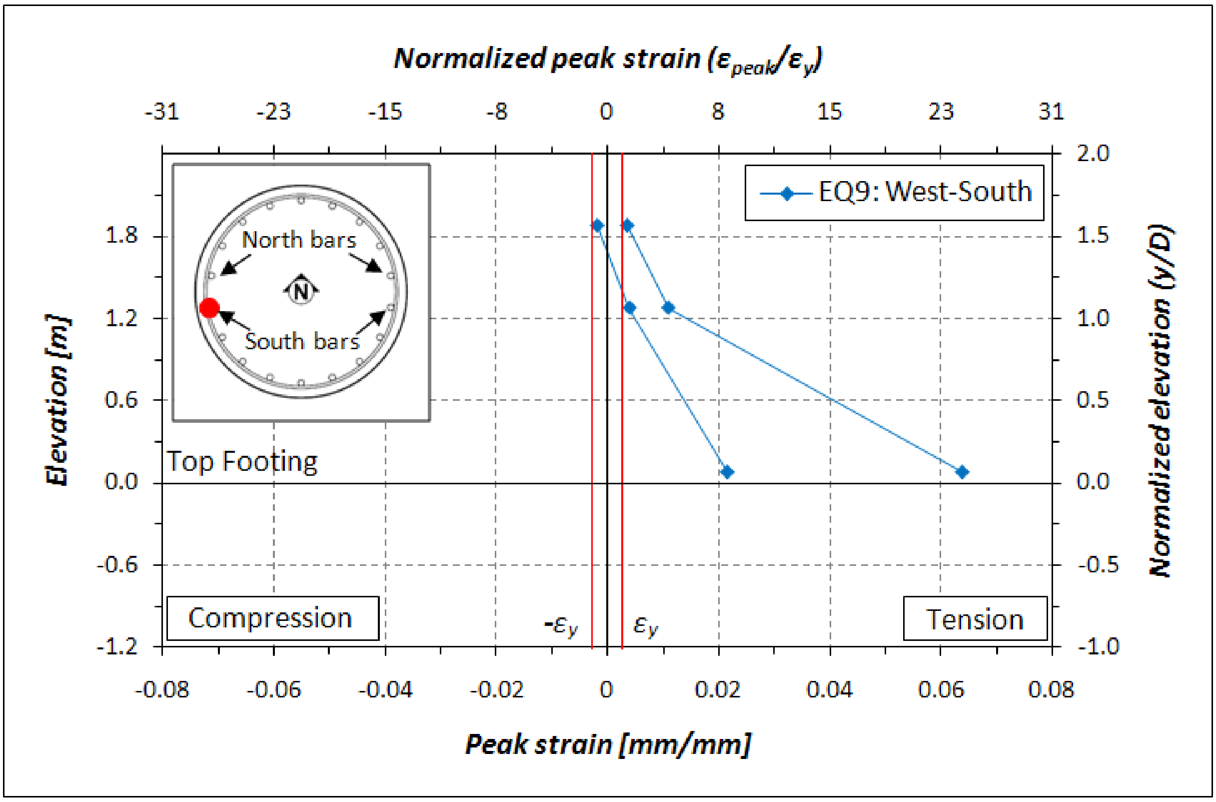

Figure 4.108: Longitudinal bar strain profile for EQ9: West side South bar

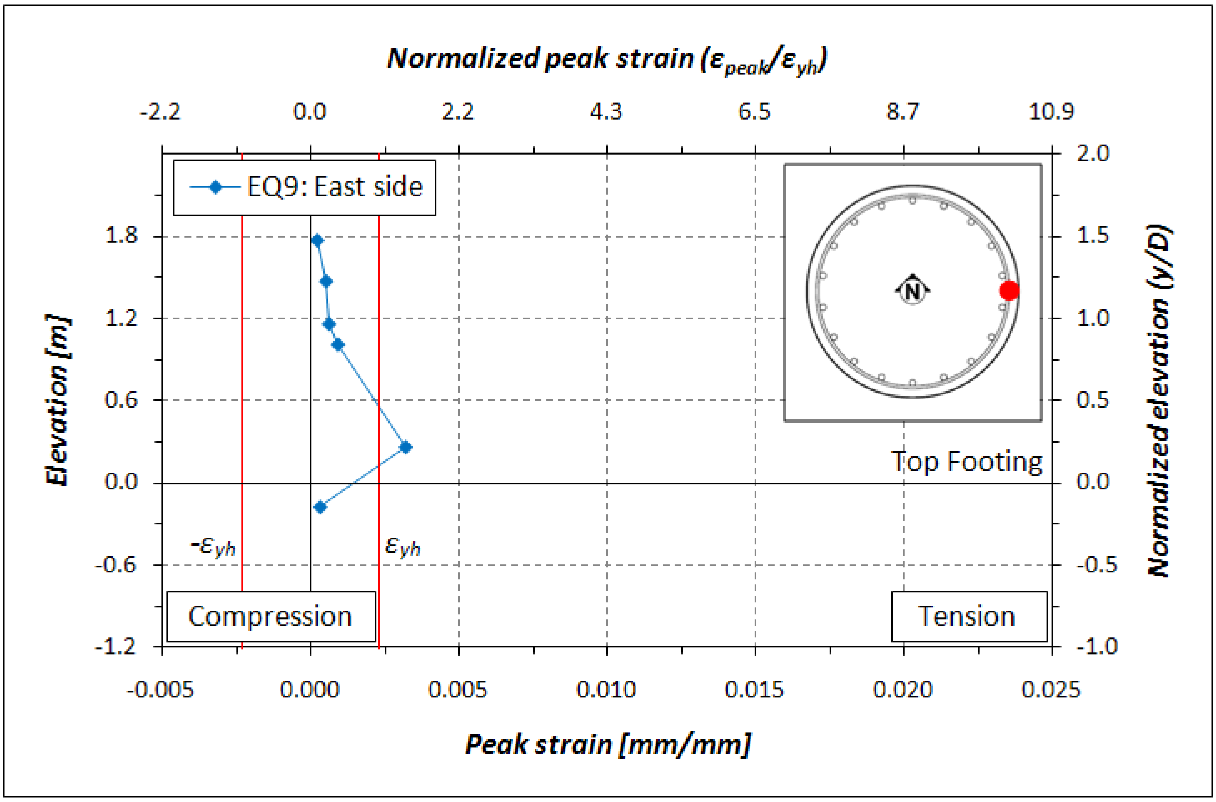

Figure 4.109: Hoops strain profile for EQ9: East side

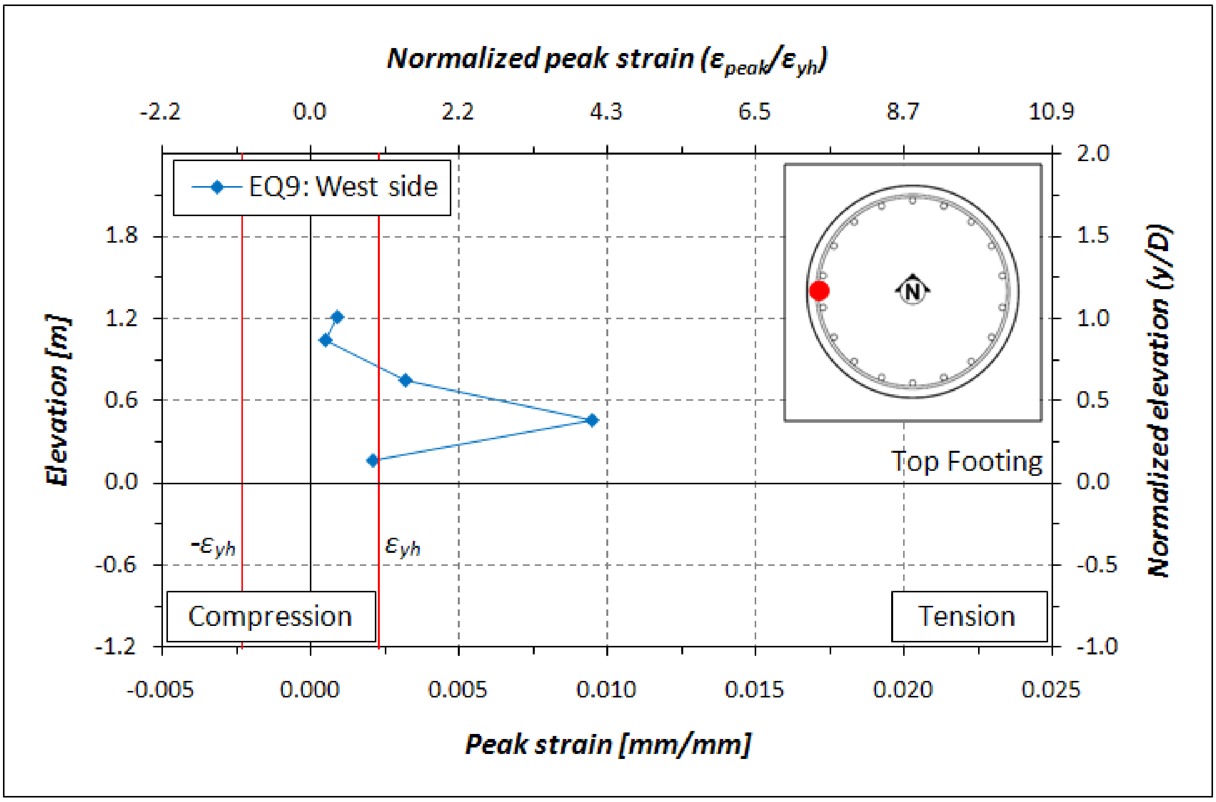

Figure 4.110: Hoops strain profile for EQ9: West side

3.2.10 EQ10 – Takatori 120% scaled

The Takatori record, scaled by 120%, was repeated again with a consistent polarity of the previous test. The objective of EQ10 was to bring the specimen to a near-collapse conditions.

During this test the superstructure impacted the safety column located on the East side. For this reason, the results obtained under EQ10 excitation does not correctly represent the column response and consequently are not reported.

Prior earthquake simulation tests resulted in a reduced column capacity caused by the fracture of five longitudinal bar. A fourth longitudinal reinforcing bar fractured on the East face of the column in this test. However, the superstructure impacted the East safety column before fracture occurred. During impact, the column displacement was 757 mm (29.79 in.). The displacement ductility and the drift ratio were 8.7 and 10.34% respectively. Vertical offset of the transverse hoops caused by the buckled longitudinal reinforcement was evident on the East side. However transverse reinforcement did not fracture. A post view of the East face of the column base is shown in Figure 4.111.

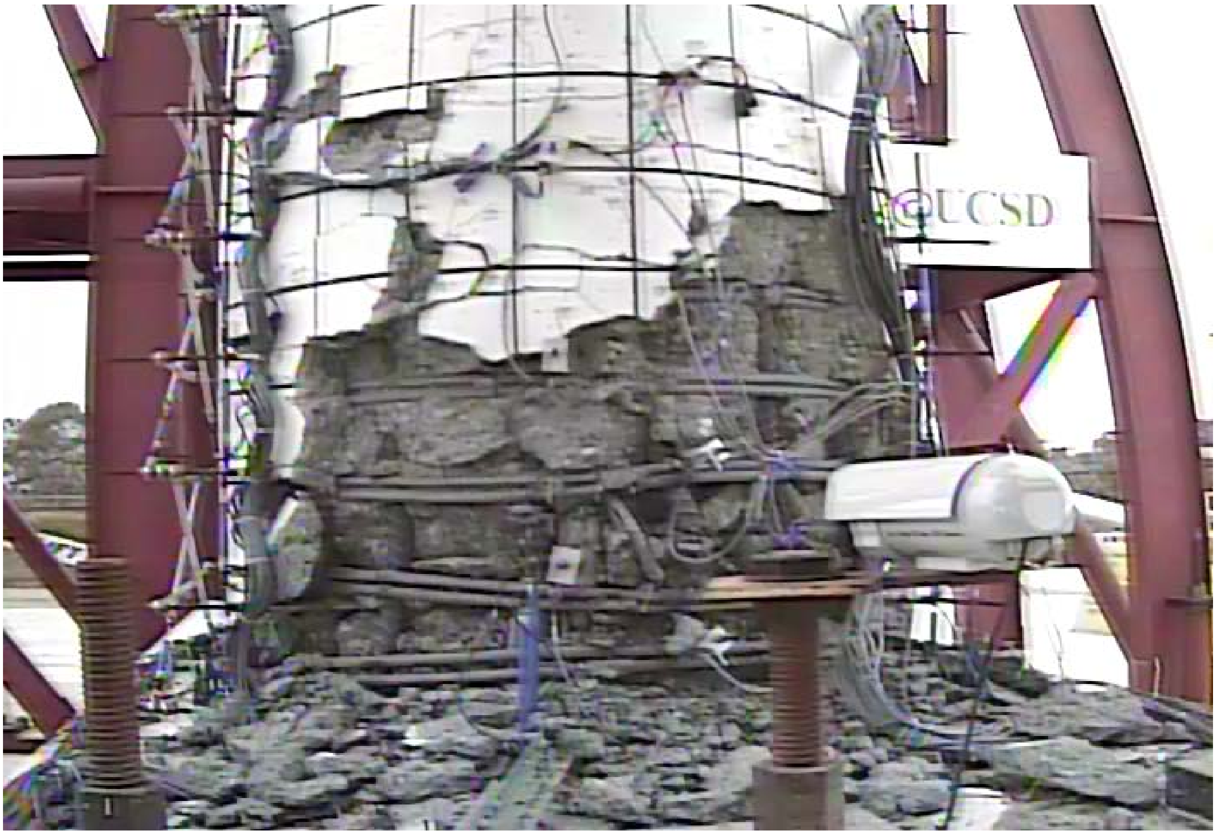

Figure 4.111: Column base post-EQ10

4.3 Tests results summary

4.3.1 Peak response parameters

Figures 4.112 to 4.117 show the peak positive and negative experimental response parameters. The peak in tension and compression of the recorded strains are summarized in Table 4.1. The experimental idealized values of yield curvature, φ_{ye}, and displacement, Δ_{ye}, are used to compute the ductilities shown in Table 4.2.

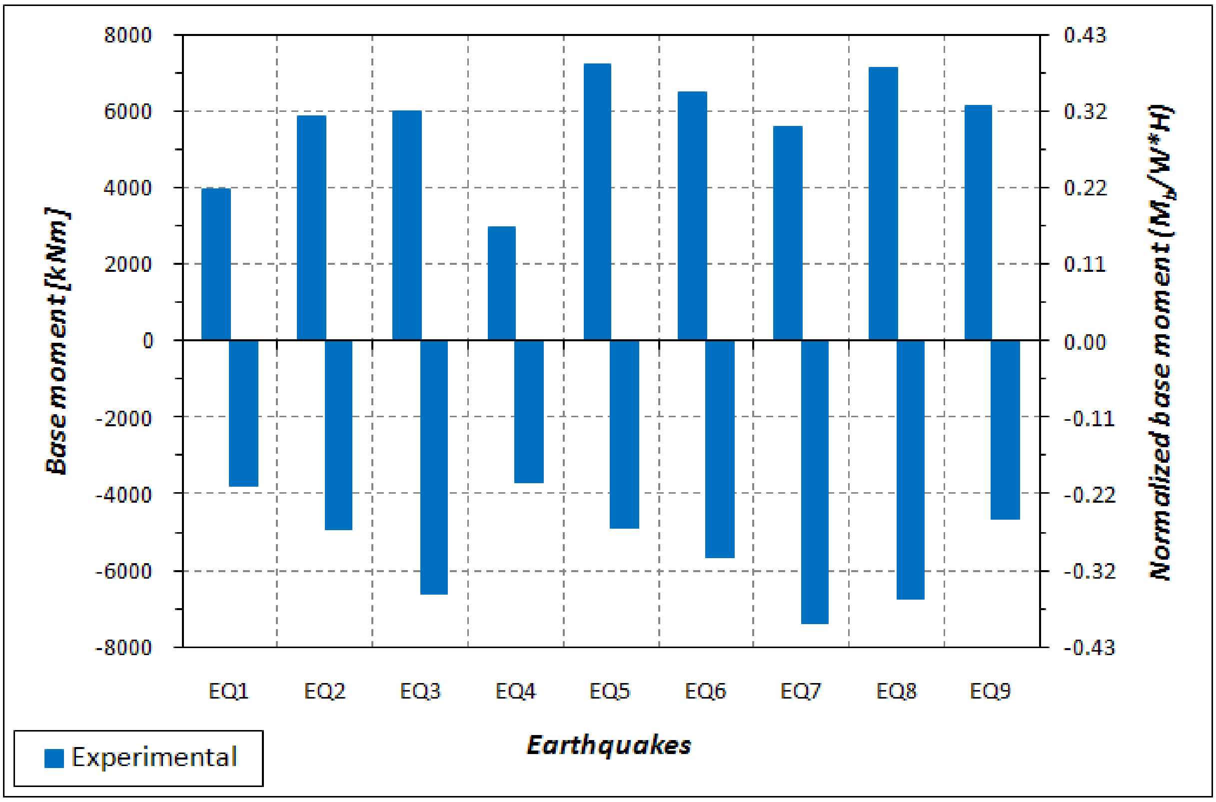

Figure 4.112: Experimental peak base moment

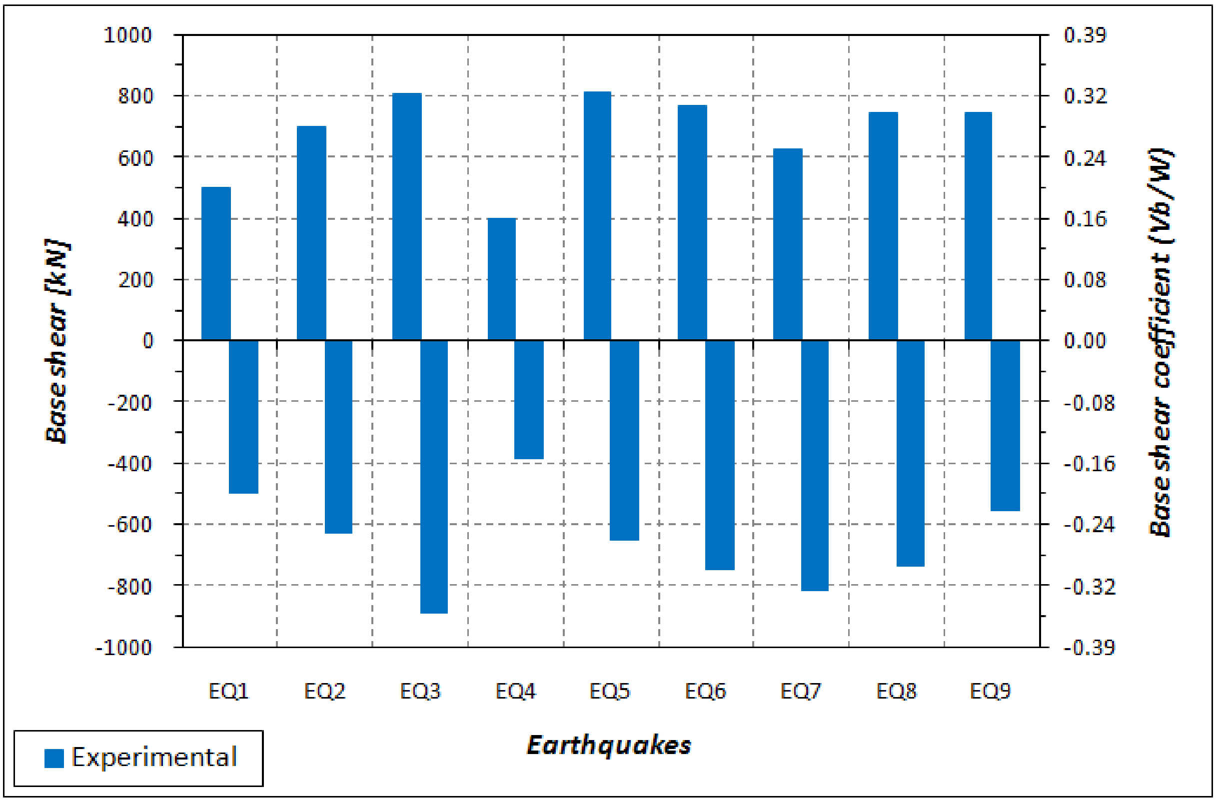

Figure 4.113: Experimental peak base shear

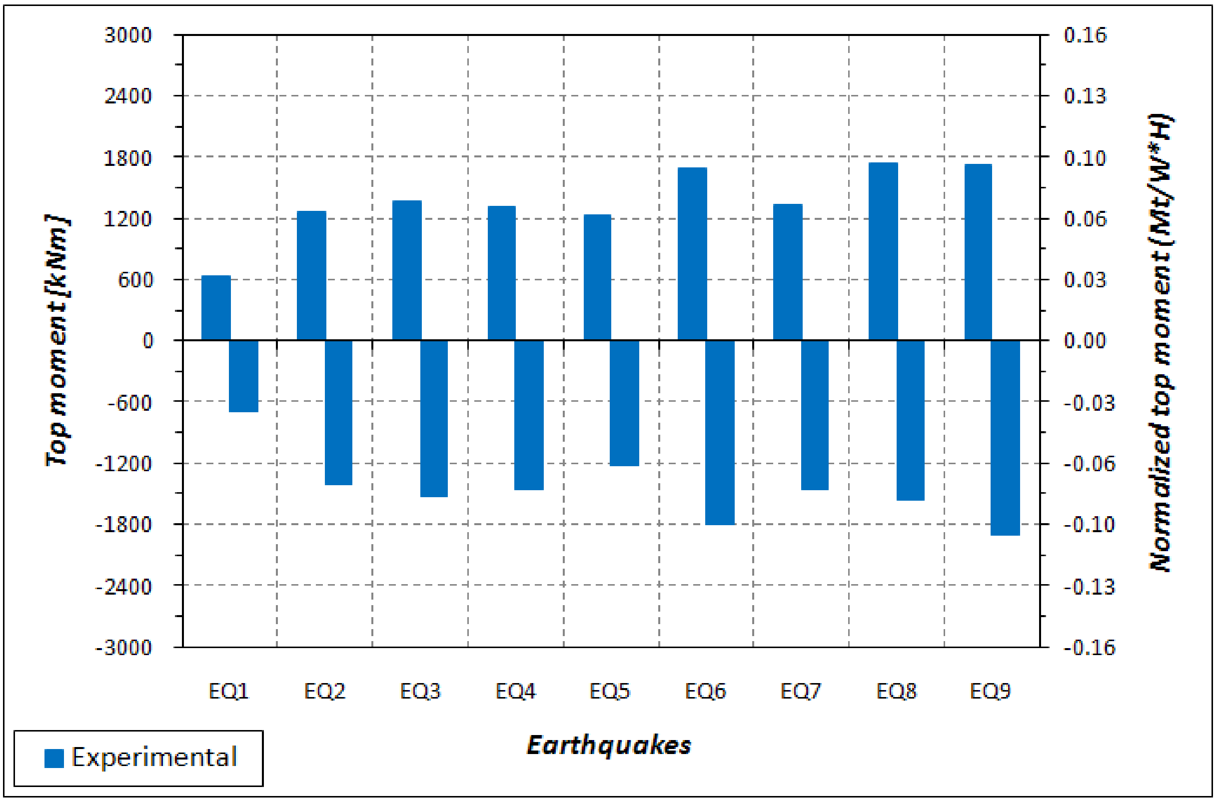

Figure 4.114: Experimental peak top moment

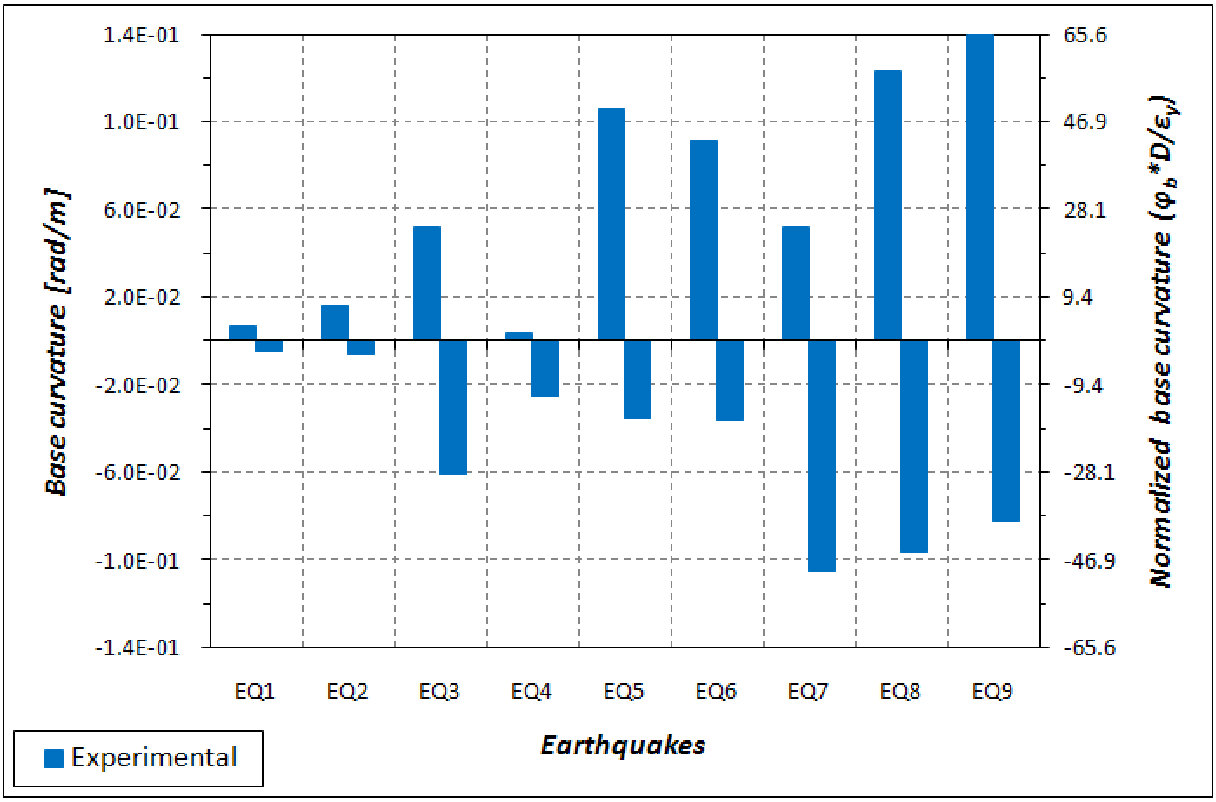

Figure 4.115: Experimental peak base curvature

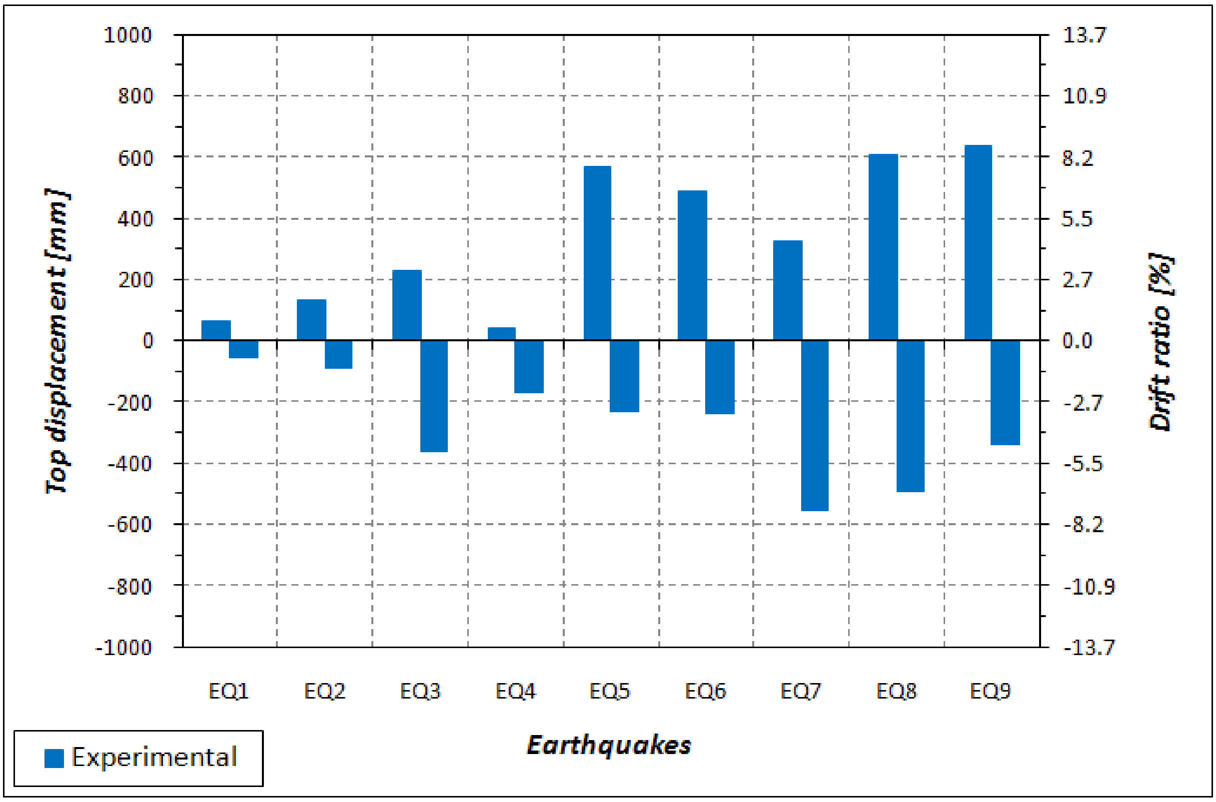

Figure 4.116: Experimental peak top displacement

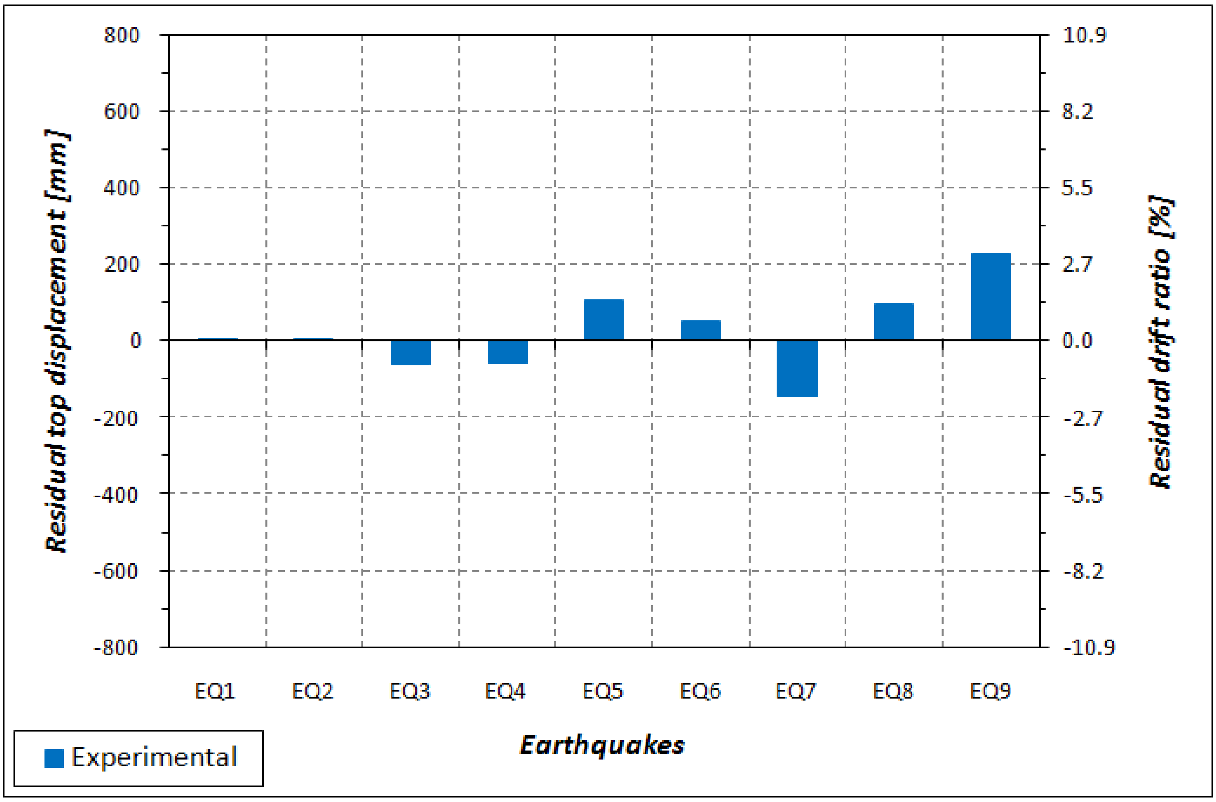

Figure 4.117: Experimental residual displacement

Test	Peak longitudinal strain (%)		Peak transverse strain (%)	
	Positive	Negative	Positive	Negative
EQ1	0.22	-0.17	0.19	-
EQ2	1.32	-0.27	0.29	-
EQ3	2.98	-1.47	0.29	-
EQ4	1.44	-0.59	0.16	-
EQ5	4.66	-1.55	2.46	-
EQ6	4.23	-1.63	1.03	-
EQ7	4.28	-0.91	0.81	-
EQ8	5.84	-0.40	1.13	-
EQ9	6.38	-0.19	0.95	-

Table 4.1: Peak strain on longitudinal and transverse reinforcement

Test	Curvature ductility	Displacement ductility
EQ1	0.81	0.69
EQ2	1.87	1.48
EQ3	7.27	4.01
EQ4	3.00	1.89
EQ5	12.60	6.33
EQ6	10.96	5.44
EQ7	12.55	6.15
EQ8	14.75	6.74
EQ9	16.70	7.06

Table 4.2: Experimental curvature and displacement ductilities

4.3.2 Displacement components

Figure 4.118 shows in percentage the influence of the three displacement components (flexure, shear, fix-end rotation) on the maximum and minimum top relative displacement. In Figure 4.119 the top displacement measured by the LVDTs are compared to the ones

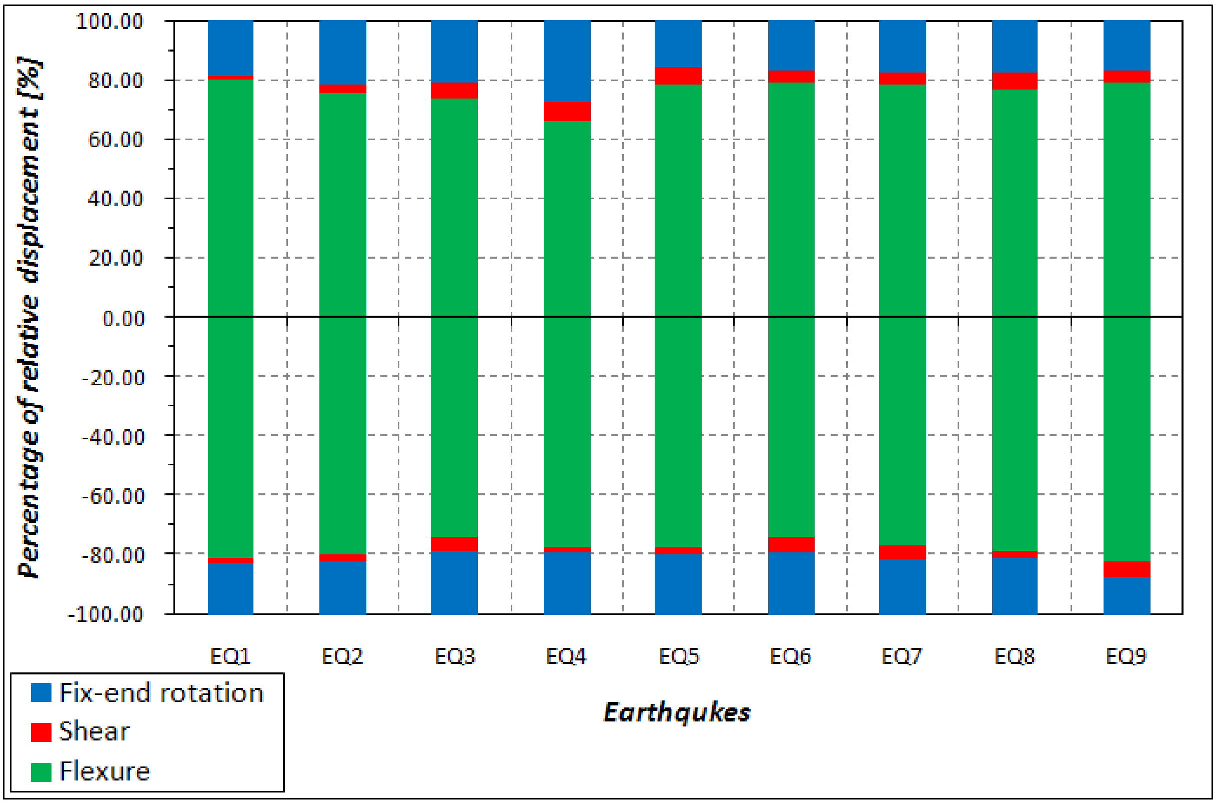

Figure 4.118: Percentage of displacement components

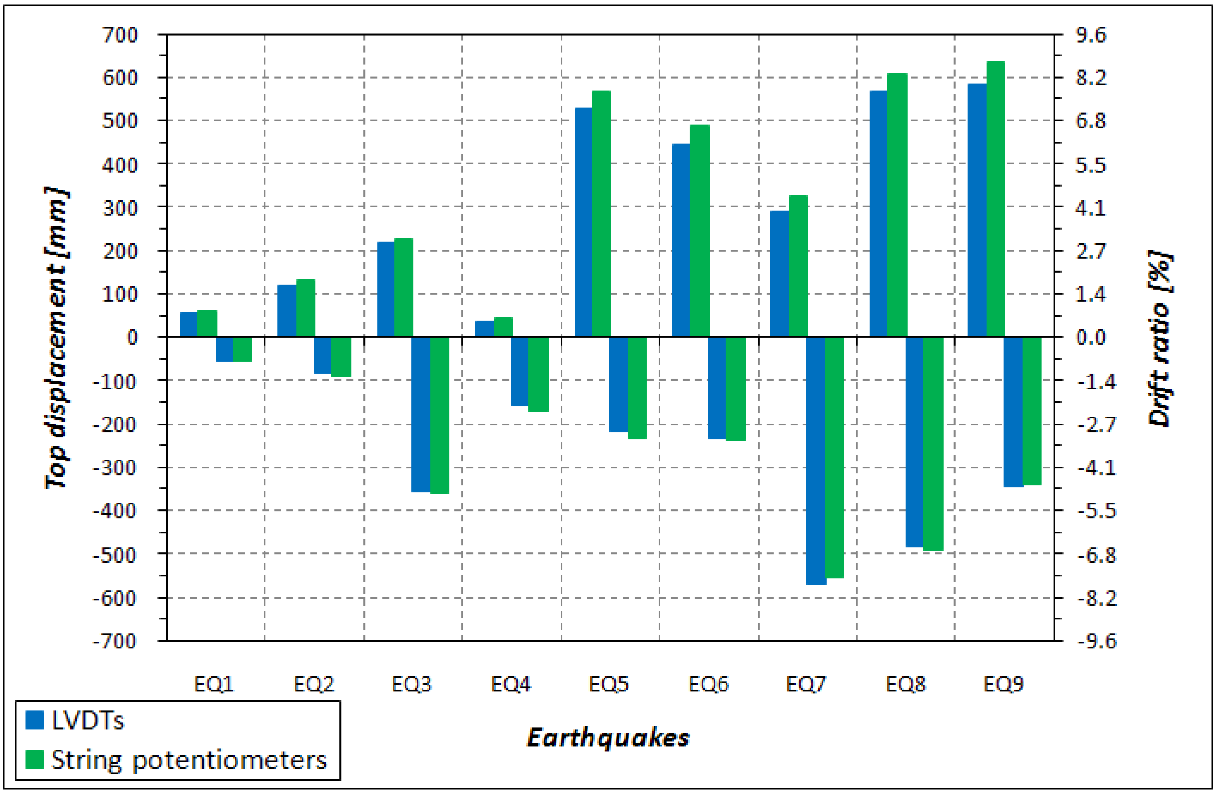

Figure 4.119: LTDTs and string potentiometers measurement of the top relative displacement

measured by the string potentiometers: good agreement is observed with errors less than 15%.

4.3.3 Summary

The column exhibited a ductile behavior, with a maximum displacement ductility of 7.06, where the displacement ductility is defined as the peak displacement recoded during seismic excitation divided by the experimental idealized yield displacement Δ_{ye}, which is equal to 90 mm (3.54 in.).

An essentially linear elastic response was obtained during test EQ1. A discontinuous and less than 0.1-mm (0.004-in.) thick crack was identified on the East, South, and West side of the column-footing interface. Localized yielding may have occurred on one of the monitored longitudinal reinforcing bar.

The column deformations exceeded the elastic limit during test EQ2. Crack propagation occurred at the column-footing interface and additional horizontal cracks formed at the base and along the column height. The presence of horizontal cracks proves a flexure-dominated behavior of the specimen. Localized yielding was measured by the strain gauges on the longitudinal bars near the column-footing interface.

A residual displacement of -63 mm (-2.49 in.), corresponding to -0.87% residual drift ratio, was observed after EQ3, proving a significant non-linearity in the column response. A recorded peak shear of 887.4 kN (199.5 kips) was the largest measured during any tests. Spalling of concrete cover was initiated under this earthquake, whit an observed maximum height of 1.143 m (3.75 ft) on the West side. All four monitored bars yielded in tension, showing a large post-elastic deformation. A yield-length of 1.5 and 1.0 column diameter can be observed on the monitored bars located at the East and West side, respectively.

A nearly linear response was recorded during test EQ4. The column substantially oscillated around an inclined configuration corresponding to the large residual displacement after EQ3. Due to damage cumulated in the specimen from the tests, resulting in a substantial period shift, Corralitos record induced a smaller demand when reproduced as EQ4 compared to EQ2. Spalled regions slightly enlarged during EQ4.

A ductile nonlinear response was obtained during EQ5. More than 51-mm (2-in) deep concrete spalling was observed on both the East and West side of the column. The spalling area laterally increased on the West side, preserving the same maximum height of 1.143 m (3.75 ft) observed at the end of EQ3. Similarly, spalling occurred on the East side with a maximum height of 762 mm (30 in.). Onset of longitudinal bar buckling was observed on this side; at least two of the visible bars were barely bent between the first and the third hoops above the column-footing interface.

No significant damage was induced in the specimen during EQ6.

A peak moment of 7378.0 kNm (5441.7 kip-ft) was recorded during EQ7 excitation. This value corresponds to the maximum overturning moment measured during the entire set of tests. Longitudinal reinforcement buckling was observed on both the East and West side of the column base, but bar fracture did not occur. The concrete core started suffering superficial crushing in proximity of the buckled bars.

Two longitudinal reinforcing bars on the East side of the column fractured during EQ8, following buckling of these uncovered bars.

Three longitudinal reinforcing bar, one on the East side and two on the West side, fractured during EQ9. Even with five bars fractured, the column preserved its vertical load carrying capacity.

A forth longitudinal reinforcing bar fractured on the East side during EQ10. However, this happened after the superstructure mass impacted the East safety column.

The specimen globally exhibited flexural-dominated behavior, as confirmed by the mainly horizontal crack pattern and the recorded instrumentation data.

The primary failure mechanism of the column consisted of buckling and subsequent fracture of the longitudinal reinforcement after hoops yielded. Fracture occurs as the consequence of stress concentration in the maximum compressive fiber of the buckled bar, in proximity of the bar rib: micro-crack form under compression and then propagate when the bar is loaded in tension. Onset and propagation of the crack can be observed in Figure 4.120.

At the end of testing, longitudinal reinforcing bars were extracted from the specimen. Buckling involved thirteen bars, which showed an average bent length of about 305 mm (12 in.), corresponding to twice the hoop spacing. Fracture completely occurred on seven buckled bars, while only onset of crack propagation was observed in other two of them. The positions and the status of any longitudinal reinforcing bar are shown in Figures 4.121 to 4.139.

Figure 4.120: Bar fracture mechanism

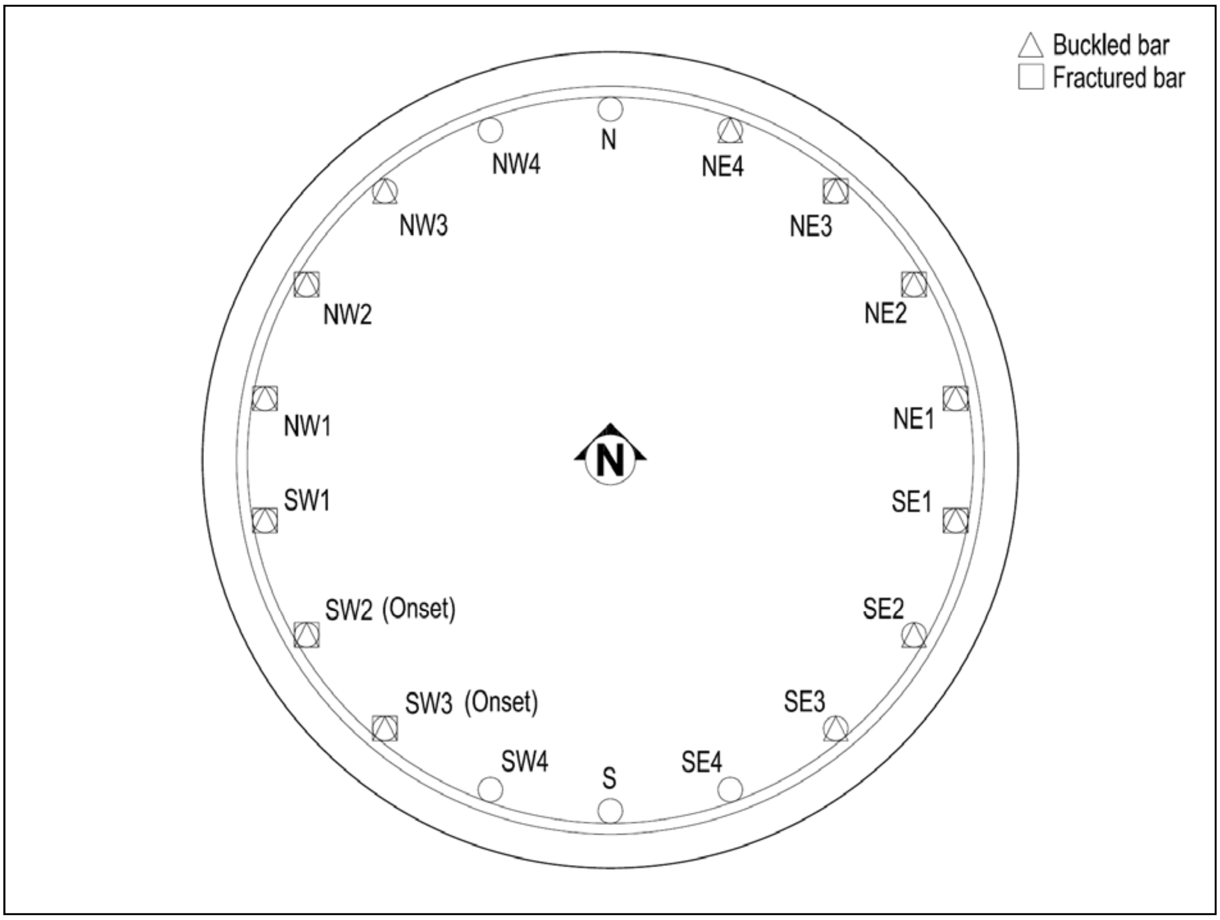

Figure 4.121: Longitudinal bars layout

Figure 4.122: SE1-bar: fractured

Figure 4.123: SE2-bar: buckled

Figure 4.124: SE3-bar: buckled

Figure 4.125: SE4-bar: straight

Figure 4.126: SW1-bar: fractured

Figure 4.127: SW2-bar: accentuated onset of crack propagation

Figure 4.128: SW3-bar: barely onset of crack propagation

Figure 4.129: SW4-bar: straight

Figure 4.130: S-bar: straight

Figure 4.131: NE1-bar: fractured

Figure 4.132: NE2-bar: fractured

Figure 4.133: NE3-bar: fractured

Figure 4.134: NE4-bar: buckled

Figure 4.135: NW1-bar: fractured

Figure 4.136: NW2-bar: fractured

Figure 4.137: NW3-bar: buckled

Figure 4.138: NW4-bar: straight

Figure 4.139: N-bar: straight

5. Comparison of analytical and experimental results

This chapter presents a comparison between experimental and analytical results, and some considerations about the evolution of the moment diagram along the column height under the earthquake sequence.

5.1 Peak response parameters

Figures 5.1 to 5.6 show a comparison of the peak positive and negative response quantities obtained from the analytical model and the experimental tests. Base moment, base curvature, base shear, top displacement, top moment, and residual displacement are considered.

Figure 5.1 shows the peak moment reached at the base of the column during each earthquake. The analytical model overestimates both the peak positive and negative moment during EQ1, with an error of +24%. Perfect agreement can be seen from the comparison of the peak positive moment obtained in EQ2, whereas an error of +19% is observed in the peak negative response. An underestimation of peak moment, in both the positive and negative bending direction, is obtained from the analytical model for EQ3, with an error of -1% and -

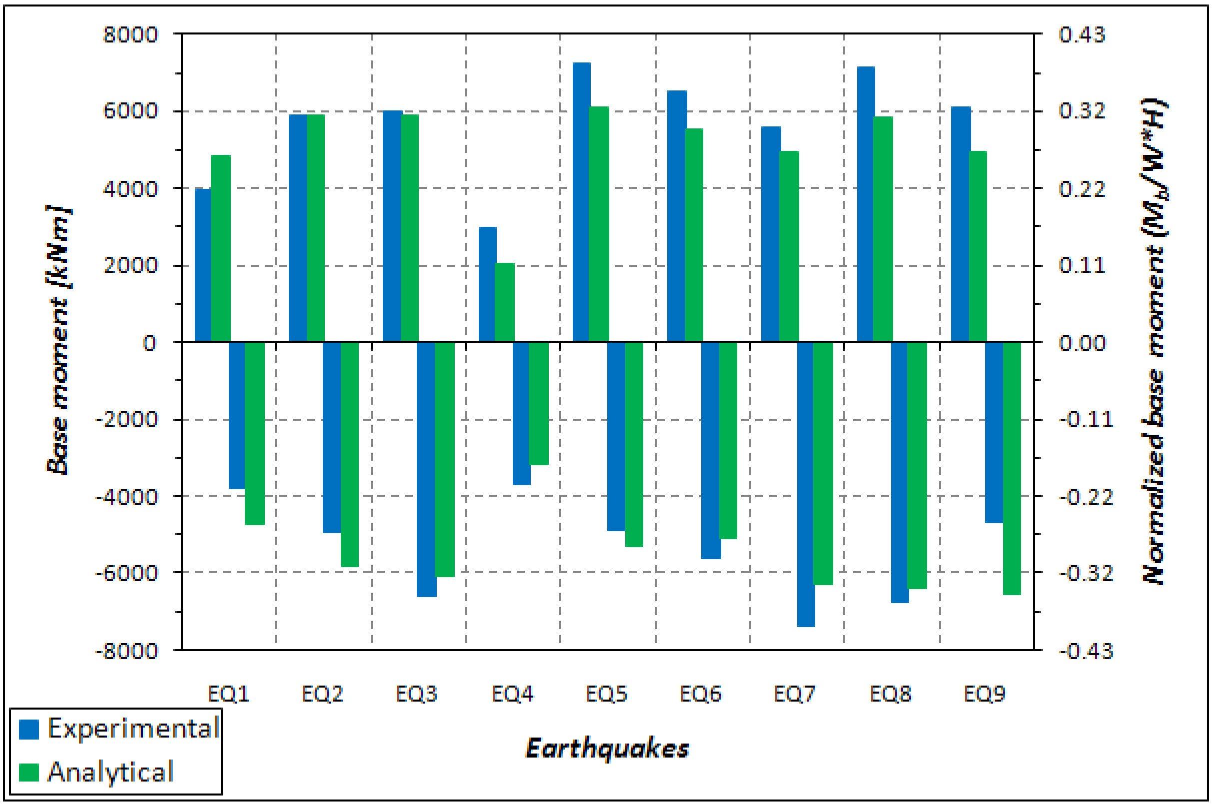

Figure 5.1: Experimental and analytical peak base moment

8%, respectively. Large disagreement can be observed from the results comparison of EQ4: -30% and -14% are respectively the errors computed for the peak positive and negative moment. After EQ4, the base moment prediction loses some accuracy; however, due to the limitation on the moment caused by section plasticization, this error remains lower than ±30%.

Figure 5.2 shows the peak base shear reached during each earthquake. The analytical model overestimates the peak shear for EQ1, with an error of +23% for the positive value and +25% for the negative one. The overestimation of the peak shear becomes larger in EQ2; the errors for positive and negative values are +42% and +30%, respectively. Good agreement between analytical and experimental results is obtained in EQ3; the positive peak shear is overestimated of 6% and the negative one underestimated of only 1%. After EQ3 the base shear response is controlled by plasticization, resulting in quite good agreement between analytical and experimental values even when deformation are badly predicted.

A less accurate prediction is obtained in terms of the peak moment at the top of the column, see Figure 5.3. The model overestimates this quantity for the first three earthquakes with a variable percentage errors; a minimum error of +13% is obtained for the peak negative moment in EQ1, and a maximum error of 67% is obtained for the peak negative moment in EQ2.

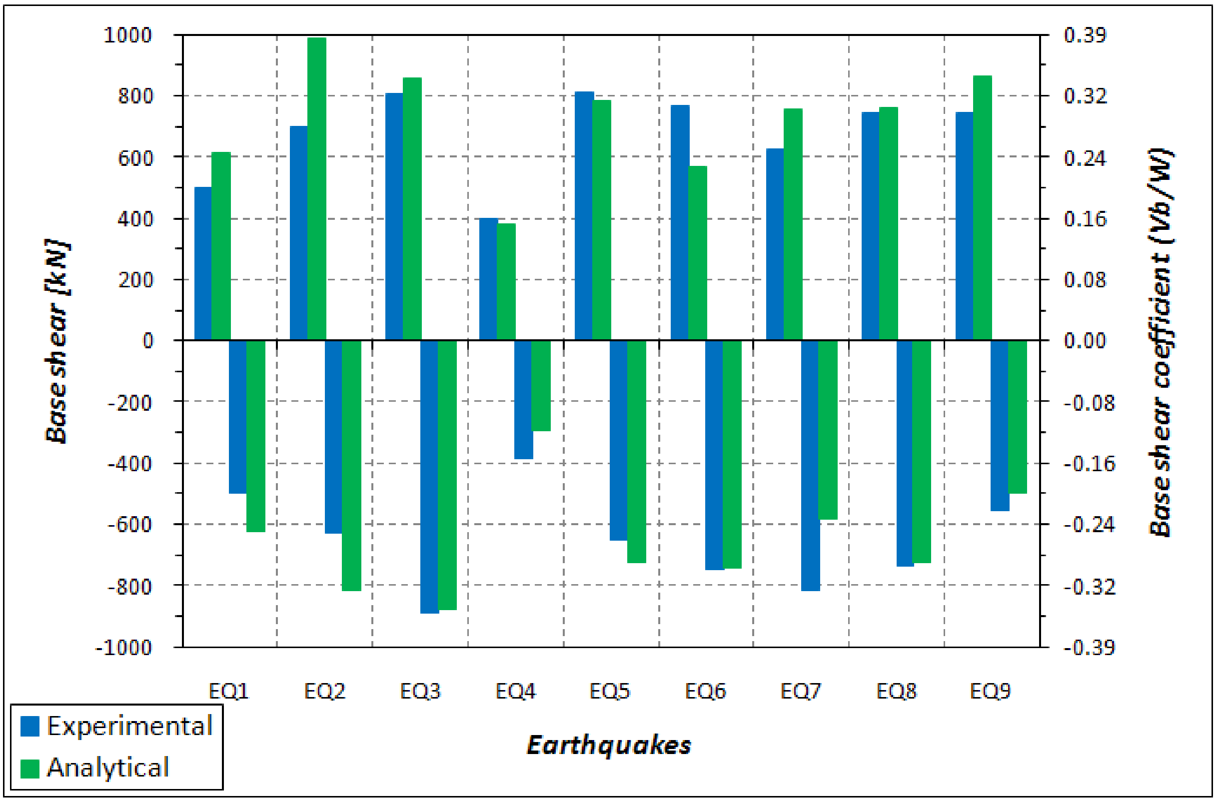

Figure 5.2: Experimental and analytical peak base shear

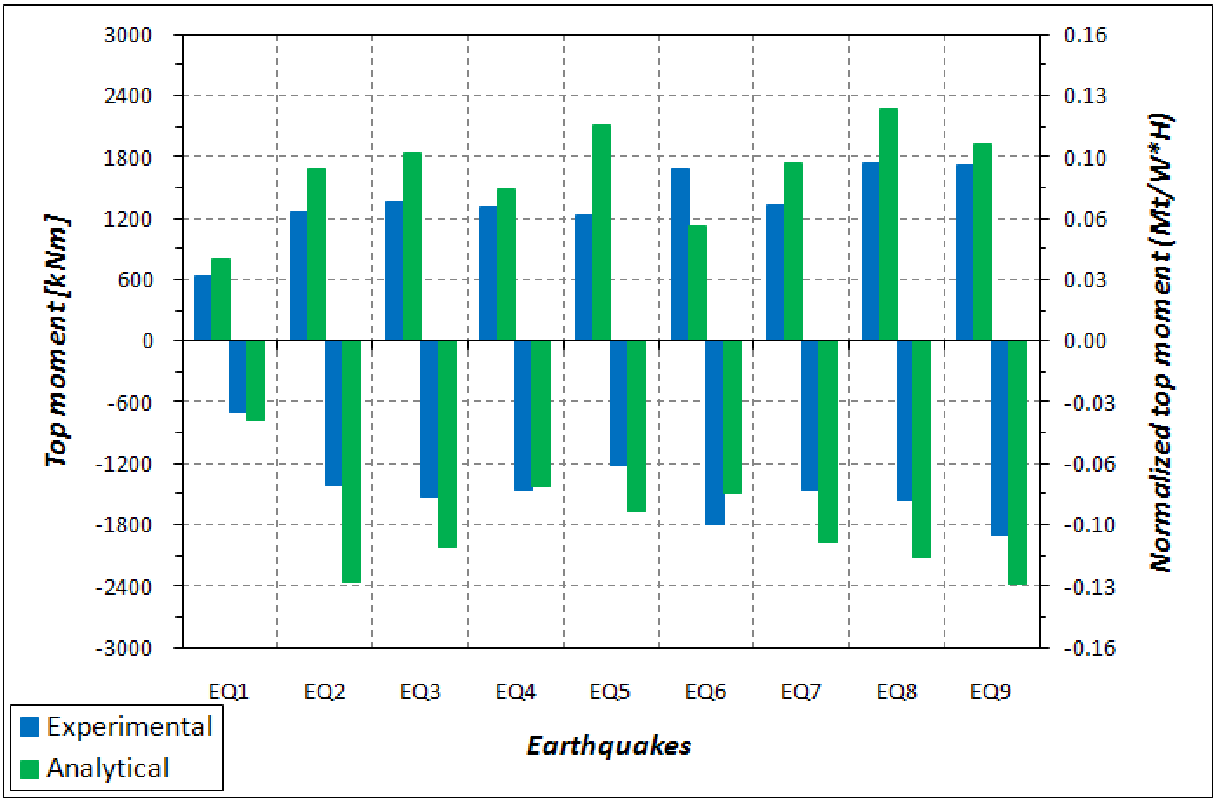

Figure 5.3: Experimental and analytical peak top moment

Large disagreement between analytical peak curvatures and experimental ones can be observed in Figure 5.4. Large differences are observed even for the first three earthquakes, where the model matches the response of the column in terms of displacement. Two causes are responsible for these errors: modeling assumptions and practical difficulties in curvature measurements.

The non reliability of the analytical model in predicting displacements after the third earthquake can be clearly identified in Figure 5.5. The peak displacement is overestimated for EQ1, with an error of +14% and +23% in the East (positive) and West (negative) direction, respectively. A good prediction of the peak displacement in both directions is observed in EQ2; the model exactly match the positive value and slightly overestimates the negative one of 2%. For EQ3 a good agreement is only obtained for the negative displacement, with an error of -1%; the positive one is affected by an error of -30%. After this earthquake, unreliable analytical values of the peak displacement are obtained, principally due to an incorrect residual displacement cumulation, see Figure 5.6.

Large error on the residual displacement can be observed starting from the beginning of the analytical simulation. Except for the first earthquake, where the residual displacement is zero in both the experimental and the analytical results, an error of +375% and +79% is

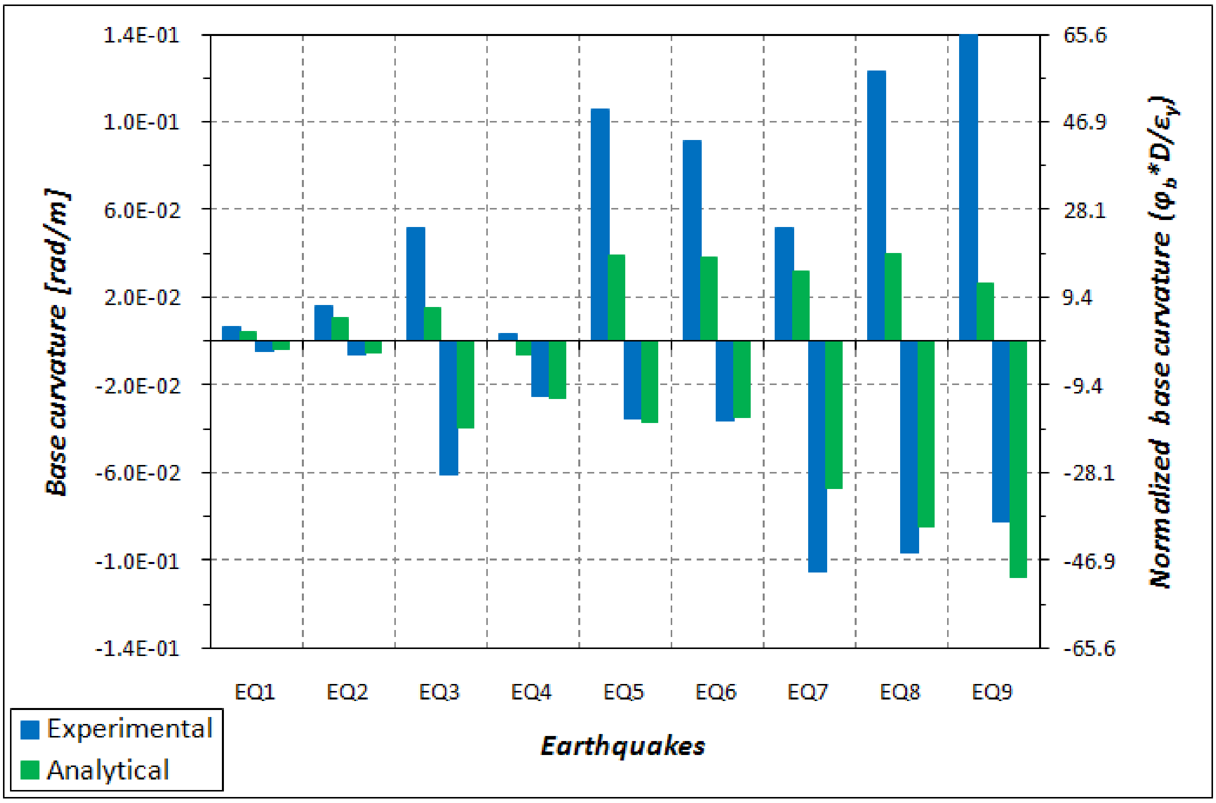

Figure 5.4: Experimental and analytical peak base curvature

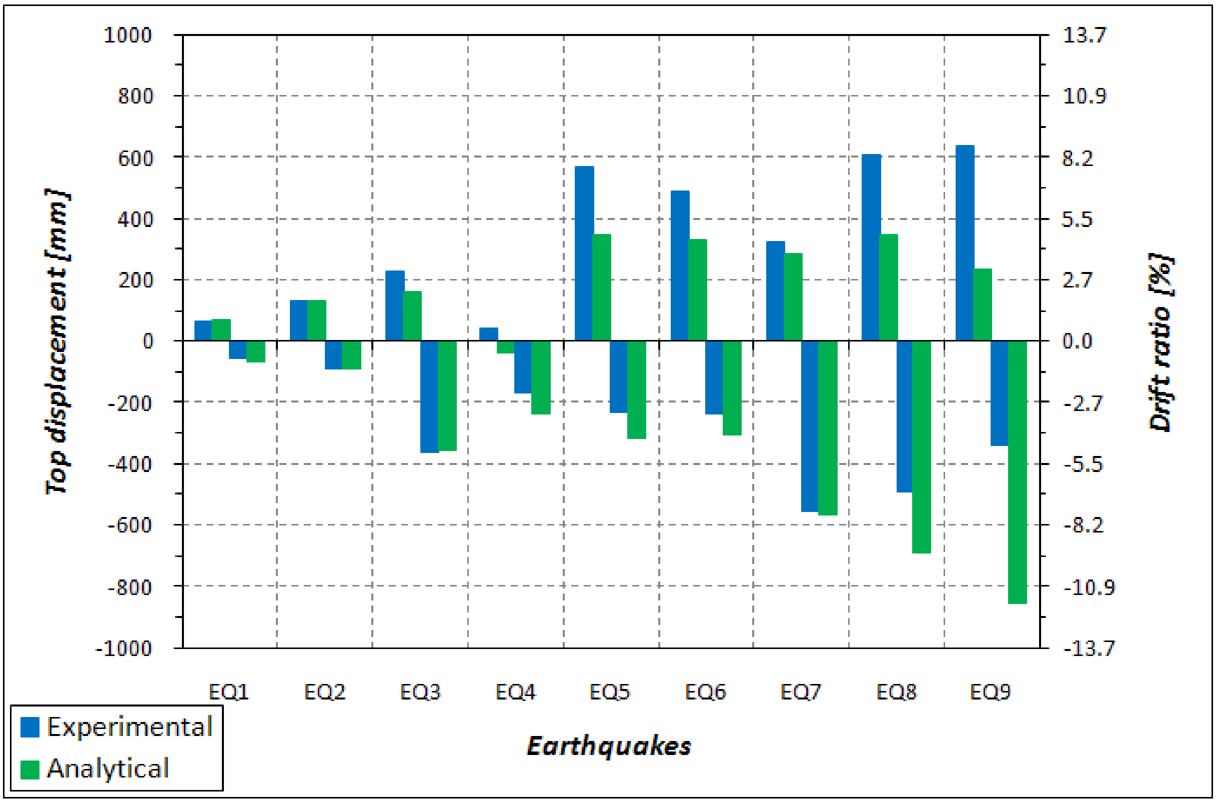

Figure 5.5: Experimental and analytical peak top displacement

obtained in EQ2 and EQ3, respectively. A large disagreement in the residual displacement after an earthquake causes a wrong initial configuration for the next one. This causes an error propagation earthquake after earthquake, compromising the reliability of the analytical model. This becomes significant after EQ3, which induces large post-elastic deformations. During testing, EQ5 inverted the sign of the residual displacement recorded at the end of EQ4, whereas the model gives the same sign, see Figure 5.6. After this point the model cumulates residual displacements in the West (negative) direction until EQ10; the experimental results, instead, show alternating signs according to the polarity of the ground motion main pulse.

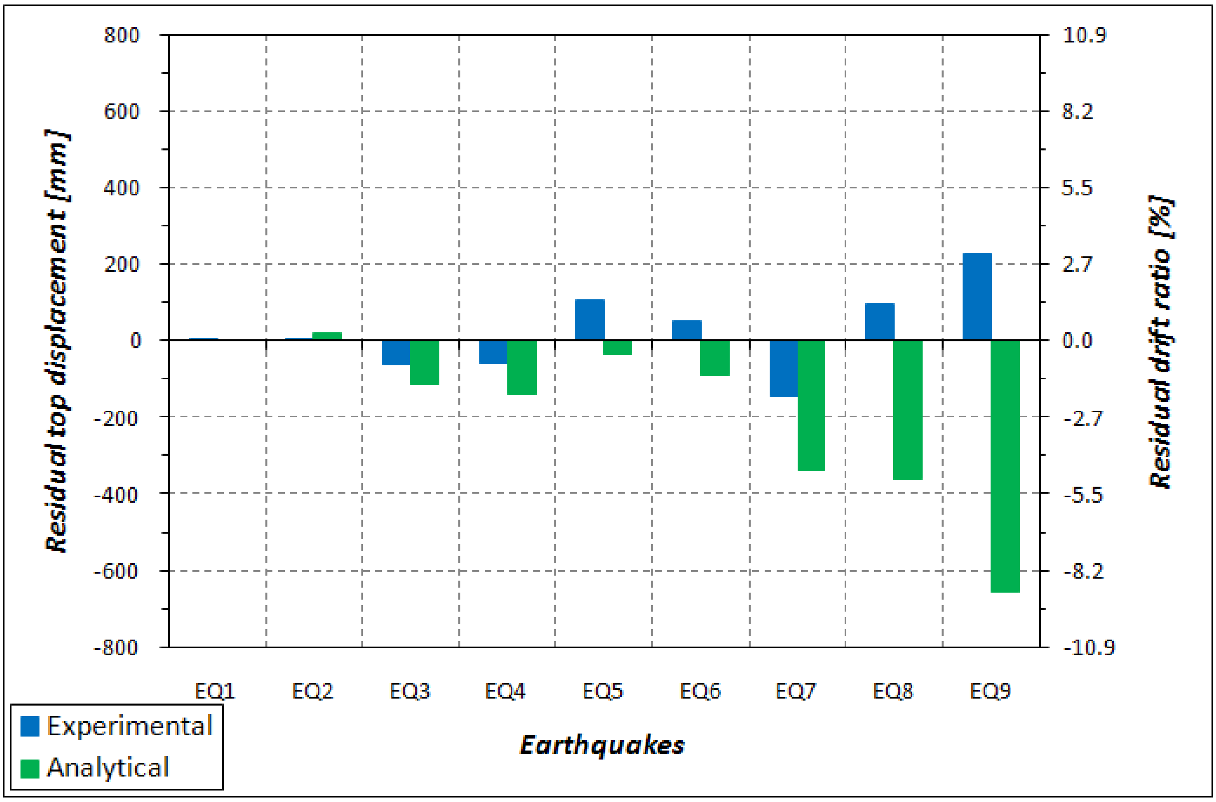

Figure 5.6: Experimental and analytical residual top displacement

5.2 Bending moment diagram

Figures 5.7 and 5.8 show a zoom of the base and the top moment time histories obtained from the experimental test and the analytical model under EQ3. As can be seen in these figures, higher modes affect the top moment more than the base one, resulting in more evident high-frequency wiggles. The shape of the moment diagram along the column height may vary during the dynamic excitation, depending on the relative sign of top and base moment, as shown in Figure 5.9.

Neglecting the distributed column mass, if a rectangular diagram occurs (Figure 5.9a), the base moment M_b, the top moment M_t, the base shear V_b and the effective height H_{eff} are given by:

$$M_b = M_t$$

$$V_b = 0$$

$$H_{eff} = \frac{M_b}{V_b} \to \infty$$

When the moment is distributed as a trapezoid (Figure 5.9b) the base moment M_b, the top moment M_t, the base shear V_b and the effective height H_{eff} are related by:

$$M_b = V_b \cdot H + M_t$$

$$V_b = \frac{M_b - M_t}{H}$$

$$H_{eff} = \frac{M_b}{V_b} > H$$

where H is the column height. After yielding, the base moment remains nearly constant, so that the base shear becomes smaller as the top moment increases. To account for this effect, the structure should be modeled at least as a two degree of freedom system, considering the horizontal translation and the rotation of the column top.

With a triangular moment diagram (Figure 5.9c) the base moment M_b, the top moment M_t, the base shear V_b and the effective height H_{eff} are given by:

$$M_b = V_b \cdot H$$

$$V_b = \frac{M_b}{H}$$

$$H_{eff} = \frac{M_b}{V_b} = H$$

where H is the column height. These relations are the ones used for a single degree of freedom system, which only accounts for the translation of the column top. The effective height is equal to the column height H.

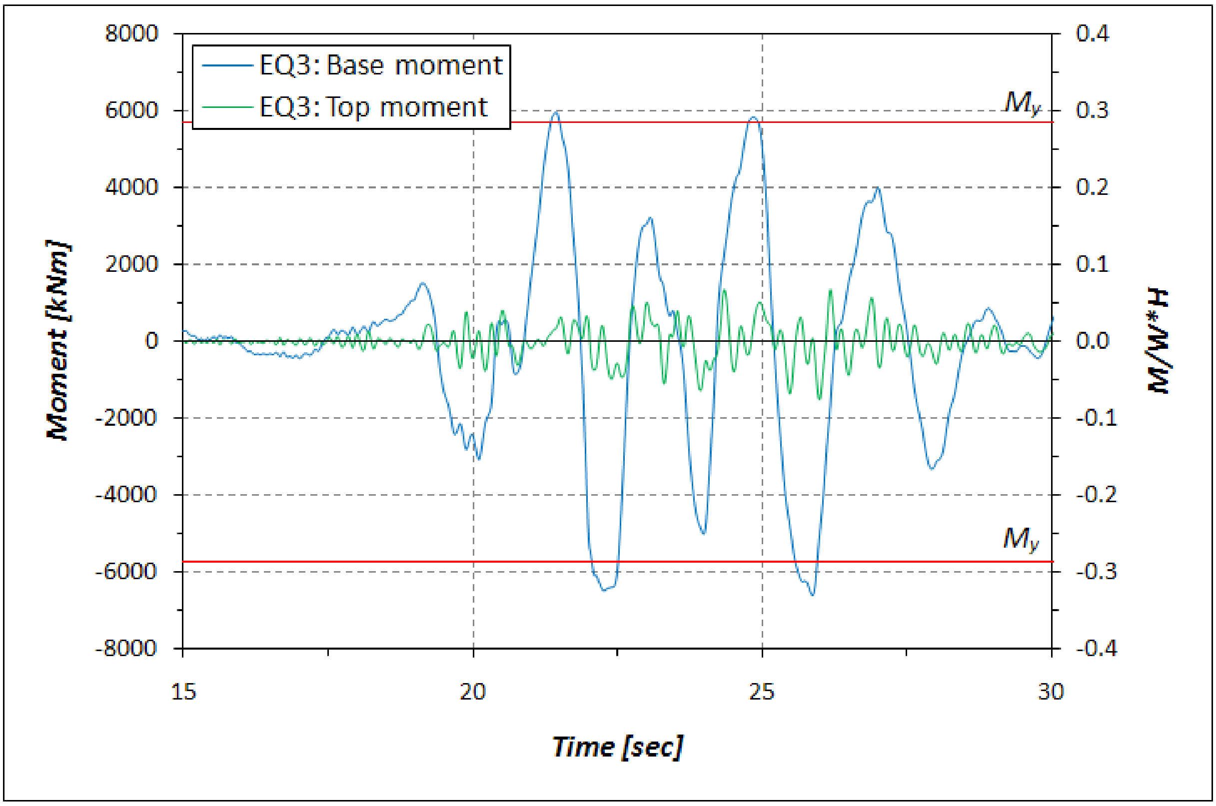

Figure 5.7: Experimental base moment and top moment time histories

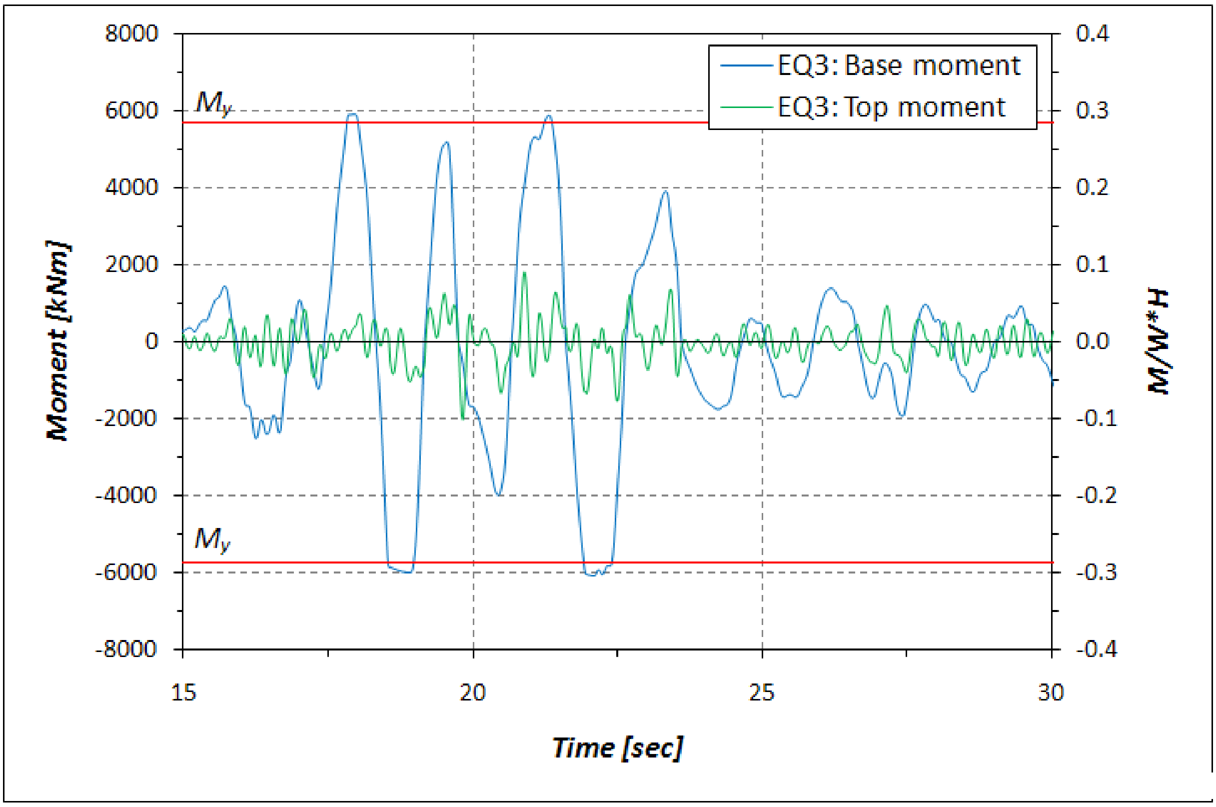

Figure 5.7: Analytical base moment and top moment time histories

The moment diagram shown in Figure 5.9d is attained when the top moment and the base moment induce a change in curvature sign. In this case, the base moment M_b, the top moment M_t, the base shear V_b and the effective height H_{eff} are given by:

$$M_b = V_b \cdot H - M_t$$

$$V_b = \frac{M_b + M_t}{H}$$

$$H_{eff} = \frac{M_b}{V_b} < H$$

For a given base moment (e. g. after plasticization) this moment distribution gives a larger base shear compared to the other ones. The effective height H_{eff} is smaller than the column height H, and is equal to elevation from the top footing to the point where the moment is equal to zero.

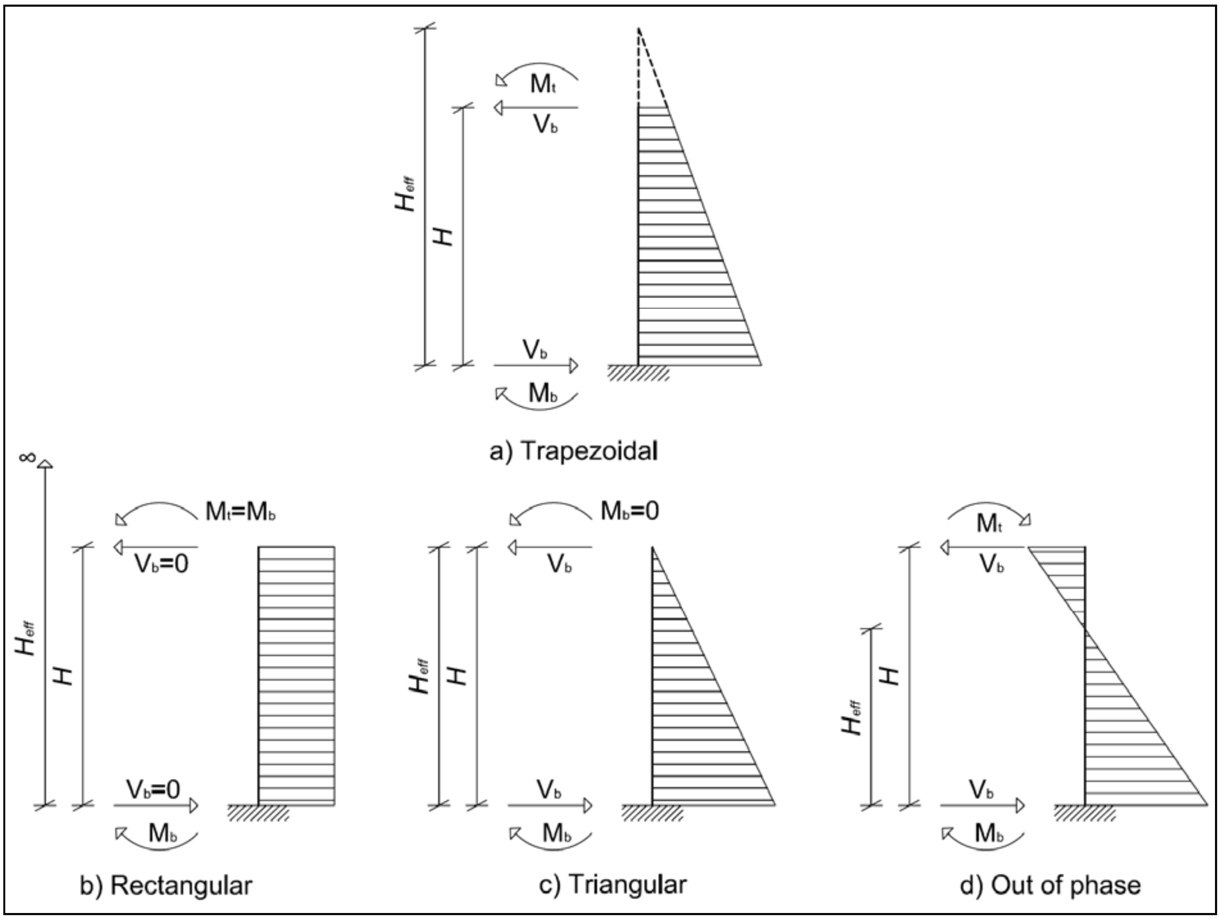

a) Trapezoidal

b) Rectangular

c) Triangular

d) Out of phase

Figure 5.7: Diagrams of the moment along the column height

6. Conclusions

Ten earthquake simulations were conducted on a full-scale bridge column built to current Caltrans design specifications. The 1.22-m (4-ft) diameter, 7.31-m (24-ft) long column was the second column ever tested at full scale under dynamic loading conditions.

Under the design earthquake (EQ3), the column exhibited maximum drift ratio of 4.93%, corresponding to a displacement ductility of 4.01. The damage observed after this earthquake simulation consisted mainly of cover spalling with no sign of longitudinal bar buckling.

Before collapsing the specimen sustained a maximum drift ratio of 8.69%, corresponding to a displacement ductility of 7.06, about twice as big as the one allowed by the specifications, which prescribe a displacement ductility of 4 for fixed base boundary conditions.

During testing, damage occurred in a concentrated plastic region at the base of the column. Figures 6.1 and 6.2 show the East and West side of the column base at the end of testing. A ductile response with large energy dissipation was recorded until the last simulated earthquake (EQ10). The behavior of the column was dominated by flexure and shear capacity was maintained throughout testing. Column cracks extended for the whole accessible height of the column by testing completion. However, concrete spalling, longitudinal bar buckling, and longitudinal bar facture were localized within 1.22 m (4 ft), or one column diameter, of the base of the column. Four longitudinal bars on the East face of the column fractured. Three longitudinal bars on the West face fractured and additional two bars developed partial cracks which did not propagate through the bar diameter. Thirteen longitudinal bars exhibited buckling deformation. Transverse hoops yielded but did not fracture and the concrete core remained largely intact, showing superficial crushing in correspondence of the buckled and fractured reinforcing bars. Through the test up to EQ10 the column fully preserved its vertical load bearing capacity.

Current design practices provided a safe and resilient structure: not only the system performed as desired under the design earthquake, maintaining gravity load carrying capacity, but it was able to sustain a much larger displacement demands before reaching collapse.

A bidimensional lumped plasticity, lumped mass model was created to predict the response of the specimen. Good agreement between the experimental and the analytical results was obtained until EQ3, when residual displacements were not relevant. After this ground motion, the residual displacements became significant and they were incorrectly anticipated by the model, resulting in an unreliable dynamic response. There were not significant errors in the prediction of the internal forces, such as base moment and base shear, whereas large errors were made in terms of deformations and top displacement.

Figure 6.1: East face of the column base at the end of testing

Figure 6.2: West face of the column base at the end of testing

7. Appendix A

Cylinders	Weight (g)	Weight (lb)	Unit weight (kN/m^3)	Unit weight (pcf)
F1-1	13350.9	29.43	23.56	149.90
F1-2	13349.8	29.43	23.55	149.89
F1-3	13340.6	29.41	23.54	149.79
F2-1	13188.0	29.07	23.27	148.08
F2-1	13375.0	29.49	23.60	150.18
F2-3	13343.0	29.42	23.54	149.82
F3-1	13304.0	29.33	23.47	149.38
F3-2	13315.0	29.35	23.49	149.50
F3-3	13166.0	29.03	23.23	147.83
AVG	**13303.6**	**29.33**	**23.47**	**149.37**

Table A.1: Weight and unit weight of footing concrete cylinders

Symbology:

F = Footing;

First number = Track number;

Second number = Cylinder number.

Cylinders	Weight (g)	Weight (lb)	Unit weight (kN/m^3)	Unit weight (pcf)
C1-1	13390.0	29.52	23.63	150.34
C1-2	13430.9	29.61	23.70	150.80
C1-3	13344.5	29.42	23.54	149.83
C2-1	13430.1	29.61	23.70	150.79
C2-2	13349.7	29.43	23.55	149.89
C2-3	13343.5	29.42	23.54	149.82
C3-1	13221.1	29.15	23.33	148.45
C3-2	13491.8	29.74	23.80	151.49
C3-3	13328.8	29.38	23.52	149.66
C4-1	13280.0	29.28	23.43	149.11
C4-2	13430.5	29.61	23.70	150.80
C4-3	13342.8	29.42	23.54	149.81
C5-1	13426.0	29.60	23.69	150.75
C5-2	13269.0	29.25	23.41	148.99
C5-3	13308.6	29.34	23.48	149.43
C6-1	13351.7	29.44	23.56	149.91
C6-2	13446.2	29.64	23.72	150.97
C6-3	13412.1	29.57	23.66	150.59
AVG	**13366.5**	**29.47**	**23.58**	**150.08**

Table A.2: Weight and unit weight of column concrete cylinders

Symbology:

C = Column;

First number = Track number;

Second number = Cylinder number.

Cylinders	Weight (g)	Weight (lb)	Unit weight (kN/m^3)	Unit weight (pcf)
M1-T1-1	13489.1	29.74	23.80	151.46
M1-T1-2	13238.2	29.19	23.36	148.64
M1-T2-3	13437.1	29.62	23.71	150.87
M1-T2-4	13192.0	29.08	23.28	148.12
M1-T3-5	13452.0	29.66	23.73	151.04
M1-T3-6	13359.8	29.45	23.57	150.00
M2-T2-1	13319.0	29.36	23.50	149.55
M2-T2-2	13371.6	29.48	23.59	150.14
M2-T3-3	13449.7	29.65	23.73	151.01
M2-T3-4	13360.0	29.45	23.57	150.01
M2-T4-5	13398.7	29.54	23.64	150.44
M2-T4-6	13187.9	29.07	23.27	148.07
M2-T5-7	13572.9	29.92	23.95	152.40
M2-T5-8	13577.0	29.93	23.96	152.44
M3-T1-1	13355.6	29.44	23.56	149.96
M3-T1-2	13363.9	29.46	23.58	150.05
M3-T2-3	13464.8	29.68	23.76	151.18
M3-T2-4	13450.7	29.65	23.73	151.03
M3-T3-5	13376.8	29.49	23.60	150.20
M3-T3-6	13414.4	29.57	23.67	150.62
M3-T4-7	13478.3	29.71	23.78	151.34
M3-T4-8	13444.8	29.64	23.72	150.96
M3-T5-9	13474.4	29.71	23.77	151.29
M3-T5-10	13544.5	29.86	23.90	152.08
M3-T6-11	13529.9	29.83	23.87	151.91
M3-T6-12	13603.7	29.99	24.00	152.74
M3-T7-13	13461.1	29.68	23.75	151.14
M3-T7-14	13428.3	29.60	23.69	150.77
AVG	**13421.3**	**29.59**	**23.68**	**150.69**

Table A.3: Weight and unit weight of superstructure concrete cylinders

Symbology:

M1 = Central block;

M2 = End blocks;

M3 = Side blocks;

Ti = Track number;

Last number = Cylinder number.

Superstructure blocks	**Weight**	
	(kN)	**(kips)**
One central block	444.1	99.8
Two end blocks	766.3	172.2
Two side-blocks	1111.9	249.9
TOT	**2322.3**	**521.9**

Table A.4: Weights of the superstructure blocks

References

Caltrans, 2004. *Bridge Design Specification*, California Department of Transportation, Sacramento, California, September 2004.

Caltrans, 2006-a. *Seismic Design Criteria*, Version 1.4, California Department of Transportation, Sacramento, California, June 2006.

Caltrans, 2006-b. *Standard Specification*, California Department of Transportation, Sacramento, California, May 2006.

Caltrans. *ARS Online (v.1.0.4)*. Web site: < http://dap3.dot.ca.gov/shake_stable/>, October 2010.

Carr, 2002. Carr A. J., *Computer Program Library, Ruaumoko*, University of Canterbury, Christchurch, New Zealand, May 2002.

Carr, 2008. Carr A. J., *Volume 2: User Manual for the 2-Dimensional Version, Ruaumoko2D*, Ruaumoko Manual, University of Canterbury, Christchurch, New Zealand, November 2008.

Chopra, 1995. Anil K. Chopra, *Dynamic of Structure - Theory and Application to Earthquake Engineering*, University of California at Berkeley, 1995.

Clough 1993. Clough R. W., and Penzein J., *Dynamic of Structures*, New York, N.Y., McGraw-Hill, Inc.

Collins and Mitchell 1991. Collins M. P., and Mitchell D., *Prestressed Concrete Structure*, Prentice-hall, Inc., Englewood Cliffs, New Jersey, 1991.

FEMA-273, 1997. *NEHRP Guidelines for the Seismic Rehabilitation of Buildings*, Federal Emergency Management Agency, Washington, D.C, October 1997.

Giberson, 1967. Melbourne Fernald Giberson, *The Response of Nonlinear Multi-story Structures Subjected to Earthquake Excitation*, California Institute of Technology, Pasadena, California, May 1967.

Kuebitz, 2002. Kuebitz K.C., *Development and Calibration of Columna, a Windows-based Moment-Curvature Program for Columns of Arbitrary Cross-section,* MS thesis, Department of Structural Engineering, UC San Diego, La Jolla, California, 2002.

Marder, 1988. Mander J. B., M. J. N. Priestely, and Park R., *Theoretical stress-strain model for confined concrete,* ASCE Journal of Structural Engineering, 114(8): 1804-1826, August 1988.

NEES. *Network for Earthquake Engineering Simulation at UC San Diego*. Web site: <http://nees.ucsd.edu/>, October 2010.

PEER. *Pacific Earthquake Engineering Research Center – PEER Ground Motion Database*. Web site: < http://peer.berkeley.edu/peer_ground_motion_database/site>, October 2010.

Priestley et al, 2007. M. J.N. Priestley, G. M. Calvi, M. J. Kowalsky, *Displacement-Based Seismic Design of Structures*, IUSS PRESS, Pavia, Italy, 2007.

Restrepo-Posada, 1994. J. I. Restrepo-Posada, *Variables Affecting Cyclic Behavior of Reinforcing Steel*, ASCE Journal of Structural Engineering, Vol. 120, No. 12, November 1994.

Schoettler 2010. Matthew John Schoettler, *Seismic Demands in Precast Concrete Diaphragms,* Department of Structural Engineering, University of California San Diego, 2010.